Spatiotemporal investigation of *Xanthomonas oryzae* pv. *oryzae* infection trajectories and the functional impact of *SWEET* promoter editing

Inaugural-Dissertation

zur Erlangung des Doktorgrades
der Mathematisch-Naturwissenschaftlichen Fakultät
der Heinrich-Heine-Universität Düsseldorf

vorgelegt von

Laura Redzich
aus Gelsenkirchen

Düsseldorf, Oktober 2025

Heinrich Heine
Universität
Düsseldorf

CEPLAS

aus dem Institut für Molekulare Physiologie,
der Heinrich-Heine Universität Düsseldorf

Gedruckt mit der Genehmigung der
Mathematisch-Naturwissenschaftlichen Fakultät der
Heinrich-Heine Universität Düsseldorf

Berichterstatter:

1. Prof. Dr. Wolf B. Frommer
2. Prof. Dr. Jane E. Parker

Tag der mündlichen Prüfung:

Eidesstattliche Erklärung

Ich versichere an Eides Statt, dass die Dissertation von mir selbständig und

ohne unzulässige fremde Hilfe unter Beachtung der „Grundsätze zur Sicherung guter wissenschaftlicher Praxis and der Heinrich-Heine Universität Düsseldorf“ erstellt worden ist.

Die Dissertation habe ich in der vorgelegten oder in ähnlicher Form noch bei keiner anderen Institution eingereicht.

Ich habe bisher keine erfolglosen Promotionsversuche unternommen.

Düsseldorf, den 30.10.2025

_____

Laura Redzich

1 Summary

Chapter 1: Zusammenfassung

Xanthomonas oryzae pv. *oryzae* (Xoo) ist ein xylembesiedelndes Bakterium, dessen Virulenz von Transkriptionsaktivator-ähnlichen Effektoren (TALe) abhängt, die *SWEET* Transporter der Wirtspflanze induzieren und so den Kohlenstofffluss umlenken. Unter Verwendung translatorischer SWEET11a-GUS-Reporterlinien, fluoreszenzmarkierter Xoo-Stämme, konfokaler Bildgebung und Elektronenmikroskopie lässt sich die Kolonisation entlang des Xylems in Phasen gliedern: Stäbchenförmige Zellen haften in der initialen und basipetalen Ausbreitung an Xylemporen, während Xoo für laterale Ausbreitung und das Überwinden von Leitbündeln in auffällig filamentöse Formen differenziert. Diese Filamente durchqueren die Bündelscheide und dringen in das Mesophyll ein, was darauf hindeutet, dass Chlorose und Nekrose nicht nur aus hydraulischer Blockade resultieren, sondern auch aus direkter Gewebeschädigung. Filamentierung, als Virulenzverstärker bei mehreren humanpathogenen Bakterien bekannt, stellt somit wahrscheinlich ein Entwicklungsprogramm dar, das die Fitness von Xoo *in planta* erhöht.

Um zu prüfen, ob Wurzeln als Eintrittspforte für Xoo dienen können, habe ich ein schnelles Wurzelinfektionsprotokoll etabliert. Der Wurzel-Clip-Assay zeigt TALe-SWEET-Gen-für-Gen-Interaktionen im Wurzelxylem: Die Induktion von *SWEET11a* markiert eine fortschreitende Wurzelinfektion, jedoch überqueren die Bakterien den Koleoptilknoten nicht und Keimlinge entwickeln keine systemischen Symptome. Rhodamin-B-Tracer bestätigen einen intakten Xylemtransport. Praktisch beschleunigt dieser Wurzel-Assay das Monitoring von SWEET-spezifischen TALe-Repertoires gegenüber der Blatt-Clip-Infektion um etwa das Vierfache.

Auf Ebene der Wirts-Promotoren zeigen eine Analyse von >3.000 Reisgenomen, Chromatinzugänglichkeits-Profilierung (MOA-seq) und translatorische Reporter-Assays, dass zentrale *SWEET*-EBEs ungewöhnlich konserviert sind, in offenem Chromatin nahe cis-Elemente liegen und die Proteinproduktion messbar justieren. Die Phänotypisierung von *sweet13*- und *sweet14* knockouts impliziert Funktionen von SWEETs unter abiotischen Konditionen. EBEs haben somit eine duale Rolle: einerseits als Suszeptibilitätsschalter, andererseits als *bona-fide* cis Elemente.

Um den TALe-Angriff in Abwehr umzulenken, verfolgte ich „TAL-Effektor-Fallen“: Prime-Editing von EBEs vor Kandidaten-Exekutorgenen und ein kombinatorisches Screening auf geteilte EBEs zwischen asiatischen und afrikanischen Xoo. Zwar gelang eine Proof-of-Concept-Integration von EBE_{AvrXa7} in den Promotor von *OsMST4* nicht, doch identifiziert die Arbeit Optimierungsansätze und stützt die Machbarkeit breit wirksamer „Designer-Exekutoren“ auf Basis von TALe-Spezifitätsregeln.

Zusammengefasst identifiziert diese Arbeit (i) einen bisher nicht beschriebenen Xoo Morphotyp während der Infektion, (ii) eine anatomische Barriere, die die Ausbreitung von der Wurzel zum Spross begrenzt, (iii) Informationen über SWEET-EBEs als duale regulatorische Knoten zur strategischen Promotor-Editierung, (iv) einen Weg zu prime-editierten „Designer-Exekutoren“ und (v) methodische Innovationen zur Erweiterung des Werkzeugkastens für die Erforschung des Xoo-Reis-Pathosystems.

2 Summary

Chapter 2: Summary

Xanthomonas oryzae pv. *oryzae* (Xoo) is a xylem-invading bacterium whose virulence depends on transcription activator–like effectors (TALes) that induce host SWEET sucrose efflux transporters and redirect the host carbon flux. Using translational SWEET11a–GUS reporter lines, fluorescently tagged Xoo, confocal imaging, and electron microscopy, colonization resolves into phases along the vasculature: rod-shaped cells attach to xylem pits during initial and basipetal progression, while Xoo differentiates into striking filamentous forms during lateral spread and vascular bundle breach. Filaments traverse bundle sheath and enter mesophyll, indicating that chlorosis and necrosis reflect not only hydraulic blockage but also direct tissue damage. Filamentation known to potentiate virulence in several human pathogens, thus likely represents a developmental program that enhances Xoo fitness *in planta*.

To probe whether roots can serve as an entry route for Xoo, I established a rapid root infection protocol. The root clipping assay demonstrates TALe–SWEET gene-for-gene interactions in root xylem: *SWEET11a* induction marks progressive root infection, yet bacteria do not cross the coleoptile node and seedlings fail to develop foliar blight. Rhodamine B tracers confirm intact xylem transport. Practically, this root assay accelerates monitoring of *SWEET* specific TALe repertoire approximately fourfold compared to leaf clip infection

At the host promoter level, a survey of >3,000 rice genomes, chromatin accessibility profiling (MOA-seq), and translational reporter assays demonstrate that key *SWEET* EBEs are unusually conserved, lie in open chromatin near core motifs, and measurably tune protein output. Phenotyping *sweet13* and*14* knockouts implicates roles in flag-leaf angle and root elongation with minimal biomass penalties. Together, EBEs emerge as dual-use cis-elements, as susceptibility switches and *bona fide* cis elements.

To convert TALe attack into defense, I pursued “TAL effector traps”: prime editing of EBEs upstream of candidate executor genes and a combinatorial screen for cross-lineage, shared EBEs. Although a proof-of-concept insertion of EBE_{AvrXa7} into the promoter of *OsMST4* insertion was not recovered, the work discusses optimization strategies and supports the feasibility of broad-spectrum, designer executors grounded in TALe specificity rules.

Collectively, this thesis (i) defines a morphogenetic switch that enables Xoo’s tissue invasion, (ii) reveals an anatomical barrier limiting root-to-shoot disease, (iii) establishes *SWEET* EBEs as dual-use regulatory hubs guiding promoter-editing design, (iv) charts a path toward prime-edited “designer executors,” and (v) delivers insights into innovative methodologies to advance the toolkit for understanding the Xoo-rice pathosystem.

3 Table of Contents

Chapter 3: Table of Contents

4 General Introduction

Understanding plant–pathogen interactions is key to effective breeding strategies

The origin of agriculture during the Neolithic Revolution (~10000 B.C.) laid the foundation for modern civilization. A cornerstone of the transition from mobile foraging to sedentary societies was crop domestication, including rice. Asian rice (*Oryza sativa*) was first domesticated in East Asia roughly 8,000–10,000 years ago, while African rice (*Oryza glaberrima*) about 3,000 years ago ((Stein *et al.*, 2018). Selection for agronomic traits such as non-shattering, synchronized ripening and increased yield narrowed genetic diversity relative to wild progenitors, with emerging evidence that domestication can erode immune receptor repertoires and, by extension, adaptive capacity (Bourne *et al.*, 2025). This reduced allelic diversity presents a structural challenge for food security as climate variability intensifies and demand for agricultural output grows (FAO, 2025; IPCC, 2022). Moreover, climate change is expected to exacerbate pathogen pressure on plants (Bebber *et al.*, 2013; Chaloner *et al.*, 2021; IPCC, 2022). Plant breeding is a central lever to generate novel plant varieties that are resilient towards abiotic and biotic challenges. Historically, breeding relied on undirected mutagenesis that introduced random genomic changes. Beneficial alleles had to be located and validated phenotypically. By contrast, directed mutagenesis enables precise locus-specific edits in elite germplasm (Chen *et al.*, 2024). Effective breeding strategies that employ directed mutagenesis require a robust understanding of plant biology, physiology, immunity and development. Therefore, in the context of disease resistance, mechanistic insights into plant-pathogen interactions at the cellular and molecular level are essential to guide rational design of resistance traits via directed mutagenesis.

Pathogens hijack host carbon allocation pathways

Higher plants allocate carbon sources from source tissues to carbon sinks. Mature photosynthetic leaves typically function as sources, fixing CO_2 and synthesizing sucrose, which is loaded into the phloem and translocated to sinks such as developing leaves, roots, fruits and seeds (Julius *et al.*, 2017). However, the source-sink relationship of carbon partitioning can be perturbed by pathogens. Infected areas can be manipulated to mimic a sink and redirect the carbon flow (Chen *et al.*, 2010; Bezrutczyk *et al.*, 2018). *Xanthomonas* bacteria induce sucrose transporter genes with transcription-activator like effectors (TALes). TALes act as eukaryotic transcription

factors and bind sequence specifically to effector binding elements (EBEs) in host gene promoters. In crop plants such as rice, cassava and cotton, *Xanthomonas* employs TALe binding to EBEs to induce *SWEET* sucrose exporter genes (Cox *et al.*, 2017; Eom *et al.*, 2019; Cohn *et al.*, 2014). Because the TALe-EBE interaction is sequence specific, single nucleotide polymorphism of the EBE can block binding (Schepler-Luu *et al.*, 2023; Oliva *et al.*, 2019; Elliott *et al.*, 2024). Thus, natural or engineered EBE polymorphisms act as recessive resistant alleles. Although engineered EBE variants do not interfere with the coding sequence of SWEETs, edits could abolish cis elements in *SWEET* promoters and disturb the endogenous regulation of *SWEET* expression.

Research objectives and thesis outline

From a physiological perspective, SWEET transporters are central to connecting source and sink tissues. From a pathology perspective, SWEETs are gates that pathogens force open to access the plant's sugar stores. This dual importance has made SWEET genes attractive targets for genetic engineering: by tweaking the "locks" on the sugar reservoirs. One potential limitation of EBE editing as a long-term solution is pathogen evolution. If a Xoo population is confronted with rice plants whose SWEET promoters it can no longer induce, there is strong selection for the pathogen to either (a) acquire new TAL effectors that recognize a different sequence in those promoters, or (b) mutate existing TAL effectors to adapt to the changed sequence. There is evidence that Xoo indeed uses TALe variability to overcome host resistance (Ji *et al.*, 2016). Therefore, it is implicate that we advance our understanding of Xoo infection biology to inform new strategies for breeding of disease resistance.
The overarching goal of this doctoral research was to deepen our understanding of how the rice bacterial blight pathogen *Xanthomonas oryzae* pv. *oryzae* interferes with plant carbon allocation networks and to develop novel strategies for disease. Specifically, I aimed to:

- **Objective 1: Elucidate the *in planta* colonization patterns and morphological adaptations of Xoo during infection.**
  I aimed to identify the spatiotemporal infection route of Xoo, including its differentiation into filamentous forms, and how this relates to accessing host sugar resources. This objective addresses a knowledge gap in Xoo infection biology – particularly, how the pathogen navigates the xylem environment and breaches into surrounding tissues *(addressed in Chapter 5., published in part as "Differentiation of Xanthomonas oryzae pv. oryzae in vitro and during rice leaf infection", BioRxiv, doi.org/10.1101/2025.10.12.680524).*

- **Objective 2: Investigate alternative infection routes of Xoo, particularly root infection and systemic movement.**
  While Xoo is traditionally known as a foliar pathogen, we explored the hypothesis that Xoo can infect rice via roots and move upward, which has implications for disease epidemiology and host-pathogen interactions in belowground tissues. I developed a rapid root inoculation system to test Xoo transmission from roots to shoots and examined whether similar molecular interactions (e.g., SWEET activation) occur in roots *(addressed in Chapter 6., published in part as "Restricted transmission of Xanthomonas oryzae pv. oryzae from rice roots to shoots detected by a rapid root infection system", BioRxiv, doi.org/10.1101/2025.08.13.670017).*

- **Objective 3: Evaluate the potential pleiotropic effects of disrupting pathogen-targeted SWEET genes on rice physiology and stress responses.**
  Building on the concept of SWEET promoter editing for resistance, I wanted to ensure that such modifications do not inadvertently make the plant more vulnerable to diverse abiotic conditions or developmental defects. Therefore, I assessed chromatin accessibility, effects of promoter truncations and exposure to diverse abiotic conditions to detect any trade-offs associated with engineered disease resistance *(addressed in Chapter 7).*

- **Objective 4: Develop a TAL effector trap strategy using prime editing.**
  In a proof-of-concept approach, I attempted to engineer rice plants to counteract the sink-strenghting effect imposed by Xoo via *SWEET* induction. To achieve this, I selected a major Xoo TALe and employed prime editing to insert its corresponding EBE upstream of a candidate defense gene (*addressed in Chapter 8).*

- **Objective 5**: **Develop and apply ratiometric Matryoshka MSucMeter sensors to monitor dynamic changes in sucrose levels during pathogen attack.**
  To better understand how Xoo alters carbon allocation *in planta*, I aimed to establish a tool for real-time sucrose detection (*addressed in Chapter 9)*.

- **Objective 6: Visualize the *Xanthomonas* injectisome *in planta* to unravel the spatial dynamics of TAL effector delivery during host colonization.**
  To better understand when and where TAL effectors are delivered into host cells, I aimed to track the localization and assembly of the type III secretion system during infection. The aim was to correlate T3SS location with host tissue colonization, cell type specificity, and effector delivery during infection (*addressed in Chapter 10)*.

- **Objective 7: Identify the *OsSWEET* promoter proxisome.**
  To gain insight into the broader regulatory environment of TAL effector-targeted susceptibility genes, I aimed to define the local nuclear proteome at *OsSWEET* promoters. Lation (*addressed in Chapter 11*).

References

Bebber, D.P., Ramotowski, M.A.T. and Gurr, S.J. (2013) Crop pests and pathogens move polewards in a warming world. *Nat. Clim. Change*, **3**, 985–988.

Bezrutczyk, M., Yang, J., Eom, J.-S., et al. (2018) Sugar flux and signaling in plant-microbe interactions. *Plant J. Cell Mol. Biol.*, **93**, 675–685.

Bourne, N., Walker-Hale, N., Dunning, L. and Chomicki, G. (2025) Domestication Reduces Plant Immune Receptor Gene Repertoires Across Lineages. *Genome Biol. Evol.*, **17**, evaf147.

Chaloner, T.M., Gurr, S.J. and Bebber, D.P. (2021) Plant pathogen infection risk tracks global crop yields under climate change. *Nat. Clim. Change*, **11**, 710–715.

Chen, F., Chen, L., Yan, Z., et al. (2024) Recent advances of CRISPR-based genome editing for enhancing staple crops. *Front. Plant Sci.*, **15**, 1478398.

Chen, L.Q., Hou, B.H., Lalonde, S., et al. (2010) Sugar transporters for intercellular exchange and nutrition of pathogens. *Nature*, **468**, 527–532.

Cohn, M., Bart, R.S., Shybut, M., et al. (2014) Xanthomonas axonopodis virulence is promoted by a transcription activator-like effector - Mediated induction of a SWEET sugar transporter in Cassava. *Mol. Plant. Microbe Interact.*, **27**, 1186–1198.

Cox, K.L., Meng, F., Wilkins, K.E., et al. (2017) TAL effector driven induction of a SWEET gene confers susceptibility to bacterial blight of cotton. *Nat. Commun. 2017 81*, **8**, 1–14.

Elliott, K., Veley, K.M., Jensen, G., et al. (2024) CRISPR/Cas9-generated mutations in a sugar transporter gene reduce cassava susceptibility to bacterial blight. *Plant Physiol.*, **195**, 2566–2578.

Eom, J.-S., Luo, D., Atienza-Grande, G., et al. (2019) Diagnostic kit for rice blight resistance. *Nat. Biotechnol.*, **37**, 1372–1379.

FAO (2025) *The third report on the state of the world's plant genetic resources for food and agriculture* 1st ed., Rome: FAO Commission on Genetic Resources for Food and Agriculture Assessments.

IPCC (2022) *Climate change 2022 – impacts, adaptation and vulnerability: working group II contribution to the sixth assessment report of the intergovernmental panel on climate change* 1st ed., Cambridge University Press, Cambridge, UK and New York, NY, USA: Cambridge University Press.

Ji, Z., Ji, C., Liu, B., Zou, L., Chen, G. and Yang, B. (2016) Interfering TAL effectors of *Xanthomonas oryzae* neutralize R-gene-mediated plant disease resistance. *Nat. Commun.*, **7**, 13435.

Julius, B.T., Leach, K.A., Tran, T.M., Mertz, R.A. and Braun, D.M. (2017) Sugar transporters in plants: new insights and discoveries. *Plant Cell Physiol.*, **58**, 1442–1460.

Oliva, R., Ji, C., Atienza-Grande, G., et al. (2019) Broad-spectrum resistance to bacterial blight in rice using genome editing. *Nat. Biotechnol.*, **37**, 1344–1350.

Schepler-Luu, V., Sciallano, C., Stiebner, M., et al. (2023) Genome editing of an African elite rice variety confers resistance against endemic and emerging *Xanthomonas oryzae* pv. *oryzae* strains. *eLife*, **12**, e84864.

Stein, J.C., Yu, Y., Copetti, D., et al. (2018) Genomes of 13 domesticated and wild rice relatives highlight genetic conservation, turnover and innovation across the genus *Oryza*. *Nat. Genet.*, **50**, 285–296.

5 Differentiation of *Xanthomonas oryzae* pv. *oryzae in vitro* and during rice leaf infection

available as preprint on bioRxiv:
https://doi.org/10.1101/2025.10.12.680524

Contributions
Experiments with GUS reporter lines were performed jointly with Zongyi Ma. Autofluorescence scans were performed with support of Andrea Restrepo-Escobar. Van Schepler-Luu and Eliza P.I. Loo supervised the rice team. Miriam Bäumers provided training in scanning electron microscopy and supported protocol optimization. I performed analyses, created the figures and wrote manuscript. Wolf. B. Frommer advised on manuscript writing and supported editing and revision.

Highlights

- Xoo produces filamentous morphology, which is transient and yields pleomorphic progenies *in vitro*
- *In planta*, initial attachment of rod-shaped Xoo is detected at xylem pits
- The Xoo infection front migrates basipetally in the vascular bundle and progresses laterally from major to minor veins via transverse veins
- Xoo breaks out of the xylem vessels and enter the neighboring xylem parenchyma
- Xoo assumes filamentous morphology that can traverse from the xylem across the bundle sheath into mesophyll tissue
- Mobility in xylem vessels depends predominantly on rod-shaped Xoo, while infection of mesophyll tissue at later stages appears to be linked to filamentous morphology

Summary

Xanthomonas oryzae pv. *oryzae* (Xoo) is classified as a xylem pathogen responsible for bacterial blight of rice causing substantial yield losses in Asia and Africa. Xoo virulence depends on the ability to trigger SWEET sucrose efflux transporters in the xylem parenchyma (XP) by injection of transcription activation like effectors (TALe) into host cells, likely to access host-derived sucrose. To establish infection, Xoo must overcome physical barriers, immune responses and the hydraulic xylem flow. To gain insights into the colonization process, we used translational *SWEET11a-GUS* reporter lines, scanning electron microscopy, and confocal laser scanning microscopy of Xoo tagged with a fluorescent protein. We found that Xoo can differentiate *in vitro* into filamentous forms. We mapped the infection route of Xoo along the vasculature, identified distinct spatiotemporal phases of Xoo colonization marked by rod-shaped and, notably, filamentous Xoo cells. Rod-shaped Xoo were found to attach to xylem pits during basipetal progression of the infection. Notably, we found that at later infection stages, Xoo could enter the XP. Strikingly, Xoo adopted a filamentous phenotype that traversed bundle sheath cells and entered mesophyll cells. Chlorosis and necrosis of leaves is thus likely not just due to blockage of xylem flow, but to direct tissue damage. Filamentation had been reported as important for virulence of human pathogens e.g. *Yersinia pestis,* uropathogenic *E. coli* and *Shigella* and had been

associated to sugar utilization in *Bacillus subtilis*. We thus hypothesize that Xoo differentiation during host colonization is critical for virulence.

Graphical abstract

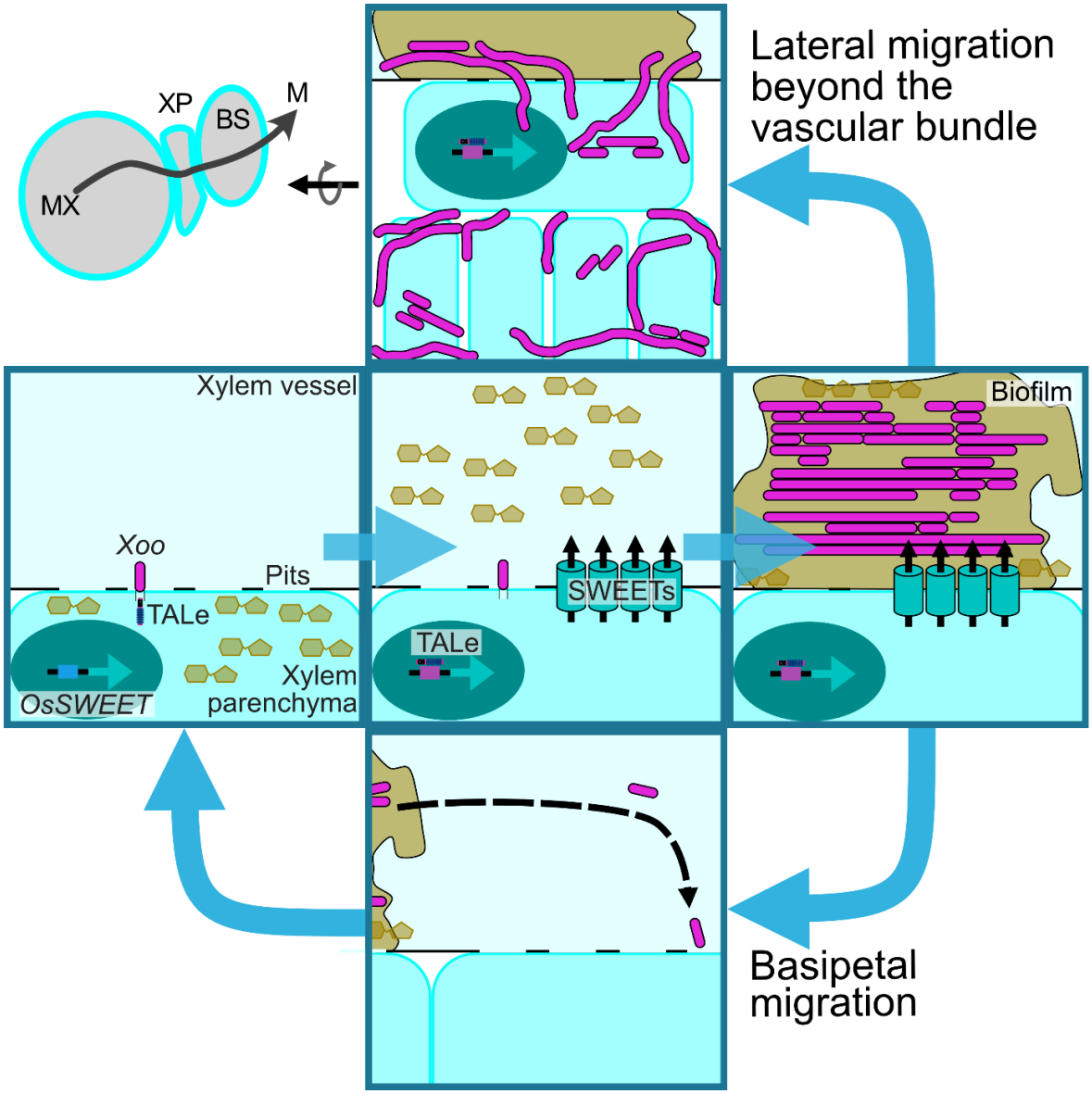

Keywords

Bacterial blight, colonization, filamentation, cell division, septation, virulence, sucrose, SWEET, pleomorphic

Introduction

Pests and pathogens cause massive yield losses worldwide and impact food security (Savary *et al.*, 2019). Among the different organism that cause losses, phytopathogenic bacteria are a major factor (Mulungu, 2024). 5-20 % of annual yield losses are reported for the causal agent of bacterial blight, *Xanthomonas oryzae* pv. *oryzae* (Xoo) in Asia and Africa (Arra *et al.*, 2025; Savary *et al.*, 2019). The gram-negative bacterium Xoo enters rice (*Oryza sativa*) leaves through hydathodes or wounds, enters xylem vessels and subsequently multiplies in the xylem (Hilaire *et al.*, 2001; Mew and Huang, 1984). A critical aspect of Xoo virulence is its dependence on host-derived sucrose (Schepler-Luu *et al.*, 2023; Oliva *et al.*, 2019; Eom *et al.*, 2019). To access sucrose, Xoo utilizes a type III secretion system (T3SS) to deliver transcription activator-like effectors (TALe) to adjacent xylem parenchyma cells (XP) that are translocated into nuclei and induce *SWEET* sucrose uniporter genes (Chen *et al.*, 2010; Eom *et al.*, 2019; Oliva *et al.*, 2019). The induction of *SWEET* uniporters likely causes sucrose efflux from XP cells, where it becomes available to Xoo through bacterial transporters and sucrose hydrolases encoded by the sucrose utilization cistron *sux* (Zöllner *et al.*, 2025).

Xoo has to overcome multiple challenges during host infection, e.g., acquire a full complement of all essential nutrients, migrate against the xylem stream, resist the forces of the flow, and evade host immune system responses. Extracellular sucrose acts as chemoattractant for Xoo, induces the production of quorum sensing molecules and taken up and metabolized by the components of the sux gene cluster of Xoo (Zhang *et al.*, 2019; Feng and Kuo, 1974; Zöllner *et al.*, 2025).

Rather than acting as solitary units, bacterial cells can form structured communities that function in unison (Ng et al., 2009). Bacteria have been shown to change cell shape or become multicellular, either as chains (i.e., chaining) or as filaments with or without septation. Septation requires treadmilling of FtsZ to produce septal peptidoglycans (Bisson-Filho *et al.*, 2017). In the absence of FtsZ and peptidoglucan synthetic activity, septate or chained filaments are produced without cell separation. *In vitro*, conditional filamentation can be triggered by a variety of factors, e.g., antibiotics,

anaerobiosis, high osmolality, pH shifts, temperature shock, or UV. Changes in nutrient supply can also induce filamentation, e.g., thymine deprivation, low or high Mg^{2+} I, high PO_4^{3-}, and limiting or excessive amino acids (Karasz *et al.*, 2022; Kunoh *et al.*, 2021; Davis *et al.*, 2015; Rizzo *et al.*, 2019). Bacterial filamentation has been described as an adaptive strategy to enhance resilience and survival under unfavorable conditions by minimizing cell division (Justice *et al.*, 2008; Yoshida *et al.*, 1986; Yamaki *et al.*, 2021), and it is important for biofilm formation and bacterial dispersal (Anbumani *et al.*, 2021; Abell-King *et al.*, 2022). Filamentation was reported as a defense mechanism to flagellate grazing (Hahn *et al.*, 1999; Corno and Jürgens, 2006).

Filaments of uropathogenic *Escherichia coli* were associated with higher tolerance to host defenses (Justice *et al.*, 2004; Justice *et al.*, 2006). It has been suggested that due to their size, filaments could be less prone to internalization by macrophages (Abell-King *et al.*, 2022; Horvath *et al.*, 2011). Several studies on the effects of antibiotics on bacterial morphology have reported filamentation in pathogens (Bos *et al.*, 2015; Lorian *et al.*, 1989), such as the effect of chelerythrine on Xoo (Yan *et al.*, 2025). Filamentation of human pathogens has been linked to important roles in virulence, e.g., for *Yersinia pestis* or *Vibrio cholerae* (Ponnusamy and Clinkenbeard, 2012; Frirdich and Gaynor, 2013; Davis *et al.*, 2015). Plant pathogens, e.g., *Xylella fastidiosa*, were reported to filament *in vitro* (Janissen *et al.*, 2015; Anbumani *et al.*, 2021; Álvarez *et al.*, 2008; Otta, 1976; Huang and Goodman, 1970; Malafaia *et al.*, 2018; Rizzo *et al.*, 2019) but their role during host colonization *in vivo*, except for *Dickeya dandtii* (Cui *et al.*, 2019) has remained elusive and only a few pathogens have been studied *in vivo* in context of host colonization (Tran *et al.*, 2022; Laloux, 2020).

Here, we found that Xoo colonies on solid agar surfaces underwent a pleomorphic shift leading to filamentous forms. In liquid cultures high salinity and elevated cell density induce conditional filamentation of Xoo *in vitro.* To explore whether Xoo can also filament during the infection of rice leaves, we tracked the infection process using imaging of reporter activity of translational SWEET11a-GUS reporter lines. Accumulation of diX Indigo (product of GUS) served as a proxy for the stage of successful injection of TALes into XP, enabling spatiotemporal mapping of Xoo during the infection process. Xoo infection appeared non-continuous within main veins at the infection front and progressed into minor and lateral veins. Data on the infection route

were then used to guide high-resolution imaging by confocal laser scanning microscopy (CSLM) and scanning electron microscopy (SEM). Rice leaf autofluorescence was overcome by tracking Xoo expressing the large Stokes shift fluorescent protein LSSmApple. At the infection front, rod-shaped Xoo were arranged perpendicular to xylem vessel pits. Strikingly, we discovered a previously unreported pleomorphic shift from rod-shaped to filamentous Xoo cells during host infection *in planta*. Time-lapse imaging revealed that filamentation was transient and asymmetric cell division yielded pleomorphic progenies. Notably, at later stages of the infection, Xoo was able to enter the XP, likely by hydrolysis of host pit cell walls. Filamentous Xoo spread laterally beyond the vascular bundle (XP and bundle sheath cells) even to the mesophyll, consistent with the observed disease symptoms that lead to chlorosis in the mesophyll and necrosis.

STAR★Methods

Key resources table

REAGENT or RESOURCE	SOURCE	IDENTIFIER
Bacterial strains		
$PXO99^{A}$	Lab of Boris Szurek, IRD	$PXO99^{A}$
$PXO99^{A}_{LSSmApple}$	This paper	$PXO99^{A}_{LSSmApple}$
ME2	Lab of Boris Szurek, IRD	ME2
Experimental models: organisms/strains		
Oryza sativa L. subsp. *japonica* cv. Kitaake	Eom et al. 2019	Wild type Kitaake
Oryza sativa L. subsp. *japonica* cv. Kitaake, pSWEET11a:*SWEET11a*-GUSplus T4, transformation event 10	Eom et al. 2019	SWEET11a-GUS, #10
Oryza sativa L. subsp. *japonica* cv. Kitaake, pSWEET11a:*SWEET11a*-GUSplus T4, transformation event 10	Eom et al. 2019	SWEET11a-GUS, #10
Oryza sativa L. subsp. *japonica* cv. Kitaake, pSWEET11a:*SWEET11a*-GUSplus T4, transformation event 8	Eom et al. 2019	SWEET11a-GUS, #8
Recombinant DNA		

pNEO:GFP	Han et al. 2008	
LSSmApple	Ejike et al. 2023	
Software		
R v4.20	R core team	www.r-project.org/
Affinity Designer	Serif	https://affinity.serif.com
GIMP	GIMP's Team	www.gimp.org/
OMERO	Center for advanced Imaging, HHU	https://cai.hhu.de/omero
Other		
Zeiss LSM 880 Airyscan	Center for advanced Imaging, HHU	
Leica TCS SP8	Center for advanced Imaging, HHU	
Zeiss Supra 55 VP	Center for advanced Imaging, HHU	
Nikon Ti Eclipse PF	Center for advanced Imaging, HHU	

Experimental model and subject details

Xanthomonas oryzae pv. oryzae culture conditions

Bacterial pre-cultures were obtained from single colonies derived from glycerol stocks streaked on NBSA plates, incubated for two days at 28°C in dark conditions (Table S1). 5 µL of bacterial pre-culture at OD_{600} 0.4 were transferred into 300 mL Erlenmeyer flasks, filled to a final volume of 50 mL NBS (1 g/L yeast extract, 3 g/L beef extract, 5 g/L peptone, 10 g/L sucrose, pH 7, 100 µg/mL kanamycin in distilled H_2O) or 500 mM NaCl in NBS. After an initial 16 hours of incubation (150 rpm, 28 °C, dark conditions), growth of cultures was monitored hourly by optical density at OD_{600}. At OD_{600} 0.4 for control and 500 mM NaCl conditions and OD_{600} 3 for high cell density conditions, bacteria were collected in ice-cold falcon tubes and centrifuged (1500 g, 4°C) for 15 min.

Plant cultivation

Rice seeds were de-husked and sterilized on a shaker at 180 rpm in 15 ml Falcon tubes filled with 75 % Ethanol and 50 % Klorix® for 2 and 5 min, respectively (Table

S2). The seeds were dried on sterile filter papers and transferred onto Magenta™GA-7 boxes containing ½ salt strength MS media (2.2 g Murashige Skoog Medium , 10 g sucrose, and 8 g Phytagel per liter, pH 5.8) with a serological tweezer under aseptic conditions. For SWEET-GUS reporter lines seeds from transformation event 8 and 10 (Eom *et al.*, 2019), medium was supplemented with 50 mg/L hygromycin B (Table S2). Seedlings were grown in a long day light regime (16 h day/8 h night) with a photosynthetic photon flux density (PPFD) of 200 µmol m^{-2} s^{-1} (PPFD-blue 40, PPFD-green 80 and PPFD-red 70 µmol m^{-2} s^{-1}), at 27°C and 80 % humidity in CLF PlantClimatics chambers (model: CU41L5).

Method details

Histochemical GUS assay

The newly emerged leaf of translational GUS reporter lines at the 4th leaf stage was infected with PXO99^{A} and ME2 inoculum after Kaufmann et al. (1973). Samples for histology were collected in ice-cold 90 % acetone and vacuum infiltrated for 10 min and incubated for 30 min. Subsequently, the fixing solution was replaced by GUS washing buffer followed by staining buffer and were infiltrated for 10 min each (Table S3). After incubation at 37°C, the enzymatic GUS reaction was stopped by replacement of GUS staining buffer with 75°C ethanol. Samples were cleared with a series of 75 %, 80 % and 90 % ethanol (Eom *et al.*, 2019). Final clearing was performed with 15 % chloral hydrate. Images were taken with the AxioZoom.V16 (Zeiss) using stitching in bright field mode.

Generation of fluorescent Xanthomonas oryzae pv. oryzae

The large Stokes shift protein LSSmApple was integrated into the expression plasmid pNEO via In-Fusion Assembly Mix (Takara) in frame with the neomycin promoter (Ejike *et al.*, 2024; Han *et al.*, 2008). After successful assembly of the pNEO:LSSmApple, the electrocompetent Xoo strain PXO99^{A} was transformed with 500 ng of plasmid DNA for 5 seconds at 2.5 kV and 200 Ω in a 0.1 cm cuvette . Cells were recovered in Recovery Medium for Expression (Sigma, CMR001-8X12ML) for 2 hours shaken at 28 °C and plated on NBSA (1 g/L yest extract, 3 g/L beef extract, 5 g/L peptone, 10 g/L sucrose, pH 7, 1.5% w/v agar, 100 µg/mL kanamycin in distilled H_2O) and stored at 28 °C in dark conditions for four days. Kanamycin tolerant transformants were selected for

fluorescence using a fluorescent Stereo Zoom Microscope (AxioZoom.V16, Zeiss) and, LSSmApple filter (excitation 488/10, emisson605/50, beamsplitter zt514). Fluorescent transformants were tested for virulence using the leaf clip infection protocol after Kaufmann et al. (1973).

Autofluorescence scan of rice leaves

Emission scans were acquired on a Leica TCS SP8 confocal microscope using a 40× water-immersion objective. Excitation was set to 405, 488, 514, and 561 nm, with notch filters applied when available to reduce laser bleed-through. Emission was collected from excitation + 20 nm to 640 nm, or up to 740 nm when chloroplast autofluorescence was included, in 10 nm steps using the PMT spectral detector. The pinhole was set to 2 Airy unit and the scan speed to 400 Hz. Detector gain and laser power were adjusted to avoid saturation across the scan. Regions of interest were selected on both the adaxial and abaxial sides of the 4th leaf. Three biological replicates were analyzed.

Preparation of infected rice samples, microscopy and image processing

Infected leaf samples were collected and submerged in fixation solution (freshly prepared 4 % PFA, 0.1 % Triton X-100 in PBS) shaken at 80 rpm, 4°C for 16 hours. Samples were washed three times in 0.1 Triton X-100 PBS as well as PBS for 10 min and chopped roughly into pieces with a razor blade. Samples were collected in a 16 well dish filled with PBS and cut into thin cross or longitudinal sections. CSLM of rice leaf sections was performed with the Zeiss LSM880 with a Plan-Apochromat 40x/1.2 objective. For selection of the infection front, infected rice leaves were observed with a fluorescent Stereo Zoom Microscope (AxioZoom.V16, Zeiss) and, LSSmApple filter (excitation 488/10, emisson605/50, beamsplitter zt514) and 63 HE mRFP filter (excitation 565/30, emission: 620/60, beamspliter FT585) for rice autofluorescence. Samples were taken 0.5 cm from front of bacteria (Figure S6). exposed to a series of ethanol concentrations after fixation and washing, from 10 % ascending by 5 % up to 99.9 % for 15 min each. After critical point drying, samples were coated with gold using an Agar Sputter Coater and imaged with a Zeiss SUPRA 55 VP SEM (EHT = 5 kV). Post-coloration of SEM images was performed in GIMP (v2.10.24).

Bacterial viability assay

After an initial 16 hours of incubation (150 rpm, 28 °C, dark conditions), growth performance of cultures was monitored hourly by OD_{600}. At OD_{600} 0.4 for control and 500 mM NaCl conditions and OD_{600} 3 for high cell density conditions, bacteria were collected in ice-cold falcon tubes and centrifuged (1500 g, 4°C) for 15 min. To test the colony forming ability of Xoo cells of different length, bacterial pellets were diluted in 150 mL of ice-cold NB (1 g/L yest extract, 3 g/L beef extract, 5 g/L peptone, pH 7, 100 µg/mL kanamycin in distilled H_2O) and filtered through 5 and 10 µm pluriStrainer into falcon tubes on ice, respectively. Bacterial flow through was centrifuged (15 min, 1500 g, 4°C) and diluted in NBS to OD_{600} 0.1. For the CFU assay, subpopulations of bacteria at OD_{600} 0.1 were diluted by 10^6 in NBS. 30 µL of diluted bacterial suspensions were evenly spread with sterile metal beads on NBSA plates supplemented with 100 µg/mL Kanamycin. CFU were quantified after three days of incubation at 28°C in dark conditions.

Microscopy of Xanthomonas oryzae pv. oryzae

For long-term life imaging of Xoo, 10 mL of bacterial culture was centrifuged for 15 min at 1500 g, 4 °C. The bacterial pellet was eluted gently with 1 mL NBS media. 5 µL of bacterial suspension was transferred to an agar-based aerated imaging chamber sealed with silicon-based grease (Fig S4). A z-stack image was acquired every 30 min for 24 hours with the Nikon Ti Eclipse PFS. For high resolution images of Xoo cells after filamentation, samples were taken from 0.5, 2, 4, 8, 10 and 16 hours after transferal to imaging chamber with CLSM (excitation 488 nm, emission 605-615 nm; Plan-Apochromat 63x/1.4 objective). Analysis was performed in Omero (v5.28.0) and ImageJ (v1.52).

Results

Phenotypic heterogeneity of in vitro colonies

Morphological plasticity is common among pathogens (Justice *et al.*, 2004; Allison *et al.*, 1992; Anbumani *et al.*, 2021; Cui *et al.*, 2019). To test whether Xoo colonies exhibit phenotypic heterogeneity on the macroscopic scale, colonies were grown for six days on solidified NBS agar plates. To quantify cross-colony variability, images of colonies were analyzed using hue, saturation and brightness (HSB) criteria (Figures 1A, S1).

The HSB color-space approach enabled pixel-level discrimination of structural and optical features across the colony surface. The analysis focused on grayscale variation of individual pixels, with the assumption that variation in brightness and saturation could reflect underlying differences in colony density and cell morphology. Based on the analysis, colonies were reproducibly segmented into three concentric growth zones, each characterized by distinct HSB profiles (Figure S1). To evaluate the phenotypic appearance of Xoo across the colony center (1), mid-zone (2) and peripheral edge (3), Xoo was visualized by CSLM (Figure 1B). Rod-shaped and filamentous Xoo cells appeared (defined as: < 5 µm - rod-shaped, > 5 µm - intermediate and filamentous) throughout all three zones. However, the colony center (1) contained the highest proportion of rod-shaped cells, while the peripheral edge (3) contained the highest number of filamentous cells (Figure 1C) The mid-zone (2) exhibited an intermediate distribution. The spatial pattern indicates that Xoo adopts morphologies in response to local microenvironments in the colony (Figure 1D).

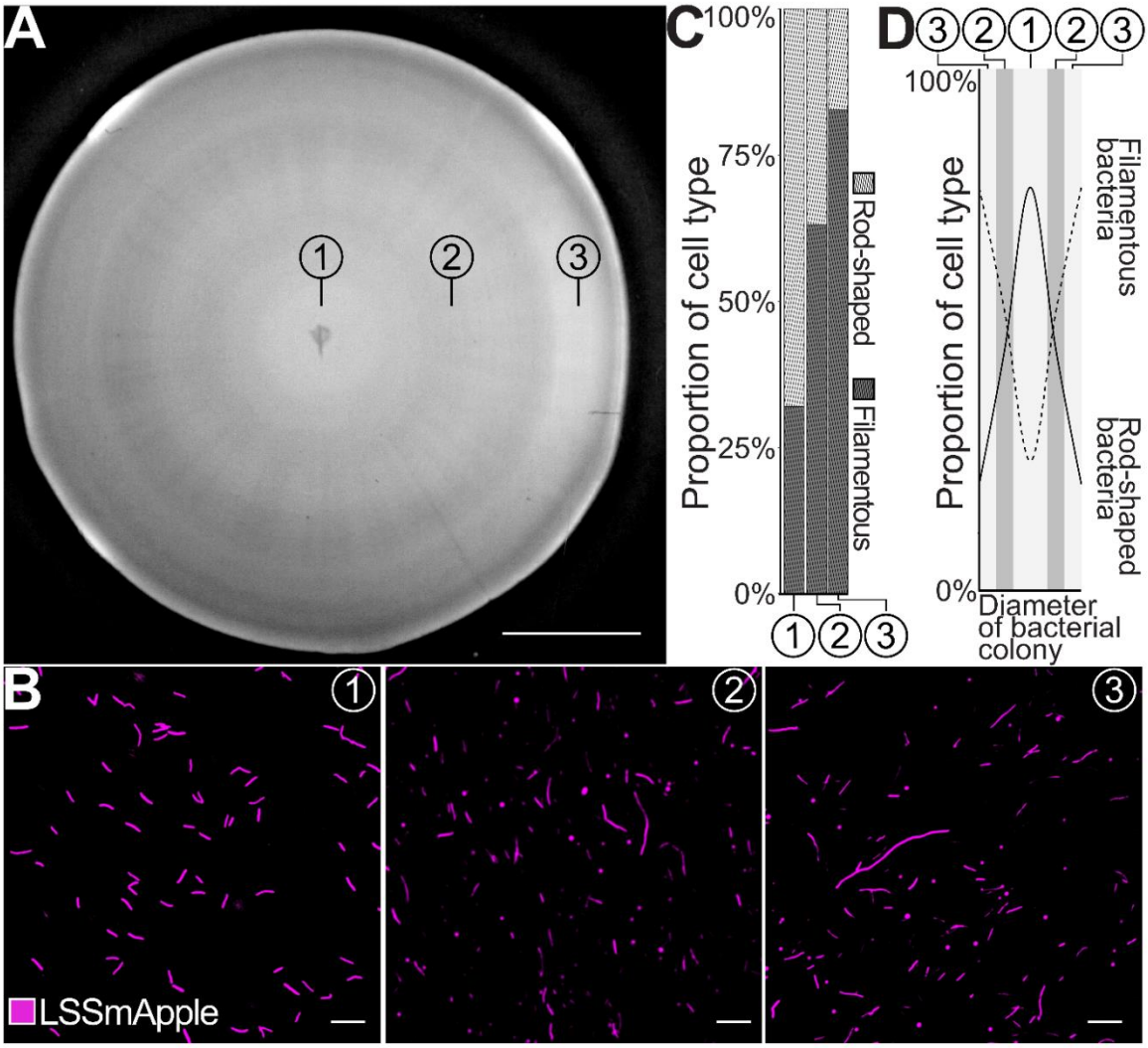

Figure 1.1. Pleomorphism and spatial zonation in Xanthomonas oryzae pv. oryzae colonies on solid media. (A). Colony-scale imaging of six-day old colonies of PXO99ALSSmApple revealed spatial zonation into three concentric regions: colony center (1), mid-zone (2) and peripheral edge (3). Scale bar: 5 mm. **(B).** Pleomorphism of PXO99ALSSmApple was discovered by high resolution microscopy of individual concentric zones. Images were taken with ZEISS LSM880 Airyscan (excitation: 488 nm, detection range: 605-615 nm) Scale bar: 10 µm. **(C).** For each concentric zone, cell lengths of 100 bacteria were quantified and grouped into rod-shaped (< 5 µm) or filamentous (cells > 5 µm, encompassing intermediate (5-10 µm) and filamentous morphologies (>10 µm)). Quantification of cell length was repeated independently three times on different colonies with comparable results **(D).** The represented bacterial morphologies across PXO99ALSSmApple colonies were illustrated based on (B).
Related to Figure S1. HSB color space segmentation of bacterial colonies.

Morphological plasticity of individual Xoo

To examine whether Xoo filamentation can be triggered independent of a surface-attached colony, we exposed bacteria to two conditions in liquid culture: 500 mM NaCl (hereafter 'high salinity') and high cell density (OD_{600} 3, hereafter 'high OD_{600}'). Bacterial cell length was assessed using CLSM (Figure 2A). High salinity caused the largest heterogeneity in cell length with a mean average of 9.6 ± 6.9 µm. Although significantly shorter, bacteria from high OD_{600} also exhibited elongated forms, with a

mean length of 4.2 ± 3.1 µm. In comparison, control cultures at OD_{600} 0.4 displayed a narrow distribution of cell lengths (mean 2.4 ± 0.6 µm) significantly different from high salinity and high OD_{600} conditions. The results indicate that Xoo filamentation can be induced *ex planta* by specific environmental cues. During host colonization, bacteria need to maintain microcolonies and need to disperse to gain access to nutrients and to spread; filaments could serve as intermediate stages. Some multinucleate filaments were shown to rapidly divide into rod-shaped cells after release from sublethal conditions (Pratt *et al.*, 2012; Yamaki *et al.*, 2021; Piao *et al.*, 2006). To explore whether reproductive activity of Xoo cells depends on cell length and growth history, we evaluated the number of colony forming units (CFU) from different morphological states. Subpopulations of <5 µm (rod-shaped)**,** 5–10 µm (intermediate)**, and** >10 µm (filamentous) cells were enriched from high OD_{600} and high salinity populations, washed, set to OD_{600} 0.1 and diluted 10^{-6} fold. CFU were quantified after four days of growth in dark conditions at 28°C. Surprisingly, founder cells from high salinity and high **OD_{600}** cultures showed differences in CFU depending on their cell length (Figure 2B). While CFU increased with increasing cell length for founder cells from high salinity cultures, CFU decreased with increasing cell length for founder cells originating from high OD_{600} cultures. Filamentous cells originating from high salinity conditions formed significantly more CFU relative to filamentous cells from high OD_{600} cultures**.** In contrast, rod-shaped cells from high OD_{600} cultures formed most colonies, intimating that rod-shaped cells were more actively reproducing within the high OD_{600} community. Intermediates originating from high salinity cultures exhibited a higher CFU compared to intermediates from high OD_{600} cultures, further supporting the observation regarding differences in reproduction activity for rod-shaped and filamentous cells between communities from different growth conditions. Our observations imply that subpopulation-specific traits differentiate with growth history.

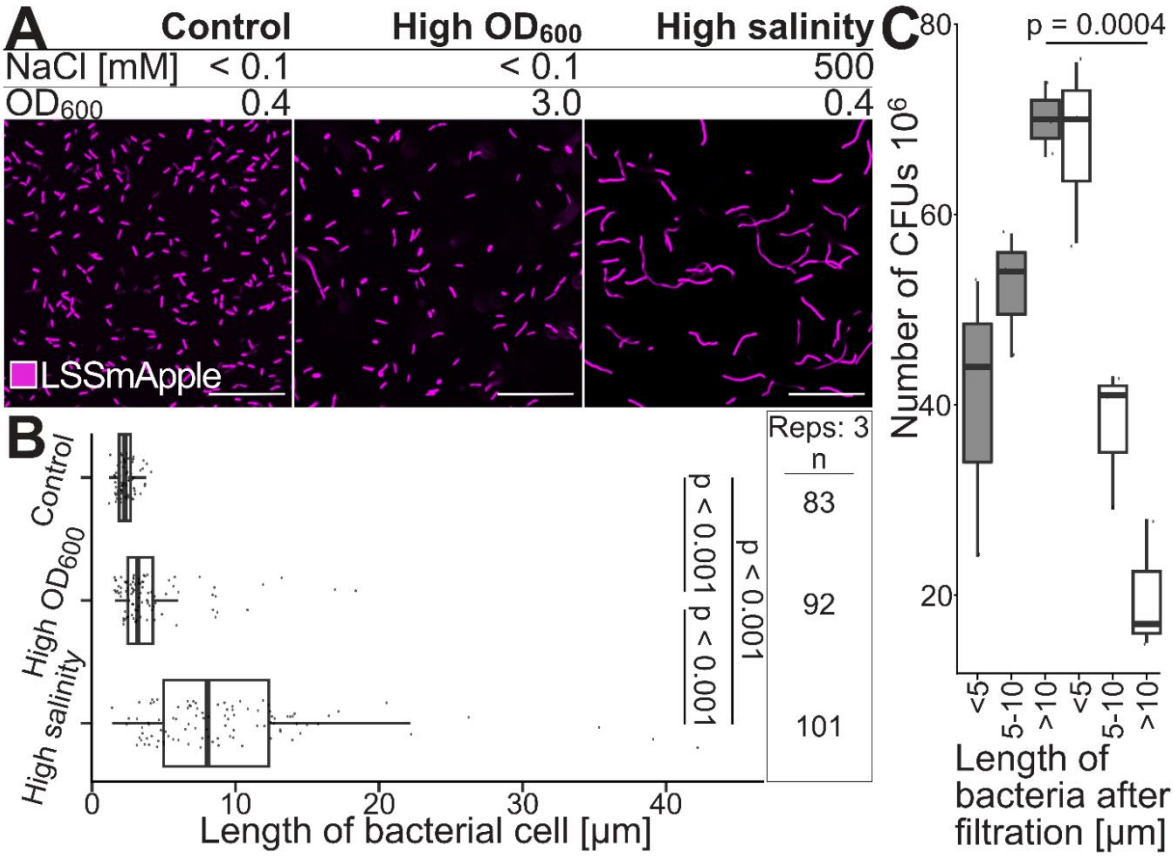

Figure 1.2. Conditional filamentation and viability of *Xanthomonas oryzae* pv. *oryzae* in response to different growth conditions in liquid culture. (A). PXO99$^{A}_{LSSmApple}$ was cultivated in liquid cultures (150 rpm, 28 °C, dark conditions) supplemented with 500 mM NaCl (high salinity) or to OD_{600} 3 (high OD_{600}) and observed by confocal laser scanning microscopy (ZEISS LSM880; excitation: 488 nm, detection range: 605-615 nm). **(B).** Cell length of PXO99$^{A}_{LSSmApple}$ cultivated to OD_{600} of 0.4 or OD_{600} of 3 in <1 mM of NaCl, and OD_{600} 0.4 in 500 mM NaCl were measured with the Segmented Line Tool in ImageJ. Data processing was performed in R. Repeated independently three times with comparable results. Scale bar: 10 µm. **(C).** High OD_{600} (white) and high salinity populations (grey) were divided by length into rod-shaped (< 5 µm), intermediate (5-10 µm) and filamentous (> 10 µm) subpopulations. Subpopulations were diluted by 10^6 and plated in triplicates onto petri dishes with 20 mL NBSA media supplemented with 100 µg/mL Kanamycin. Colony forming units were quantified after three days at 28 °C, dark conditions. Data processing was performed in R. CFU assay was independently repeated three times with comparable results.

Filament differentiation

To explore the potential role of subpopulation-specific traits, differentiation of filaments was observed by time lapse imaging of filamentous Xoo using transmission light microscopy and CSLM (Figure 3). Filaments initially underwent further elongation, extending from 13.4 ± 3.2 µm to 28.3 ± 5.1µm after 3 hours. After elongation, elongated filaments showed septum formation as soon as 4 hours after transferal to imaging chamber, with septa positioned at irregular intervals along the cell body (indicated by arrows, Figure 3 A, B, S2,3). The septation events ultimately led to

asymmetric division and re-establishment of a morphologically heterogeneous population of filamentous, intermediate and rod-shaped cells. After 17 hours, the culture exhibited a dense mixed population, demonstrating that morphologically diverse bacterial populations can be reconstituted from filamentous cells. Different from the unipolar growth of *Corynebacteriu matruchotii* or *Leptrothis cholodnii,* Xoo showed a bipolar elongation phase and irregular septation, followed by asymmetric divisions (Figure 3C). Phenotypic heterogeneity was reconstituted from filamentous parental cells, indicating that pleomorphism is likely connected to intracommunity communication and potentially to subpopulation specific traits.

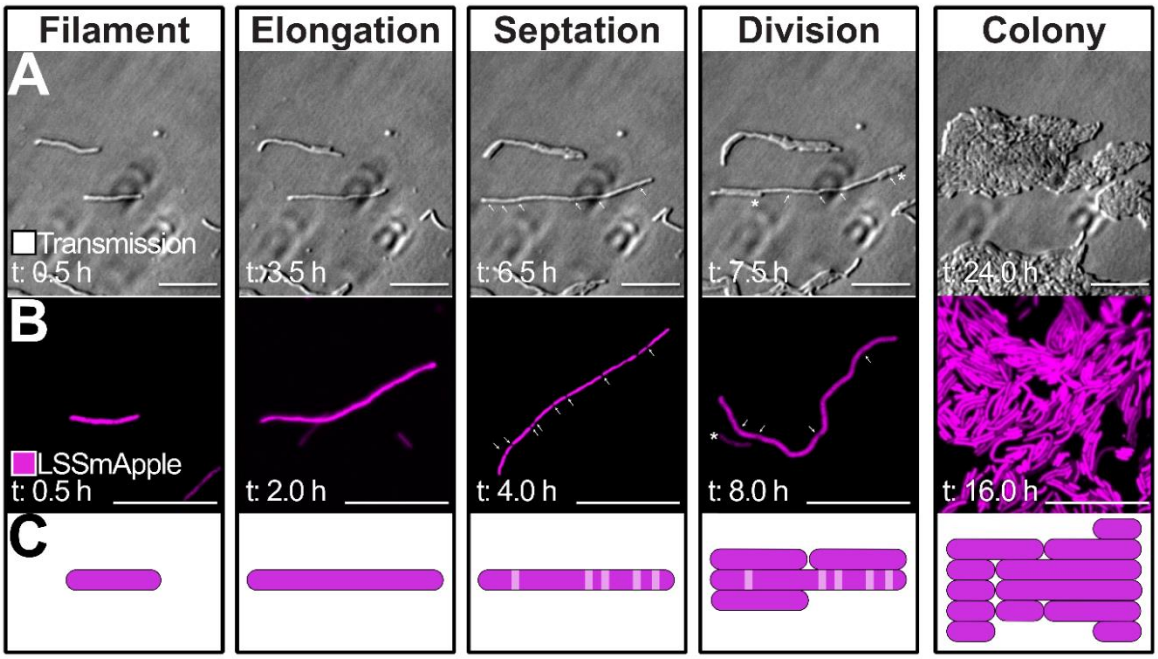

Figure41.3. Filamentous *Xanthomonas oryzae* pv. *oryzae* initiate the formation of new colonies that display phenotypic heterogeneity following a developmental program. Filamentous PXO99$^{A}{}_{LSSmApple}$ separated by filtration from cultures grown in high salinity (OD_{600} 0.4, 500 mM NaCl) and placed onto NBSA media within the aerated imaging set-up (Figure S4). **(A).** Individual filaments were observed for 24 hours using transmission light microscopy (bright field, Nikon Ti Eclipse PFS). Representative images of bacteria at different time points after release from high salinity conditions are shown. Z-stack images were obtained every 30 minutes for 24 hours (Figure S5). Experiments were repeated independently three times with comparable results. Scale bar: 10 µm. **(B).** PXO99$^{A}{}_{LSSmApple}$ were observed by confocal laser scanning microscopy (ZEISS LSM880; excitation: 488 nm, detection range: 605-615 nm). Representative images at different time points after release of PXO99$^{A}{}_{LSSmApple}$ from high salinity conditions are shown. Experiments were repeated independently three times with comparable results. Scale bar: 10 µm. **(C).** Cartoon of developmental program followed by filamentous PXO99$^{A}{}_{LSSmApple}$ derived from high salinity conditions after placement onto fresh media. Filaments were observed to elongate in a bipolar fashion. Asymmetric septation was succeeded by division into pleomorphic colonies.
Related to Figures:
Figure S2. Assembly of an agar-based aerated imaging chamber.
Figure S3. Time-lapse imaging of filamentous *Xanthomonas oryzae* pv. *oryzae*.

Reporter-based mapping of the infection route

We used a combination of bacterial (fluorescent Xoo) and host reporters (GUS reporter lines) to trace the infection. For effective virulence, Xoo must induce at least one of the clade III *SWEET* genes. We used translational SWEET11a-GUS reporter lines to map a specific stage of the infection route of Xoo, i.e., successful attachment to xylem walls, successful formation of the T3SS and injection of the TALe (Chen *et al.*, 2012; Eom *et al.*, 2019). Accumulation of the GUS product diX Indigo served as proxy indicator for this infection stage (Figure 4). As expected, diX Indigo accumulated during infection with PXO99$^{A}_{LSSmApple}$, which harbors the *SWEET11a* inducing TALe PthXo1, but was absent during infection with the ME2 control strain lacking cognate TALe able to target a clade III *SWEET* promoter (Figure 4A). From the clipping site, progressive basipetal infection was detected; initially in main veins, subsequently in transverse and minor veins (Figure 4A). Using emission scans of rice leaves we identified the large Stokes shift protein LSSmApple to be suited to overcome rice tissue autofluorescence at excitation with 488 nm (Figure S4). The *SWEET11a* inducing Xoo strain PXO99^{A} was transformed with a LSSmApple cassette (PXO99$^{A}_{LSSmApple}$). PXO99$^{A}_{LSSmApple}$ was then used to monitor the bacteria in the rice leaf at different stages by fluorescence microscopy (Figures 4B). Overall, the patterns were highly similar, however the GUS reporter assay had higher sensitivity also for identifying the bacterial infection front (Figure 4C).

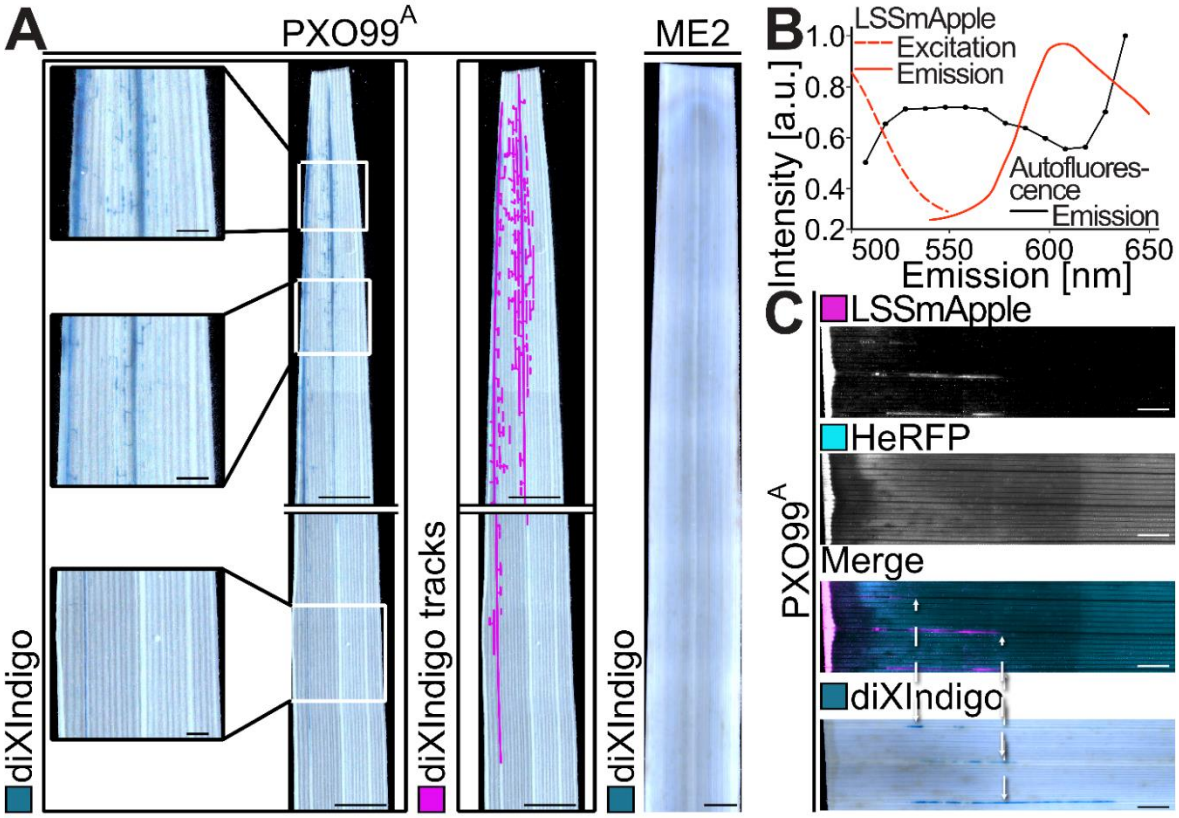

Figure 1.4. Mapping of the infection process using SWEET11a-GUS reporter lines and Xoo expressing a fluorescent protein PXO99$^{A}_{LSSmApple}$. (A). diX Indigo accumulation at 4 days after leaf clipping infection (Kauffman, 1973) with PXO99^{A} and ME2 observed with the ZEISS Axiozoom.V16. Representative images from three leaves per treatment from three independent experiments performed with two independent pSWEET11a:SWEET11a-GUSplus lines (transformation event #8 and #10)(Eom *et al.*, 2019). Enlarged sections of the top, mid and bottom zone of the leaf indicated by squares (scale bar: 2 mm). diX Indigo served as indicator for bacterial presence and was tracked in ImageJ (pink, scale bar: 1 cm). ME2 served as negative control (scale bar: 1 cm). **(B).** Emission scan of rice leaves at 488 nm excitation identified LSSmApple as suitable, monochromatically excitable protein to circumvent autofluorescence of rice leaves. **(C).** Leaves infected with PXO99$^{A}_{LSSmApple}$ were observed 3 dpi with fluorescence microscopy (Zeiss Axiozoom.V16). Subsequently, GUS histochemistry was applied to the same samples. Front of infection depicted by diX Indigo and LSSmApple are indicated by dashed lines. Experiment was repeated three times independently on five leaves each with comparable results. Scale bar: 1 cm.
Related Figures:
Figure S4. Autofluorescence scans of rice leaves.
Figure S5. Selection of infection front for SEM.

Distinct cell morphologies during host colonization

SEM and CLSM were employed to investigate Xoo morphologies at different infection stages at single cell resolution by monitoring PXO99$^{A}_{LSSmApple}$ fluorescence and SEM. Guided by spatiotemporal patterns of Xoo infection established through translational *SWEET11a*-GUS reporter line assays (Figure 4A), we analyzed fixed sections of infected rice leaves corresponding to the infection front and the subsequent progression of the infection (Figure S5). In tissue sections at the bacterial front of infection, rod-shaped PXO99$^{A}_{LSSmApple}$ were exclusively observed within the xylem

vessel (Figure 5). Remarkably, the majority of PXO99$^{A}_{LSSmApple}$ cells located within or in contact with xylem vessel pits (Figures 5A,B). The pit localization is likely the optimal site for T3SS injection due to the thinned cell walls and the site of SWEET-based sucrose efflux. Within the group of PXO99$^{A}_{LSSmApple}$ located in xylem vessel pits, 45 % of cells appeared to be orientated perpendicular to the xylem vessel wall (on average in twelve biological replicates; Figures 5C,D), either caused by polar adhesins or polar T3SS attachment.

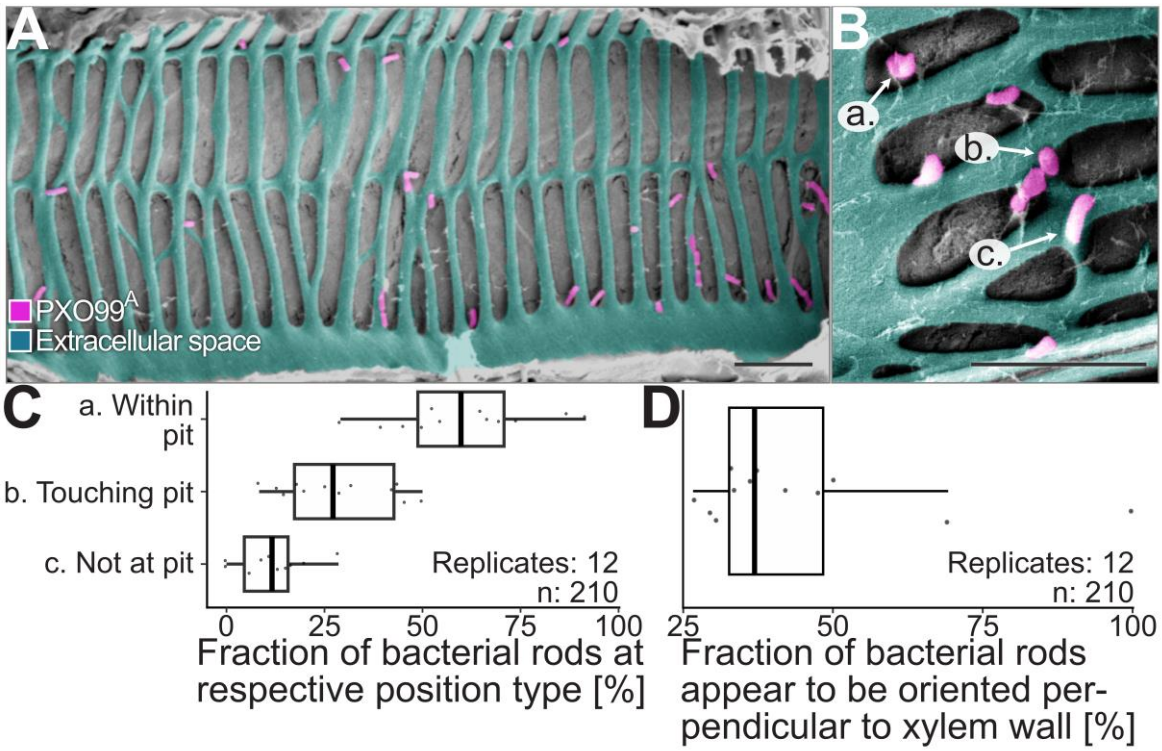

Figure 1.5. Rod-shaped Xanthomonas oryzae pv. oryzae locate predominantly to xylem pits near the infection front. (A). Samples were taken from the infection front (Figure S6) and processed for scanning electron microscopy. Images were taken scale bar: 5 µm. Post-processing was performed in GIMP (v2.10.24; pink: bacteria, turquoise: secondary xylem vessel wall). **(B).** Location of Xoo was categorized as within pit (a.), touching pit (b.) and not at pit (c.). Representative images of categories a., b., and c. are presented. Post-processing was performed in GIMP (v2.10.24; pink: bacteria, turquoise: secondary xylem vessel wall). Scale bar: 5 µm. **(C).** Location of Xoo at the infection front from twelve images from five leaves. Experiment was repeated independently three times with comparable results. Data processing in R. **(D).** Appearance of Xoo to be orientated perpendicular within the 210 bacterial cells analyzed from (C). Experiment was repeated independently three times with comparable results. Data processing performed in R.
Related Figures:
Figure S5. Selection of infection front for SEM.

The region spanning 3–5 cm from the leaf tip at six days post infection (dpi) were chosen as representative of an established infection stage of vascular colonization (Figures 6A, S4). At the 6-dpi stage, PXO99$^{A}_{LSSmApple}$ displayed striking morphological polymorphism, with a prominent filamentous form not previously documented for Xoo

in planta. SEM revealed high cell density accumulation of filamentous cells within xylem vessels, often filling substantial portions of the lumen (Figure 6 B,C). CLSM also detected filamentous cells in the metaxylem of major and minor veins (Figures 7, S7-9).

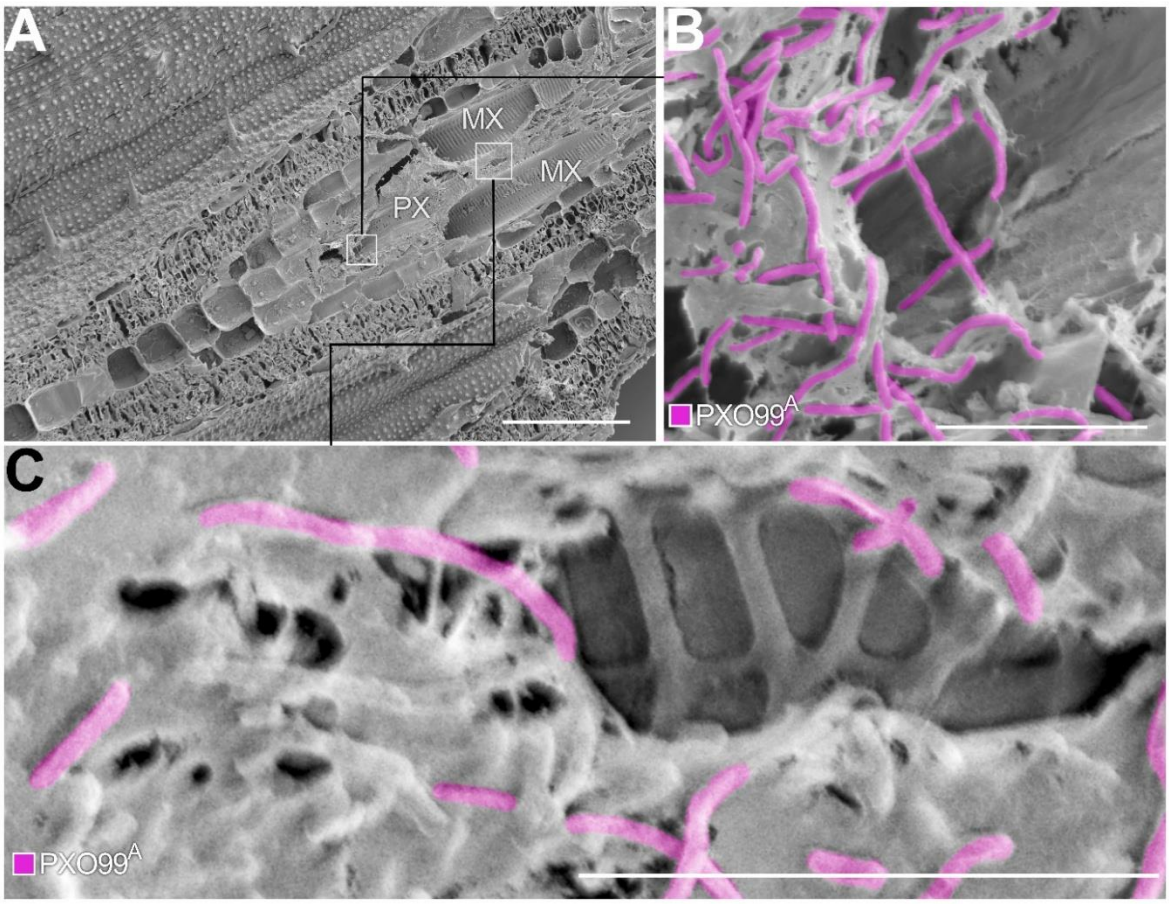

Figure 1.6. Filamentation of Xanthomonas oryzae pv. oryzae during host colonization is detected apoplasmically in xylem vessels and intracellularly in xylem parenchyma and adjacent cells. Samples corresponding to an advanced stage of colonization (3-5 cm from the leaf tip at 6 dpi, Figure 4) were fixed and subjected to SEM. Experiment was performed three times independently with comparable results. **(A).** Overview of infected rice leaf section by SEM, scale bar: 100 µm. Squares indicate regions were magnified images (B, C) were taken. Protoxylem (PX; magnification (B).) is located adaxially to metaxylem vessels (MX, magnification (C). **(B).** Filamentous *Xanthomonas oryzae* pv. *oryzae* were observed in bacterial aggregates associated with the protoxylem, scale bar: 10 µm. Post-processing was performed in GIMP (v2.10.24; pink: bacteria). **(C).** Filamentous *Xanthomonas oryzae* pv. *oryzae* were associated with metaxylems, scale bar: 10 µm. Post-processing was performed in GIMP (v2.10.24; pink: bacteria).
Related to Figures:
Figure S6. Scanning electron microscopy of *Xanthomonas oryzae* pv. *oryzae* colonization *in planta* and vascular bundle structure in rice leaves.

Vascular bundle breach and lateral migration of filamentous Xoo at late stages

Notably, at late infection stages (6 dpi, 3-5 cm from infection site) SEM imaging revealed rod-shaped Xoo inside XP cells (Figure S6), likely a consequence of pit membrane rupture resulting from weakened cell walls due to xylan degradation by

secreted Xoo xylanases, providing access to all the nutrients present in the dying XP (Rajeshwari *et al.*, 2005). CLSM independently detected Xoo in XP (Figure 7). Notably, we found evidence for filamentous Xoo to progress from the xylem via the XP and bundle sheath even into the mesophyll (Figure 7, S7-9). Both rod shaped and filamentous cells were observed outside the xylem vessels. Filamentous cells traversed cell walls. How the cells achieved the penetration, and how, remains to be determined. We observed some variability in different leaves and in independent experiments, likely representing different stages of the progression of the infection (Figures S8, S9). In general, the depth of penetration was higher in primary veins as compared to secondary veins, consistent with the progression, in which primary veins were infected earlier compared to secondary veins as observed in the SWEET-GUS reporter assays (Figure 4). In some cases, the bacteria were still mainly present inside the xylem vessels; in other cases, penetrance into neighboring cells was observed (Figure S8A,B; S9A). In some cases, Xoo filaments accumulated highly in bundle sheath cells (S8 C,D, S9D), and in other cases, the filaments entered the mesophyll (mesophyll cell identifiable by high chlorophyll autofluorescence)(Figure S8C,D; S9D). We surmise that the differences are due to differences in the stage of infection, and that they represent representative illustration of the progression from xylem vessels to XP to bundle sheath and ultimately the mesophyll. Thus, rather than infecting rice leaves in a single static morphology, Xoo undergoes dynamic shape transitions *in planta*, processes with likely central importance for virulence.

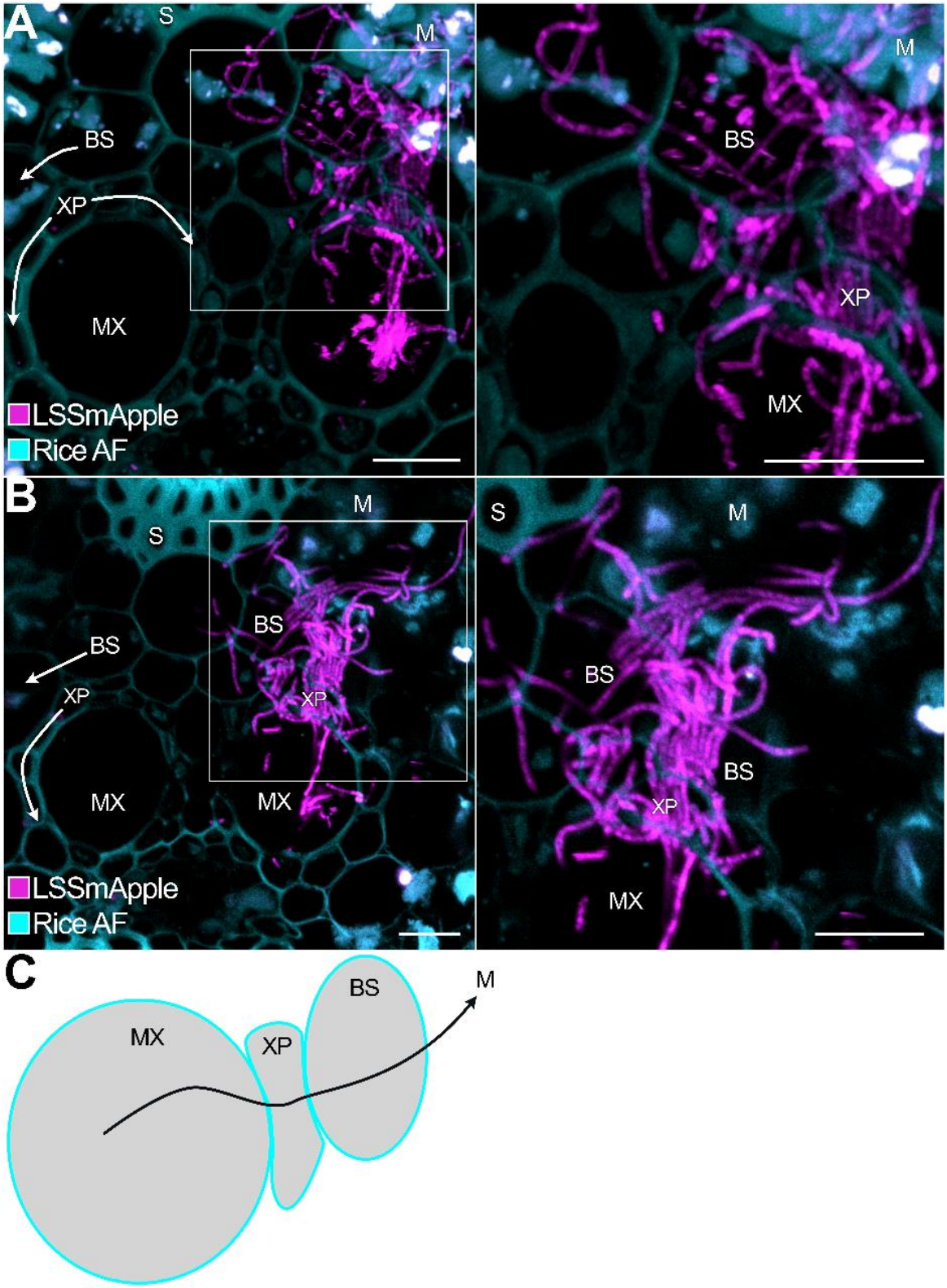

Figure 1.7. Filamentous Xanthomonas oryzae pv. oryzae traverse vascular bundle. Samples corresponding to an advanced stage of colonization (3-5 cm from the leaf tip at 6 dpi, Figure 4) were fixed and subjected CLSM microscopy. Experiment was performed three times independently with comparable results. **(A, B).** Cross-section of *Xanthomonas oryzae* pv. *oryzae* during colonization, scale bar: 10 µm. Inlets indicated by white squares. $PXO99^{A}{}_{LSSmApple}$ (pink), rice autofluorescence (turquoise). **(C).** Lateral migration route of Xoo from metaxylem vessels to xylem parenchyma and bundle sheath to mesophyll tissue. MX: metaxylem, XP: xylem parenchyma, BS: bundle sheath, M: mesophyll tissue, S: sclerenchyma.
Related to Figures:

Figure S4. Autofluorescence scans of rice leaves.
Figure S7. Overview of rice leaf cross section.
Figure S8. Colonization pattern of *Xanthomonas oryzae* pv. *oryzae* in cross sections of major veins visualized by CLSM.
Figure S9. Colonization pattern of *Xanthomonas oryzae* pv. *oryzae* in cross sections of minor veins visualized by CLSM.

Discussion

Using a combination of wide filed, SEM and CLSM imaging of Xoo labelled with the large Stokes shift fluorescent protein LSSmApple, we found that Xoo can differentiate to produce morphologically different forms, from rod-shaped bacilli to non-septated filaments to septated filaments both *in vitro* and during the infection of rice. Filamentation can be triggered *in vitro* by extreme conditions such as high salinity or high density, however the filamentation is reversible. Colony-forming ability was shown to differ between bacilli and filaments within the bacterial population. These reversible transitions may have a varieties of benefits during the infection process, e.g. by increasing the surface that can attach to the xylem walls to withstand the xylem sap flow to penetration of host cell layers to spread beyond the vascular bundle, demonstrating that Xoo is a xylem-spreading pathogen that at later stages of the infection can become necrotrophic, and thus can be defined as a hemi-biotroph. Not surprisingly, Xoo is therefore in some aspects similar to the closely related non-vascular *Xanthomonas oryzae pv. oryzicola*, which differs from Xoo not having CsbA, a cellobiohydrolase gene, as a key determinant of the difference between vascular and non-vascular life styles (Gluck-Thaler *et al.*, 2020). Vascular and non-vascular pathogens of *Brassicaceae, Xanthomonas campestris* pv. *campestris* (Xcc) and pv. *raphani* differ in their CRISPR/Cas repertoires. Loss of CRISPR/Cas increased genome plasticity and enabled the accumulate virulence factors (e.g. XopN) that enabled niche adaption of Xcc to vasculature (Paauw *et al.*, 2025). Notably, these findings may be of relevance for other xylem pathogens and possibly beyond plant diseases.

Xoo is not xylem-limited and displays phenotypic heterogeneity during vascular bundle breach

Xanthomonas species encompass vascular and non-vascular pathogens. Non-vascular pathogens e.g. *Xanthomonas oryzae* pv. *oryzicola* invade plants through stomata and colonize mesophyll tissue. Vascular pathogens e.g. *Xanthomonas*

campestris pv. *campestris* (Xcc) and Xoo are able to colonize xylem vasculature despite its scarce nutrient availability and the rapidly flowing xylem stream. At stomata, immune hubs like BAK1/BKK1 interact with pattern recognition receptors for specific pathogen cues e.g. flagellin and mediate stomata closure. At hydathodes, defense layers of plant immunity appear to be restricted to immune hubs and lack specific pattern recognition receptors (Paauw *et al.*, 2023; Cerutti *et al.*, 2017). It has been hypothesized that vascular pathogens hijack guttation droplets at hydathodes to be reabsorbed into the epithem when xylem pressure decreases under low water availability and low humidity. While initial plant invasion into the epithem appears to be less demanding for vascular pathogens because of the limited plant defense layers at hydathodes, Type II Secretion System (T2SS) secreted cell wall degrading enzymes (CWDEs) are essential for the degradation of xylem tracheid apices and progression into xylem vasculature from the epithem (Paauw *et al.*, 2023). To our knowledge, the ability of the vascular-spreading Xoo to not only gain entry into the xylem vasculature but also exit the xylem vessels had not been reported before. Our observations indicate that Xoo is not restricted to basipetal migration along xylem vasculature (Figure 7). For colony expansion beyond xylem vasculature, Xoo is required to surpass pit elements of the xylem vessel. Xylem pits are composed of a pliant pit membrane (pectin and hemicelluloses e.g. heteroxylan) in contact with the plasma membrane of adjacent xylem parenchyma cells (Yadeta and Thomma, 2013; Wang *et al.*, 2022). Plausibly, the CWDEs essential for xylem vasculature entry after epithem colonization can also degrade xylem pits and enable pathogen spread to xylem parenchyma cells (Cao *et al.*, 2020; Gluck-Thaler *et al.*, 2020). Transcriptomic studies of Xoo reported the upregulation of xylanases *in planta* (Kim *et al.*, 2016; Rajeshwari *et al.*, 2005), which enable Xoo to degrade pits composed of heteroxylan (Wang *et al.*, 2022) to xylose and provide a passageway to adjacent XP cells. In addition, we observed that pleomorphic adaption into filamentous phenotypes appeared crucial for migration outside the vascular bundle: filaments spread from xylem vessels to XP and bundle sheath cells to mesophyll tissue (Figure 7) Individuals of the same species can exhibit different behaviors of so-called phenotypic heterogeneity within one colony, benefitting the population rather than the individual (bet-hedging strategy). Division of labor, achieved by heterogeneity has been reported for plant-pathogens (Cui *et al.*, 2019; López-Pagán *et al.*, 2025; Anbumani *et al.*, 2021). Filamentous Xoo were observed at advanced

infection stages, where bacterial cell density probably culminated within the xylem vessel, which could be attributed to quorum-sensing signals, as seen in *X. fastidiosa* where cell density and exposure to quorum-sensing signals triggered filamentation (Anbumani *et al.*, 2021). Pleomorphic bacteria could possibly perform distinct roles. For instance, filaments could bridge the gap between separated subpopulations within xylem vessels for basipetal migration and outside the vascular bundle, similar to observations of *X. fastidiosa ex planta* (Anbumani *et al.*, 2021). In *X. fastidiosa*, filamentous cells act as anchors of biofilm due to their irreversible attachment to surfaces and an enhanced production of extracellular polymeric substances (Janissen *et al.*, 2015). Due to their increased surface, an increased amount of afimbrial adhesins could mediate adherence to adjacent colonization sites. In contrast to the potential anchoring role of filaments at high cell density, the increased length of filamentous bacteria could fit significantly more pili compared to rod-shaped bacilli and fulfill a dispersal role within the bacterial population. Filamentous bacteria have been associated with rapid dispersal via swarming (Liu *et al.*, 2020; Möller *et al.*, 2013; Kearns and Losick, 2003; Gode-Potratz *et al.*, 2011; Allison *et al.*, 1992). Since we observed the ability of Xoo filaments to found new pleomorphic colonies by differentiation and division (Figure 3), filamentous dispersal could lead to efficient and rapid colony expansion. Whether Xoo filaments fulfill specific tasks within the bacterial population associated to swarming and dispersal or non-motile anchoring remains to be investigated. Filaments of other bacterial species have been associated with both, non-motility (Cui *et al.*, 2019) or dispersal (Möller *et al.*, 2013; Laloux, 2020; Liu *et al.*, 2020; Kearns and Losick, 2003; Anbumani *et al.*, 2021; Gode-Potratz *et al.*, 2011).

Although the mechanisms and intracellular signaling pathways underlying filamentation remain poorly defined, diverse cues ultimately converge to regulate the cell division machinery. For instance, the SOS response and the UDP-glucose pathway induce inhibitors of FtsZ ring assembly and lead to lateral growth but inhibited cell division (Dajkovic *et al.*, 2008; Cordell *et al.*, 2003; Hill *et al.*, 2013; Weart *et al.*, 2007; Sargent, 1975). Filaments of *Bordetella antropi* were reported to be induced under high UDP-glucose conditions enabling cell-to-cell dispersal (Tran *et al.*, 2022). Hence, a next step is to explore the effect of the nutrient status on Xoo filamentation. During primary infection, Xoo redirects the sucrose flow via induction of *SWEETs* to the site of infection at pits. One may hypothesize that at later stages of infection, XP

sucrose reservoirs may have been exploited. While nutrient excess will boost Xoo proliferation, Xoo cells within the same microcolony will likely compete for nutrients at high cell density. Effects of clustered growth of filaments has been discussed as primarily negative due to impaired motility and increased competition for resources (Claessen *et al.*, 2014). In other bacteria, low nutrient levels (Davis *et al.*, 2015; Kunoh *et al.*, 2021; Steinberger *et al.*, 2002), as well as conditions with high nutrient levels have been described to induce filamentation (Cui *et al.*, 2019; Rizzo *et al.*, 2019).

Infection front predominated by rod-shaped Xoo at xylem vessel pits

In the xylem vessels, Xoo faces low microbial competition (McCully, 2001; Yadeta and Thomma, 2013) but needs to withstand and migrate against the bulk laminar flow of the xylem sap. Bacterial attachment to xylem vessel walls is mediated by adhesins (Li *et al.*, 2020; Das *et al.*, 2009). Bacterial migration within the xylem vessel occurs bidirectionally by type IV twitching and flagellar swimming (Li *et al.*, 2020; Caires *et al.*, 2020). We found that at the infection front, Xoo frequently localized in xylem pits, and many cell aligned perpendicular to xylem vessel pits (Figure 5). Likely, pit membranes, which are composed of hemicellulose are an easier target for Xoo T3SS injection compared to the stiff and highly suberized secondary cell walls of the xylem vessel walls (Wang *et al.*, 2022). 45 % of Xoo cells appeared to be orientated perpendicular to pit membranes, indicating that adherence and possibly T3SS secretion are polarized (Figure 5). Upon injection of TALe, *SWEET* induction redirects the sucrose flux to the nutrient scarce xylem sap. When the plant cannot contain Xoo infection by deposition of tyloses, thickening of xylem vessel walls or other defense responses (Hilaire *et al.*, 2001; Yadeta and J. Thomma, 2013), Xoo migration will progress.

Route of Xoo infection detected with translational SWEET-GUS reporter lines

To date, the colonization route of Xoo during infection was deduced from the appearance of the chlorotic (pale yellow) and necrotrophic (grey) lesions after leaf clip infection (Kauffman, 1973). Our analysis here relied on the pathogen's requirement for *SWEET* gene induction and resolved colonization patterns more sensitively than lesion lengths. Translational SWEET11a-GUS reporter lines enabled accurate spatiotemporal resolution of bacterial distribution, revealing a basipetal infection pattern from main veins through transverse veins to minor veins. Notably the infection

process was found to be non-contiguous, but to occur via formation of new colonies that migrated basipetally. Only strains carrying the SWEET11a-inducing TAL effector PthXo1 induced diX Indigo accumulation, confirming the effector dependency of the Xoo-rice pathosystem (Eom *et al.*, 2019; Redzich *et al.*, 2025). The migration of Xoo within rice vasculature corresponds to leaf vein architecture and likely reflects a strategy for systemic spread and nutrient acquisition. Mapping of the Xoo infection route helped us to examine specific phases of colonization using CLSM and SEM.

Conditional filamentation of Xoo lead to different viability of filaments *in vitro*

On agar plates, Xoo colonies developed a zonal architecture with three concentric regions. Each zone displayed different optical properties and distinct mixtures of rod-shaped bacilli and filamentous cells (Figure 1). The colony center contained mostly rod-shaped cells, while the periphery was enriched in filamentous forms. This spatial organization likely reflects gradients in nutrients, oxygen, and cell signaling molecules. Filaments were also observed for Xoo exposed to high salinity or high OD_{600} in liquid cultures (Figure 2). Our findings are consistent with bacterial pathogen responses to environmental conditions, where filamentation often serves as an conditional phenotypic change to enhance resilience (Justice *et al.*, 2008), compared to obligate filamentous species (Dubnau and Losick, 2006; Herrero *et al.*, 2016; Chandra and Chater, 2014). When populations were separated by cell length and growth history, filamentous cells from high salinity cultures produced the highest number of CFU, indicative of high active reproduction (Figure 3). By contrast, filamentous cells from high-density cultures formed fewer colonies. Our data imply that depending on the status of the originator population, filamentous cells can share the same phenotypic features but differ in their viability. Filamentation in Xoo appears to represent a conditional response of bacteria to environmental conditions. The *in vitro* system may allow us in the next step to identify differences in gene expression in bacilli and filamentous stages, e.g. by RNAseq, as a basis for generating mutants to explore the mechanism of reversible filamentation and their role in host colonization.

Xoo filaments can revert into pleomorphic colonies

To gain insights into the developmental program of filamentation, filamentous cells were observed by time lapse over a 24-hour period in a live imaging set-up.

Filamentous cells elongated after transferal to imaging chamber , subsequently forming septa at irregular positions and then divided asymmetrically (Figure 3). The divisions generated a mixed population containing rod-shaped, intermediate, and filamentous cells, as described for other bacteria (Yamaki *et al.*, 2021; Cayron *et al.*, 2023; Rossetti *et al.*, 2011). The reversible transition of filamentous to pleomorphic cell morphology indicates that filamentation represents a transient stage rather than a terminal state. In contrast to the unipolar growth observed for *Corynebacteriu matruchotii* and *Leptrothis cholodnii* (Kunoh *et al.*, 2021; Chimileski *et al.*, 2024), bipolar peptidoglycan synthesis appeared to occur in Xoo. In the context of host colonization, reversible filamentation could allow the mobilization of cells for further colonization in the basipetal direction in leaves and the foundation of new colonies, as observed in the SWEET-GUS-reporter system population expansion. Mutants defective in the different steps of this cycle in conjunction with the reporter systems developed here may help to gain insights into the exact process.

Data availability

Raw and meta data are available at: https://doi.org/10.60534/8d4s9-ywr51

Acknowledgements

We thank Joon Seob Eom for initial experiments on infection progression in rice leaves as monitored using a stably transformed translational SWEET11a-GUS line. We also thank Sebastian Hänsch and Steffen Köhler from the Center for Advanced Imaging (CAi) for training, continuous advice and support with both confocal and SEM imaging and data analysis. We thank Dominik Brilhaus (CEPLAS) for training and advice on ARC generation, publication of raw and meta data and Tom Boissonnet (CAi) for microscopy data management. This work was supported by grants from Deutsche Forschungsgemeinschaft (DFG, German Research Foundation) - Collaborative Research Center SFB1535, project ID 458090666/CRC1535/1; Deutsche Forschungsgemeinschaft (DFG, German Research Foundation) under Germany´s Excellence Strategy – EXC-2048/1 – project ID 390686111 (CEPLAS2), and the Alexander von Humboldt Professorship to WF. LR was supported by a stipend from the Heinrich Böll Stiftung and CEPLAS.

Declaration of interests

The authors declare no competing interests.

Author contributions

LR and WBF conceived the study. LR, ZYM and AR performed experiments. VSL and EL supervised the team. MB supported LR for SEM on rice leaves. LR, ZYM and WBF performed analyses. LR and WBF wrote the manuscript.

References

Abell-King, C., Costas, A., Duggin, I.G. and Söderström, B. (2022) Bacterial filamentation during urinary tract infections. *PLOS Pathog.*, **18**, e1010950.

Allison, C., Coleman, N., Jones, P.L. and Hughes, C. (1992) Ability of *Proteus mirabilis* to invade human urothelial cells is coupled to motility and swarming differentiation. *Infect. Immun.*, **60**, 4740–4746.

Álvarez, B., López, M.M. and Biosca, E.G. (2008) Survival strategies and pathogenicity of *Ralstonia solanacearum* phylotype II subjected to prolonged starvation in environmental water microcosms. *Microbiology*, **154**, 3590–3598.

Anbumani, S., Silva, A.M. da, Carvalho, I.G.B., et al. (2021) Controlled spatial organization of bacterial growth reveals key role of cell filamentation preceding *Xylella fastidiosa* biofilm formation. *Npj Biofilms Microbiomes*, **7**, 1–12.

Arra, Y., Hutin, M., Biasco, C., Thomas, E., Devanna, B.N., Auguy, F., Loo, E.P.I., Szurek, B. and Frommer, W.B. (2025) Stacking of bacterial blight resistance genes in three rice varieties to protect against a disease outbreak in East Africa and Madagascar. *BiorXiv*.

Bisson-Filho, A.W., Hsu, Y.-P., Squyres, G.R., et al. (2017) Treadmilling by FtsZ filaments drives peptidoglycan synthesis and bacterial cell division. *Science*, **35**, 739–743.

Bos, J., Zhang, Q., Vyawahare, S., Rogers, E., Rosenberg, S.M. and Austin, R.H. (2015) Emergence of antibiotic resistance from multinucleated bacterial filaments. *Proc. Natl. Acad. Sci.*, **112**, 178–183.

Caires, N.P., Guimarães, L.M.S., Hermenegildo, P.S., Rodrigues, F.A., Badel, J.L. and Alfenas, A.C. (2020) Bidirectional colonization and biofilm formation by *Erwinia psidii* in eucalypt plants. *Plant Pathol.*, **69**, 549–558.

Cao, J., Chu, C., Zhang, M., He, L., Qin, L., Li, X. and Yuan, M. (2020) Different cell wall-degradation ability leads to tissue-specificity between *Xanthomonas oryzae* pv. *oryzae* and *Xanthomonas oryzae* pv. *oryzicola*. *Pathogens*, **9**, 187.

Cayron, J., Dedieu-Berne, A. and Lesterlin, C. (2023) Bacterial filaments recover by successive and accelerated asymmetric divisions that allow rapid post-stress cell proliferation. *Mol. Microbiol.*, **119**, 237–251.

Cerutti, A., Jauneau, A., Auriac, M.-C., Lauber, E., Martinez, Y., Chiarenza, S., Leonhardt, N., Berthomé, R. and Noël, L.D. (2017) Immunity at cauliflower hydathodes controls systemic infection by *Xanthomonas campestris* pv. *campestris* . *Plant Physiol.*, **174**, 700–716.

Chandra, G. and Chater, K.F. (2014) Developmental biology of *Streptomyces* from the perspective of 100 actinobacterial genome sequences. *Fems Microbiol. Rev.*, **38**, 345–379.

Chen, Hou, B.-H., Lalonde, S., et al. (2010) Sugar transporters for intercellular exchange and nutrition of pathogens. *Nature*, **468**, 527–532.

Chen, L.-Q., Qu, X.-Q., Hou, B.-H., Sosso, D., Osorio, S., Fernie, A.R. and Frommer, W.B. (2012) Sucrose efflux mediated by SWEET proteins as a key step for phloem transport. *Science*, **335**, 207–211.

Chimileski, S., Borisy, G.G., Dewhirst, F.E. and Mark Welch, J.L. (2024) Tip extension and simultaneous multiple fission in a filamentous bacterium. *Proc. Natl. Acad. Sci.*, **121**, e2408654121.

Claessen, D., Rozen, D.E., Kuipers, O.P., Søgaard-Andersen, L. and Wezel, G.P. van (2014) Bacterial solutions to multicellularity: a tale of biofilms, filaments and fruiting bodies. *Nat. Rev. Microbiol.*, **12**, 115–124.

Cordell, S.C., Robinson, E.J.H. and Löwe, J. (2003) Crystal structure of the SOS cell division inhibitor SulA and in complex with FtsZ. *Proc. Natl. Acad. Sci.*, **100**, 7889–7894.

Corno, G. and Jürgens, K. (2006) Direct and indirect effects of protist predation on population size structure of a bacterial strain with high phenotypic plasticity. *Appl. Environ. Microbiol.*, **72**, 78–86.

Cui, Z., Yang, C.-H., Kharadi, R.R., Yuan, X., Sundin, G.W., Triplett, L.R., Wang, J. and Zeng, Q. (2019) Cell-length heterogeneity: a population-level solution to growth/virulence trade-offs in the plant pathogen *Dickeya dadantii*. *PLoS Pathog.*, **15**, e1007703.

Dajkovic, A., Mukherjee, A. and Lutkenhaus, J. (2008) Investigation of regulation of FtsZ assembly by SulA and development of a model for FtsZ polymerization. *J. Bacteriol.*, **190**, 2513–2526.

Das, A., Rangaraj, N. and Sonti, R.V. (2009) Multiple adhesin-like functions of *Xanthomonas oryzae* pv. *oryzae* are involved in promoting leaf attachment, entry, and virulence on Rice. *Mol. Plant Microbe Interact.*, **22**, 73–85.

Davis, K.M., Mohammadi, S. and Isberg, R.R. (2015) Community behavior and spatial regulation within a bacterial microcolony in deep tissue sites serves to protect against host attack. *Cell Host Microbe*, **17**, 21–31.

Dubnau, D. and Losick, R. (2006) Bistability in bacteria. *Mol. Microbiol.*, **61**, 564–572.

Ejike, J.O., Sadoine, M., Shen, Y., et al. (2024) A monochromatically excitable green–red dual-fluorophore fusion incorporating a new large Stokes shift fluorescent protein. *Biochemistry*, **63**, 171–180.

Eom, J.-S., Luo, D., Atienza-Grande, G., et al. (2019) Diagnostic kit for rice blight resistance. *Nat. Biotechnol.*, **37**, 1372–1379.

Feng, T.-Y. and Kuo, T.-T. (1974) Bacterial leaf blight of rice plant VI. Chemotactic responses of *Xanthomonas oryzae* to water droplets exudated from water pores on the leaf of rice plants. *Bot. Bull. Academica Sinica*, **16**, 126–136.

Frirdich, E. and Gaynor, E.C. (2013) Peptidoglycan hydrolases, bacterial shape, and pathogenesis. *Curr. Opin. Microbiol.*, **16**, 767–778.

Gluck-Thaler, E., Cerutti, A., Perez-Quintero, A.L., et al. (2020) Repeated gain and loss of a single gene modulates the evolution of vascular plant pathogen lifestyles. *Sci. Adv.*, **6**, eabc4516.

Gode-Potratz, C.J., Kustusch, R.J., Breheny, P.J., Weiss, D.S. and McCarter, L.L. (2011) Surface sensing in *Vibrio parahaemolyticus* triggers a programme of gene expression that promotes colonization and virulence. *Mol. Microbiol.*, **79**, 240–263.

Hahn, M.W., Moore, E.R.B. and Höfle, M.G. (1999) Bacterial filament formation, a defense mechanism against flagellate grazing, is growth rate controlled in bacteria of different phyla. *Appl. Environ. Microbiol.*, **65**, 25–35.

Han, S.-W., Park, C.-J., Lee, S.-W. and Ronald, P.C. (2008) An efficient method for visualization and growth of fluorescent *Xanthomonas oryzae* pv. *oryzae in planta*. *BMC Microbiol.*, **8**, 164–173.

Herrero, A., Stavans, J. and Flores, E. (2016) The multicellular nature of filamentous heterocyst-forming cyanobacteria W. Margolin, ed. *FEMS Microbiol. Rev.*, **40**, 831–854.

Hilaire, E., Young, S.A., Willard, L.H., McGee, J.D., Sweat, T., Chittoor, J.M., Guikema, J.A. and Leach, J.E. (2001) Vascular defense responses in rice: peroxidase accumulation in xylem parenchyma cells and xylem wall thickening. *Mol. Plant-Microbe Interact. MPMI*, **14**, 1411–1419.

Hill, N.S., Buske, P.J., Shi, Y. and Levin, P.A. (2013) A moonlighting enzyme links *Escherichia coli* cell size with central metabolism. *PLoS Genet.*, **9**, e1003663.

Horvath, D.J., Li, B., Casper, T., Partida-Sanchez, S., Hunstad, D.A., Hultgren, S.J. and Justice, S.S. (2011) Morphological plasticity promotes resistance to phagocyte killing of uropathogenic *Escherichia coli*. *Microbes Infect.*, **13**, 426–437.

Huang, P.-Y. and Goodman, R.N. (1970) Morphology and ultrastructure of normal rod-shaped and filamentous forms of *Erwinia amylovora*. *J. Bacteriol.*, **102**, 862–866.

Janissen, R., Murillo, D.M., Niza, B., et al. (2015) Spatiotemporal distribution of different extracellular polymeric substances and filamentation mediate *Xylella fastidiosa* adhesion and biofilm formation. *Sci. Rep.*, **5**, 9856–9866.

Justice, S.S., Hung, C., Theriot, J.A., Fletcher, D.A., Anderson, G.G., Footer, M.J. and Hultgren, S.J. (2004) Differentiation and developmental pathways of uropathogenic *Escherichia coli* in urinary tract pathogenesis. *Proc. Natl. Acad. Sci.*, **101**, 1333–1338.

Justice, S.S., Hunstad, D.A., Cegelski, L. and Hultgren, S.J. (2008) Morphological plasticity as a bacterial survival strategy. *Nat. Rev. Microbiol.*, **6**, 162–168.

Justice, S.S., Hunstad, D.A., Seed, P.C. and Hultgren, S.J. (2006) Filamentation by *Escherichia coli* subverts innate defenses during urinary tract infection. *Proc. Natl. Acad. Sci. U S A*, **52**, 19884–19889.

Karasz, D.C., Weaver, A.I., Buckley, D.H. and Wilhelm, R.C. (2022) Conditional filamentation as an adaptive trait of bacteria and its ecological significance in soils. *Environ. Microbiol.*, **24**, 1–17.

Kauffman, H. (1973) An improved technique for evaluating resistance of varieties to *Xanthomonas oryzae* pv. *oryzae*. *Plant Dis. Rep*, **57**, 537–541.

Kearns, D.B. and Losick, R. (2003) Swarming motility in undomesticated *Bacillus subtilis*. *Mol. Microbiol.*, **49**, 581–590.

Kim, S., Cho, Y.-J., Song, E.-S., Lee, S.H., Kim, J.-G. and Kang, L.-W. (2016) Time-resolved pathogenic gene expression analysis of the plant pathogen *Xanthomonas oryzae* pv. *oryzae*. *BMC Genomics*, **17**, 345–360.

Kunoh, T., Yamamoto, T., Sugimoto, S., Ono, E., Nomura, N. and Utada, A.S. (2021) *Leptothrix cholodnii* response to nutrient limitation. *Front. Microbiol.*, **12**, 691563.

Laloux, G. (2020) Shedding light on the cell biology of the predatory bacterium *Bdellovibrio bacteriovorus*. *Front. Microbiol.*, **10**, 3136.

Li, Yilang, Yan, Y., Deng, S., et al. (2020) The *Xanthomonas oryzae* pv. *oryzae* type IV pilus alignment subcomplex protein PilN contributes to regulation of bacterial surface-associated behaviours and T3SS system. *Plant Pathol.*, **69**, 744–755.

Liu, M.M., Coleman, S., Wilkinson, L., et al. (2020) Unique inducible filamentous motility identified in pathogenic *Bacillus cereus* group species. *ISME J.*, **14**, 2997–3010.

López-Pagán, N., Rufián, J.S., Luneau, J., Sánchez-Romero, M.-A., Aussel, L., Vliet, S. van, Ruiz-Albert, J. and Beuzón, C.R. (2025) *Pseudomonas syringae* subpopulations cooperate by coordinating flagellar and type III secretion spatiotemporal dynamics to facilitate plant infection. *Nat. Microbiol.*, **10**, 958–972.

Lorian, V., Ernst, J. and Amaral, L. (1989) The post-antibiotic effect defined by bacterial morphology. *J. Antimicrob. Chemother.*, **23**, 485–491.

Malafaia, C.B., Barros, M.P.D., Macedo, A.J., Guerra, M.D.L., Souza, E.B.D., Correia, M.T.D.S. and Silva, M.V.D. (2018) Biofilm formation by phytopathogenic bacteria *Acidovorax citrulli* subsp. *citrulli* and *Ralstonia solanacearum*. *J. Environ. Anal. Prog.*, 347–355.

McCully, M.E. (2001) Niches for bacterial endophytes in crop plants: a plant biologist's view. *Funct. Plant Biol.*, **28**, 983–990.

Mew, T.W. and Huang, J.S. (1984) Scanning electron microscopy of virulent and avirulent strains of *Xanthomonas campestris* pv. *oryzae* on rice leafs. *Phytopath.*, 74:635-641.

Möller, J., Emge, P., Vizcarra, I.A., Kollmannsberger, P. and Vogel, V. (2013) Bacterial filamentation accelerates colonization of adhesive spots embedded in biopassive surfaces. *New J. Phys.*, **15**, 125016.

Mulungu, E. (2024) Unmasking the hidden threat: a review of damage and losses due to phytopathogenic bacteria. *J. Curr. Opin. Crop Sci.*, **5**, 250–263.

Ng, W.-L. and Bassler, B.L. (2009) Bacterial quorum-sensing network architectures. *Annu. Rev. Genet.*, **43**, 197–222.

Oliva, R., Ji, C., Atienza-Grande, G., et al. (2019) Broad-spectrum resistance to bacterial blight in rice using genome editing. *Nat. Biotechnol.*, **37**, 1344–1350.

Otta, J.D. (1976) *Pseudomonas syringae*: rough colony type mutants and filamentous cells. *Phytopath.*, 249–252.

Paauw, M., Hulten, M. van, Chatterjee, S., Berg, J.A., Taks, N.W., Giesbers, M., Richard, M.M.S. and Burg, H.A. van den (2023) Hydathode immunity protects the *Arabidopsis* leaf vasculature against colonization by bacterial pathogens. *Curr. Biol.*, **33**, 697-710.e6.

Paauw, M., Schravesande, W.E.W., Taks, N.W., Rep, M., Pfeilmeier, S. and Burg, H.A. van den (2025) Evolution of a vascular plant pathogen is associated with the loss of CRISPR-Cas and an increase in genome plasticity and virulence genes. *Curr. Biol.*, **35**, 954-969.e5.

Piao, Z., Sze, C.C., Barysheva, O., Iida, K. and Yoshida, S. (2006) Temperature-regulated formation of mycelial mat-like biofilms by *Legionella pneumophila*. *Appl. Environ. Microbiol.*, **72**, 1613–1622.

Ponnusamy, D. and Clinkenbeard, K.D. (2012) *Yersinia pestis* intracellular parasitism of macrophages from hosts exhibiting high and low severity of plague. *PLOS ONE*, **7**, e42211.

Pratt, Z.L., Chen, B., Czuprynski, C.J., Wong, A.C.L. and Kaspar, C.W. (2012) Characterization of osmotically induced filaments of *Salmonella enterica*. *Appl. Environ. Microbiol.*, **78**, 6704–6713.

Rajeshwari, R., Jha, G. and Sonti, R.V. (2005) Role of an *in planta*-expressed xylanase of *Xanthomonas oryzae* pv. *oryzae* in promoting virulence on rice. *MPMI*, **18**, 830–837.

Redzich, L., Arra, Y., Loo, E.P.I. and Frommer, W.B. (2025) Restricted transmission of *Xanthomonas oryzae* pv. *oryzae* from rice roots to shoots detected by a rapid root infection system. *bioRxiv*.

Rizzo, M.G., Nicolò, M.S., Franco, D., De Plano, L.M., Chines, V., Moscato, F., Crea, G., Gugliandolo, C. and Guglielmino, S.P.P. (2019) Glutamine-induced filamentous cells of *Pseudomonas mediterranea* CFBP-5447T as producers of PHAs. *Appl. Microbiol. Biotechnol.*, **103**, 9057–9066.

Rossetti, V., Filippini, M., Svercel, M., Barbour, A.D. and Bagheri, H.C. (2011) Emergent multicellular life cycles in filamentous bacteria owing to density-dependent population dynamics. *J. R. Soc. Interface*, **8**, 1772–1784.

Sargent, M.G. (1975) Control of cell length in *Bacillus subtilis*. *J Bacteriol*, **1**, 7–19.

Savary, S., Willocquet, L., Pethybridge, S.J., Esker, P., McRoberts, N. and Nelson, A. (2019) The global burden of pathogens and pests on major food crops. *Nat. Ecol. Evol.*, **3**, 430–439.

Schepler-Luu, V., Sciallano, C., Stiebner, M., et al. (2023) Genome editing of an African elite rice variety confers resistance against endemic and emerging *Xanthomonas oryzae* pv. *oryzae* strains. *eLife*, **12**, e84864.

Steinberger, R.E., Allen, A.R., Hansma, H.G. and Holden, P.A. (2002) Elongation correlates with nutrient deprivation in *Pseudomonas aeruginosa* unsaturated biofilms. *Microb. Ecol.*, **43**, 416–423.

Tran, T.D., Ali, M.A., Lee, D., Félix, M.-A. and Luallen, R.J. (2022) Bacterial filamentation as a mechanism for cell-to-cell spread within an animal host. *Nat. Commun.*, **13**, 693.

Wang, H., Yang, H., Wen, Z., et al. (2022) Xylan-based nanocompartments orchestrate plant vessel wall patterning. *Nat. Plants*, **8**, 295–306.

Weart, R.B., Lee, A.H., Chien, A.-C., Haeusser, D.P., Hill, N.S. and Levin, P.A. (2007) A metabolic sensor governing cell size in bacteria. *Cell*, **130**, 335–347.

Yadeta, K. and Thomma, B. (2013) The xylem as battleground for plant hosts and vascular wilt pathogens. *Front. Plant Sci.*, **4**, 97.

Yadeta, K.A. and J. Thomma, B.P.H. (2013) The xylem as battleground for plant hosts and vascular wilt pathogens. *Front. Plant Sci.*, **4**, 97.

Yamaki, S., Kawai, Y. and Yamazaki, K. (2021) Long filamentous state of *Listeria monocytogenes* induced by sublethal sodium chloride stress poses risk of rapid increase in colony-forming units. *Food Control*, **124**, 107860.

Yan, Y., Wang, J., Zhao, N., Cui, D. and Zhao, M. (2025) Antibacterial effect and mechanism of chelerythrine on *Xanthomonas oryzae* pv. *oryzae*. *Microorganisms*, **13**, 953–972.

Yoshida, S., Udou, T., Mizuguchi, Y. and Tanabe, T. (1986) Salt-induced filamentous growth of a *Salmonella* strain isolated from blood. *J. Clin. Microbiol.*, **23**, 192–194.

Zhang, C., Lv, M., Yin, W., Dong, T., Chang, C., Miao, Y., Jia, Y. and Deng, Y. (2019) *Xanthomonas campestris* promotes diffusible signal factor biosynthesis and pathogenicity by utilizing glucose and sucrose from host plants. *MPMI*, **32**, 157–166.

Zöllner, N.R., Long, J., Song, C., et al. (2025) A critical role of sux cistron-mediated sucrose uptake for virulence of the rice blight pathogen *Xanthomonas oryzae* pv. *oryzae*. *BiorXiv*, 2025.06.02.657373.

Supplementary Material

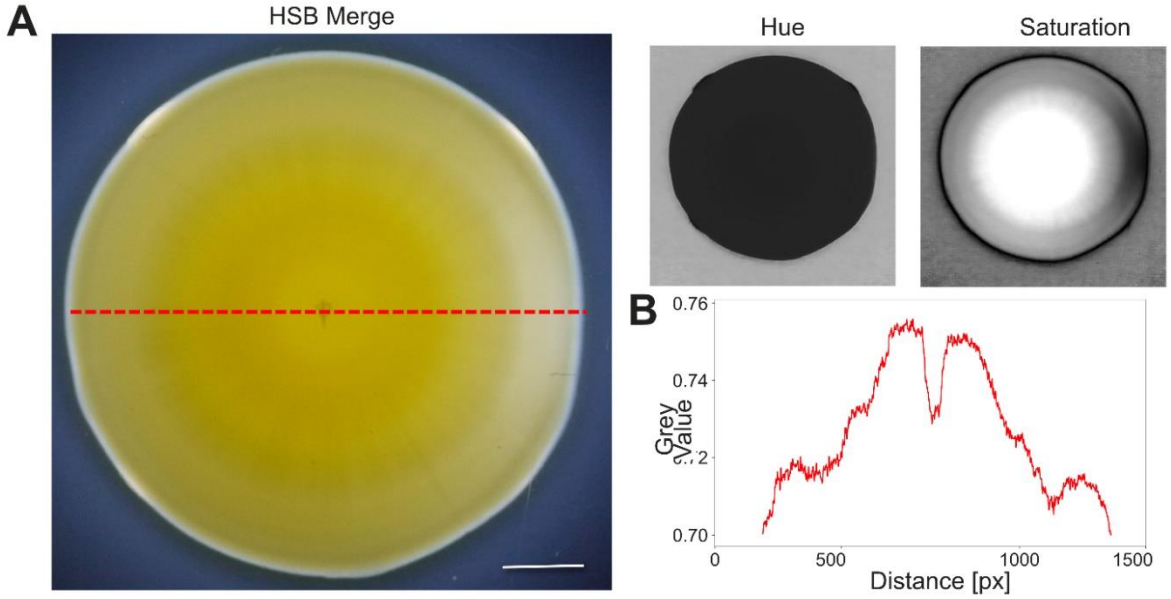

Figure S1.1. HSB color space segmentation of bacterial colonies. (A). Colonies were analyzed in the hue-saturation-brightness (HSB) color space to enable pixel-level discrimination of structural and optical features across the colony surface. **(B).** Segmentation was based on the grayscale value of pixels analyzed for pixels on the red-line in the HSB merge image.

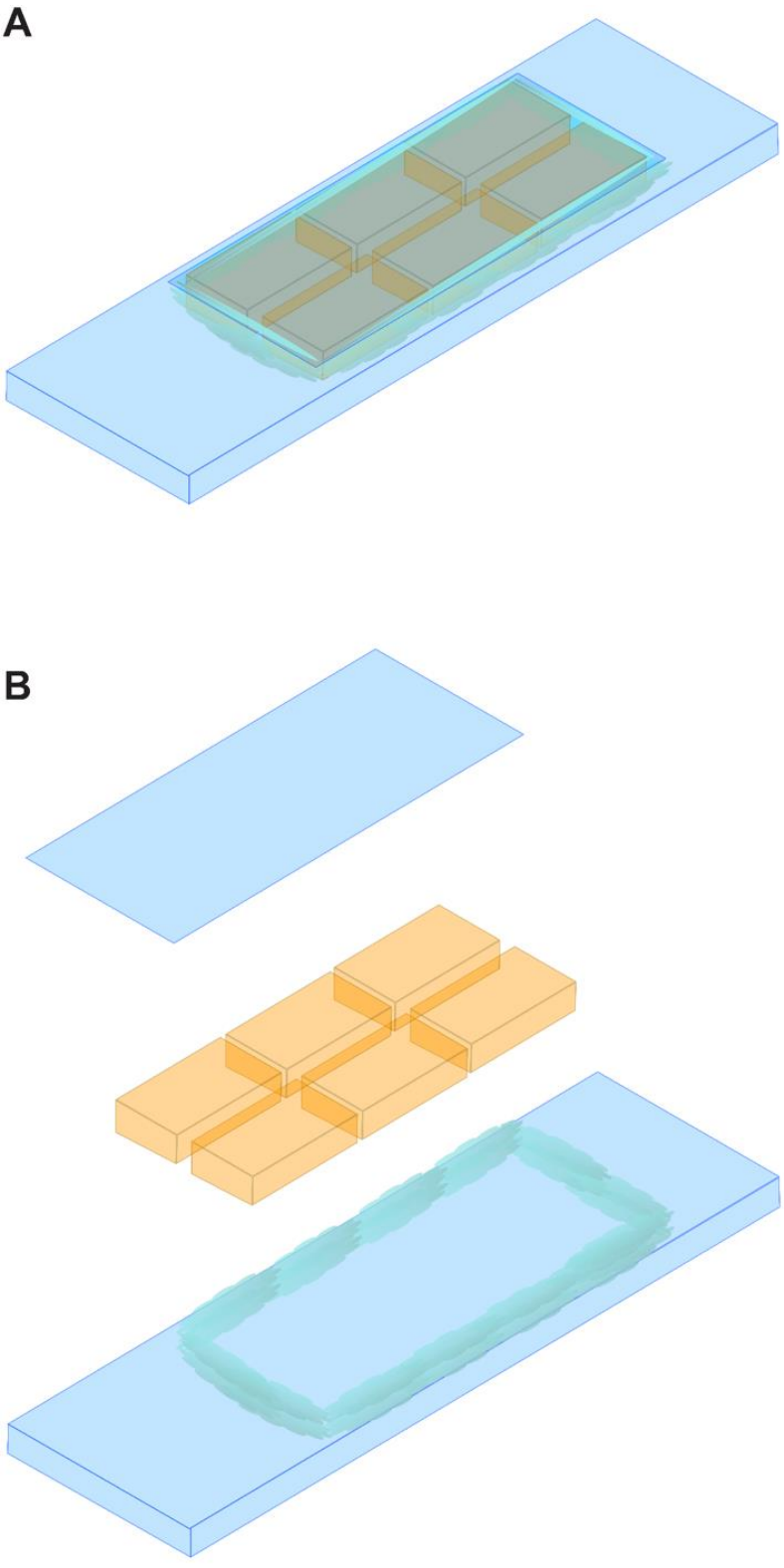

Figure S1.2. Assembly of an agar-based aerated imaging chamber. The chamber was constructed by placing six thin, evenly poured NBSA media blocks onto a glass slide to in 0.5 cm distance to maintain aeration. Imaging dish and cover glass was surrounded with a rim of silicon grease to prevent desiccation. Long-term live-cell imaging was performed with Zeiss Immersol W immersion liquid.

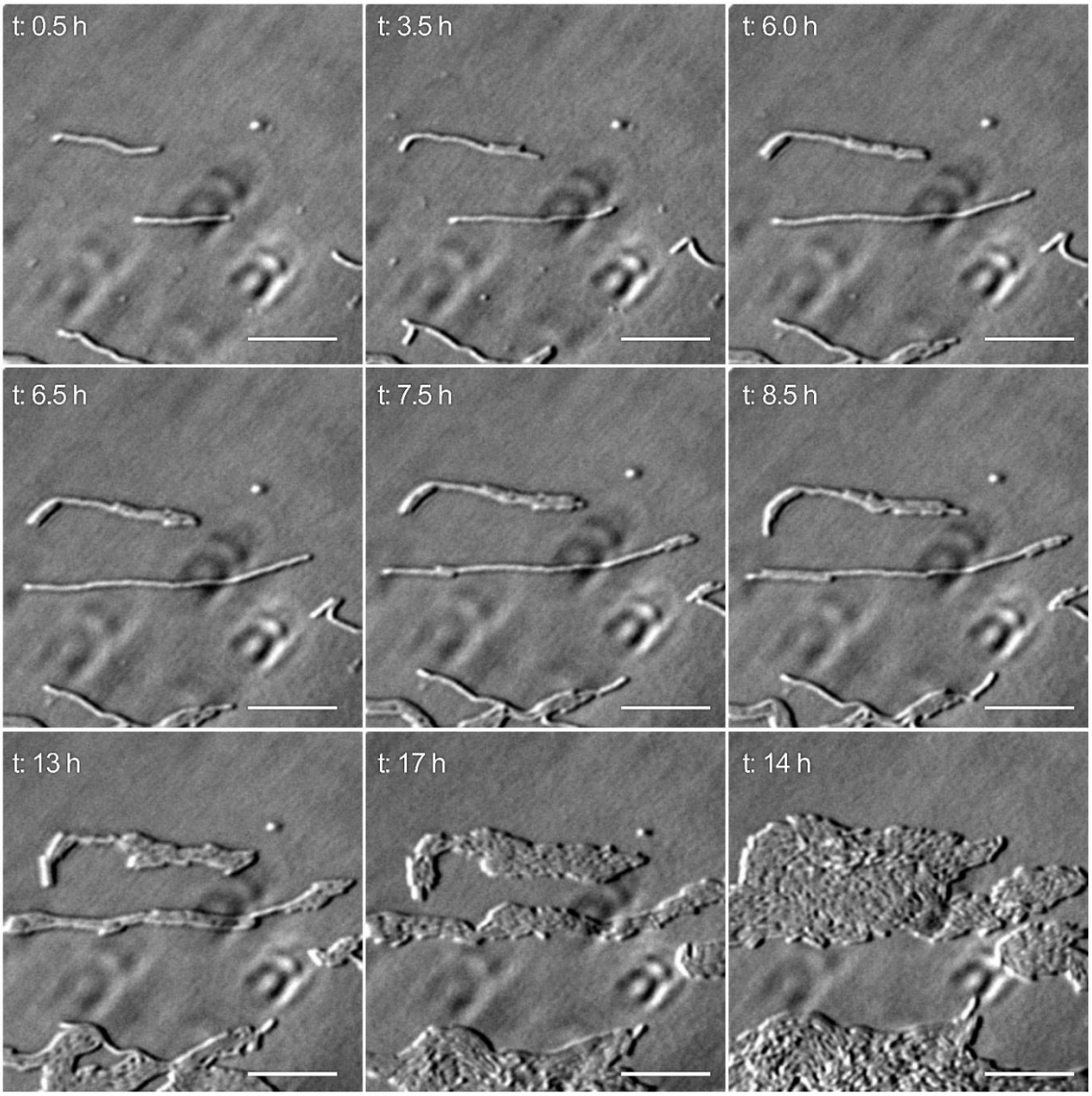

Figure S1.3. Time-lapse imaging of filamentous *Xanthomonas oryzae* pv. *oryzae*. Filamentous cells were separated by filtration from cultures grown in high salinity (OD_{600} 0.4, 500 mM NaCl) and transferred onto NBSA medium within the aerated imaging chamber (Figure S4). Individual filaments were monitored for 24 h by bright-field microscopy (Nikon Ti Eclipse PFS). Representative images at selected time points are shown; Z-stacks were acquired every 30 min for 24 h. Scale bar: 10 µm.

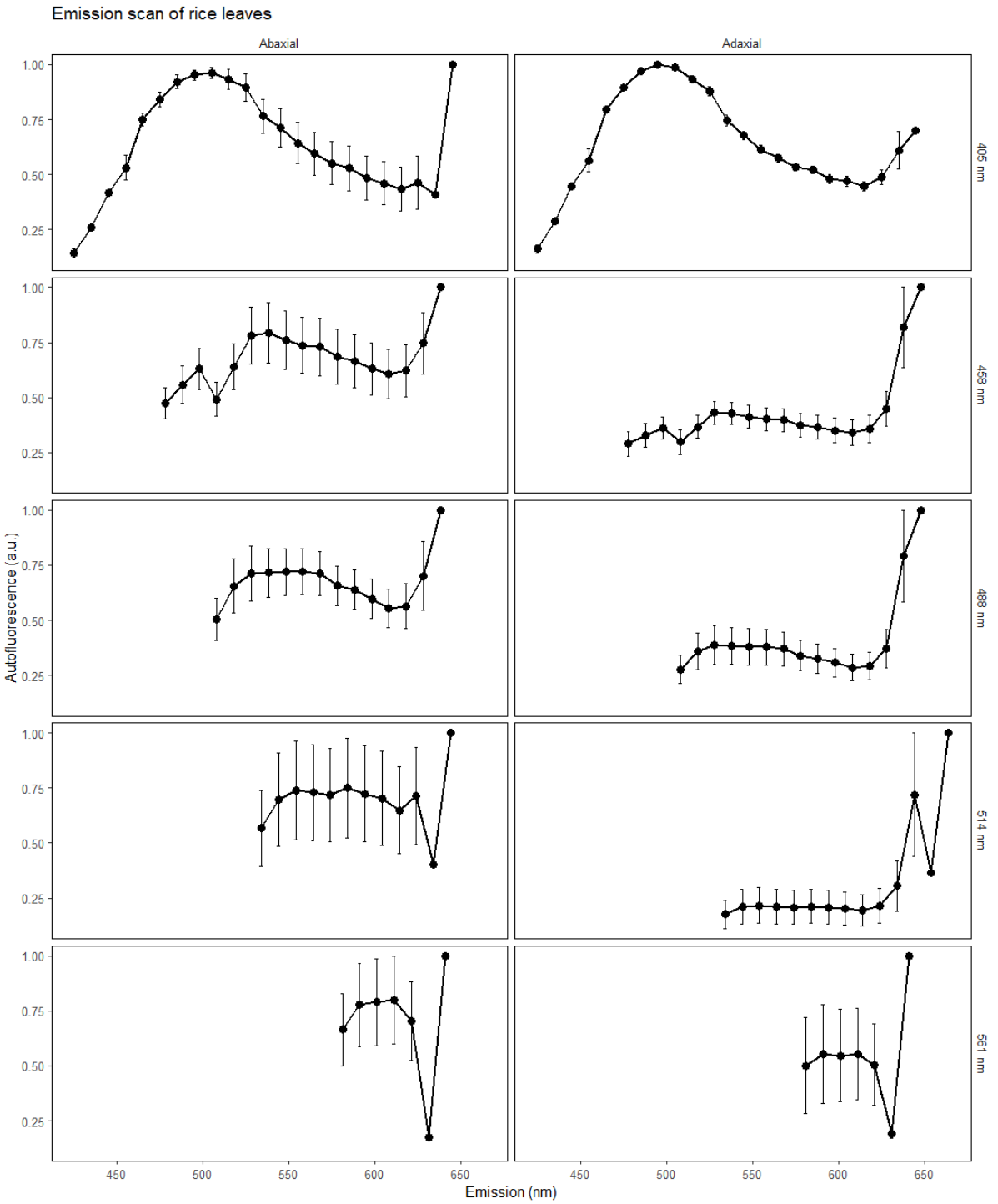

Figure S1.4. Autofluorescence scans of rice leaves. Emission spectra were acquired on a Leica TCS SP8 using a 40× water-immersion objective with excitation at 405, 488, 514, and 561 nm. Emission was collected in 10 nm steps from excitation +20 nm up to 640 nm (peak at 740 nm: chloroplast autofluorescence). Regions of interest were recorded on adaxial and abaxial surfaces of the fourth leaf, with three biological replicates analyzed.

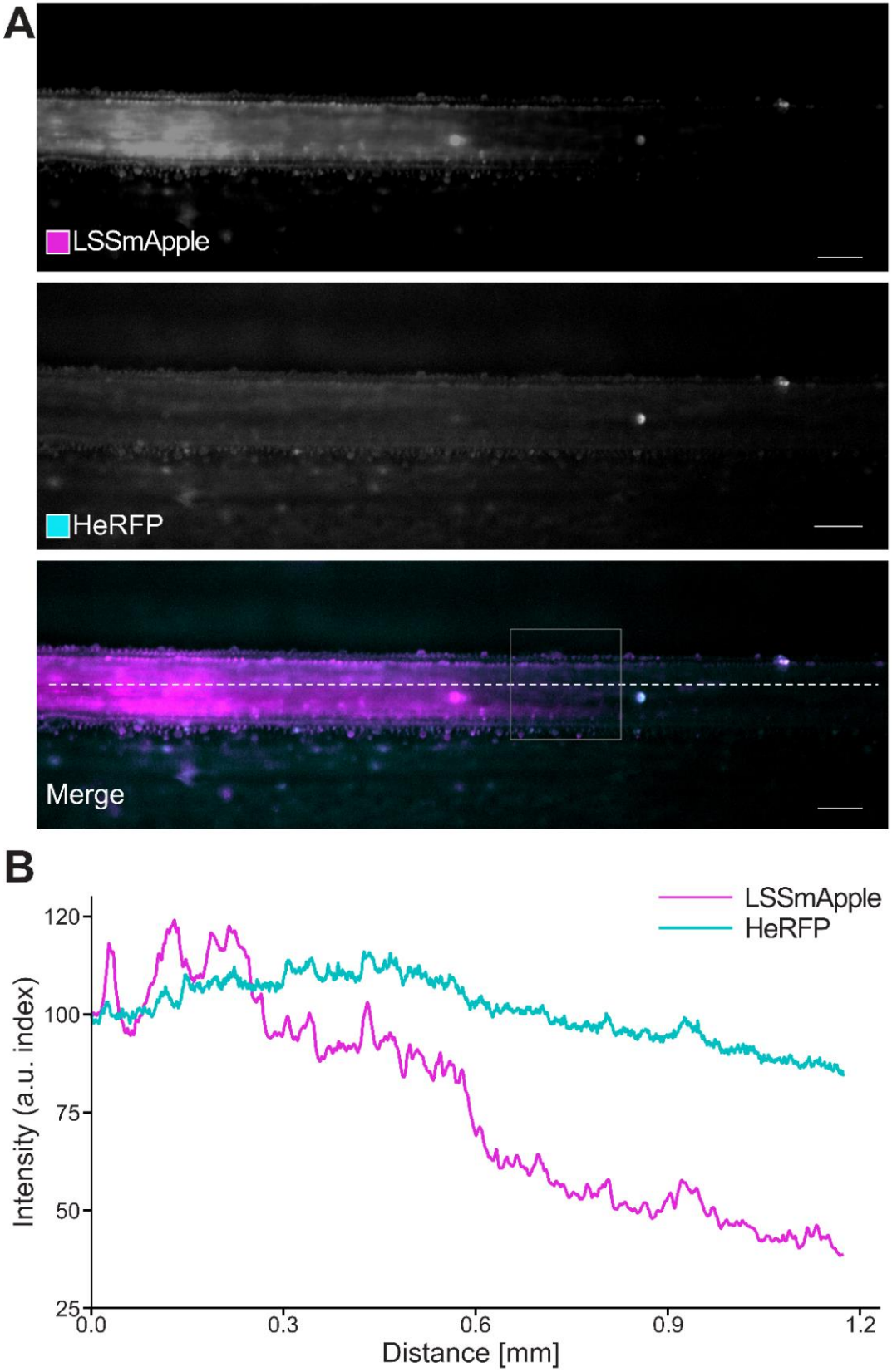

Figure S1.5. Identification of the infection front for SEM with PXO99$^{A}_{LSSmApple}$. For scanning electron images of the infection front, regions spanning at ~0.5 cm from the visible infection front observed by PXO99$^{A}_{LSSmApple}$ fluorescence signal were selected. (A) Images of rice xylem colonized by PXO99$^{A}_{LSSmApple}$. Selected region for processed for SEM analyzes indicated by square (B) Fluorescence intensity profile of LSSmApple compared to rice autofluorescence detected with 63 HE mRFP filter (indicated by dashed line in A).

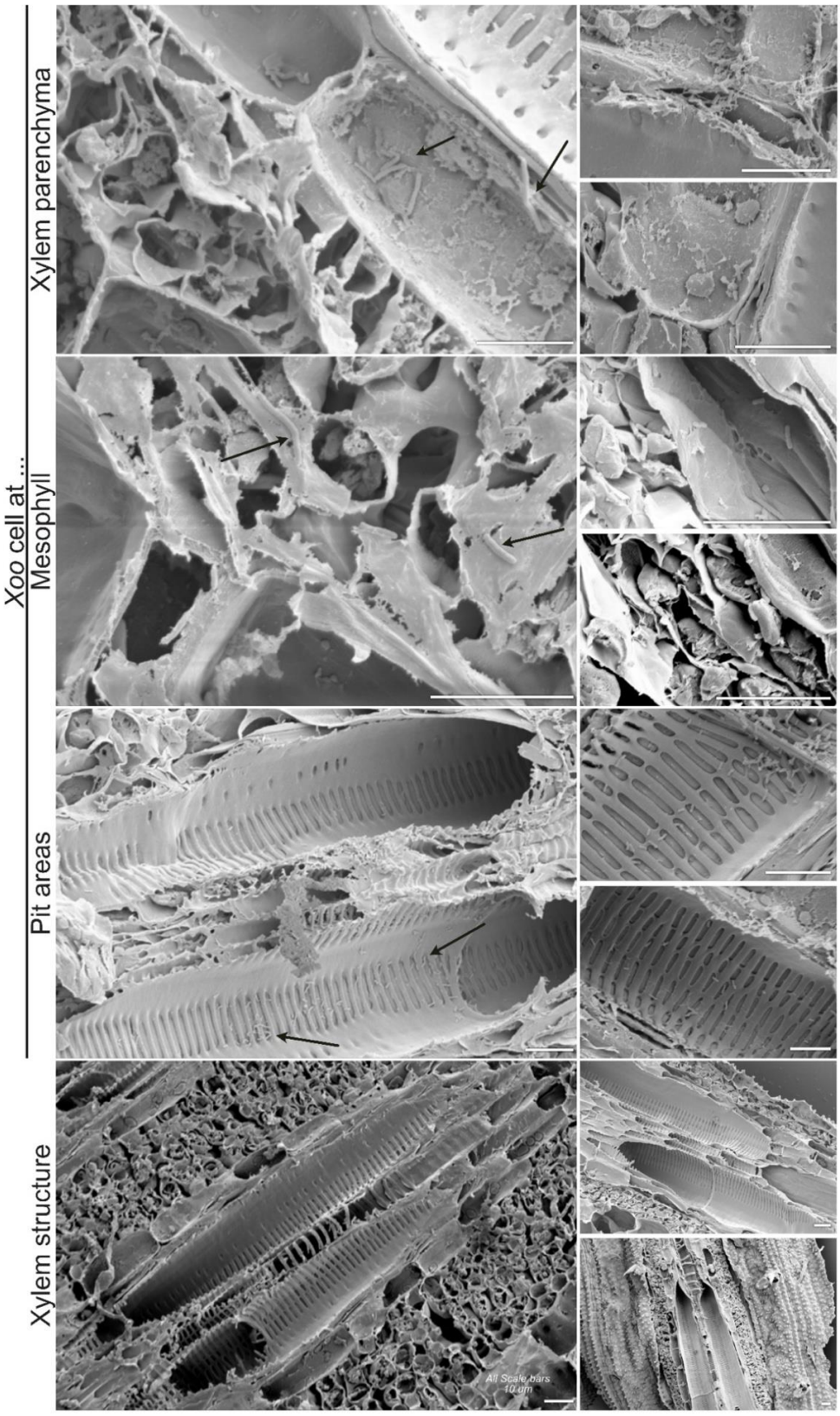

Figure S1.6. Scanning electron microscopy of *Xanthomonas oryzae* pv. *oryzae* colonization *in planta* and vascular bundle structure in rice leaves. Representative SEM images showing Xoo localization and xylem ultrastructure in infected rice leaves. Xoo cells (black arrows) within XP (first panel). Xoo cells detected in mesophyll tissue (second panel). Xoo cells at xylem pits in metaxylem vessels (Third panel). Detailed view of overall vascular bundle architecture in rice, highlighting metaxylem vessels, tracheids and xylem parenchyma cells of the xylem (fourth panel). Scale bars: 10 µm.

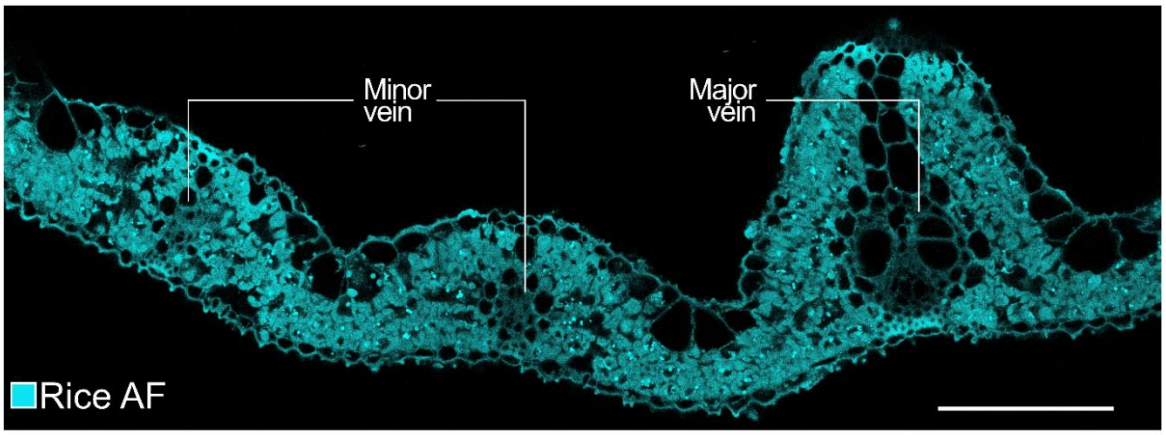

Figure S1.7. Overview of rice leaf cross section. Cross section of rice leaf. Shown here: two secondary veins and a primary vein. Rice autofluorescence at 488 nm excitation shown in turquoise. Scale bar: 100 µm.

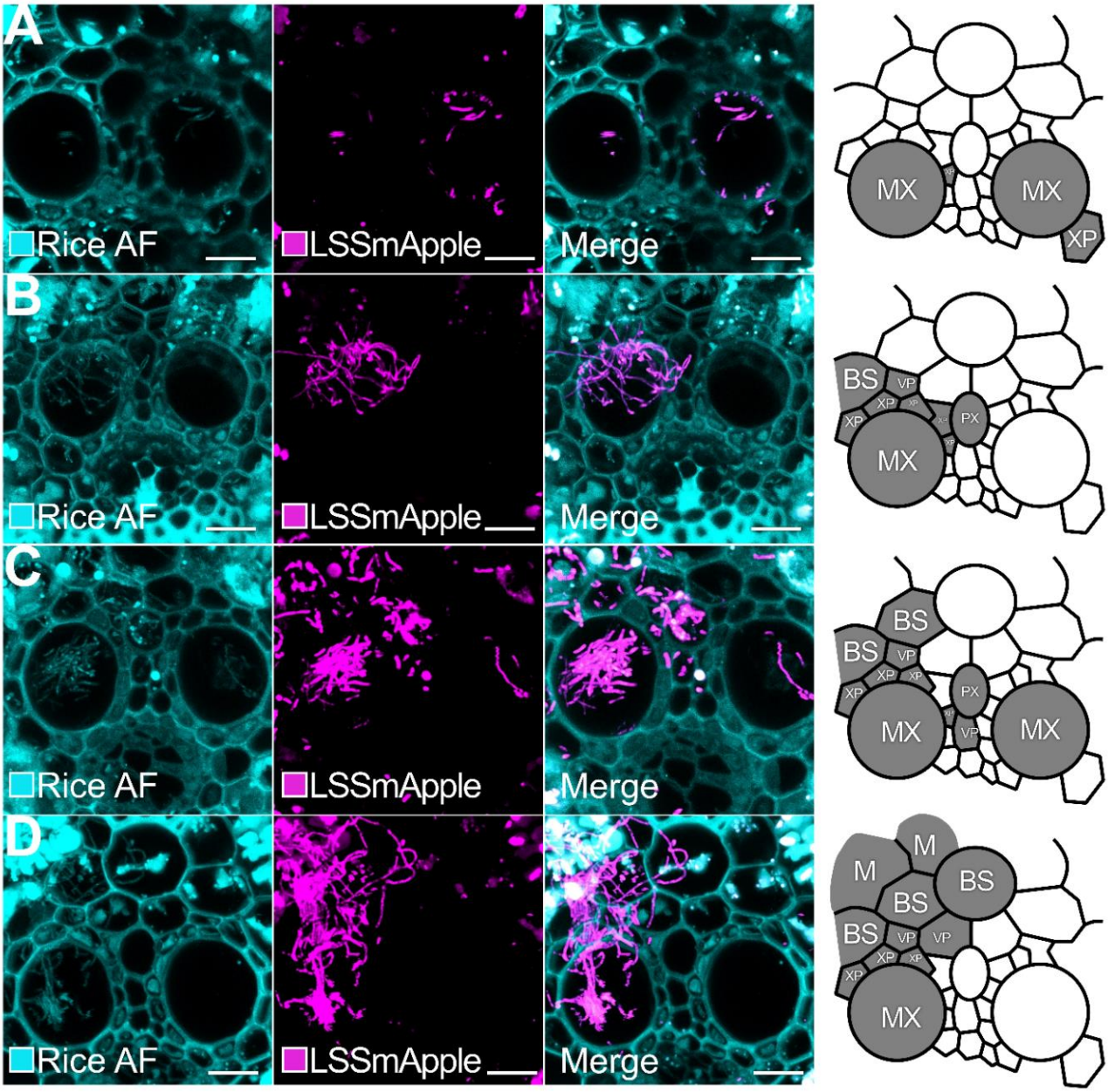

Figure S1.8. Colonization pattern of Xoo in cross sections of major veins visualized by CLSM. Representative images of filamentous Xoo observed in leaves of three independent experiments with 4 individual plants each. Apparent dispersal pattern of filamentous Xoo (grey) indicated in right column. **A)** Short filamentous Xoo (< 7 µm) observed in metaxylem and parenchyma cells. Biological replicate 3 from independent experimental repeat 3 (same independent repeat as in in Fig. S8B). **B)** Individual filaments of Xoo appear to reach lengths of 30 µm (observed here in 2D). Filaments traversed from metaxylem vessels to xylem parenchyma and bundle sheath cells. Biological replicate 3 from independent experimental repeat 3 (same independent repeat as in in Fig. S8A). **C)** Filamentous Xoo >10 µm in the two metaxylem vessels. Apparent rod-shaped Xoo observed in xylem tracheid and xylem parenchyma cells. Biological replicate 1 from independent experimental repeat 2. **D)** Filamentous Xoo observed in metaxylem, xylem parenchyma, bundle sheath cells and mesophyll tissue. Individual filaments appear to reach lengths of 35 µm. Biological replicate 2 from independent experimental repeat 1. Major vein cell pattern for cartoon was derived from S8D. MX: metaxylem vessel, BS: Bundle sheath cell, VP: vascular parenchyma cell, XP: xylem parenchyma cell M: mesophyll. Scale bar: 10 µm.

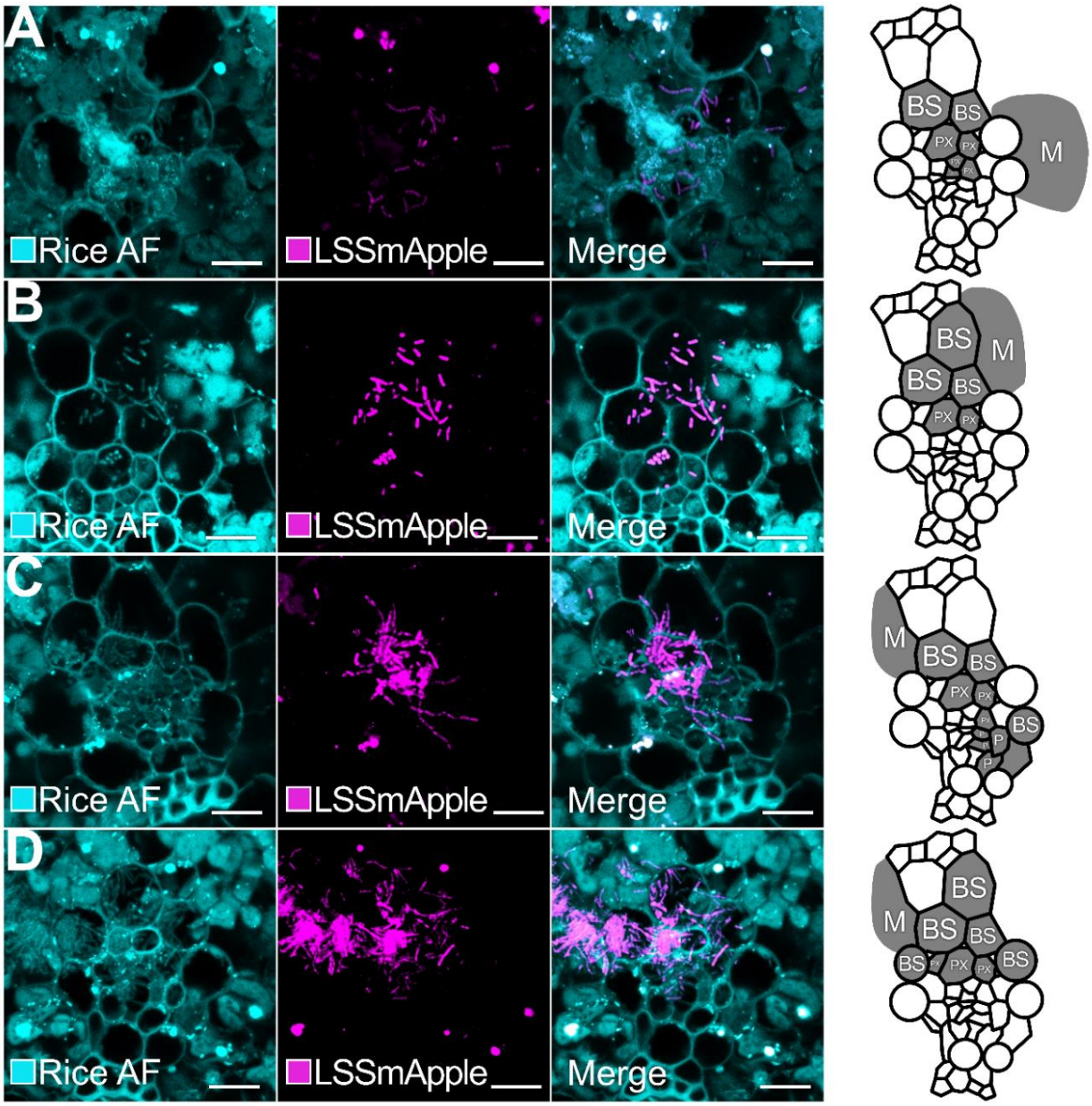

Figure S1.9. Colonization pattern of Xoo in cross sections of minor veins visualized by CLSM. Representative images of filamentous Xoo observed in leaves of three independent experiments with 4 individual plants each. Apparent dispersal pattern of filamentous Xoo (grey gradient) indicated in the cartoon (rightmost column). **A)** Individual filaments of Xoo appear to be up to 12.4 µm long. Filaments traverse from protoxylem to bundle sheath cells. Elongated Xoo cells appear to be septated. Biological replicate 3 from independent repeat 2

(same independent repeat as in Figure S9D). **B)** Short filamentous Xoo observed in protoxylem, bundle sheath and mesophyll tissue (approximately 6-8 µm). Other Xoo cells appeared rod-shaped in protoxylem and bundle sheath cells. Biological replicate 1 from independent experimental repeat 1. **C)** Filamentous Xoo (approximately up to 21.2 µm long) observed in protoxylem and bundle sheath cells. Xoo cells appear to be septated. Biological replicate 4 from independent experimental repeat 3. **D)** Filamentous Xoo breach from protoxylem to bundle sheath and mesophyll tissue. High density of filamentous Xoo cells appear to cluster in parallel in bundle sheath cells and mesophyll tissue. Filamentous are approximately between 10-16 µm long. Biological replicate 1 from independent experimental repeat 2. (same independent repeat as in Figure S9A) Minor vein cell pattern for cartoon was derived from S9C and S9D. BS: Bundle sheath cell, PX: protoxylem (xylem parenchyma and tracheids), P: phloem, M: mesophyll. Scale bar: 10 µm.

Table S1.1. Xoo strains used in this study. All strains were retrieved from the -80 °C glycerol stocks.

Strain	TALe	Targeted EBE sequence	Targeted *SWEET*
PXO99[A]	PthXo1	GCATCTCCCCCTACTGTACACCAC	*SWEET11a*
PXO99[A]	PthXo1	GCATCTCCCCCTACTGTACACCAC	*SWEET11a*
ME2	-		non-virulent

Table S1.2. Rice lines used in this study. All lines were retrieved from the rice seed stocks and tested for Hygromycin B resistance.

Name	Transformation Event	Characteristics	Generation
B01069	[8-3]	pSWEET11a:g*SWEET11a*-GUSplus	T4
B01075	[10-2]	pSWEET11a:g*SWEET11a*-GUSplus	T4

Table S1.3. Recipes for solutions for GUS histochemistry

Washing buffer

Component	Final concentration	For 50 ml
0.5 M EDTA	10 mM	1 ml
100 mM phosphate buffer pH 7	50 mM	25 ml
10 % triton X-100	0.1 %	0.5 ml
50 mM potassium ferrocyanide	1 mM	1 ml
50 mM potassium ferricyanide	1 mM	1 ml
methanol	20 %	10 ml
sterile water		Ad 50 ml

X-Gluc staining buffer

Component	Final concentration	For 50 ml
0.5 M EDTA	10 mM	1 ml
100 mM phosphate buffer pH 7	50 mM	25 ml
10 % Triton X-100	0.1 %	0.5 ml
50 mM potassium ferrocyanide	1 mM	1 ml
50 mM potassium ferricyanide	1 mM	1 ml
methanol	20 %	10 ml
100 mM X-Gluc	2 mM	1 ml
sterile water		Add 50 ml

100 mM phosphate buffer, pH 7

Component	Volume
0.5 M sodium phosphate dibasic (Na_2HPO_4)	3 ml
1 M sodium phosphate monobasic (NaH_2PO_4)	1 ml

100 mM X-Gluc solution

Component	Final concentration	For 50 ml staining solution
X-Gluc	100 mM	50 mg
DMSO		1 ml

6 Restricted transmission of *Xanthomonas oryzae* pv. *oryzae* from rice roots to shoots detected by a rapid root infection system

available as preprint on bioRxiv:
https://doi.org/10.1101/2025.08.13.670017

Contributions
The root clipping infection protocol was jointly developed with Yugander Arra. Yugander Arra performed experiments to trace *kresek*.
I performed the clipping infection, analyzed data, created figures and wrote the manuscript. Wolf B. Frommer advised on writing the manuscript and supported in editing and revision. Eliza P.I. Loo supervised team.

Chapter 6: Restricted transmission of *Xanthomonas oryzae* pv. *oryzae* from rice roots to shoots detected by a rapid root infection system

Abstract

Xanthomonas oryzae pv. *oryzae* (Xoo), the causal agent of bacterial blight in rice, is primarily studied in the context of foliar infections. However, infected stubble and irrigation water may serve as reservoirs and be responsible for seedling stage root infections in the field, especially during transplanting. Here, we established a coleoptile crown root-based infection protocol to investigate whether gene-for-gene interactions between Xoo TAL effectors and *SWEET* sucrose uniporter susceptibility genes occur in the root xylem, and whether the disease can propagate from roots to seedling shoots. Using translational SWEET11a-GUS reporter lines under control of the native SWEET11a promoter, we observed progressive infection as indicated by accumulation of SWEET11a-GUS fusion protein in infected coleoptile crown roots. However, we did not detect progression of GUS accumulation beyond the coleoptile node, nor did we detect blight symptoms on the young leaves. Notably, the xylem, at least during early stages of infection remained functional as shown by Rhodamine B tracer, consistent with transfer of xylem constituents via living cells at the coleoptile node that did not allow bacteria to pass. Furthermore, the root infection protocol is a ~4x faster compared to standard leaf-clipping assays (roots assay: 11 days from sowing, compared to 39 days for clip infection), enabling more rapid assessment of TAL effector repertoire and plant defense responses with translational SWEET-GUS reporter lines. Our findings expand our understanding of Xoo infection routes and provide a valuable tool for resistance testing and pathogen surveillance.

Introduction

Rice serves as a crucial staple food for developing countries in Asia and Africa (Balasubramanian *et al.*, 2007). Bacterial blight, caused by the bacterial pathogen *Xanthomonas oryzae* pv. *oryzae* (Xoo), ranks among the most detrimental rice diseases (Liu *et al.*, 2014; Savary *et al.*, 2019; Swings and Civerolo, 1993). Surveys of bacterial blight outbreaks prevalently report the blight symptom on leaves of plants at the tillering stage. A severe form of bacterial blight is *kresek* (Javanese: sound of dead leaves) causing complete wilting and lethality of rice at the seedling stage. *Kresek* was associated to Xoo after *kresek* symptoms were first reported in Indonesia and predominantly occurred when seedlings were transplanted from nurseries to the field. (Goto, 1964). The route by which Xoo infects seedlings, namely via leaves or roots,

had remained an open question. Irrigation water and infected rice stubble left in the field after harvest could serve as a reservoir and later as primary inoculum source during the next cropping season (Nyvall, 1999; Ou, 1985; Niño-Liu *et al.*, 2006). Consistent with this observation, Xoo had been detected in soil and root samples from leaf infected plants (Ritbamrung *et al.*, 2025).

The infection mechanism of Xoo in leaves relies on a direct gene-for-gene interaction between bacterial transcription activation like effectors (TALes) and *SWEET* promoters. TALe function act as eukaryotic transcription factors to specifically induce transcription of host *SWEETs* by binding to effector binding elements within *SWEET* promoters (Chen *et al.*, 2010; Chen *et al.*, 2012). Genome editing of the TALe bindings site in the *SWEET* promoters conferred robust resistance to Xoo (Eom *et al.*, 2019; Oliva *et al.*, 2019; Schepler-Luu *et al.*, 2023). TALe-triggered induction of *SWEET* genes is *essential* for virulence and occurs gene-for-gene specifically. For example, the TALe PthXo1 from the *Xoo* strain PXO99^{A} activates *SWEET11a*, while AvrXa7 of PXO86 induces *SWEET14* (Oliva *et al.*, 2019; Luo *et al.*, 2021). The ME2 mutant of PXO99^{A} lacking PthXo1 was avirulent and is typically used as a control (Yang and White, 2004).

The standard approach for Xoo pathogenicity and resistance testing in rice both in greenhouses and by breeders in the field is leaf clipping assay (Kauffman, 1973), in which leaf tips are cut with scissors that had previously been dipped in Xoo suspensions. The length of lesion from the clipping site measured two weeks post-infection serves as an indicator of the degree of susceptibility/resistance to Xoo. Here we explored whether rice seedling roots can be infected to evaluate a potential transmission through the xylem from root to shoot, and to develop a fast and reliable protocol for rapid testing of gene-for-gene interaction between TALe and *SWEETs* in rice using reporter lines containing a translational SWEET11a-β-glucuronidase (GUS) fusion under control of the native SWEET11a promoter for root infections (Eom *et al.*, 2019). We observed TALe specific induction of *SWEET11a* by the strain PXO99^{A}. In contrast to mobility of the small molecule fluorescent dye Rhodamine B, no transmission of the bacteria from coleoptile crown roots to the shoot were observed. The new root assay enables rapid testing of strains within two weeks, approximately four times faster compared to the Kauffman assay (Kauffman, 1973).

Material and Methods

Plant material and growth conditions

Rice seeds (Table S1) were dehusked, placed in 15 mL Falcon tubes and sterilized on an orbital shaker at 180 rpm in 15 ml Falcon tubes first for 2 min in 75 % ethanol and then for 5 min in 50 % of a commercial bleach product (2.8 g sodium hypochlorite/ 100g water). Seeds were dried on sterile filter paper and transferred into Magenta™GA-7 boxes containing ½ salt strength MS medium (2.2 g Murashige Skoog Medium (Murashige and Skoog, 1962), 10 g sucrose, 8g Phytagel per liter, pH 5.8) containing 50 mg/L hygromycin B (transgenic lines, Table S1) using serological tweezers under aseptic conditions. Seedlings were grown in a 16 h day/8 h night regime with photosynthetic photon flux densities (PPFD) of 200 µmol m^{-2} s^{-1} [PPFD-blue: 40, PPFD-green: 80, PPFD-red: 70 µmol m^{-2} s^{-1}] at 27°C, 80 % humidity in CLF PlantClimatics chambers (model: CU41L5).

Xanthomonas oryzae pv. *oryzae* inoculum preparation

Xoo cultures (for strains cf. Table S2).) were prepared from glycerol stocks on PSA plates (10 g/L peptone, 1 g/L glutamic acid, 10 g/L sucrose, and 20 g/L agar, pH 7.0). After three days at 28°C in dark conditions, three colonies were picked and placed onto fresh PSA plates. Plates were incubated for additional two days. For the suspension inoculum, Xoo was scraped off the plates, resuspended in sterile water and adjusted to OD_{600} 0.5. For the infection, 10 ml of the Xoo suspension was transferred to a 50 ml glass beaker.

Root clip infection

6-day old seedlings were carefully removed from Magenta™GA-7 boxes and rinsed with phosphate-buffered saline (10 mM phosphate, 2.68 mM potassium chloride, 140 m sodium chloride, pH 7.4) to remove residual media. Tips of coleoptile crown roots were cut at 2/3 of their total length (2 cm from the root tip; total length at this stage approximately 3 cm). Tips of cut roots were dipped in Xoo inoculum for 10 min (Fig S1) before transfer to DYI hydroponic growth boxes (DYI boxes; empty 3x5 cm 1000 µL pipette tip boxes) filled with Yoshida media (Table S3). Boxes were placed into a PlantClimatics chamber (CU36L) in a 16 h day/8 h night regime at 27°C and 80 %

humidity. The evaporation of Yoshida media was monitored daily and the complete media were exchanged accordingly.

Histochemical GUS assay

For histochemical GUS assays, at 9 am in the morning, seedlings were removed from the DYI boxes, cut approximately 1 cm above the root-shoot interface and collected in 15 ml Falcon tubes containing ice-cold 90 % acetone. Root samples were vacuum infiltrated for 10 min and incubated for 30 min at room temperature. Subsequently, samples were placed in GUS washing buffer followed by staining buffer and were vacuum infiltrated for 10 min each (buffer compositions: Table S4). The enzymatic reaction was stopped after 10 h incubation at 37°C and samples were cleared by replacement of GUS staining buffer with 75 % ethanol for 24 hours.

Rhodamine B assay

To trace translocation of solutes from roots to shoots, Rhodamine B was used as a small molecule tracer (Wang *et al.*, 2022). plants were transferred from the DYI boxes to a double container set-up at 4 dpi (Fig. S2). Both containers were filled with Yoshida media. Either the inner container with infected roots, or the outer container with the newly emerged roots was supplemented with 0.5 mM Rhodamine B (Sigma, 79754). Images were taken 6 days after transfer to the double container set-up (10 dpi).

Imaging and analysis

Images were taken with a fluorescent Stereo Zoom Microscope (AxioZoom.V16, Zeiss), equipped with a metal halide illuminator (HXP 200C, Zeiss), CMOS cam-era (ORCA-Flash 4.0, Hamamatsu), and PlanNeoFluar objective. For histochemical GUS assays a transparent glass background was used in bright field mode. Rhodamine B was visualized with 63 HE mRFP (ex: 572/25, em: 629/62) on a black background slide. The total length of coleoptile crown roots, the distribution of diX Indigo accumulation, in particular the distance of the diX Indigo front as an indicator of successful infection, and fluorescence were assessed by the segmented line and measurement tools in ImageJ. Analysis was carried out in R (4.05) and RStudio (1.2) employing the R packages tidyverse, ggpubr, ggrepel, lubridate, tigris, sf, dyplr, gapminder, openxlsx, forcats, ggplot2.

Results

Successful infection of rice roots by Xanthomonas oryzae pv. oryzae

To be able to monitor TALe-induced clade III SWEETs, a suite of reporter lines that carry translational SWEET-GUS fusions under control of the respective SWEET promoters had been developed and validated (Eom et al. 2019). We recently showed that diX Indigo accumulation in the reporter lines can serve as a specific indicator for TALe activity from different strains. Moreover the reporter lines can be used for monitoring the progression of the *Xoo* infection, in particular at a stage at which Xoo had successfully established a Type III Secretion System and injected TALe into host cells (Eom *et al*., 2019; Redzich *et al.*, 2025). To explore whether there is a base level of SWEET11a-GUS in different root types, GUS histochemistry was performed on uninfected plants. While crown roots from the coleoptile node with first order lateral roots (hereafter: coleoptile crown roots, Fig S1) did not accumulate diX Indigo, adventitious nodal roots without lateral roots (hereafter: post-embryonic roots) showed SWEET11a-GUS accumulation, indicating a role for SWEET11a in these roots (Fig S3,16). Therefore, only coleoptile roots, but not post-embryonic roots, were used for analysis of potential *SWEET11a* induction in roots infected with PXO99^{A}. Coleoptile crown roots were clipped and immersed with the apical region in *Xoo* inoculum for 10 minutes. In contrast to control treatment using ME2 control strain infections (Yang and White, 2004; Eom *et al*., 2019), PXO99^{A} caused diX Indigo accumulation in the root vasculature (Fig 1A, B). When roots of SWEET11a-GUS expressing lines were infected with *Xoo* strain PXO86, which carries AvrXa7 targeting the promoter of *SWEET14,* but which has no TALe to induce *SWEET11a*, no diX Indigo accumulation was detectable, demonstrating that PXO99^{A} must have been able to successfully been able to inject pthXo1 into host cells and to induce SWEET11a. Notably, the front of *SWEET11a* induction, represented by diX Indigo, advanced ~0.4 cm per day after infection (Fig 1C), indicating that the bacteria progressively infected the root at this velocity. The distance of the diX Indigo front as an indicator of the progression of the infection from the clip site progressed further between 2 and 4 dpi (days post infection), while no further progression was observed at the shoot-root axis (Fig S4). In no case did we diX Indigo in the shoot (except for wound-induced staining at the cut site). Thus, in comparison to the leaf clipping method performed on 4-week-old plants and lesion scoring two weeks dpi, the root infection protocol is ~4x faster (11 days from

germination to evaluation: 6 days seedling growth; 4 days infection; 1 day for GUS histochemistry).

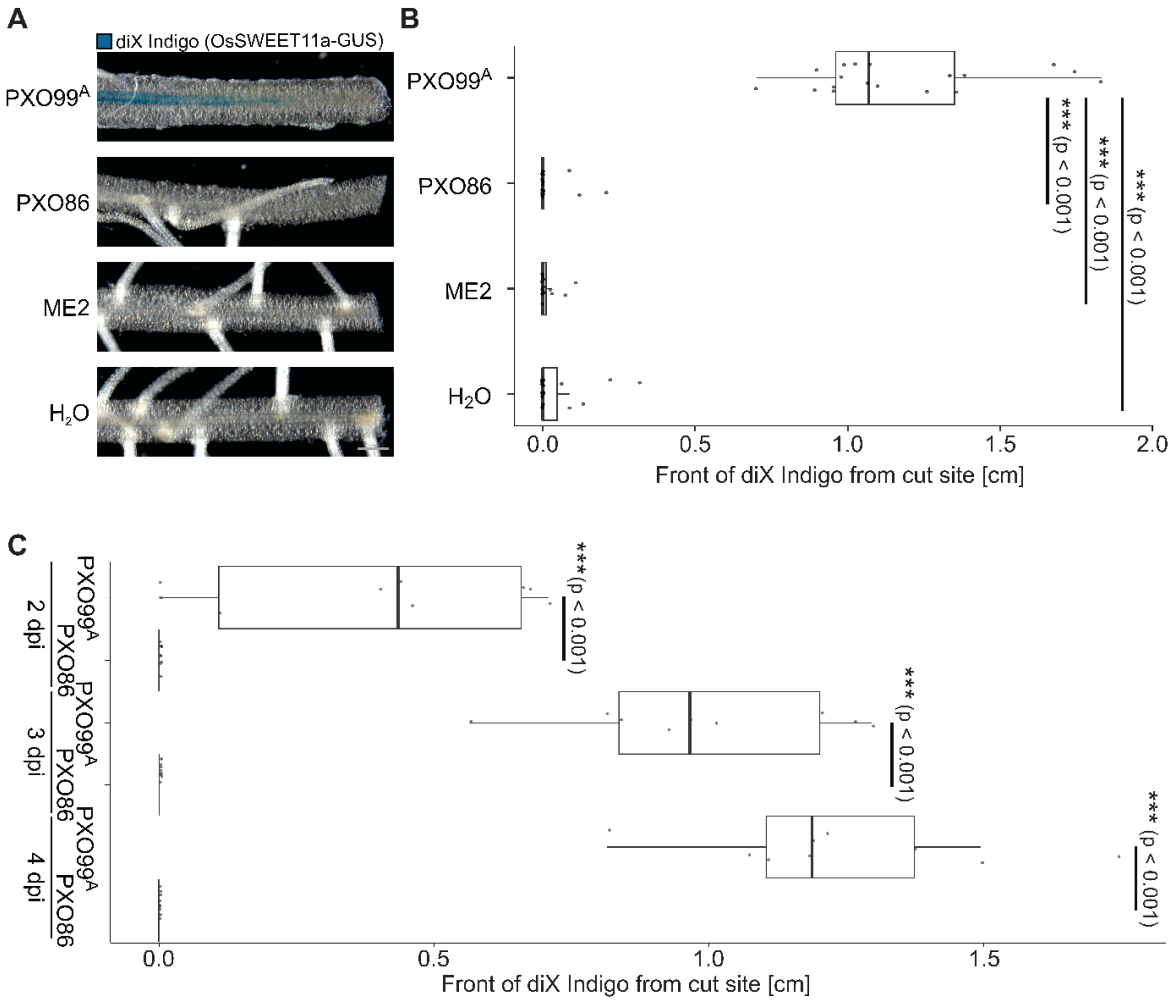

Figure 2.1. **Xoo strain-specific induction of GUS activity in SWEET11a-GUS reporter lines after infection of coleptile crown roots.** diX Indigo accumulated after infection with PXO99A, but not after mock, ME2 or PXO86 infections. A) diX-Indigo accumulation at (4 dpi) after infection with PXO99A, PXO86, ME2 or mock (water) in the root vasculature observed with the Zeiss Axiozoom V16 and processed in ImageJ (bar: 0.5 mm). Representative images from 50 roots per treatment from three independent experiments performed with two independent pSWEET11a:SWEET11a-GUSplus lines (independent transformants: line #8 and #10)(Eom et al. 2019)(Table S2.1). B) Progression of the infection as indicated by the distance of the diX Indigo front from the cutting site in coleoptile crown roots treated with PXO99A, PXO86, ME2, or H2O at 4 dpi. Measurements were performed in ImageJ with the *Segmented Line* Tool. Data processing performed in R. C) Time-dependent progression of the infection as indicated by the distance of the diX Indigo front from the cutting site in coleoptile crown roots 2, 3 and 4 dpi after PXO99^{A} infection. PXO86 served as a control. Repeated independently three times with comparable results.

Restricted vascular progression of Xoo to aerial tissue in rice

Kresek symptoms prevalently cause wilting of seedling coleoptile and leaves. One may speculate that wounds at roots, e.g. during transplanting, could serve as an entry route for infection. Plant debris, irrigation water and soil may serve as reservoirs for Xoo. Consistent with the inability of Xoo to progress beyond the coleoptile node, we did not

observe disease *kresek* symptoms in the seedlings using the same infection method (Fig S5). The inability to enter the shoot might be due to rapid blockage of the xylem in response to wounding. To evaluate whether the xylem is blocked, a double-container set up was generated in which infected coleoptile crown and non-infected post-embryonic roots were immersed in separate compartments with hydroponic media. Rhodamine B was used as fluorescent marker for xylem mobility (Wang *et al.*, 2022). Rhodamine B was detected x days after addition Roots clipped and transferred into the double container set-up 4 dpi (Fig 2). Ten days post infection, the progression of Rhodamine B was evaluated in leaves 5 cm above the coleoptile node with fluorescence microscopy. Post-embryonic roots showed translocation of Rhodamine B into major and minor veins of the leaf, demonstrating functional xylem translocation. The inability of bacteria to pass the coleoptile node must thus be due toother reasons. Bacterial infections were apparently able to block the xylem transport 4-10 days after infection, Rhodamine B translocation was undetectable, indicating that at later stages of infection, xylem transport is blocked.

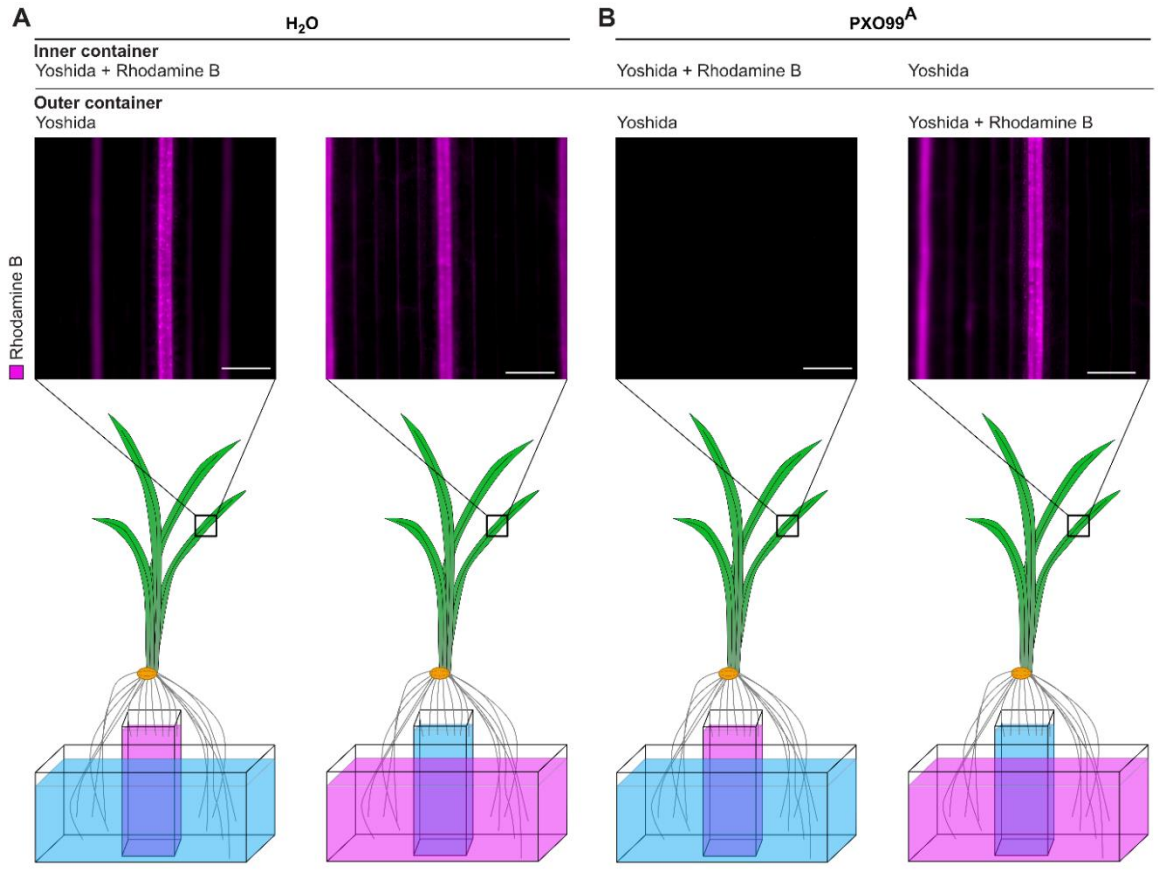

Figure 2.2. Root-to-shoot xylem connectivity in seedlings before and after *Xoo* infection assayed using Rhodamine B as a tracer. A) Rhodamine translocation from coleoptile crown roots (left) or postembryonic roots (right) in uninfected seedlings. 10-day-old seedlings were transferred to a double container set up 4 days after

clipping coleoptile crown roots. Roots were immersed in Yoshida medium (blue) or Yoshida medium supplemented with Rhodamine B (purple), respectively. Bottom shows cartoon of setup, top shows Rhodamine B fluorescence in the veins of seedling leaves 5 cm above the coleoptile node acquired using a Zeiss Axiozoom V16 and processed in ImageJ and Omero (n=3). B) Rhodamine translocation from coleoptile crown roots (left) or postembryonic roots (right) in *Xoo*-infected seedlings. 10-day-old seedlings were transferred to a double container set up 4 days after clipping coleoptile crown roots and infection by *Xoo* for 10 minutes. Scale bar: 1 mm. Repeated independently three times with comparable results.

Discussion

Xoo infects the xylem and its virulence depends critically on the induction of host SWEET sucrose transporters in the xylem parenchyma by bacterial TALe (Eom *et al.*, 2019; Oliva *et al.*, 2019; Chen *et al.*, 2010; Chen *et al.*, 2012; Schepler-Luu *et al.*, 2023). Xoo acquires host-derived sucrose in the xylem with the help of transporters and enzymes of the *Sux* gene cluster (Zöllner *et al.*, 2025). Importantly, key virulence functions and virulence depend on the ability to utilize sucrose (Zöllner *et al.*, 2025). At present, six different TALe have been identified that are utilized by different *Xoo* strains and which each target a specific SWEET paralog in rice (Oliva *et al.*, 2019). The targeted SWEETs are part of a specific clade of six sucrose uniporters (Wu *et al.*, 2022). While all six clade 3 SWEETs can function as susceptibility genes for Xoo, only three have been found so far to be targeted by Xoo strains (Streubel *et al.*, 2013). Breeding of resistance and genome editing are effective tools for controlling bacterial blight, however new strains have either emerged that break resistance or disease outbreaks were caused by inadvertent introduction of strains from other areas or even continents (Raveloson *et al.*, 2023; Schepler-Luu *et al.*, 2023; Sciallano *et al.*, 2023). It is thus critical to develop tools that enable rapid identification of SWEET genes targeted by emerging Xoo strains as a basis for rapid development of new lines that carry suitable promoter edits on SWEET promoters (Eom *et al.*, 2019; Oliva *et al.*, 2019; Schepler-Luu *et al.*, 2023).

To enable rapid identification of which SWEET is targeted by an emerging Xoo strain, we developed a SWEET^{R} kit, which included full gene translational SWEET-GUS reporter lines (Eom *et al.*, 2019; Wu *et al.*, 2022). These reporter lines also enable the monitoring of the infection process using the Kauffman leaf clipping assay, which is typically performed on four- to six-week-old plants and recording symptoms 14 days post infection (Redzich *et al.*, 2025). Because plants are most vulnerable towards Xoo within 21 days after germination, it is necessary for reliable infection scoring, that plants are infected at the maximum tillering stage at about four weeks after germination

(Kauffman, 1973). If plants are infected at earlier developmental stages using the leaf clipping method, *kresek* symptoms can bias the lesion scoring results towards higher susceptibility (Mew *et al.*, 1979).

The aim of this study was fourfold: (i) evaluate whether Xoo can infect wounded roots, (ii) explore whether the infection of roots depends, similar as for leaves, on the induction of SWEETs, (iii) whether the bacteria can migrate from roots to shoots, and (iv) develop a faster test system to identify which SWEET is targeted by a Xoo strain with unknown TALe repertoire.

(i) Using two rice lines carrying translational SWEET11a-GUS fusion driven by the *SWEET11a* promoter, we found that *Xoo* can infect the root xylem in the same manner as the leaf xylem after wounding (root tip clipping). The reporter lines also enabled monitoring the progression of the infection in roots over time. The assay could only be used in coleoptile crown roots, since postembryonic roots had base levels of SWEET11a and thus induction could not be observed against the background.

(ii) The induction of SWEET11a was specific for the strain PXO99^{A}, which produces the TALe PthXo1 that targeted the SWEET11a promoter.

(iii) Interestingly, SWEET induction occurred only in the roots and did not progress beyond the coleoptile node. We also did not observe any symptoms in the shoot post root infection, indicating that Xoo cannot pass from coleoptile crown roots to the shoot xylem. In contrast, the small molecule dye Rhodamine B was effectively translocated to the shoot. Nodal translocation zones contain three distinct vascular bundles: enlarged vascular bundles (EVBs), transit vascular bundles (TVBs) and diffuse VB (DVBs, (Yamaji and Ma, 2014). Xoo would need to either translocate via the nodal vascular anastomosis to the DVB, or exit xylem vessels of EVBs to living xylem transfer cells to the DVB connecting to the upper node. Alternatively, *Xoo* would need to travel along the TVB to the multitude of xylem vessels of EVBs to reach the leaf (Yamaji and Ma, 2014; Schwab *et al.*, 2016). Likely due to the discontinuity of the vessel and the transfer of xylem constituents via living cells, the dye could be transferred, but not the Xoo cells. Because Xoo did not translocate to leaves, likely the infection was restricted to roots and systemic infection as described for *kresek* did not occur. The results shown here indicate that *kresek* symptoms are not caused by plant entry of Xoo by root

wounding after transplantation, but rather are transmitted via shoots. We also did not observe *kresek* symptoms when all roots had been clipped. However, that the exposure to Xoo in our experiments was limited to 10 minutes, it is conceivable that long term exposure may also lead to transmission via newly emerging roots. Of note, at later stages of infection, translocation of Rhodamine B ceased, indicating that the bacteria blocked xylem flow either due to clogging by biofilm, tylosis or due to xylem cell death.

(iv) Leveraging the suite of SWEET-GUS reporters from presented in Eom *et al.* 2019, the root infection assay of translational SWEET-GUS reporter lines allows for four-times faster screening for *SWEET* induction, i.e. results can be obtained within 11 days. Full development of the assay for all six SWEETs will require testing of the base levels of the other five clade 3 SWEETs in the different root types.

The root infection protocol developed here provides a fast method to screen naturally occurring TALe variants and support pathogen surveillance. We surmise that after analysis of the base levels of SWEET-GUS reporter activity of all six clade 3 SWEET -GUS reporter lines the test could be expanded to rapidly evaluate which SWEET is targeted by a novel TALe of an emerging strain (Eom *et al.*, 2019; Wu *et al.*, 2022). Furthermore, the infection protocol might be a promising tool to test TALe functionality and plant defense responses.

Data availability

Raw data are available at https://doi.org/10.60534/7s2cg-r2j06

Funding

This work was supported by grants from Deutsche Forschungsgemeinschaft to WBF (DFG, German Research Foundation) - Collaborative Research Center SFB1535, project ID 458090666/CRC1535/1 the Alexander von Humboldt Professorship (WBF); funds from Germany´s Excellence Strategy – EXC-2048/1 – project ID 390686111 (Deutsche Forschungsgemeinschaft, CEPLAS) to WBF and LR; fellowships to LR from Heinrich-Böll-Stiftung, and to YA by the Alexander von Humboldt Foundation, and support from the Director, CSIR-Central Institute of Medicinal and Aromatic Plants, India.

References

Balasubramanian, V., Sie, M., Hijmans, R.J. and Otsuka, K. (2007) Increasing rice production in Sub-Saharan Africa: Challenges and opportunities. *Adv. Agron.*, **94**, 55–133.

Chen, Hou, B.-H., Lalonde, S., et al. (2010) Sugar transporters for intercellular exchange and nutrition of pathogens. *Nature*, **468**, 527–532.

Chen, L.-Q., Qu, X.-Q., Hou, B.-H., Sosso, D., Osorio, S., Fernie, A.R. and Frommer, W.B. (2012) Sucrose efflux mediated by SWEET proteins as a key step for phloem transport. *Science*, **335**, 207–211.

Eom, J.-S., Luo, D., Atienza-Grande, G., et al. (2019) Diagnostic kit for rice blight resistance. *Nat. Biotechnol.*, **37**, 1372–1379.

Freschet, G.T., Pagès, L., Iversen, C.M., et al. (2021) A starting guide to root ecology: strengthening ecological concepts and standardising root classification, sampling, processing and trait measurements. *New Phytol.*, **232**, 973–1122.

Goto, M. (1964) *"Kresek"* and pale yellow leaf, systemic symptoms of bacterial leaf blight of rice caused by *Xanthomonas oryzae* . *Plant Dis. Rep*, **48**, 858–861.

Kauffman, H. (1973) An improved technique for evaluating resistance of varieties to *Xanthomonas oryzae* pv. *oryzae*. *Plant Dis. Rep*, **57**, 537–541.

Liu, W., Liu, J., Triplett, L., Leach, J.E. and Wang, G.L. (2014) Novel insights into rice innate immunity against bacterial and fungal pathogens. *Annu. Rev. Phytopathol.*, **52**, 213–241.

Luo, D., Huguet-Tapia, J.C., Raborn, R.T., White, F.F., Brendel, V.P. and Yang, B. (2021) The *Xa7* resistance gene guards the rice susceptibility gene *SWEET14* against exploitation by the bacterial blight pathogen. *Plant Commun.*, **2**.1-11.

Mew, T.W., Vera Cruz, R. C. Reyes and B. A. Zaragoza (1979) Study of *Kresek* (wilt) of the bacterial blight syndrome. *IRRI Research Paper Series*, **39**, 1–7.

Murashige, T. and Skoog, F. (1962) A revised medium for rapid growth and assays with tobacco tissue cultures. *Physiol. Plant.*, **15**, 473–479.

Niño-Liu, D.O., Ronald, P.C. and Bogdanove, A.J. (2006) *Xanthomonas oryzae* pathovars: model pathogens of a model crop. *Mol. Plant Pathol.*, **7**, 303–324.

Nyvall, R.F. (1999) *Field Crop Diseases* 3rd edition., Ames: Iowa State University Press.

Oliva, R., Ji, C., Atienza-Grande, G., et al. (2019) Broad-spectrum resistance to bacterial blight in rice using genome editing. *Nat. Biotechnol.*, **37**, 1344–1350.

Ou, S.H. (1985) *Rice Diseases* 2nd edition., Aberystwyth: The Cambrian News.

Raveloson, H., Rabekijana, R., Rakotonanahary, N.M., Szurek, B., Muller, B., Brocke, K. vom and Hutin, M. (2023) First report of bacterial leaf blight disease of rice caused by *Xanthomonas oryzae* pv. *oryzae* in Madagascar. *Plant Dis.*, **107**, 2510.

Redzich, L., Ma, Z.-Y., Schepler-Luu, V., Loo, E.P.I. and Frommer, W.B. (2025) Differentiation of *Xanthomonas oryzae* pv. *oryzae* *in vitro* and during host colonization. *BiorXiv*.

Ritbamrung, O., Inthima, P., Ratanasut, K., Sujipuli, K., Rungrat, T. and Buddhachat, K. (2025) Evaluating *Xanthomonas oryzae* pv. *oryzae* (*Xoo*) infection dynamics in rice for distribution routes and environmental reservoirs by molecular approaches. *Sci. Rep.*, **15**, 1408.

Savary, S., Willocquet, L., Pethybridge, S.J., Esker, P., McRoberts, N. and Nelson, A. (2019) The global burden of pathogens and pests on major food crops. *Nat. Ecol. Evol.*, **3**, 430–439.

Schepler-Luu, V., Sciallano, C., Stiebner, M., et al. (2023) Genome editing of an African elite rice variety confers resistance against endemic and emerging *Xanthomonas oryzae* pv. *oryzae* strains. *eLife*, **12**, e84864.

Schwab, F., Zhai, G., Kern, M., Turner, A., Schnoor, J.L. and Wiesner, M.R. (2016) Barriers, pathways and processes for uptake, translocation and accumulation of nanomaterials in plants. *Nanotoxicology*, **10**, 257–278.

Sciallano, C., Auguy, F., Boulard, G., Szurek, B. and Cunnac, S. (2023) The complete genome resource of *Xanthomonas oryzae* pv. *oryzae* CIX2779 includes the first sequence of a plasmid for an African representative of this rice pathogen. *Mol Plant Microbe Interact*, **36**, 73–77.

Streubel, J., Pesce, C., Hutin, M., Koebnik, R., Boch, J. and Szurek, B. (2013) Five phylogenetically close rice genes confer TAL effector-mediated susceptibility to *Xanthomonas oryzae* pv. *oryzae*. *New Phytol.*, **200**, 808–819.

Swings, J.G. and Civerolo, E.L. eds. (1993) *Xanthomonas* 1st edition., Dordrecht: Springer Netherlands.

Wang, H., Yang, H., Wen, Z., et al. (2022) Xylan-based nanocompartments orchestrate plant vessel wall patterning. *Nat. Plants*, **8**, 295–306.

Wu, L.-B., Eom, J.-S., Isoda, R., et al. (2022) *OsSWEET11b*, a potential sixth leaf blight susceptibility gene involved in sugar transport-dependent male fertility. *New Phytol.*, **234**, 975–989.

Yamaji, N. and Ma, J.F. (2014) The node, a hub for mineral nutrient distribution in graminaceous plants. *Trends Plant Sci.*, **19**, 556–563.

Yang, B. and White, F.F. (2004) Diverse members of the AvrBs3/PthA family of Type III effectors are major virulence determinants in Bacterial Blight disease of rice. *Mol Plant Microbe Interact*, **17**, 1192–1200.

Zöllner, N.R., Long, J., Song, C., et al. (2025) A critical role of sux cistron-mediated sucrose uptake for virulence of the rice blight pathogen *Xanthomonas oryzae* pv. *oryzae*. *BiorXiv*, 2025.06.02.657373.

Supplementary Material

Figure S2.1. Clipping of coleoptile crown roots in root infection protocol. Coleoptile crown roots with first order lateral roots emerge from coleoptile node. Post-embryonic adventitious crown roots without lateral roots emerging from the first node were not clipped. Tips of coleoptile crown roots were cut at 2/3 of their total length (2 cm from the root tip; total length at this stage approximately 3 cm. Root systems shown before and after clipping. Nomenclature as proposed by the International Society of Root Research (Freschet *et al.*, 2021).Ventral (left) and dorsal (right). Scale bar: 1 cm.

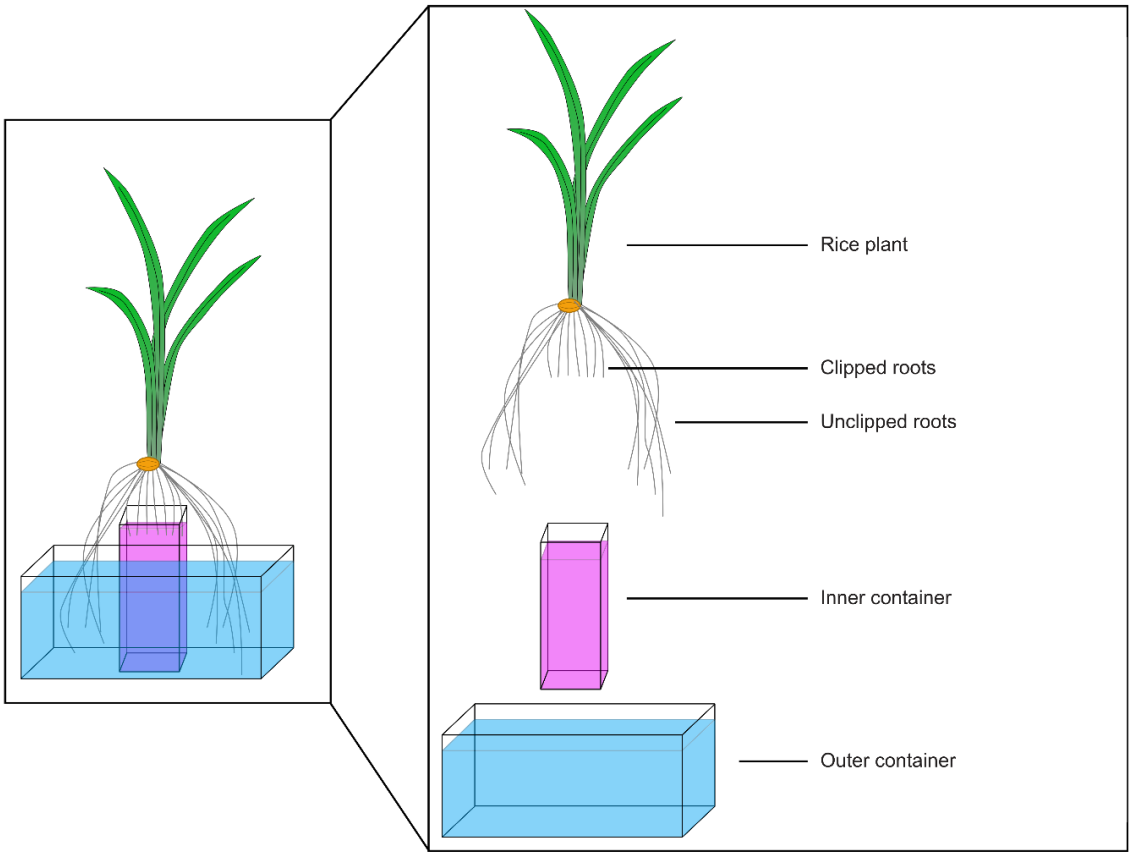

Figure S2.2. Double container set-up to track translocation of solutes clipped and non-clipped roots to leaf vasculature. A 50 mL plastic beaker (inner container) was glued onto the bottom of a 3x5 cm 1000 µL pipette tip box (outer container). By the addition of Rhodamine B to the outer or inner container, translocation via unclipped or clipped roots were investigated. Plants were stabilised with tape and wooden toothpicks.

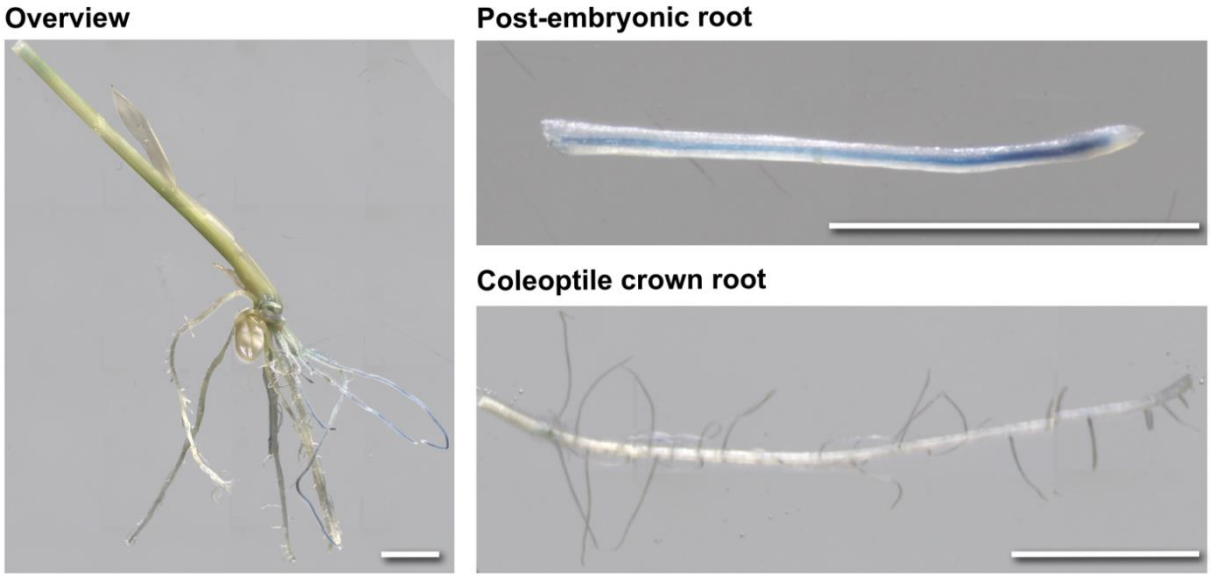

Figure S2.3. Accumulation of diX Indigo in uninfected root system. Coleoptile crown roots with first order lateral roots did not accumulate diX Indigo. Post-embryonic adventitious crown roots without lateral roots accumulated diX Indigo independent of TALe induction. Scale bar: 0.5 cm.

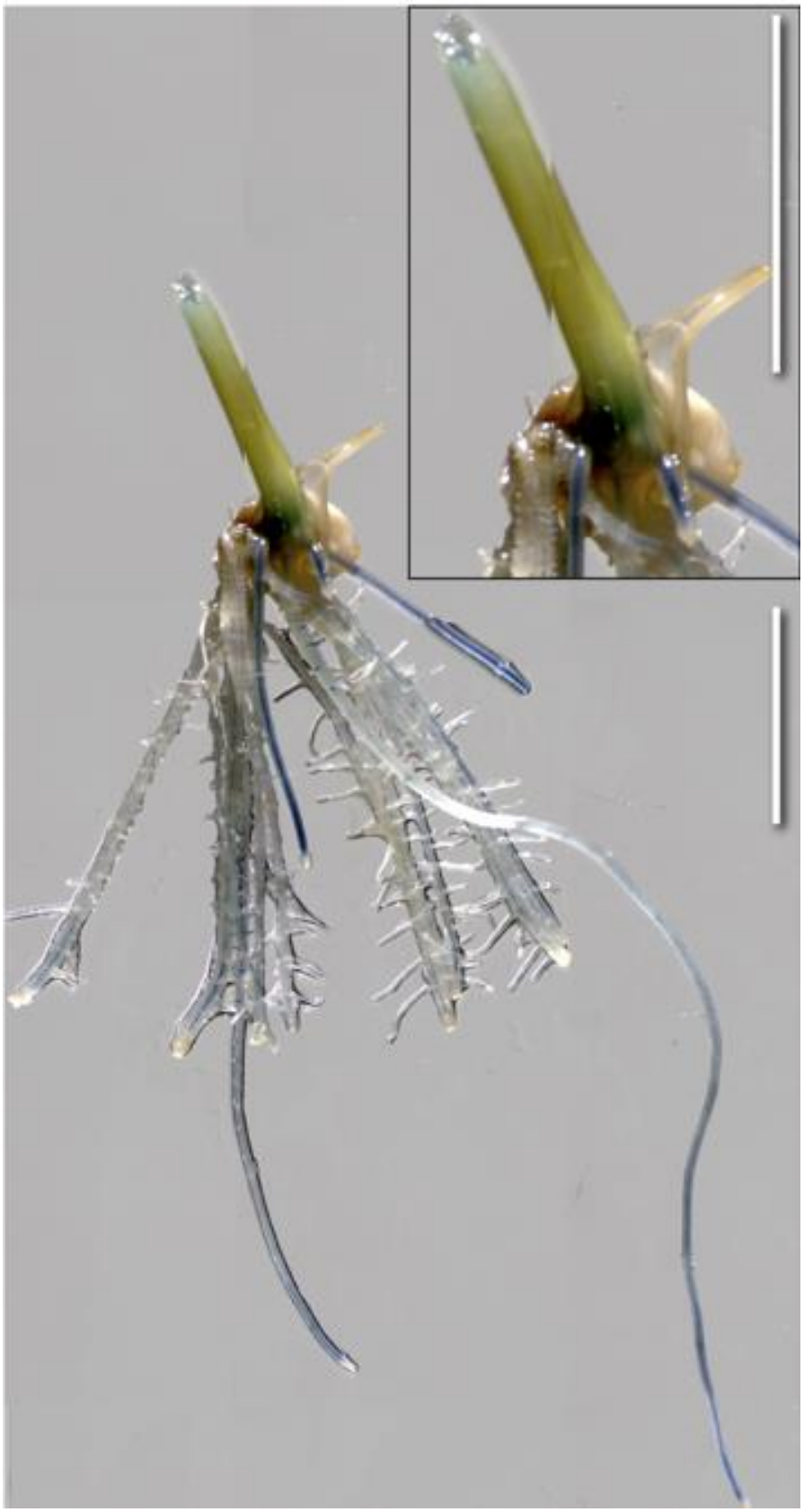

Figure S2.4. diX Indigo accumulation is restricted to roots. Coleoptile crown roots with first order lateral roots and post-embryonic crown roots accumulated diX Indigo. diX Indigo was not observed in the shoot (except at the cutting site). Scale bar: 1 cm.

Figure S2.5. Phenotype of seedlings seven days post infection. Roots were clip infected with PXO99^{A}, PXO86 and mock treated with H_2O. *Kresek* symptoms were not observed. Scale bar: 2 cm.

Table S2.1 Overview of rice lines. All lines were retrieved from the rice seed stocks and tested for Hygromycin B resistance.

Name	Transformation Event	Characteristics	Generation	Resistance Ratio
B01069	[8-3]	pSWEET11a:SWEET11a-GUSplus	T4	1.0
B01075	[10-2]	pSWEET11a:gSWEET11a-GUSplus	T4	1.1

Table S2.3 Stock solutions for Yoshida media. For 4 liters of working solution, add 2.5 ml of each stock solution and adjust to pH 5.8 with KOH.

Stock order	Ele-ment	Chemical	Preparation (g/10 L H_2O)	Remarks
1	N	NH_4NO_3	914	Final volume of 10 L
2	P	$NaH_2PO_4.H_2O$	403	Final volume of 10 L
3	K	K_2SO_4	717	Final volume of 10 L
4	Ca	$CaCl_2$	886	Final volume of 10 L
5	Mg	$MgSO_4.7H_2O$	3240	Final volume of 10 L

Micronutrients

7	Mn	$MnCl_2.4H_2O$	15	Prepare separately, mix and adjust final volume of 10 L
8	Mo	$(NH_4)_6.Mo_7O_{24}.4H_2O$	0.74	
9	B	H_3BO_3	9.34	
10	Zn	$ZnSO_4.7H_2O$	0.35	
11	Cu	$CuSO_4.5H_2O$	0.31	
12	Fe	Fe-Na-EDTA	104	

Table S2.4 Recipes for solutions for GUS histochemistry

Washing buffer

Component	Final concentration	For 50 ml
0.5 M EDTA	10 mM	1 ml
100 mM phosphate buffer, pH 7	50 mM	25 ml
10 % triton X-100	0.1 %	0.5 ml
50 mM potassium ferrocynide	1 mM	1 ml
50 mM potassium ferricynide	1 mM	1 ml
Methanol	20 %	10 ml
Sterile water		Ad 50 ml

X-Gluc staining buffer

Component	Final concentration	For 50 ml
0.5 M EDTA	10 mM	1 ml
100 mM phosphate buffer, pH 7	50 mM	25 ml
10 % Triton X-100	0.1 %	0.5 ml
50 mM potassium ferrocyanide	1 mM	1 ml
50 mM potassium ferricynide	1 mM	1 ml
Methanol	20 %	10 ml
100 mM X-Gluc	2 mM	1 ml
Sterile water		Add 50 ml

100 mM Phosphase buffer, pH 7

Component	Volume
0.5 M sodium phosphate dibasic (Na_2HPO_4)	3 ml
1 M sodium phosphate monobasic (NaH_2PO_4)	1 ml

100 mM X-Gluc solution

Component	Final concentration	For 50 ml staining solution
X-Gluc	100 mM	50 mg
DMSO		1 ml

7 Evaluation of effects of EBE edits on plant physiology under varying abiotic conditions

Contributions

The experimental process for MOA sequencing was performed jointly with Max Blank. Data processing and analysis was performed with support of Amelie Kok, Duong Hi Thi Doan, Julia Engelhorn and Thomas Hartwig. Truncated EBE-GUS reporter lines were generated with support of Melissa Stiebner, Assja Crepcia-Pevzner and Jungil Yang. The second repetition of salinity experiments was performed with DAAD-RISE student Charlotte Anker.

Abstract

Effector binding elements (EBEs) within *OsSWEET* promoters are key determinants of plant susceptibility to *Xanthomonas oryzae* pv. *oryzae*. While editing EBEs provides durable resistance against TAL effector mediated induction of *OsSWEETs*, the potential consequences for endogenous *OsSWEET* regulation and abiotic stress tolerance remain poorly undersootd. In this chapter, the EBE sequence diversity in rice, chromatin accessibility within *OsSWEET* promoters and phenotypic responses of functional *sweet* knock-out lines under different abiotic conditions are examined. Analysis > 3000 rice genomes identified only one natural variation of EBE_{PthXo1}, indicating a functional conservation beyond TAL effector binding. Chromatin accessibility profiling indicated that EBEs frequently coincide with open chromatin and overlap with predicted transcription factor binding motifs, supporting a dual role of EBEs in pathogen susceptibility and endogenous gene regulation. Truncated EBE reporter assays demonstrated that alteration in EBE sequence affected OsSWEET protein abundance with EBE_{PthXo1} truncations enhancing OsSWEET11a accumulation and EBEPthXo2B deletions reducing OsSWEET13 levels. Functional knock-out plants revealed physiological roles for OsSWEETs in plant architecture and abiotic adaptation: *sweet13* mutants exhibited increased flag leaf angles under low light, while *sweet14* mutants displayed reduced root length. Together, these findings highlight the importance of EBEs as cis regulatory elements, link OsSWEET activity to plant architecture and provide critical insights for the design of EBE-editing strategies that balance biotic resistance with agronomic performance.

Introduction

TALes mimic eukaryotic transcription factors

Transcription-Activation-Like effectors (TALes) are effectors from the genus *Xanthomonas* belonging to γ-proteobacteria that mimic eukaryotic transcription factors. At the C-terminus, TALes carry a nuclear localisation signal (NLS) flanked by an acidic transcriptional activation domain. The N-terminus harbours a signal for Type-III-system secretion. At the center, TALes are constituted by a repeat domain (Zhu *et al.*, 1998). TALes acquire nucleotide specificity at the 12^{th} and 13^{th} position of each repeat within the approximately 34 amino acid repeat domain (Boch and Bonas, 2010; Yang and White, 2004; Mücke *et al.*, 2019). When a TALe is injected via the Type-III-

secretion system into the host cell, the N-terminal NLS sequence provokes its translocation to the nucleus. Subsequently, transcriptional induction of *OsSWEETs* is triggered sequence specifically to the bound DNA region called Effector Binding Element (EBE). In the pathosystem of rice and *Xoo*, three of the six sucrose transporting *OsSWEETs* are targeted by TALes (Oliva et al., 2019). When targeted by artificial TALes, all six sucrose transporting *OsSWEETs* act as susceptibility genes (Streubel *et al.*, 2013; Wu *et al.*, 2022b). The central disease mechanism is based on the redirection of sucrose flux towards *Xoo* caused by the TALe binding to its cognate EBE in the *OsSWEET* promoter.

Sequence variation in the Effector Binding Element confers resistance to *Xanthomonas oryzae* pv. *oryzae*

OsSWEET11a, OsSWEET13 and OsSWEET14 are clade III sucrose uniporters that facilitate transport along the concentration gradient. The ectopic induction by TALes manipulates the quantity of OsSWEET protein and enhances sucrose flux towards the apoplasm. Polymorphisms in the targeted EBE inhibits TALe binding and confers resistance. EBE editing as mode of EBE-based resistance has been successfully applied in genome editing approaches (Eom *et al.*, 2019; Oliva *et al.*, 2019; Schepler-Luu *et al.*, 2023).

Given the selective pressure on susceptibility genes and the gene-for-gene interaction between TAL effectors and *OsSWEET*s, it is likely that multiple naturally occurring EBE variations have arisen.

One of the earliest identified bacterial blight resistance genes, *xa13*, has been cloned in 2006 (Chu, Fu, *et al.*, 2006; Yang and White, 2004b). Four years later, *xa13* was characterized as the recessive *OsSWEET11a* allele within the SWEET family (L., Q., Chen *et al.*, 2010; L., Q., Chen *et al.*, 2012; Antony *et al.*, 2010). In parallel, the TALe interacting EBE in the promoter region of *OsSWEET11a/Xa13* was identified and characterized with truncated promoter variants (Chu, Yuan, *et al.*, 2006). The rice variety IRBB13 was identified as PthXo1 resistant variety with a large promoter insertion (Chu, Yuan, *et al.*, 2006; Yuan *et al.*, 2011). However, the precise position of EBE_{PthXo1} disruption and sequence of insertion fragment are not reported.

For *OsSWEET13* and *OsSWEET14*, genetic variation of EBEs was assessed with the 3000 rice genome panel (Wang *et al.*, 2018; Zaka *et al.*, 2018). For *OsSWEET13*, a 2

bp deletion within EBE_{PthXo2} and a single nucleotide substitution for EBE_{AvrXa7} in *OsSWEET14* were reported among 3000 sequenced genomes of Asian rice cultivars (Zaka *et al.*, 2018). Both EBE variants led to resistance to *Xoo* strains equipped with respective TAL effectors.

Apart from R genes amplified across rice varieties in domesticated rice by breeding programs, wild rice varieties could carry a greater suite of EBE variants. However, to date, only one EBE variant within *OsSWEET14* from *Oryza barthii* is reported. A 18 bp deletion disrupts the EBEs of TAL effectors TalC, PthXo3 and AvrXa7 (Hutin *et al.*, 2015).

The role of OsSWEETs during diverse abiotic conditions

Abiotic stresses such as drought, salinity, low light, and extreme temperatures disrupt sugar homeostasis and challenge source–sink dynamics in plants. To adapt to these fluctuating conditions, plants must orchestrate carbon allocation by either increasing the levels of sugar transporters to redistribute assimilates and mitigate stress effects, or by restricting carbon flow to conserve resources during growth arrest. Under drought and salinity stress, transcriptional and translational levels of *OsSWEET13* and *OsSWEET15* have been shown to accumulate and result in higher soluble sugar levels in the phloem (Mathan *et al.*, 2021). Probably, the higher level of soluble sugars in the vasculature serves as a osmotic protectant and supports the redistribution of sugars towards sinks. Rapid development under stress seems to be promoted by higher OsSWEETs levels (Mathan *et al.*, 2021). OsSWEETs also respond to low light and short photoperiods, which limit carbon assimilation. Shade-tolerant rice cultivars upregulate *OsSWEET13*, *OsSWEET2B*, and *OsSWEET16* transcript levels under prolonged low light, redirecting available sugars to developing panicles and sustaining grain filling despite reduced photosynthetic capacity (Panigrahy *et al.*, 2019).

Plants will be exposed to multifactorial abiotic stresses due to climate change. Genome editing approaches for biotic stress tolerance need to consider potential detrimental effects on plant abiotic stress tolerance.

Relevance of Effector Binding Elements in endogenous management of OsSWEET levels

Based on the concept of an evolutionary arms race, a plethora of allelic EBE diversity would be expected. Contradictory, only a minor number of allelic EBE variants are reported (Chu, Yuan, *et al.*, 2006; Hutin *et al.*, 2015; Zaka *et al.*, 2018). Possibly, EBE sequences are crucial in the endogenous management of *OsSWEETs* and harbor cis-elements for transcription factor binding. I used available sequences of more than 3000 rice genomes to investigate whether other EBE_{PthXo1} variants occur, to characterize the IRBB13 insertion and to identify its origin (Research Question 1).

OsSWEETs are uniporters that transport sugars passively along the concentration gradient. However, managing carbon flux from the symplasm to the apoplasm is of outmost importance for the plant to manage source-sink dynamics. Hence, it is likely that OsSWEET levels are managed at multiple checkpoints i.g. transcriptionally and translationally. Transcriptional regulation may be achieved by cis elements and chromatin state. Regulatory sites within *OsSWEET* promoters are to be identified and characterized (Research Question 2).

Whether EBEs are important for or overlap with regulatory sites for endogenous management of *OsSWEET* transcription is not understood. In the field, edited plants will be subjected to adverse climate conditions and need to rapidly assimilate to changing environments. Because I lack the possibility to test genome edited plants in the field, I used functional *sweet* knock-out plants to mimic maximal disturbance of OsSWEET levels. I aim to investigate whether the absence of functional OsSWEET protein may lead to an impaired physiology (Research Question 3).

Research Questions

The aim of this project was to identify open chromatin sites and cis regulatory elements within *OsSWEET* promoters with a focus on the potential effect of mutations in the EBE on plant physiology and stress tolerance.

I. What is the naturally occurring EBE_{PthXo1} diversity and where do variants originate from?
II. How is *OsSWEETs* transcription administered?
    a. What cis elements are present in *OsSWEET* promoters?

b. Which promoter regions are in an accessible chromatin state?
c. Which region of the EBE sequence is essential for maintenance of native *OsSWEET* protein levels?

III. Are functional *sweet* knock-outs impaired in their tolerance to abiotic stress?
a. Are phenotypic parameters altered under salinity stress?
b. Does a short day, low light regime lead to altered leaf traits?

Material and Methods

Analysis of 3k rice genome and transcription factor motif prediction

Genomic data was downloaded from the 3000 rice genomes project website (iric.iiri.org/projects/3000-rice-genomes-project; Wang et al., 2018). Complementary rice genomes were identified using the 5' end of *OsSWEET11a* exon 1 (5'-CCGGGTTAGCCATGGACAAGAAACCTC-3') as input to NCBI Blast. Alignment of a total of 3023 genomic sequences was performed in Geneious Prime® (version 2024.0.4, Dotmatics). Prediction of transcription factor binding motifs within *SWEET* promoters was performed with databases of JASPAR and EnsembleTFpredictor (Figure S3.1,Boyer et al., 2023; Portales-Casamar et al., 2010).

Preparation of samples for MOA sequencing

Plants were grown at 8 hour day 30°C and 16 hour night at 25°C with relative humidity set to 50-70 % and supplemental LED at 400 µmol/$m^{-2}s^{-1}$ (Valoya BX100 NS1). MOA sequencing was performed on three biological replicates with each 5 times 10 cm of leaf tissue from the leaf tip of the 4th leaf of Kitaake plants at the 4th leaf stage. For the fixation and isolation of nuclei, the leaf tissue was homogenized with a mortar and pestle in liquid N_2. For crosslinking of chromatin, 10 mL fixation buffer was freshly complemented with phenatrolin, PMSF and PFA and kept on ice before 2 g of sample material was added (Table S3.1). The samples were vigorously pipetted until no visible tissue fragments remained. Samples were then incubated on a shaker at 40 rpm for 10 min at 22°C. The crosslinking reaction was stopped with addition of 1.2 mL of 2.5 M glycine. The sample was then shaken at 40 rpm for 5 min at 22°C. The reaction mixture was supplemented to a total volume of 45 mL with MNase Digestion Buffer (MDB, Table S3.1). After centrifugation at 1500 rpm for 10 min at 4°C, the supernatant was discarded and the pellet was resuspended in 6 mL of MDB supplemented with 1 % Triton X-100. Tissue disruption was performed using a Polytron in three 10-second

bursts, with the sample kept at 4°C. The homogenate was filtered through two layers of Miracloth into a fresh tube. The volume was adjusted to 15 ml with MDB, followed by centrifugation at 2000 × g for 15 minutes at 4°C. The supernatant was discarded, and the pellet was resuspended in 15 ml of ice-cold MDB. Centrifugation and resuspension was repeated twice. The final pellet was resuspended in 2.2 ml of ice-cold MDB containing 1% Triton X-100, divided into four 500 µl aliquots and kept at -80°C. The remaining volume (200 µl) was used for DAPI staining to confirm the presence of intact nuclei by fluorescence microscopy. One drop of Fluoroshield™ with DAPI (Sigma-Aldrich) was added to 20 µl of each sample. Nuclei visualization was performed using 400× magnification and a cyan/blue filter suitable for DAPI at a Stereo Zoom Microscope (AxioZoom.V16, Zeiss).

For the MNase digest, 7.8 µL of a serial dilution of MNase in MDB (160 U/mL – 0 U/mL) was added to 70 µL of freshly thawed nuclei aliquots. After gentle pipetting, the samples were incubated at 37°C for 15 minutes. To terminate the MNase digestion and to degrade residual RNA, 8 µl of a mixture containing 2.5 µg RNase A and 3 µmol EGTA was added to each sample and incubated at room temperature for 30 minutes. Following RNase treatment, 400 µL of the de-crosslinking master mix (1.25% sodium dodecyl sulfate, 187.5 mM NaCl, 250 µg/mL proteinase K in nuclease-free H_2O) was added to each sample. The samples were incubated at 65°C for 10 hours to complete de-crosslinking, then kept at 4°C.

DNA samples were purified using a three-step organic extraction protocol followed by a column-based cleanup. Initially, an equal volume of phenol was added to each sample. After vigorous shaking for 1 minute, the samples were centrifuged at 14,000 × g for 15 minutes. The upper aqueous phase was carefully transferred to a new 2 ml tube. Next, an equal volume of phenol:chloroform:isoamyl alcohol (25:24:1, v/v/v) was added. Samples were mixed thoroughly and centrifuged at 14,000 × g for 15 minutes. The aqueous phase was transferred to a new 2 ml tube, followed by the addition of an equal volume of chloroform:isoamyl alcohol (24:1, v/v). After thorough mixing and a final centrifugation at 14,000 × g for 15 minutes, the upper phase was transferred to a new tube. DNA was purified using the Monarch® DNA Purification Kit (NEB).

Sequencing and Analysis of MOA samples

The library for next-generation sequencing was prepared with 250 ng of DNA with the NEBNext® Ultra™ II DNA Library Prep (NEB). Quantity was assessed with Qubit Fluorometer (Thermo Fisher Scientific) and fragment size distribution was assessed with an Bioanalyzer HS DNA chip (Agilent). The samples were sequenced using rowing barrel sequencing at the Max Planck-Genome-Centre at the Max Planck Institute for Plant Breeding Research, Cologne, Germany. Sequencing results were prepared for analysis with SeqPurge and FLASH (Magoč and Salzberg, 2011; Sturm *et al.*, 2016). Mapping was performed using the STAR protocol (Dobin *et al.*, 2013). The normalized coverage of reads that overlap 1 bp was extracted as BIG WIG file. MACS3 was used for calling of statistically significant reads (Zhang *et al.*, 2008). Reads have been visualized using Integrative Genomics Viewer (Robinson *et al.*, 2011).

Construct cloning for truncated EBE lines and plant transformation

Translational GUS reporter constructs from Eom et al. (2019) were taken as template for truncated EBE-GUS lines. For each EBE, primers were designed to either omit amplification of the entire EBE, the first or second half of EBE sequence, respectively by PCR. After amplification and fragment size assessment on an agarose gel via gel electrophoresis, purified gel fragments were ligated with T4 ligase (Thermo Fisher Scientific). *E. coli* TOP10 were transformed with ligated constructs via heat shock (45 sec at 42°C) and incubated at 37°C for 16 hours. Single colonies were picked for validation of truncated EBE sequence within GUSplus vector backbone by sequencing. Validated constructs were incorporated into *A. tumefaciens* by electroporation. Rice calli were transformed with truncated EBE-GUS constructs via inoculation with *A. tumefaciens* (detailed protocol in Chapter 4). For each construct, T_3 seeds of 20 independent transformation events were amplified from hygromycin tolerant T_0 transformants.

Assessment of SWEET protein levels in truncated EBE-GUS lines

Rice plants were grown in the green house at a 8 hour light/16 hour dark regime at 30°C and 25°C, respectively, with relative humidity set to 50-70 % and supplemental LED at 400 µmol/$m^{-2}s^{-1}$ (Valoya BX100 NS1). At the 4th leaf stage, 3 leaf disks (10 mm diameter) were punched from each biological replicate in submerged in ice cold 90 % acetone. The histochemical GUS staining protocol was performed subsequently

(Chapter 2). After the reaction was stopped in 75 % ethanol, the samples were incubated in chloral hydrate for clearing. Leaf disks were washed in phosphate saline solution and placed on square disks filled with 50 mL water agar (2 % agar in distilled H_2O) for imaging. Images were taken with a fluorescent Stereo Zoom Microscope (AxioZoom.V16, Zeiss), equipped with a metal halide illuminator (HXP 200C, Zeiss) and a CMOS camera (ORCA-Flash 4.0, Hamamatsu). Analysis of GUS staining abundance as proxy for SWEET protein accumulation dependent on EBE truncation was performed in ImageJ by quantification of RGB intensity measurement.

Abiotic stress experiments

A hydroponic growth set-up was used for abiotic stress experiments. Functional knock out and wild type plants were grown in 5 L boxes in individual holes and stabilized by a carbon mesh. Boxes were filled with 4 L of Yoshida media (Table S3.2). Yoshida media was exchanged weekly. Functional knock out lines were genotyped by sequencing (Table S3.3).

For salinity experiments, Yoshida media was supplemented with 100 mM NaCl. Aeration of plant roots was ensured by an implemented air pump (Figure 3.4A). Phenotypic measurements were taken after seven days of exposure to NaCl. Experiments were performed three times, of which two times five sucrose transporting *sweets* (*sweet11a, 12, 13, 14 and 15*) were included. In the third experiment, two independent knock out lines of *sweet11a, sweet12* and *sweet14* were included. Experiments were performed in the Incrementum 1500 plant cabinet (Bronson) using a long day light regime (16 h day/8 h night) with a photosynthetic photon flux density (PPFD) of 200 µmol m^{-2} s^{-1} with PPFD-blue of 40 µmol m^{-2} s^{-1}, PPFD-green of 80 µmol m^{-2} s^{-1} and PPFD-red of 70 µmol m^{-2} s^{-1}), at 28°C and 80 % humidity.

For the flag leaf experiment, two repetitions were performed where plants of two independent functional knock out lines of *sweet13* at the 5th leaf stage were exposed to a short day and low light regime (8 hour light/14 hour dark; of 80 µmol m^{-2} s^{-1} with PPFD-blue of 20 µmol m^{-2} s^{-1}, PPFD-green of 40 µmol m^{-2} s^{-1} and PPFD-red of 35 µmol m^{-2} s^{-1}). After two weeks of short day and low light conditions, photos were taken using a commercial digital camera. The flag leaf angle was determined in ImageJ.

Results

Limited sequence variety in EBEs indicates high conservation

The fit of the EBE sequence with the TAL effector RVD array is essential for the induction of *OsSWEET* genes. If TAL effector binding is disrupted, ectopic *OsSWEET* activation is interrupted and the plants exhibit resistance to Xoo (Eom *et al.*, 2019; Oliva *et al.*, 2019). Notably, variations in EBEs are rarely reported. To investigate whether natural alterations in EBE sequences exist, I analyzed the promotor sequence (~2 kb) of *OsSWEET11a* from the 3000 Rice Genomes Project and additional available genomic data from sequenced varieties (Wang *et al.*, 2018). Sequences of three varieties, IRBB13, Improved Samba Mahsuri and JN564603_S113 displayed an altered EBE_{PthXo1} sequence (Figure 3.1A). An identical 255 bp long insert has been found to be inserted at position -213 from the ATG of *OsSWEET11a* (Supplemental Figure S3.2). Transposase marks at the flanks of the insert have not been detected e.g. 5'-TAA-3'-insert-5'-TAA-3'. Since only one type of altered EBE_{PthXo1} sequence was identified, I hypothesize that the EBE_{PthXo1} is highly conserved and that its sequence likely plays a role in the regulation of further biological processes that involve *OsSWEET11a*.

Open chromatin regions coincide with predicted binding motifs in *OsSWEET* promoters and occasionally encompass EBE

As the above mentioned results and literature review indicates, EBE sequences seem to be conserved among the majority of rice genomes. Potentially, the EBE sequence is crucial to orchestrate *OsSWEET* transcription. To determine whether EBEs carry responsive cis elements for transcription factors, I used prediction tools to examine potential transcription factor binding motifs and used MOA sequencing to acquire information about the chromatin state at the loci of *OsSWEET11a, OsSWEET13* and *OsSWEET14.* Additionally, translational GUS reporter lines were used to investigate the effect of truncated EBE sequences on OsSWEET protein level.

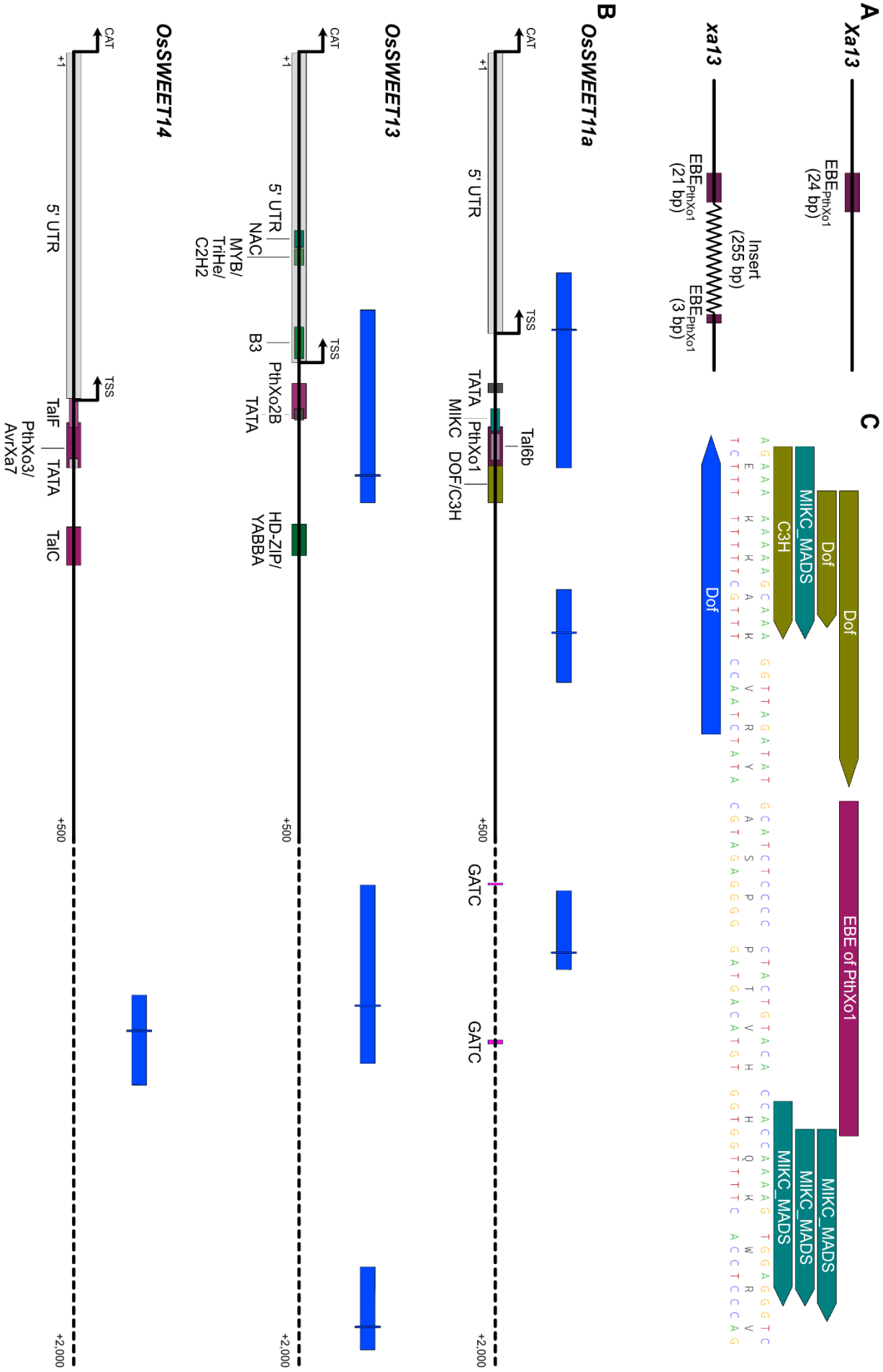
A
Xa13
EBE PthXo1 (24 bp)
xa13
EBE PthXo1 (21 bp)
Insert (255 bp)
EBE PthXo1 (3 bp)
C
Dof
Dof
MIKC_MADS
C3H
Dof
EBE of PthXo1
MIKC_MADS
MIKC_MADS
MIKC_MADS
B
OsSWEET11a
CAT
+1
5' UTR
TSS
TATA
PthXo1
MIKC DOF/C3H
Tal6b
+500
GATC
GATC
+2,000
OsSWEET13
CAT
+1
5' UTR
NAC
MYB/
TriHe/
C2H2
B3
PthXo2B
TATA
TSS
HD-ZIP/
YABBA
+500
+2,000
OsSWEET14
CAT
+1
5' UTR
TSS
TalF
TATA
TalC
PthXo3/
AvrXa7
+500
+2,000

Figure 3.1. Promoter architecture of *OsSWEETs*. (A) Dominat *OsSWEET11a* (*Xa13*) and recessive resistant allele of *OsSWEET11a* (*xa13*). 255 bp disruption of EBEPthXo1 in xa13 confers resistance to Xoo carrying PthXo1. EBEPtXho1 is bisected into 21 bp and 3 bp fragments by insert. (B) MOA sequencing reveals open chromatin sites flanking *OsSWEET11a*, *OsSWEET13* and *OsSWEET14* (statistically confident MOA peaks are shown in dark blue). (C) Motifs of transcription factors were determined with MEME suite and JASPAR. Motifs overlap-ping with the $EBE_{PthXo2b}$ were not predicted.

For all three investigated *OsSWEET* promoters, statistically confident open chromatin sites were identified by MOA sequencing, depicted in dark blue in Figure 3.1B. Interestingly, open chromatin sites associated with two EBE sequences, EBE_{PthXo1} and $EBE_{PthXo2B}$.

For EBE_{PthXo1}, two binding motifs for transcription factors from the families DOF and C3H were predicted at the 5' end (Figure 3.1C). DOF TFs are expected to bind directly adjacent to EBE_{PthXo1}; C3H TFs within in a 10 bp distance. At the 3' end, the binding motif of MIKC TF shares an overlap of 3 bp with EBE_{PthXo1}. Two G boxes were identified at -594, -1109 and -1150 within the *OsSWEET11a* promoter (Figure 3.1C).

Translational GUS reporter lines with truncated EBE sequences were generated for *OsSWEET11a* and *OsSWEET13* (Figure 3.2A). Quantification of OsSWEET protein levels was assessed by imaging and analysis in Fiji (Figure 3.2B).

Truncations in the EBE_{PthXo1} sequence did not alter OsSWEET11a protein abundance when the first 12 nucleotides were absent (Figure 3.2C). However, when the second half of the EBE_{PthXo1} was absent, OsSWEET11a protein level was significantly enhanced ($p < 0.001$) compared to the wild type EBE_{PthXo1} sequence (Figure 3.2 A,C).

A comparable increase of OsSWEET11a abundance was detected, when the entire sequence of EBE_{PthXo1} was lacking ($p < 0.001$, Figure 3.2C). No significant differences were discovered when truncations of the second half of EBE_{PthXo1} were compared with truncation of the first half (Figure 3.2 A, C).

A


EBE PthXo1
-226 from ATG
WT TATGCATCTCCCCCTACTGTACACCACCAAAAGTGGAGGGTCTCCAACTATATAAACAC
Δ bp 1-12 TAT----------ACTGTACACCACCAAAAGTGGAGGGTCTCCAACTATATAAACAC
Δ bp 13-24 TATGCATCTCCCCCT----------CAAAAGTGGAGGGTCTCCAACTATATAAACAC
Δ bp 1-24 TAT----------CAAAAGTGGAGGGTCTCCAACTATATAAACAC
EBE PthXo2B
-233 from ATG
WT CCTATATAAAGCACCACAACTCCCTTCATT
Δ bp 1-12 CCTAT----------AACTCCCTTCATT
Δ bp 13-21 CCTATATAAAGCACCAC---------CATT
Δ bp 1-21 CCTAT----------CATT

B

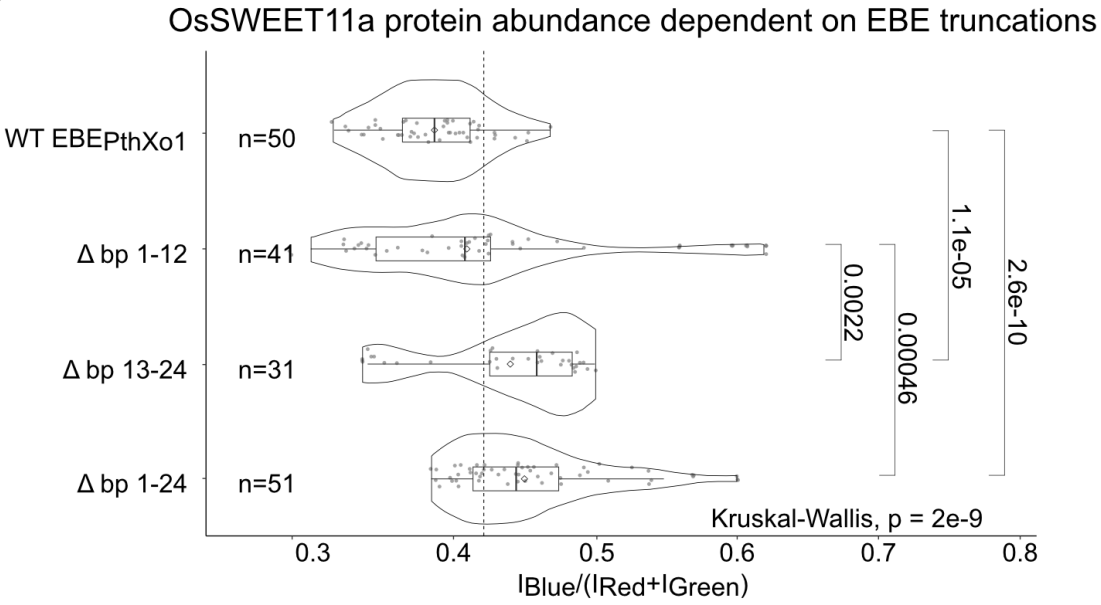
OsSWEET11a protein abundance dependent on EBE truncations
WT EBEPthXo1
Δ bp 1-12
Δ bp 13-24
Δ bp 1-24
n=50
n=41
n=31
n=51
0.0022
0.00046
1.1e-05
2.6e-10
Kruskal-Wallis, p = 2e-9
0.3
0.4
0.5
0.6
0.7
0.8
IBlue/(IRed+IGreen)

C

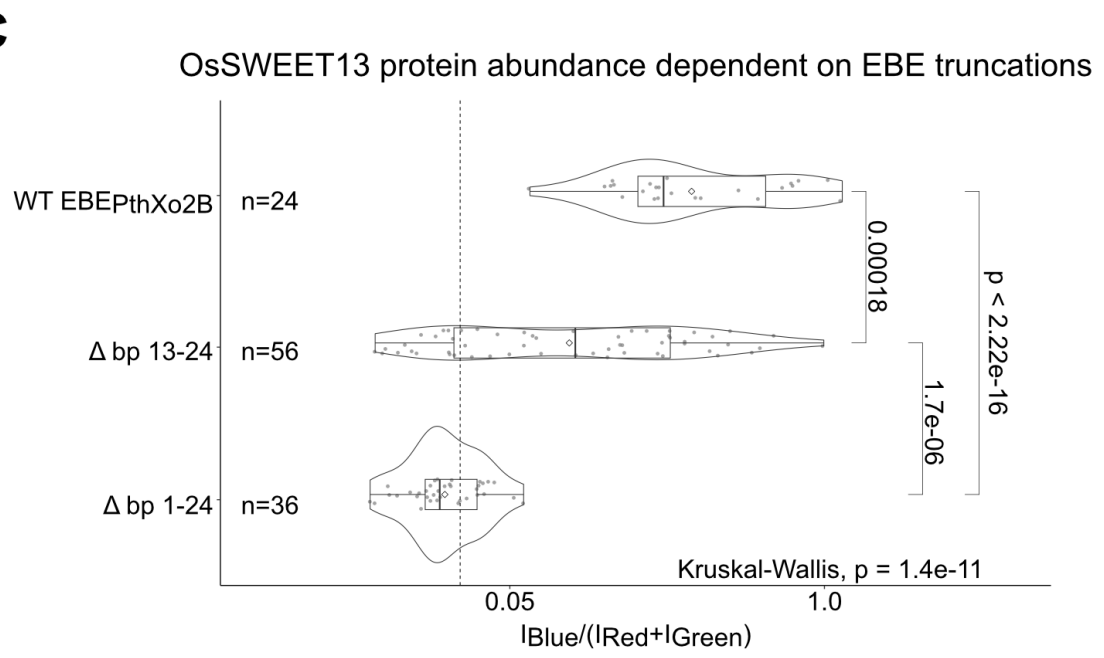
OsSWEET13 protein abundance dependent on EBE truncations
WT EBEPthXo2B
Δ bp 13-24
Δ bp 1-24
n=24
n=56
n=36
0.00018
1.7e-06
p < 2.22e-16
Kruskal-Wallis, p = 1.4e-11
0.05
1.0
IBlue/(IRed+IGreen)

Figure 3.2 Truncations in EBE sequence result in increased protein level for EBEPthXo1 and reduced protein level for EBEPthXo2B. (A) Truncated versions of EBEPthXo2B and EBEPthXo1 fused to translational GUS reporters. (B) Analysis of protein quantification from leaf disks was performed with semi-automated script in Fiji. Exemplary leaf disk values indicate protein abundance. (C, D) SWEET11a and SWEET13 protein level abundance dependent on EBE truncations. Sample size (n), significant p-values from Kruskal-Wallis test are indicated by brackets.

For *OsSWEET13*, an open chromatin site was identified at the $EBE_{PthXo2B}$ within the *OsSWEET13* promoter (Figure 3.1B). Within the euchromatin sequence, a binding motif of the transcription family B3 was present. Interestingly, B3 is adjacent to the 3' end of the transcription start site. Within the 5' UTR sequence, two additional binding motifs were discovered. None of the predicted motifs overlapped with the $EBE_{PthXo2B}$ (Figure 3.1B). $EBE_{PthXo2B}$ overlaps with the TATA box in the *OsSWEET13* promoter. Plausibly, the absence of the entire $EBE_{PthXo2B}$ results in a reduced abundance of OsSWEET13 protein, given the TATA box is missing in these mutants as well (Figure 3.2A, D).

A single euchromatin site was identified to cover the promoter of *OsSWEET14*. Transcription factor bindings sites were not detected within the open chromatin sequence nor spanning the three EBEs for TalC, TalF and PthXo3 (Figure 3.1B).

Despite the efficient application of reporter lines, phenotypic characteristics remain inaccessible within the wild-type background because non-truncated *OsSWEET* promoters are in place. Functional SWEET knockouts were used to simulate maximal disruption of OsSWEET levels under low light and salinity stress.

Flag leaf angles are defined by OsSWEET transporter presence

An erect flag leaf angle improves light penetration to the lower canopy and leads to an enhanced photosynthetic efficiency even under suboptimal light conditions (Acevedo-Siaca *et al.*, 2021). As a place of carbon fixation, flag leaves act as source for sugar transport to sink tissues through apoplasmic phloem loading, mediated by OsSWEET transporters. The flag leaf angles of two independent functional knock out events of *OsSWEET13,* with a 4 bp and 10 bp deletion in the first exon, respectively, were screened under low light and short day conditions (FIG 3.3A). Compared to wild-type, both *sweet13* lines exhibited a greater median of flag leaf angle (Fig. 3.3B). However, *sweet13-1* plants exhibited a wide range of flag leaf angles. The leaf angle of *sweet13-2* was significantly increased compared to wild-type plants.

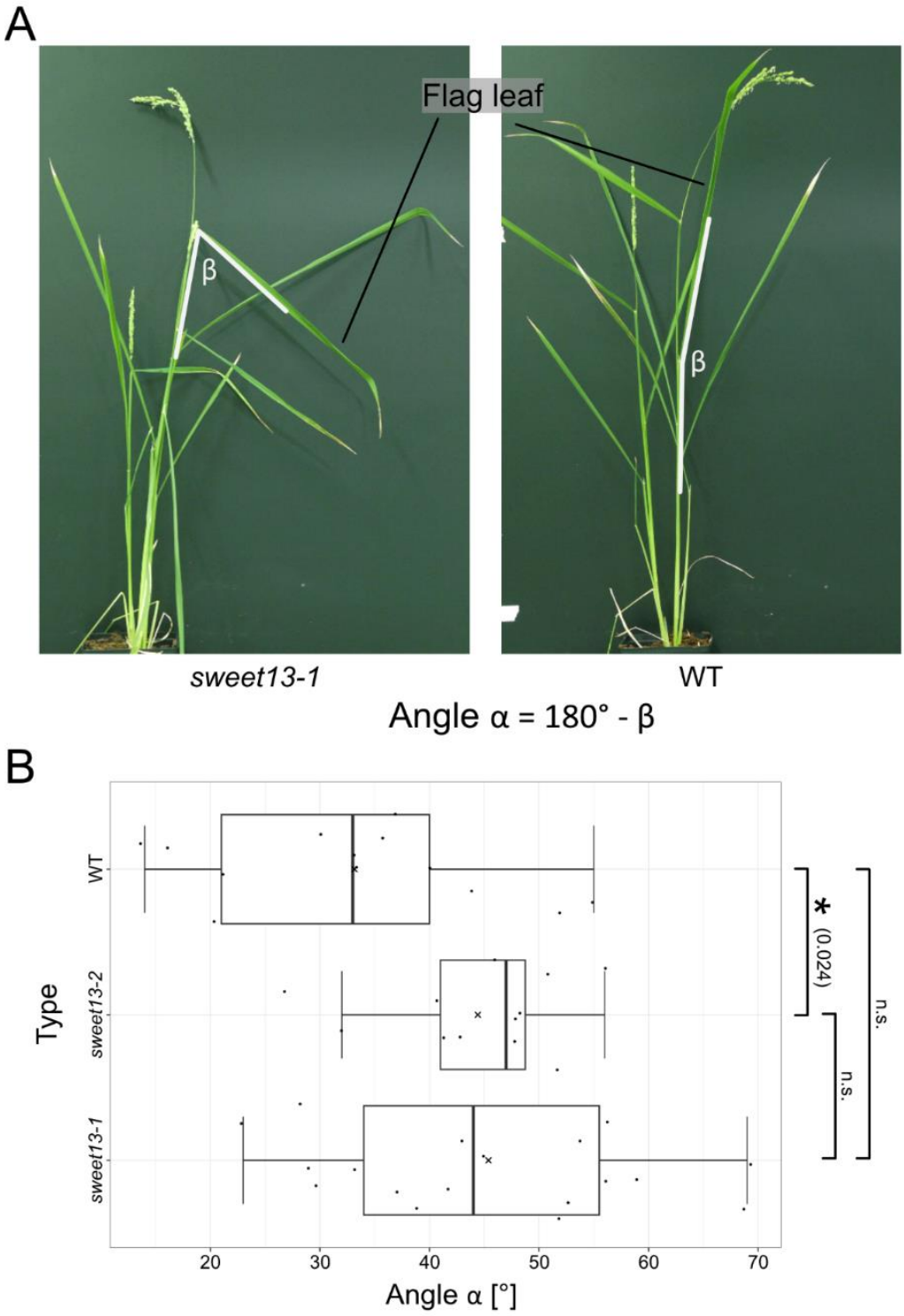

Figure 3.3. Flag leaf angle in *sweet13* mutant rice plants under low light and short day growth conditions. A) Representative picture of *sweet13* (line 1) and wild-type (WT) under short day and low light. The flag leaf and the angle β between the flag leaf blade and stem are indicated. The flag leaf angle α was calculated as α = 180 ° - β. B) Quantifiaction of flag leaf angles (α) in wild-type (WT), *sweet13* (line 1 and 2). Box plots show the median, interquartile range and individual data points. Statistical significance was determined using ANOVA in R. p-value < 0.05 was considered significant, non-significant differences in flag leaf angle are indicated by 'n.s'.

Leaf traits, such as the flag leaf angle influence light capture and photosynthesis and directly affect overall plant performance(Acevedo-Siaca *et al.*, 2020) . Overall plant performance also contributes to stress resilience, including salinity tolerance.

The absence of OsSWEETs does not affect phenotypic characteristics under salinity

Soil salinization is caused by climate change, seawater intrusion and irrigation practices. Salt stress causes excessive sodium (Na^+) accumulation in plant tissues, which competes with essential potassium (K^+). Key genes such as *Salt Overly Sensitive (SOS)*, *High-Affinity K^+ Transporter (HKT)*, and *NHX* transporters play crucial roles in regulating salt tolerance by maintaining ion balance and cellular homeostasis (Deinlein *et al.*, 2014). Functional *sweet* knock out plants were exposed to high salinity stress in a hydroponic growth set-up (Figure 3.4A). After one week of exposure, length of viable shoot, total plant, total shoot, total root, necrotic leaf and the mass of dry root and shoot weight were measured (Figure S3.3).

Between treatments within each genotype and in comparisons between wild-type and functional knock out lines, *sweet14* exhibited a significantly reduced root length under both, control and salt-stressed conditions (Figure 3.4B). In the first and second repetition of the experiment, one event for each of the five functional *sweet* knock out lines was utilized. In the third repetition of the experiment, two independent functional *sweet14* were tested. While the root length of *sweet14* was significantly reduced in the first experiment, only the trend of a reduced root length was observed in the second and third experiment (Figure 3.4C). The standard variation of root lengths among three repetitions for *sweet14* and wild type lines was ±2.1 and ±1.6 cm, respectively. The deviation was lowest for wild-type plants in experiment three (SD = ±1.1) and for *sweet14* in experiment one (SD = ±1.4). Although the trend for a significant reduction of root length was observed for *sweet14* in all three repetitions, the root mass between wild-type and *sweet14* was not observed to be reduced (Figure 3.4 D). A dependency of the trait by the plant position within the box was tested for and not observed in all three experiments (data not shown).

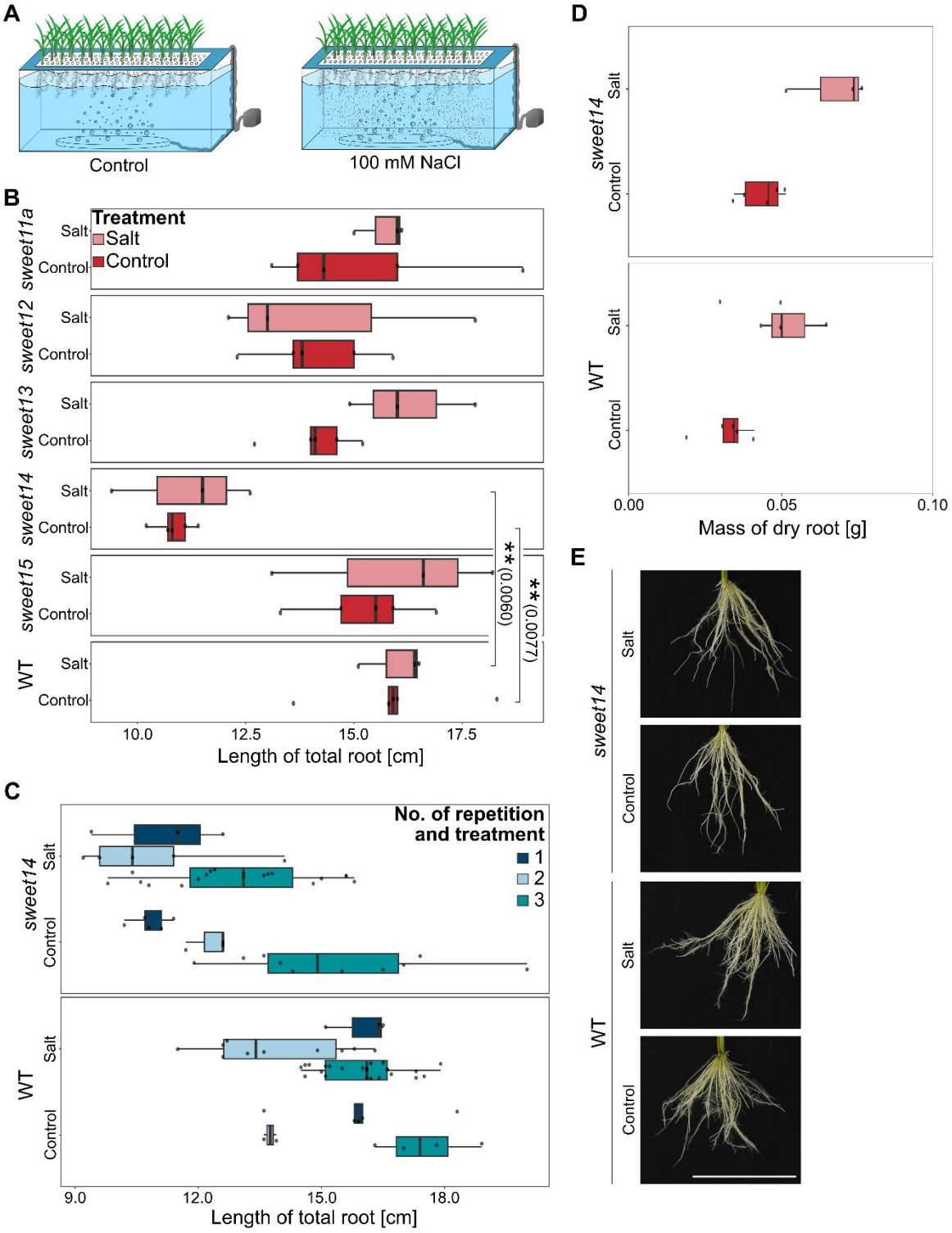

Figure173.4. Total root length of functional *sweet* knock-out plants under 100 mM NaCl growth conditions A) Schematic representation of the hydroponic growth set-up for rice plants under control and 100 mM NaCl growth conditions. B) Quantifiifaction of total root length in functional knock-out lines of clade III *OsSWEETs* (*sweet11a, sweet12, sweet13, sweet14, sweet15*) and wild-type plants exposed to 100 mM NaCl or control growth conditions. Box plots display median, interquartile range and individual data points. Statistical differences between control and 100 mM NaCl conditions were assessed with ANOVA using R. Data shown from one experiment, experiments were performed three times (Figure S3.3). C) Comparison of root length between wild-type and *sweet14*. Boxplots from three independent experiments are differentiated by dark blue (repetition 1), light blue (repetition 2) and turquoise (repetition 3). D) Dry root mass of wild-type and *sweet14* plants under control and 100 mM NaCl growth conditions. Data shown from one experimental repetition E) Images of root systems from wild-type and *sweet14* plants that were grown in 100 mM NaCl and control growth conditions. Scale bar: 10 cm.

Discussion

Open chromatin sites and conservation of EBEs indicate their regulatory Importance

Contrary to my hypothesis for arms race between *Xoo* and EBEs within *OsSWEET* promoters, EBEs showed low variety between rice accessions. This study demonstrates that the EBE_{PthXo1} sequence is highly conserved across rice genomes. Although thousands of accessions were screened for EBE_{PthXo1} variation, only a single insertional variant was identified (Figure 3.1A). The lack of natural variation implies that the EBE region probably fulfills essential regulatory functions beyond its role in pathogen susceptibility. The conservation aligns with my hypotheses that EBEs operate as dual-use elements and serve as recruitment platforms for pathogen effectors and native transcriptional machinery, respectively. This finding underscores the potential importance of EBEs in endogenous transcriptional control and raises the possibility that this sequence contributes to the endogenous regulation of *OsSWEET11a*.

Chromatin accessibility profiling with MOA sequencing identified euchromatin regions at the promoters of *OsSWEET11a, OsSWEET13* and *OsSWEET14.* In case of EBE_{PthXo1} (within the promoter of *OsSWEET11a*) and for $EBE_{PthXo2B}$ (within the promoter of *OsSWEET13*), accessible chromatin sites partially overlapped with the respective EBEs (Figure 3.1B). The results demonstrate that EBEs are not only central to TAL effector recognition but probably also integral to the endogenous regulation of *OsSWEET* gene expression. The conservation of EBE_{PthXo1} across diverse rice genomes, together with the close proximity of transcription factor motifs supports the hypothesis that EBEs are functionally relevant in native promoter activity. Interestingly, the predicted transcription factor motifs remained intact in the 255 bp insertion variant of *OsSWEET11a* (Figure 3.1C).

OsSWEET protein levels were found to be altered in truncated EBE-GUS lines. In *OsSWEET11a*, the second half of the EBE exerted a stronger influence on protein levels than the first half. EBE truncations revealed that deletion of nucleotides 13 to 24 led to a significant increase in *OsSWEET11a* protein abundance, while deletion of the first half produced no measurable effect (Figure 3.2C). Because transcript levels of *OsSWEET11a* are in low abundance within leaves and accessible chromatin sites

were detected, it is possible that repressive protein occupies nucleotides 13 to 24 within EBE_{PthXo1} (ricexpro.dna.affrc.go.jp; Wu et al., 2022). MOA sequencing relies on protein occupancy at DNA sites during Mnase digestion, hence, occupation by repressive proteins could have led to the accessible chromatin site detected for EBE_{PthXo1} (Figure 3.1B). However, employed tools for transcription factor motif prediction did not report a putative repressor binding site (Fig 1C).

Conversely, full deletion of $EBE_{PthXo2B}$ in *OsSWEET13* caused a significant reduction in protein expression. The overlap between $EBE_{PthXo2B}$ and the TATA box likely explains this outcome (Figure 3.1B). The findings indicate that EBEs serve not only as susceptibility element during pathogen infection but also as structurally and functionally integrated elements of core promoter architecture.

OsSWEET transporters are involved in developmental architecture and adaption to abiotic conditions

Analysis of *sweet13* and *sweet14* knockout lines identified roles for *OsSWEET* transporters in developmental trait determination and abiotic stress response. Under short-day and low-light conditions, two independent *sweet13* lines displayed increased flag leaf angles compared to wild-type plants (Figure 3.3B). An erect flag leaf angle improves light interception and supports efficient carbon assimilation, particularly under shaded or suboptimal conditions. My findings point to *OsSWEET13* as a potential genetic determinant influencing plant structure and light-use efficiency.

In a separate assay, *sweet14* mutants exhibited a consistent reduction in root length under both control and saline environments, while root and shoot biomass remained comparable to wild-type plants (Figure 3.4). This phenotype suggests a developmental constraint on root elongation rather than an impaired salt stress tolerance. As sugar distribution affects root development, *OsSWEET14* likely facilitates phloem unloading or local carbohydrate supply required for root elongation.

The findings place *OsSWEETs* into a broader physiological framework that links carbon allocation to the plant phenotype. *OsSWEETs* influence traits that determine source-sink relationships, stress resilience, and plant architecture, all of which shape crop performance under variable abiotic conditions.

Implications for genome editing strategies on OsSWEET promoters and potential improvements

In the absent possibility to test edited lines under multifactorial abiotic stresses in the field, I have exposed functional *sweet* knock out lines to abiotic stress conditions. Thus, maximal disturbance of OsSWEETs was simulated. Although *sweet14* and *sweet13* showed deviations to wild type plants in root length and flag leaf angle, an effect for the majority of tested *OsSWEETs* was not observed. Investigations of *OsSWEET* promoters enhanced our knowledge of accessible chromatin sites and locations of putative transcription factor binding motifs. Nevertheless, reads of MOA sequencing revealed long sequences (>100 bp) and confidential MOA peaks were not accurate enough to allow direct cis element read-out. To identify cis elements within *OsSWEET* promoters, MOA sequencing could be employed on F1 hybrids of *Oryza sativa* spp. *japonica* and *Oryza sativa* spp. *indica*. Single nucleotide polymorphisms between *japonia* and *indica* rice would allow to map MOA reads allele specifically within F1 hybrids. Hence, an exposure to abiotic or biotic stress that results in a differential chromatin occupancy between *japonica* and *indica* alleles, could provide a refined picture of accessible chromatin regions and cis elements. Moreover, a parallel monitoring of RNA levels by RNA sequencing would allow to discriminate between chromatin occupancy of repressive or activating transcription factors. An analysis across the F1 genome under specific conditions might build a foundation to investigate expressive quantitative trait loci (eQTLs) coupled to accessible chromatin sites. Thus, further insights into links between genotype and phenotype could be gathered.

Promoter truncation experiments within EBEs using translational reporter constructs revealed the effect of EBE truncations on OsSWEET protein level. The current study performed histochemical GUS assays as proxy for protein level across multiple events for each construct. To minimize the size of experimental set-ups and increase the accuracy of comparison between constructs, the number of truncated EBE-GUS copies within the genome should be evaluated. Evaluation of EBE-GUS copy numbers could be performed by digital droplet PCR (ddPCR). ddPCR relies on the assumption that the genomic template DNA within each partition of ddPCR plate is diluted to the single template level. Digestion of genomic DNA with EcoRI before addition to the reaction mix amplifies the probability of single template distribution among partitions and provides conditions for the assumption of Poisson distribution. Absolute

quantification of copies can be concluded if approximately half of the total partitions show a successful PCR reaction read out and the Poisson distribution criteria is met.

Conclusion

This study demonstrates that EBEs within *OsSWEET* promoters are highly conserved and functionally integrated into native transcriptional regulation. The minimal sequence diversity observed for EBEPthXo1 across thousands of rice genomes suggests evolutionary constraints, likely reflecting its dual role in susceptibility to TAL effectors and endogenous control of *OsSWEET* expression. Chromatin accessibility mapping and transcription factor motif prediction further support that EBEs act a regulatory cis elements. Reporter assays revealed that truncation of EBEs has effects on OsSWEET protein level. Functional analyses of *sweet* knock-out lines uncovered roles for *OsSWEETs* in flag leaf architecture and root development, linking sugar transport to adaption to abiotic conditions and plant architecture. Importantly, most knock-outs did not display broad abiotic stress sensitivity, suggesting that EBE edits can be implemented with limited detrimental effects.

In conclusion, EBEs represent regulatory elements of dual biological relevance: they serve as susceptibility determinants in pathogen interactions and as functional sites in endogenous promoter regulation. For the development of durable and climate resilient rice varieties, EBE-targeted genome editing must therefore consider both, pathogen resistance and the preservation of SWEET mediated contribution to plant physiology and adaption of abiotic stress tolerance.

References

Acevedo-Siaca, L.G., Coe, R., Quick, W.P. and Long, S.P. (2021) Variation between rice accessions in photosynthetic induction in flag leaves and underlying mechanisms. *J. Exp. Bot.*, **72**, 1282–1294.

Acevedo-Siaca, L.G., Coe, R., Wang, Y., Kromdijk, J., Quick, W.P. and Long, S.P. (2020) Variation in photosynthetic induction between rice accessions and its potential for improving productivity. *New Phytol.*, **227**, 1097–1108.

Antony, G., Zhou, J., Huang, S., Li, T., Liu, B., White, F. and Yang, B. (2010) Rice *xa13* recessive resistance to bacterial blight is defeated by induction of the disease susceptibility gene *Os-11N3*. *Plant Cell*, **22**, 3864–3876.

Boch, J. and Bonas, U. (2010) *Xanthomonas* AvrBs3 family-type III effectors: discovery and function. *Annu. Rev. Phytopathol.*, **48**, 419–436.

Boyer, K., Li, L., Li, T., Zhang, B. and Zhao, G. (2023) MORA and EnsembleTFpredictor: An ensemble approach to reveal functional transcription factor regulatory networks. *PLOS ONE*, **18**, e0294724.

Chen, L.Q., Hou, B.H., Lalonde, S., et al. (2010) Sugar transporters for intercellular exchange and nutrition of pathogens. *Nature*, **468**, 527–532.

Chen, L.Q., Qu, X.Q., Hou, B.H., Sosso, D., Osorio, S., Fernie, A.R. and Frommer, W.B. (2012) Sucrose efflux mediated by SWEET proteins as a key step for phloem transport. *Science*, **335**, 207–211.

Chu, Z., Fu, B., Yang, H., et al. (2006) Targeting *xa13*, a recessive gene for bacterial blight resistance in rice. *TAG Theor. Appl. Genet. Theor. Angew. Genet.*, **112**, 455–461.

Chu, Z., Yuan, M., Yao, J., et al. (2006) Promoter mutations of an essential gene for pollen development result in disease resistance in rice. *Genes Dev.*, **20**, 1250–1255.

Deinlein, U., Stephan, A.B., Horie, T., Luo, W., Xu, G. and Schroeder, J.I. (2014) Plant salt-tolerance mechanisms. *Trends Plant Sci.*, **19**, 371–379.

Dobin, A., Davis, C.A., Schlesinger, F., Drenkow, J., Zaleski, C., Jha, S., Batut, P., Chaisson, M. and Gingeras, T.R. (2013) STAR: ultrafast universal RNA-seq aligner. *Bioinforma. Oxf. Engl.*, **29**, 15–21.

Eom, J.-S., Luo, D., Atienza-Grande, G., et al. (2019) Diagnostic kit for rice blight resistance. *Nat. Biotechnol.*, **37**, 1372–1379.

Hutin, M., Sabot, F., Ghesquière, A., Koebnik, R. and Szurek, B. (2015) A knowledge-based molecular screen uncovers a broad-spectrum *OsSWEET14* resistance allele to bacterial blight from wild rice. *Plant J. Cell Mol. Biol.*, **84**, 694–703.

Magoč, T. and Salzberg, S.L. (2011) FLASH: fast length adjustment of short reads to improve genome assemblies. *Bioinforma. Oxf. Engl.*, **27**, 2957–2963.

Mathan, J., Singh, A. and Ranjan, A. (2021) Sucrose transport in response to drought and salt stress involves ABA-mediated induction of *OsSWEET13* and *OsSWEET15* in rice. *Physiol. Plant.*, **171**, 620–637.

Mücke, S., Reschke, M., Erkes, A., et al. (2019) Transcriptional reprogramming of rice cells by *Xanthomonas oryzae* TALEs. *Front. Plant Sci.*, **10**, 162.

Oliva, R., Ji, C., Atienza-Grande, G., Huguet-Tapia, J.C., Perez-Quintero, A., Li, T., Eom, J.-S., et al. (2019) Broad-spectrum resistance to bacterial blight in rice using genome editing. *Nat. Biotechnol.*, **37**, 1344–1350.

Panigrahy, M., Ranga, A., Das, J. and Panigrahi, K.C.S. (2019) Shade tolerance in Swarnaprabha rice is associated with higher rate of panicle emergence and positively regulated by genes of ethylene and cytokinin pathway. *Sci. Rep.*, **9**, 6817.

Portales-Casamar, E., Thongjuea, S., Kwon, A.T., et al. (2010) JASPAR 2010: the greatly expanded open-access database of transcription factor binding profiles. *Nucleic Acids Res.*, **38**, D105–D110.

Robinson, J.T., Thorvaldsdóttir, H., Winckler, W., Guttman, M., Lander, E.S., Getz, G. and Mesirov, J.P. (2011) Integrative Genomics Viewer. *Nat. Biotechnol.*, **29**, 24–26.

Schepler-Luu, V., Sciallano, C., Stiebner, M., et al. (2023) Genome editing of an African elite rice variety confers resistance against endemic and emerging *Xanthomonas oryzae* pv. *oryzae* strains. *eLife*, **12**, e84864.

Streubel, J., Pesce, C., Hutin, M., Koebnik, R., Boch, J. and Szurek, B. (2013) Five phylogenetically close rice genes confer TAL effector-mediated susceptibility to *Xanthomonas oryzae* pv. *oryzae*. *New Phytol.*, **200**, 808–819.

Sturm, M., Schroeder, C. and Bauer, P. (2016) SeqPurge: highly-sensitive adapter trimming for paired-end NGS data. *BMC Bioinformatics*, **17**, 208.

Wang, W., Mauleon, R., Hu, Z., et al. (2018) Genomic variation in 3,010 diverse accessions of Asian cultivated rice. *Nature*, **557**, 43–49.

Wu, L.-B., Eom, J.-S., Isoda, R., et al. (2022) OsSWEET11b, a potential sixth leaf blight susceptibility gene involved in sugar transport-dependent male fertility. *New Phytol.*, **234**, 975–989.

Yang, B. and White, F.F. (2004) Diverse members of the AvrBs3/PthA family of type III effectors are major virulence determinants in bacterial blight disease of rice. *Mol. Plant. Microbe Interact.*, **17**, 1192–1200.

Yuan, T., Li, X., Xiao, J. and Wang, S. (2011) Characterization of *Xanthomonas oryzae*-responsive cis-acting element in the promoter of rice race-specific susceptibility gene *Xa13*. *Mol. Plant*, **4**, 300–309.

Zaka, A., Grande, G., Coronejo, T., et al. (2018) Natural variations in the promoter of *OsSWEET13* and *OsSWEET14* expand the range of resistance against *Xanthomonas oryzae* pv. *oryzae*. *PLOS ONE*, **13**, e0203711.

Zhang, Y., Liu, T., Meyer, C.A., et al. (2008) Model-based Analysis of ChIP-Seq (MACS). *Genome Biol.*, **9**, R137.

Zhu, W., Yang, B., Chittoor, J.M., Johnson, L.B. and White, F.F. (1998) AvrXa10 contains an acidic transcriptional activation domain in the functionally conserved C terminus. *Mol. Plant Microbe Interact.*, **11**, 824–832.

Supplementary Material

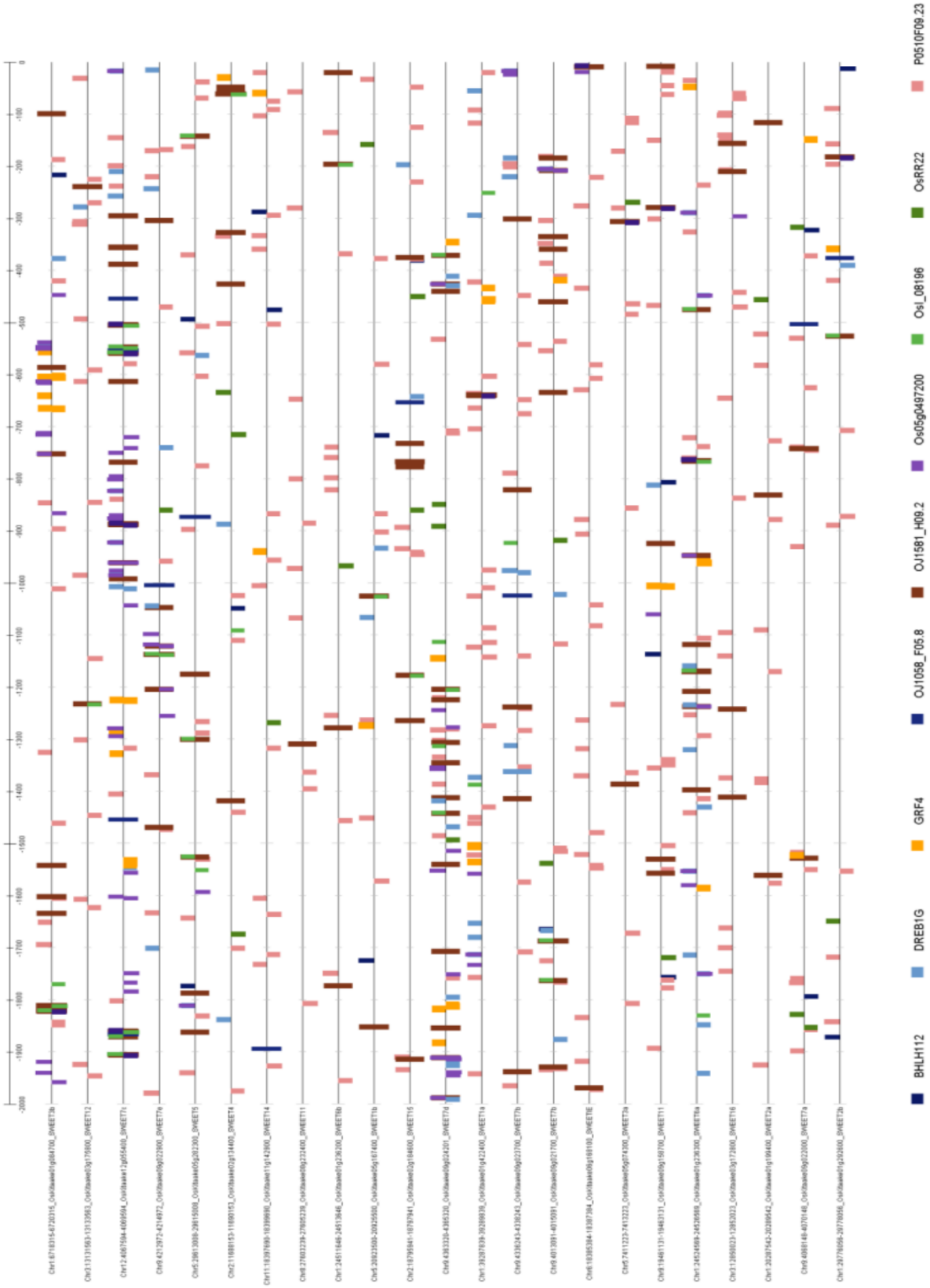

Figure S3.1 Transcription factor binding motif predictions with JASPAR across OsSWEETs. 2000 bp upstream of rice *OsSWEET* genes were extracted and subjected to transcription factor motif prediction with JASPAR.

>255 bp insertion sequence from IRBB13, Improved Samba Mashuri, S1113
ATTAACTCCAAACTCAAGTTCGTTTATGAGAAACAAAAAAGACAAATTTCAGGTGAATAGTGTCCT
GTTACTATTCACCTGAAATTTGTCTTTTTTGTTACTCCTAAACGAAGTTGAGTTTGAACTTGAGATT
TGGTGAGAATGTATTTCATATCTACACCTATCTCTAGTATTTTTTTCATGAATTTATAAAACTTTTAG
GTATGATTTTCACGAGTTTTCAACACTTAGCTCATTTTCACCGGATATGTCCCC

Figure S3.2. 255 bp sequence disrupting EBEPthXo1 resulting in recessive resistant allele of *OsSWEET11a* (*xa13*).

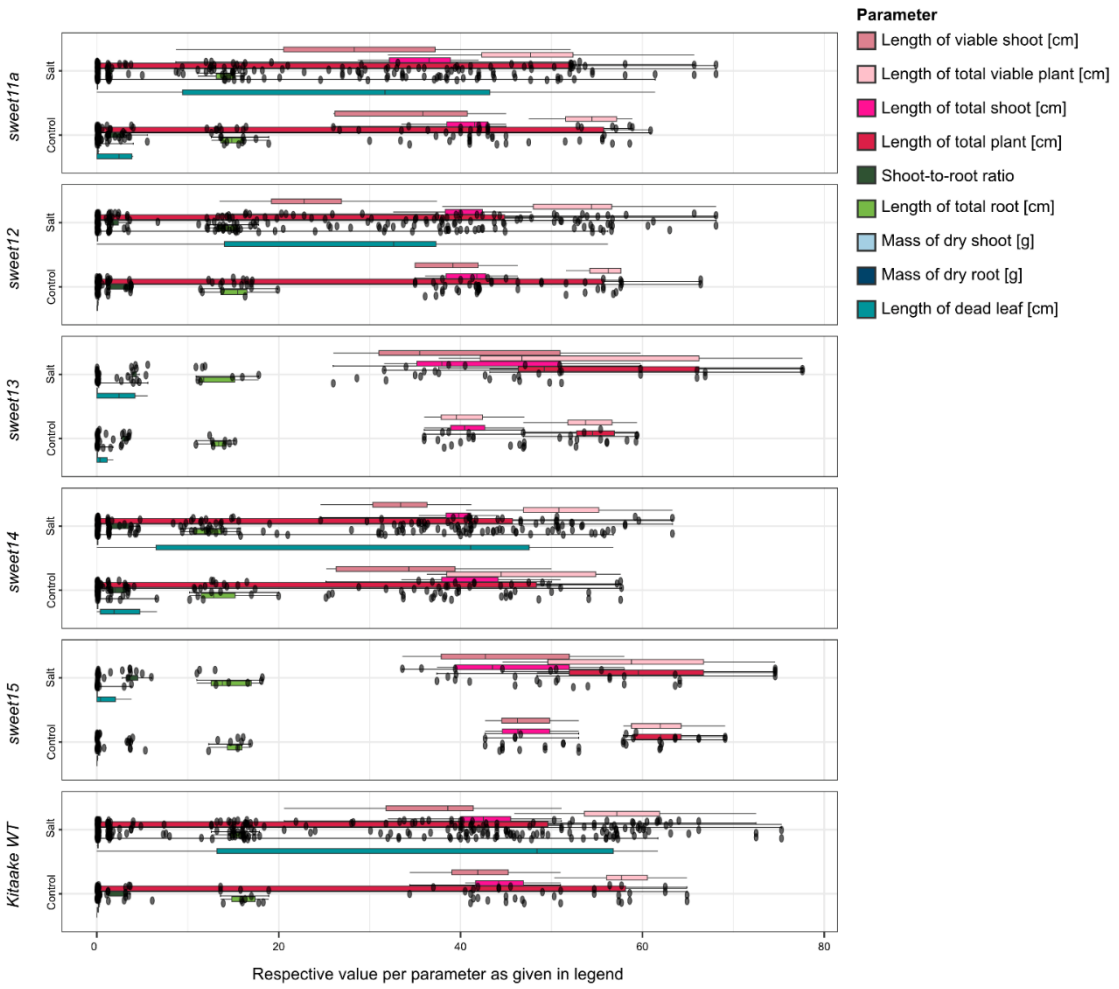

Figure S3.3 Phenotypic measurements for five clade III *sweet* functional knock-outs under control and 100 mM NaCl growth conditions. Box plots summarizing multiple morphologicaltraits of *sweet11a, sweet12, sweet13, sweet14, sweet15 and* wild-type plants (Kitaake WT) grown hydroponically under control or salt (100 mM) conditions. Measured parametered include: Measured parameters include: length of viable shoot (light pink), length of total viable plant (light rose), length of total shoot (magenta), length of total plant (dark red), shoot-to-root ratio (dark green), length of total root (light green), mass of dry shoot (dark gray), mass of dry root (blue), and length of dead leaf (turquoise). Each dot represents an individual plant. Box plots indicate median values,

interquartile ranges, and variability across biological replicates.Statistics and plotting was performed in R. Data from one experimental repetition is displayed.

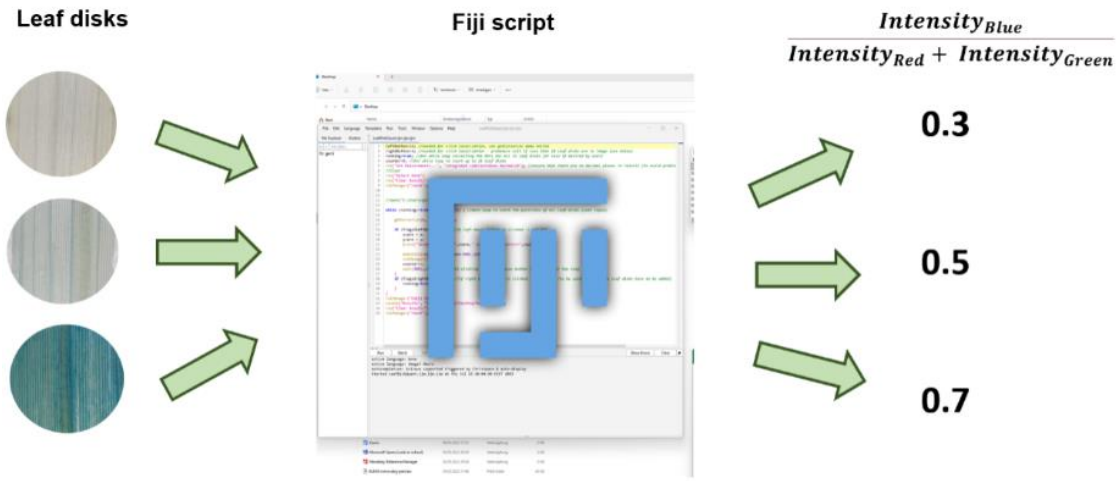

Figure S3.4 Quantification of SWEET protein accumulated evaluated by diX Indigo using a Fiji-based image analysis script. Leaf disks were anaylzed using a custom Fiji script. The script quantifies the intensity of blue diX Indigo by calculating the color intensity ratio of intensity of blue divided by the sum of red and green intensities yielding quantitative values that reflect the relative blue intensity in each sample.

Table S3.1. Recipes for buffers used for preparation of samples for MOA sequencing.

Fixation Buffer – Total volume	50 mL
Buffer A	6 mL
1.6 M Sorbitol	12 mL
1 M Dithiothreitol (DTT)	60 µL
Polyamines	60 µL
Phenantrolin	50 µL
Phenylmethylsulfonylfluorid (PMSF)	100 µL
16 % Paraformaldehyde (PFA)	3.1 mL
Distilled H_2O	Fill up to 50 mL

10x buffer A	**Final concentration**	**For 250ml**
2,2′-(Piperazine-1,4-diyl)di(ethane-1-sulfonic acid) (PIPES)	150mM	11.39g
KCl	800mM	14.91g
NaCl	200mM	2,92g

N,*N*'-(Ethane-1,2-diyl)bis[*N*-(carboxymethyl)glycine] (EDTA)	5mM	0.365g
3,12-Bis(carboxymethyl)-6,9-dioxa-3,12-diazatetradecane-1,14-dioic acid (EGTA)	20mM	1.9g
Distilled H_2O		To 250 mL

Mnase digestion buffer (MDB)	**Final concentration**	**For 1 L**
N-2-Hydroxyethylpiperazin-N-2-ethansulfonsäur (HEPES)	50mM	12g
Glycerol	12.50%	125ml
KCl	25mM	1.87g
MgCl	4mM	0.381g
CaCl	1mM	0.111g

Bring to pH 7.6 with KOH; in distilled H_2O

Table S3.2 Stock solutions for Yoshida media. For 4 liters of working solution, add 2.5 ml of each stock solution and adjust to pH 5.8 with KOH.

Stock order	**Ele-ment**	**Chemical**	**Preparation (g/10 L H_2O)**	**Remarks**
1	N	NH_4NO_3	914	Final volume of 10 L
2	P	$NaH_2PO_4.H_2O$	403	Final volume of 10 L
3	K	K_2SO_4	717	Final volume of 10 L
4	Ca	$CaCl_2$	886	Final volume of 10 L
5	Mg	$MgSO_4.7H_2O$	3240	Final volume of 10 L

Micronutrients

7	Mn	$MnCl_2.4H_2O$	15	Prepare separately, mix and adjust final volume of 10 L
8	Mo	$(NH_4)_6.Mo_7O_{24}.4H_2O$	0.74	
9	B	H_3BO_3	9.34	
10	Zn	$ZnSO_4.7H_2O$	0.35	
11	Cu	$CuSO_4.5H_2O$	0.31	
12	Fe	Fe-Na-EDTA	104	

Table S3.3. Sequences of oligos used for genotyping of functional sweet knock-out lines. Primers amplify fragments of approximately 500 bp.

Primer	Sequence 5‘ – 3‘
LR045_F_sweet11ko	TCTGGCTAGTTTCTAGCTGGT
LR046_R_sweet11ko	CAGCAATTAACCTGAATTTGA
LR047_F_sweet13ko	ACACATTGAACTCTTCTTCAGAG
LR048_R_sweet13ko	AATGAAGGGAATGTCTTAGTTGT
LR049_F_sweet14ko	AAGCCTTCAAGCAAAGCAAA
LR050_R_sweet14ko	TTGGCAACAAAAGTGGAACA

8 Engineering TAL effector traps with Prime Editing

Contributions

Bing Yang advised on design of Prime Editing constructs. Melissa Stiebner supported plant transformation.

Abstract

Rice possesses executor resistance genes that are able to trap injected transcription activation like effectors (TALes) within their promoters by effector binding elements (EBEs). The mechanism of executor resistance genes tricks Xanthomonas oryzae pv. oryzae (Xoo) to induce defense genes when it delivers TALes into rice host tissues. While the overall TALe structure is highly conserved, naturally occurring variations in repeat variable di-residues (RVD) length and RVD tolerance to different nucleotides introduces significant versatility to TALes. To date, the possibility that different RVD arrays target the same EBE sequence has not been explored. Xoo relies on redirecting sugar flux towards its infection sites for successful colonization. If the redirection of sugar flux fails, Xoo is unable to establish an infection. To counter Xoo, I have attempted to use prime editing to integrate EBEs upstream of potential resistance genes. Furthermore, I have aimed to identify common EBEs that could provide broad-spectrum resistance against a range of known Xoo strains. While this study presents key methodological advances, the intended edit was not successfully generated with prime editing. The combinatorial script predicted numerous putative EBEs underscoring the need for more robust bioinformatic approaches to manage and prioritize candidates within large and complex datasets.

Introduction

Executor R Genes trap TAL effectors

Plants counter pathogen attacks with a sophisticated innate immune system. Pattern Recognition Receptors (PRRs) located on plant cell surfaces are able to perceive Pathogen-Associated Molecular Patterns (PAMPs), e.g. flagellin, the primary component of the bacterial flagellum (Felix *et al.*, 1999). Upon recognition of PAMPs, the first layer of immune response, known as Pathogen-Triggered Immunity (PTI), is activated. PTI is species-independent and considered to serve as a form of basal resistance. In return, pathogens have evolved effectors with the ability to suppress PTI either by disruption of PAMP detection or subsequent signaling cascades. In response, plants have developed mechanisms to directly or indirectly detect these effectors, initiating a second layer of defense called Effector-Triggered Immunity (ETI) (Jones and Dangl, 2006). Most resistance (R) genes encode Nucleotide-binding Leucine-rich Repeat (NLR) proteins, which share conserved structural features and mediate

effector recognition. Based on their N-terminal domains, NLRs are categorized into Toll/interleukin-1 receptor-like NLRs (TNLs) or coiled-coil domain NLRs (CNLs) (Jones and Dangl, 2006; Meyers *et al.*, 2005).

In the ongoing evolutionary arms race between pathogen and host, the ETI response is constantly challenged by the emergence of novel pathogen effector variants. For instance, the CNL *OsXa1* is targeted by Xoo by interfering with TAL effectors (iTALes) with truncated C-termini. Presumably, iTALes act as decoys for TALes, and can mitigate plant immune response. Notably, a survey of published Xoogenomes revealed that iTALes are more prevalent in Asian than in African Xoo strains (Ji *et al.*, 2020).

In addition to NLRs, rice is equipped with a structurally different set of R genes, called executor R genes. Executor R genes are induced by TAL effectors from invading Xoo. As a consequence, susceptibility and R genes are induced by the gene-for-gene interaction between TALe and EBE upon TALe injection. Four executor R genes have been cloned from rice: *OsXa7, OsXa10, OsXa23* and *OsXa27* (Tian *et al.*, 2014; Wang *et al.*, 2015; Wu *et al.*, 2008). To date, for the TALes AvrXa10, AvrXa23 and AvrXa27 no contribution to virulence was shown. In contrast, AvrXa7 appears to exhibit a dual role: AvrXa7 induces *OsSWEET14* and thereby redirects the nutrient flux to the infection site. Simultaneously, AvrXa7 is “trapped” by an EBE upstream of the executor R gene *OsXa7* (Zhang *et al.*, 2015). The induction of executor R genes initiates programmed cell death, a key feature of the hypersensitive response (HR). HR involves a plethora of processes, including nutrient sequestration and formation of physical barriers. As consequence of the HR, the growth of biotrophic pathogens can be restricted (Nakagami *et al.*, 2024).

It has been hypothesized that our knowledge of executor R genes in rice, compared to other species, is a result of the widespread use of effector-dependent germplasm screening methods in the rice-Xoo pathosystem (Nowack *et al.*, 2022). Rather than an actual absence of executor R genes in other species, the disparity of identified executor R genes among pathosystems likely reflects a methodological bias and advantage of the identified and sequenced TALeome for resistance breeding.

Executor R genes rely on the underlying mechanism of “single repeat to single base” binding between TALe and EBE. TAL effector-based technologies are employed

across a wide range of applications. However, the RVD composition present in commercially available kits differ significantly from RVDs naturally occurring in TALes(Cermak *et al.*, 2011; Sanjana *et al.*, 2012).

TAL effector sequence specificity depends on RVD composition

TAL effectors exhibit a highly conserved structural organization, with variability confined to the 12th and 13th amino acid of the repeat variable di-residues (RVDs) within the repeat domain. The amino acid at position 12 contributes to stabilizing the RVD loop, while the 13th amino acid establishes specific interactions with the target nucleotide via hydrogen bonding and van der Waals forces (Deng *et al.*, 2012). The binding specificity of RVDs and their impact on overall TALe functionality have been extensively studied to identify RVDs capable of precisely targeting specific DNA sequences (Boch et al., 2009; Yang et al., 2014). The development of genome editing technologies and DNA-specific binding systems based on TALes has significantly increased interest in RVDs with high specificity for individual nucleotides. Among the early characterized RVDs, NI, NG, and HD demonstrated strong binding affinities for adenine (A), thymine (T), and cytosine (C), respectively. In contrast, RVDs such as NN, NH and NK, which target guanine (G), exhibit broader nucleotide binding tolerance and can bind other bases (Christian *et al.*, 2012; Cong *et al.*, 2012). The development of modular toolkits for TAL cloning has facilitated rapid assembly of custom RVD arrays to create TALes tailored to specific DNA sequences (Table S1 and S2; Cermak et al., 2011; Sanjana et al., 2012).

While the vast majority of RVDs contain 34 amino acids, two common exceptions exist in the TALe repertoire of Xoo (Becker *et al.*, 2022). The absence of the 13th amino acid constitutes a 33 amino acid RVD which is typically labelled with a * and considered to bind any nucleotide. 35 amino acid long RVDs carry an additional proline at position 33 which has been shown to not impact the binding of the repeat domain (Richter *et al.*, 2014; Römer *et al.*, 2010). In addition to the common length variations of 33 and 35 amino acids within a RVD, any longer or shorter RVDs have been termed aberrant repeats. Such length variation are displayed in AvrXa7 and PthXo3, which target overlapping EBEs in the *OsSWEET14* promoter (Richter et al., 2014) as well as TalBK and PthXo2 targeting *OsSWEET13* (Becker *et al.*, 2022; Oliva *et al.*, 2019) . Aberrant RVDs offer binding flexibility to the TALe and allow for mismatches in the downstream sequence (Becker *et al.*, 2022; Richter *et al.*, 2014; Streubel *et al.*, 2012). Another

prevalent repeat variant is a degenerated RVD at the N terminal repeat domain characterized by a tryptophan residue at position W232 that targets the initial thymine commonly found in EBEs (Boch *et al.*, 2009; Stella *et al.*, 2013).

Comparative analysis of the TAL effector repertoires from African and Asian Xoo strains revealed no conserved TAL effector (Tran *et al.*, 2018; Oliva *et al.*, 2019). However, the variability in RVD length and its corresponding impact on binding specificity to EBEs, along with the inherent flexibility of the 13th amino acid to accommodate different nucleotides due to side-chain interactions and van der Waals forces, suggests that TAL effectors with different RVD compositions may target the same EBE sequence.

Therefore, bioinformatic approaches to consider binding tolerances of RVDs and their combinations within repeat domains could potentially identify a functionally conserved EBE between African and Asian Xoo strains. The identification of conserved EBEs across Xoo would enable new breeding strategies with a broad resistance spectrum for African and Asian strains.

Retrieval of sugars from the infection site can boost plant resistance

Sugars play a dual role in plant pathogen interactions (Bezrutczyk *et al.*, 2018). The role for sugar as carbon source has been shown for bacterial and fungal pathogens that would invade plants with the primary goal to access sugars needed for reproduction (Chen *et al.*, 2010). However, an alternative role for sugar is to act as defense trigger. The accumulation of sugars at the infection site restricts pathogen proliferation by induction of defense pathways e.g. salicylic acid (Yamada and Mine, 2024). In the pathosystems of *Botrytis cinerea-Arabidopsis thaliana* and *Puccina striiformis*-wheat, hexose/H+ symporters potentially display examples for the sugar feeding vs. signaling hypotheses. In the *Arabidopsis thaliana-Botrytis cinera* pathosystem, the retrieval of hexoses via hexose/H+ symporter AtSTP13 from the apoplasm was shown to enhance plant resistance (Lemonnier *et al.*, 2014; Yamada *et al.*, 2016). In contrast, two mutations in the wheat homologue of AtSTP13, TaSTP13, lowered the affinity for hexose transport and increased resistance. Hence, in the wheat-rust/powdery mildew pathosystems, enhanced sugars at the infection site seem trigger plant defense responses (Huai *et al.*, 2020; Moore *et al.*, 2015; Yamada and Mine, 2024).

In the interaction of *Xoo* with rice, TALes bind to EBEs within the *OsSWEET* promoter. When EBEs are mutated, *OsSWEET* induction does not occur. Consequently, plants are resistant to Xoo (Eom *et al.*, 2019; Oliva *et al.*, 2019). Because Xoo infection relies on sugars, I assume that increasing levels of sugar uptake transporters would diminish the amount of sugars at the infection site and increase plant resistance. To modulate the available pool of sugars *in planta* during infection, I used genome editing.

Genome Editing revolutionized plant breeding

Genome editing techniques rely on induced double strand breaks (DSB) of DNA. Two repair mechanisms are employed to join a DSB back together. Non-homologous end joining (NHEJ) fuses broken DNA ends, often small insertions or deletions are integrated. Homologous recombination (HR) uses a homologous DNA template to accurately repair the break.

Zinc finger nucleases and transcription activator-like effector nucleases rely on DNA binding motifs coupled with a FokI nuclease to create DSBs. In contrast, Clustered Regularly Interspaced Short Palindromic Repeats (CRISPR)/Cas depends on a guide RNA to direct the Cas nuclease to the DNA target site. For all common genome editing techniques, DSB can be introduced at specifically targeted DNA sites. However, only random mutations will be integrated by NHEJ and the effect of mutation has to be evaluated. The newest development in genome editing, prime editing, overcomes the disadvantage of random mutations and offers the possibility to integrate SNPs but also whole sequences at a specific DNA locus.

Prime editing is a versatile genome engineering approach that combines a Cas9 (H840A) nickase with a reverse transcriptase (RT) to introduce precise genetic changes without creating double-stranded breaks. The activity of both enzymes is guided by a specialized RNA molecule known as the prime editing guide RNA (pegRNA). This pegRNA consists of several components: a spacer sequence that directs the Cas9 (H840A) nickase to the target DNA site, a scaffold region, a reverse transcriptase template (rtT), a primer binding site (PBS), and a stabilizing 3’ pseudoknot. The spacer anneals to the complementary DNA strand in a 3’–5’ orientation and must include a protospacer adjacent motif (PAM) for effective targeting. Once the Cas9 (H840A) introduces a nick in the target strand, the RT uses the PBS and rtT to synthesize a new DNA segment containing the desired edit. The rtT is

typically identical to the wild type sequence except at the site of mutation, and it can be designed to terminate efficiently using additional nucleotides such as TGC, GC, or C. The 3' pseudoknot plays a crucial role in pegRNA stability by preventing degradation from cellular RNases. A secondary nick on the non-edited strand, positioned roughly 100 bp from the edit site, can be introduced to improve editing efficiency by favoring a 5' flap cleavage.

Rationale / Aims of this project

Based on the knowledge of EBE – TALe interaction and the competitions for sugars during Xoo infection, I aimed to create novel executor R genes using prime editing. For the design of a promising strategy for novel executor R genes, I aimed to:

- identify whether African and Asian Xoo share common EBEs despite their divergent TALe repertoire.
- integrate an EBE in the promoter of a hexose uptake transporter in rice to test whether plant resistance towards Xoo would be increased.

Material and Methods

Cloning of Prime Editing Constructs

Constructs for Prime Editing were provided by Bing Yang (University of Missouri) and are based on publications by Gupta et al., 2024 and Jiang et al., 2022. Principles of recombinational Gateway cloning were used to integrate the target specific oligos (spacer, extension and nick) from the entry vector pAG79 into the binary expression vector pAG168. Three respective oligos, spacer, extension and the separate nick oligo, need to be designed target specifically and are integrated via restriction ligation cloning into pAG79 (Table S3). Oligo pairs were annealed by heating in equimolar amounts to 95°C for 10 min and subsequent cooling in 5 min steps to 20°C in 5°C steps. For the integration of the spacer oligo into pAG79, the pAG79 backbone is digested with BsmBI and the spacer oligo can be ligated by the 5' overhang sites of "tgca" on the forward spacer and "aaac" on the reverse spacer. The extension oligo and reverse transcriptase template was designed with plantgenomeediting.net. To prevent a spill-over of the reverse transcriptase into the PBS, the rtT can be extended by TGC, GC or C to favour the termination. A non-interfering linker based on the sequences of spacer, rtT, PBS and scaffold was designed with pegLIT. For cloning of extension and nick oligo into pAG79, the extension oligos carried "gtgc" forward and "cgcg" reverse overhangs. The nick forward "gata" and the nick reverse "aaac". pAG79 with spacer was digested with BsaI and ligation with extension and nick oligo was catalysed by T4 ligase. Importantly, digest and ligation was performed in the same reaction volume since a fragment of the backbone was re-ligated to separate the nick oligo from the pegRNA. In the last cloning step, the encoding sequence for the oligos, the motif and scaffold RNA were integrated into the binary plasmid pAG168 by a gateway LR reaction.

Plant transformation and genotyping

Kitaake callus cells derived from scutella were isolated from sterilised dehulled rice seeds grown on R1 media (4.3 g/L MS salts and vitamins (Duchefa M0225), 30 g/L sucrose, 0.5 g/L MES, 300 mg/L casamino acid, 2.878 g/L L-proline, 2 mg/L 2, 4-D, 4 g/L Phytagel™, pH 5.8 adjusted with KOH in ddH_2O) for two weeks at 28°C in dark conditions.

Agrobacterium tumefaciens strain LBA4404/pVS1-VIR2 carrying the respective pAG168 plasmid and LBA4404/pVS1-VIR2 lacking a binary expression plasmid were grown on YEP Agar plates (10 g/L yeast extract, 10 g/L peptone, 5 g/L NaCl, 8 g/L agar, pH 7.0 in in ddH_2O) for two days at 28°C in dark conditions. *A. tumefaciens* colonies were suspended in AAM media (4.3 g/L MS salts and vitamins (Duchefa M0225), 68.5 g/L sucrose + 0.5 g/L MES, 36 g/L glucose, 500 mg/L casamino acid, 6 mM L-glutamine, 2 mM L-aspartic Acid, 1 mM L-arginine, 0.1 mM glycine, pH 5.2 adjusted with KOH in ddH_2O) to OD_{600} 0.4. Calli were immersed in the bacterial suspension, gently shook for 5 min and dried on sterilized filter paper to remove excess bacteria. After inoculation, calli were grown on RS2 media (4.3g/L MS salts and vitamins (Duchefa M0225), 30 g/L sucrose, 0.5 g/L MES, 10 g/L glucose, 300 mg/L casamino acid, 2 mg/L 2, 4-D, 4 g/L Phytagel™, 0.02 mg/mL acetosyringone, pH 5.2 adjusted with KOH in ddH_2O) for three days at 25°C under dark conditions.

Antibiotic resistance screening was used to identify calli with successfully integrated T-DNA by transfer to R3 media containing hygromycin (4.3 g/L MS salts and vitamins (Duchefa M0225), 30 g/L sucrose + 0.5 g/L MES, 300 mg/L casamino acid, 2.878 g/L L-proline 2 mg/ L 2, 4-D, 4 g/L Phytagel™, 150 mg/L timentin, 50 mg/L hygromycin, pH 5.8 adjusted with KOH in ddH_2O) for two weeks at 28°C under dark conditions. After a repetition of antibiotic screening on R3 media, calli were transferred to R3.5 media (4.3 g/L MS salts and vitamins (Duchefa M0225), 30 g/L sucrose + 0.5 g/L MES, 300 mg/L casamino acid, 2.878 g/L L-proline, 1 mg/L 2, 4-dichlorophenooxyacetic acid, 0.5 mg/L kinetin, 4 g/L Phytagel™, 50 mg/L timentin, 50 mg/L hygromycin, pH 5.8 adjusted with KOH in ddH_2O) for two weeks at 28°C in dark conditions. For the regeneration of plants, calli were transferred to R4 media (4.3 g/L MS salts and vitamins (Duchefa M0225), 30 g/L sucrose, 0.5 g/L MES, 2 g/L casamino acid, 30 g/L sorbitol, 2 mg/L kinetin, 1 mg/L 1-naphtaleneaacetic acid, 4 g/L Phytagel™, 150 mg/L timentin, 50 mg/L hygromycin, adjusted to pH 5.8 with KOH in ddH_2O) and R4.5 media (4.3 g/L MS salts and vitamins (Duchefa M0225), 30 g/L sucrose, 0.5 g/L MES, 2 g/L casamino acid, 30 g/L sorbitol, 2 mg/L kinetin, 1 mg/L 1-naphtaleneaacetic acid, 4 g/L Phytagel™, 150 mg/L timentin, adjusted to pH 5.8 with KOH in ddH_2O) for two weeks each under continuous light conditions (photosynthetic photon flux density (PPFD) of 200 µmol m^{-2} s^{-1} with PPFD-blue of 40 µmol m^{-2} s^{-1}, PPFD-green of 80 µmol m^{-2} s^{-1} and PPFD-red of 70 µmo m^{-2} s^{-1} at 27°C and

80 % humidity in CLF PlantClimatics chambers (model: CU41L5). Root growth of arising plantlets was facilitated by transfer to R5.5 media (2.15 g/L MS salts and vitamins (Duchefa M0225), 15 g/L sucrose, 0.5 g/L MES + 2 g/L Phytagel™, 150 mg/L timentin, pH 5.8 adjusted with KOH in ddH_2O).

Leaf tissue was harvested from hygromycin tolerable T_0 transformants and homogenized in liquid nitrogen with metal beads by TissueLyser III (QIAGEN). Genomic DNA was isolated with the NucleoSpin Plant II (Machery-Nagel) and set to 50 ng/µL. 500 bp DNA fragments covering the location of edit were amplified using the GoTaq® Green Master Mix. PCR products were gel purified and sequence was verified Sanger sequencing (performed by Microsynth™). Analysis of sequences was performed by alignment with the *in silico* sequence in Geneious Prime® (version 2024.0.4).

Combinatorial computing to identify potential common EBEs

RVD sequences of TAL effectors were extracted from AnnoTale (Grau *et al.*, 2016) and provided by Alvaro Perez-Quintero (Institut de Recherche pour le Développement, France). RVD binding specificities were approached by using published position-weight matrixes and experimental data (Pérez-Quintero *et al.*, 2015; Yang *et al.*, 2014). Script was run by Linux command-line terminal on “HILBERT” high computing interface provided by Heinrich-Heine University, Düsseldorf (Figure S4.1).

Results

TAL effectors of African and Asian Xoo differ in length and composition

Analysis of the TAL effector repertoire of African and Asian Xoo strains revealed that TAL effectors differ in length and RVD composition (Figure 4.1). In Asian strains, 1,289 TAL effectors were identified across 78 strains, encompassing 19 distinct RVD types. Asian TAL effectors contain five aberrant repeat types (n*, ng, ni, nn, ns) with a total of 219 occurrences, in addition to three variable repeat types (H*, N*, and S*). In contrast, African strains include 261 TALes across 29 strains, with a lower diversity of 9 RVD types. The N* repeat appears 174 times in African TALes, whereas aberrant repeats (n*, ng, ni, nn, ns) remain exclusive to Asian TALes (Fig 4.1A). Despite differences in composition, the majority of TALes carry 20 RVDs in African and Asian Xoo strains, respectively (Fig 4.1B).

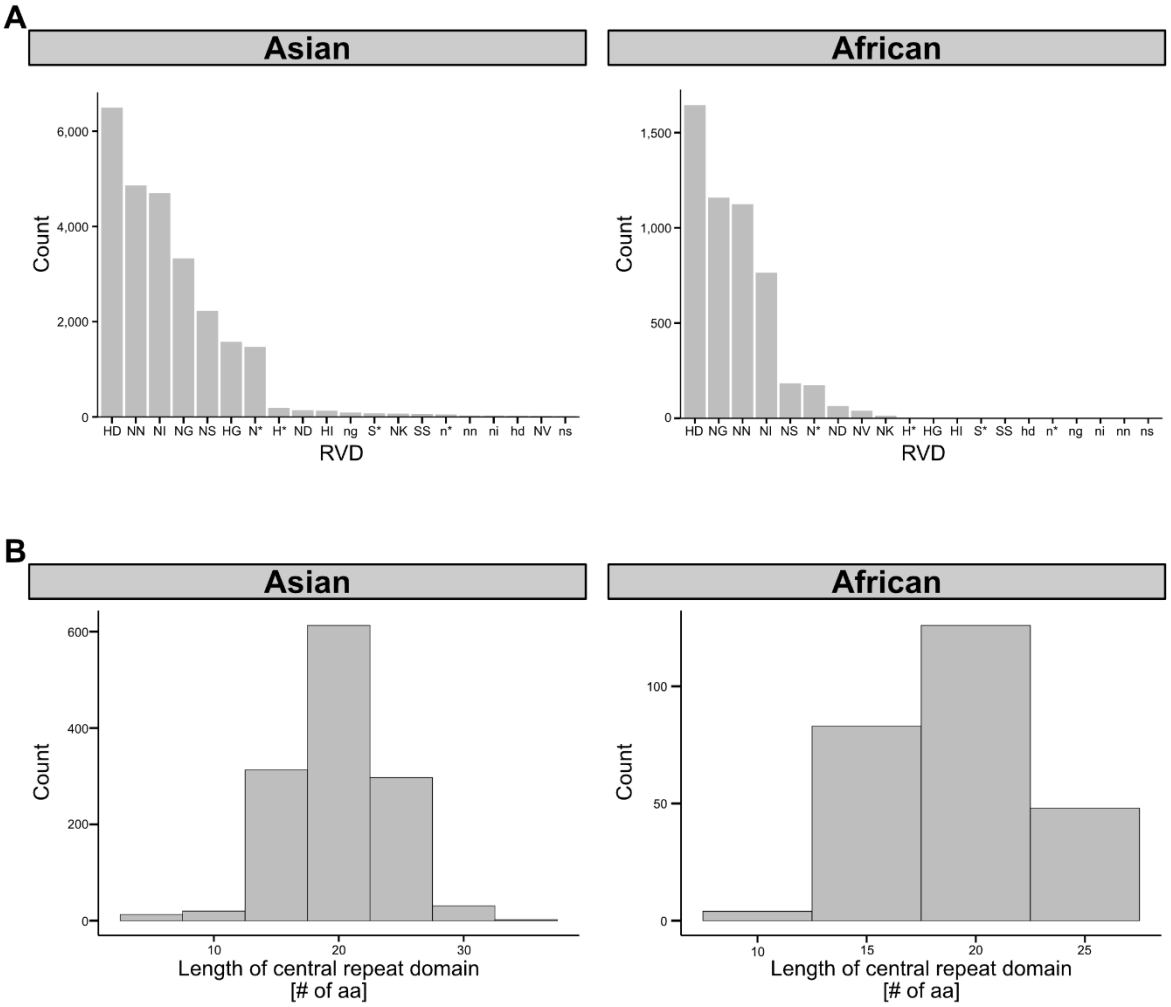

Figure 4.1. Composition and length of RVD arrays of TALes from African and Asian Xoo. (A) Occurrence of RVD type within Asian or African Xoo. (B) Length of RVD arrays between African and Asian Xoo. Information on RVD occurrence and number of RVDs within one TALe were extracted from data on TALes provided by AnnoTale (Grau *et al.*, 2016). Analysis was performed in R.

Combinatorial approach reveals putative EBEs for RVD arrays

Tolerances of RVD target specificity demonstrate potential similarities of EBE sequences between African and Asian *Xoo* strains (Fig 4.2A). To further examine the theoretical TALe binding potential, a permutated combinatorial approach identified putative EBE sequences targeted by RVD sequences. The permutation generator script using HILBERT High-Performance Computing generated possible EBE sequences for individual TALe classes (Fig 4.2B). The threshold for nucleotide binding affinity was set to 20% to ensure the identification of higher confidence EBEs. The combinatorial analysis revealed putative EBEs classified according to TALe groups. For example, the RVD sequence of TalBH21 (CP047493: 3218210-3222863:+1) from *Xoo* IXO792 is predicted to bind 65,022 EBEs. The results reveal an extensive range of putative EBEs for each TALe and point at a plethora of potentially targeted EBEs within one *Xoo* strain.

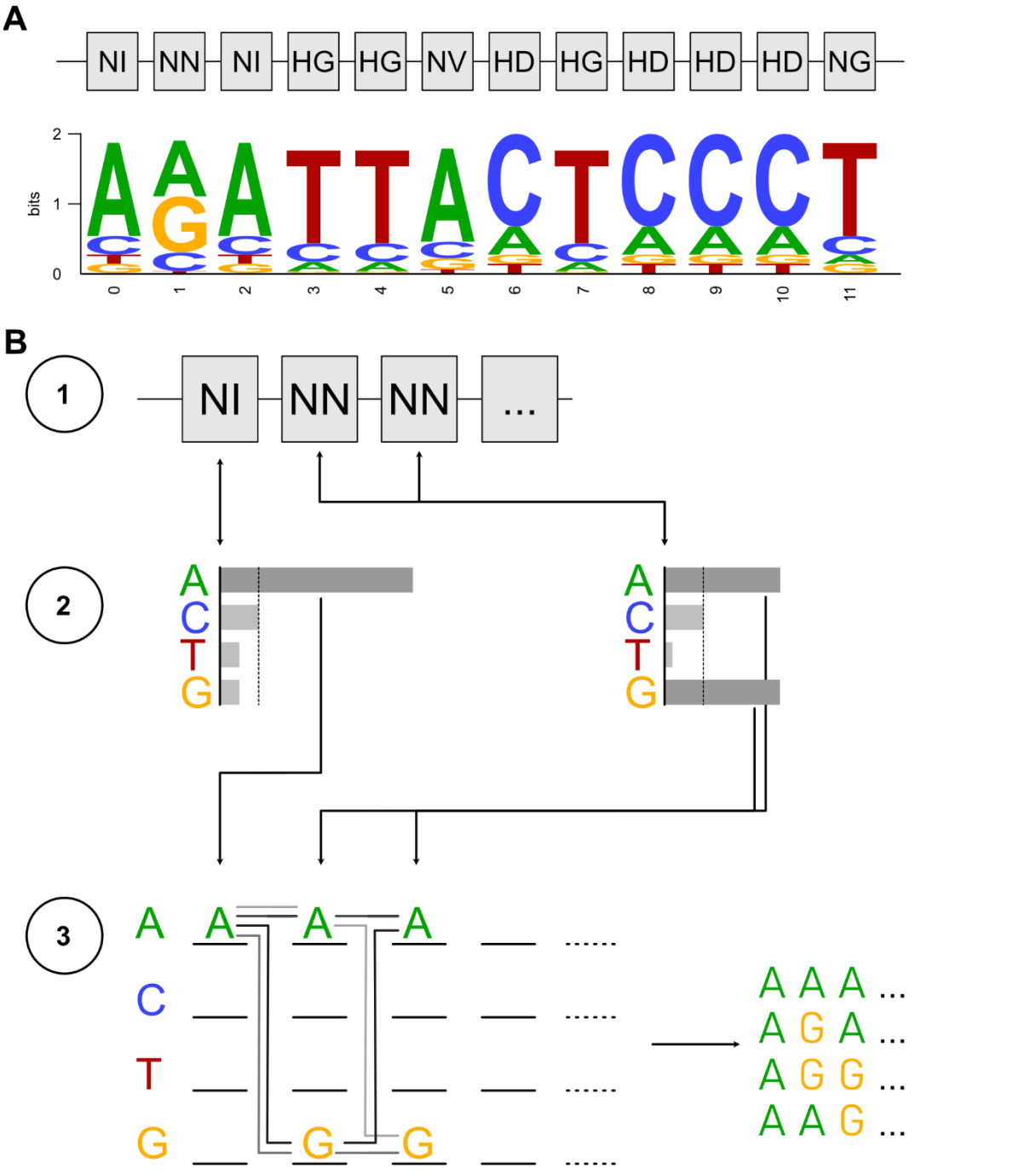

Figure 4.2. Variability of EBE sequences based on RVD array specificity. (A) RVD array with predicted binding motifs based on position weight matrix with 20 % specificity threshold. (B) Conceptual scheme for combinatorial script. RVD specificity is determined (1) and first entry of sequence is set (2). The second RVD has equal binding potentials for adenosine and guanine, the EBE sequence is amplified accordingly (3).

The proof-of-concept pegRNA template was not integrated

Literature search identified hexose uptake transporters as novel candidate executor R genes. Sugar retrieval via AtSTP13 enhances resistance in A. thaliana against *Pseudomonas spp.* and suggests that reduction of available sugar at the infection site can restrict pathogen proliferation. In the rice- Xoo pathosystem, executor hexose uptake transporter R genes would facilitate the retrieval of apoplasm-available carbon sources into the cytoplasm and be induced upon Xoo invasion. A homology analysis of AtSTP13 against the proteome of *Orzya sativa* Japonica Group (NCBI ID: 39947) revealed OsMST4 as AtSTP13 homologue (Query Cover = 98 %, E-value = 0). To experimentally confirm whether *OsMST4* functions as an executor R gene upon induction, I attempted to integrate the EBE of AvrXa7 into the promoter of *OsMST4*. However, contrary to expectations, genotyping of 48 T_0 plants revealed either (Type I) no discrepancies to the wild type sequence recovered from plants inoculated with *A. tumefaciens* lacking T-DNA or (Type II) a 23 base pair deletion at the 3' end of the nick RNA binding element (Fig 4.3).

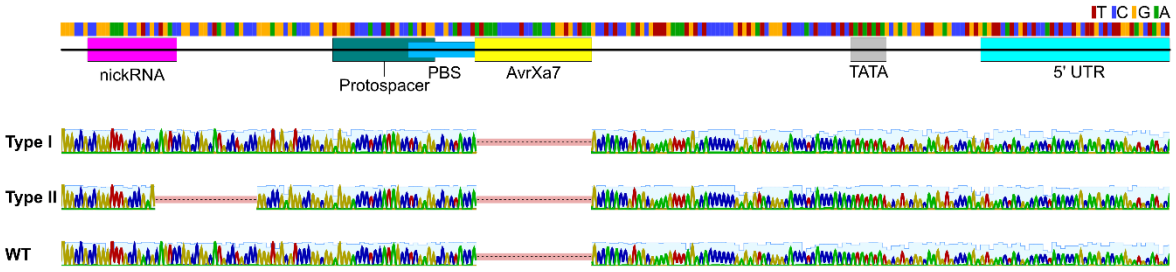

Figure 4.4. Alignment of attempted OsMST4 edit with genotyped sequences. OsMST4 edit with EBE_{AvrXa7} in silico as reference sequence for amplified sequences from T_0 transformants. Sequences were categorized in Type I and Type II edits. Type I sequences show no alteration to tissue cultured regenerated wild type plants. Type II plants display unintended edit at 3' of nick oligo binding site.

Discussion

RVD diversity of TALes differs between Asian and African Xoo populations

The observed differences in RVD composition and TAL effector repertoires between African and Asian Xoo strains highlight the wide range of potentially targeted EBEs. The apparent greater diversity in the Asian Xoo population may be influenced by a sampling bias, as the African sample set was limited in size and collected over a shorter timeframe (Loo *et al.*, 2025). Nevertheless, the total number of TALes appear to be reduced in African strains (9 TALes) compared to Asian Xoo strains (11-18 TALes) and *Xanthomonas oryzae* pv. *oryzicola* (*Xoc*, 24-28 TALes) (Grau *et al.*, 2016;

Tran *et al.*, 2018; Wilkins *et al.*, 2015). Previous studies indicate that African Xoo strains share greater genetic similarity with *Xanthomonas oryzae* pv. *oryzicola* (Xoc) than with Asian Xoo strains (Diallo *et al.*, 2023; Schepler-Luu *et al.*, 2023). Compared with other *Xanthomonadales,* Xoc does not carry inverted repeat sequences at the flanks of TAL effector genes (Ferreira *et al.*, 2015). Potentially, the inability to form mobile cassettes is the same for African and could be a reason for the reduced number of recombination events and number of TALes within African Xoo genomes. African Xoo has been exposed to a different R gene suite by their host plants compared to Asian Xoo. Likely, the spatial separation and independent evolution of African and Asian Xoo strains has benefitted their genomic and TAL effector divergence.

Combinatorial programming revealed vast number of putative EBEs

TAL effectors with divergent RVD sequences have been observed to bind the same EBE as in case of $TalB_{BAI3}$ and $TalB_{MAI1.}$ Despite six RVD polymorphisms, both Tal effectors recognize the same EBE within the promotor of *OsERF#123*, which highlights the broad range of TAL effector binding capabilities. Therefore, it is important to consider the nucleotide tolerance in RVD mediated EBE recognition. Another example involves $TalF_{BAI3}$ and $TalF_{MAI1,}$ where a polymorphism in five RVDs, including a change from HD (specific for cytosine) to NN (which is considered to tolerate adenine and guanine) disrupts EBE binding by $TalF_{BAI3}$ (Tran et al., 2018).

A single Tal effector has been also shown to dually target two EBEs. Tal6b/AvrXa27A binds to EBEs in the promoters of both *OsSWEET11a* and *OsXa27A* (Xu *et al.*, 2023). Tal6b/AvrXa27A, carried by multiple Asian *Xoo* strains, differs from AvrXa27 at the 12th RVD position, where N* (a RVD with broad nucleotide tolerance) is replaced by NG (specificity to thymine). Contrary to predictions based on RVD binding tolerances, the loss of N***** appears to enhance binding to *OsSWEET11a* (Xu *et al.*, 2023)**.** The replacement of a broadly tolerant RVD with a more specific thymine-binding RVD (NG) may have conferred an evolutionary advantage, potentially allowing *Xoo* strains to escape recognition by the executor resistance gene *OsXa27***.** MAI1 also exhibits dual targeting of one TAL effector, $TalB_{MAI1}$, to two EBEs, *OsTFX1* and *OsERF#123* (Tran *et al.*, 2018).

A compelling example that illustrates the versatility of RVD binding is the ability of two phylogenetically distinct TAL effectors to recognize the same EBE. The Asian *Xoo* strain PXO99^{A} and the African *Xoo* strain MAI1 carry PthXo6$_{PXO99^{A}}$ and TalB$_{MAI1}$, respectively, that both target the same EBE within *OsTFX1* (Tran et al., 2018). *OsTFX1* encodes a basic leucine zipper transcription factor and has been identified as susceptibility gene targeted by Asian *Xoo* (Sugio *et al.*, 2007). Another example for the functional convergence of TALes from phylogenetically distant *Xanthomonas* is the EBE within the promotor of M*eSWEET10a* by the Tal effectors Tal23 from vascular Xam668 and Tal20 from non-vascular *Xanthomonas* species targeting cassava (Zárate-Chaves *et al.*, 2023).

Although computational predictions provide valuable insights, experimental validation remains essential. A combinatorial approach for identifying a shared EBE among Asian and African *Xoo* strains showed potential, but a more efficient alignment strategy is required. One possible solution involves clustering EBEs based on similarities in their initial nucleotide sequences. Instead of aligning individual EBEs, aligning pre-clusteredEBE groups could improve both the speed and accuracy of predictive analyses.

Designer executor R genes could be engineered with Prime Editing

Varietal resistance appears to be the most effective way to control Bacterial Blight (Jiang et al., 2020). Since the identification of the first resistance gene, *OsXa1*, in 1967, over 45 resistance genes have been mapped or characterized (Sakaguchi, 1967; Yoshimura *et al.*, 1998). Prime Editing strikes as a promising technology to engineer novel candidate R genes; however, the integration of the EBE$_{AvrXa7}$ in this study was not successful. Several factors may have influenced the efficiency of Prime Editing, including biological, technical, and component delivery-related constraints. Insufficient expression levels in target cells, cellular toxicity, and inadequate delivery of Prime Editing components can hinder the editing process. Suboptimal nuclear localization and inefficiencies in the pegRNA´s secondary structure, primer binding site length, or the reverse transcriptase template sequence may also contribute to reduced editing success. Additionally, degradation of pegRNA, chromatin accessibility limitations, inefficient nicking of the non-edited strand, and competition between DNA repair pathways may further impede precise editing. If competing DNA repair pathways were active, unintended insertions or deletions might have been expected.

The cell cycle phase also plays a critical role in prime editing efficiency, as homologous recombination, the preferred repair pathway for precise edits but less prevalent compared to NHEJ, is most active during the S and G_2 phases (Choi *et al.*, 2020). Synchronization of cells to S and G_2 phases, particularly by arrest at the G_1/S boundary, has been reported to improve Prime Editing efficiency by up to 30% (Schene *et al.*, 2022). Low transcriptional activity at the target site can reduce editing efficiency but strategies such as CRISPR-mediated transcriptional activation may enhance outcomes by increasing chromatin accessibility (Xu et al., 2024). Additional challenges include the occurrence of unintended insertions or deletions; off-target effects from pegRNA or nicking guide RNA, and inefficient reverse transcriptase activity could be addressed by improved pegRNA engineering (Nelson *et al.*, 2022).

Despite the challenges addressed, the prime editing components used in this study have generated successful edits in other studies (Gupta et al., 2023; Jiang et al., 2022; Jiang et al., 2020).

Conclusion

This study aimed to engineer novel executor R genes using prime editing by integration of EBEs into promoters of potential R genes in rice. The findings provide insights into the sequence specificity of TAL effectors and the potential for cross-strain EBEs to enhance broad-spectrum resistance against Xoo. Computational analysis revealed extensive variation in RVDs of African and Asian Xoo strains, yet, identified potential shared EBEs. Thus, the theoretical feasibility of designing resistance genes with broader specificity could be shown.

Despite the capability of prime editing, the integration of EBE_{AvrXa7} into the promoter of the candidate executor R gene *OsMST4* was not successful, thereby highlighting challenges in editing design and efficiency. Several factors likely contributed to this outcome, including insufficient expression of prime editing components, limitations in nuclear localization, suboptimal pegRNA secondary structure, inefficient primer-binding site design, and degradation of pegRNA.

Although the integration of the proof-of-concept EBE was unsuccessful in this study, prime editing remains a promising tool for resistance gene engineering. The combinatorial computational approach to identify shared EBEs between African and

Asian Xoo strains provides a foundation for future efforts in engineering broad-spectrum resistance. By refining prime editing strategies and addressing current technical limitations, the development of designer executor R genes remains a viable strategy for durable resistance against bacterial blight in rice.

References

Becker, S., Mücke, S., Grau, J. and Boch, J. (2022) Flexible TALEs for an expanded use in gene activation, virulence and scaffold engineering. *Nucleic Acids Res.*, **50**, 2387–2400.

Bezrutczyk, M., Yang, J., Eom, J.-S., et al. (2018) Sugar flux and signaling in plant-microbe interactions. *Plant J. Cell Mol. Biol.*, **93**, 675–685.

Boch, J., Scholze, H., Schornack, S., Landgraf, A., Hahn, S., Kay, S., Lahaye, T., Nickstadt, A. and Bonas, U. (2009) Breaking the code of DNA binding specificity of TAL-type III effectors. *Science*, **326**, 1509–1512.

Cermak, T., Doyle, E.L., Christian, M., et al. (2011) Efficient design and assembly of custom TALEN and other TAL effector-based constructs for DNA targeting. *Nucleic Acids Res.*, **39**, e82.

Chen, L.Q., Hou, B.H., Lalonde, S., et al. (2010) Sugar transporters for intercellular exchange and nutrition of pathogens. *Nature*, **468**, 527–532.

Choi, E.-H., Yoon, S., Koh, Y.E., Seo, Y.-J. and Kim, K.P. (2020) Maintenance of genome integrity and active homologous recombination in embryonic stem cells. *Exp. Mol. Med.*, **52**, 1220–1229.

Christian, M.L., Demorest, Z.L., Starker, C.G., et al. (2012) Targeting G with TAL effectors: A comparison of activities of TALENs constructed with NN and NK repeat variable di-residues. *PLoS ONE*, **7**, e45383.

Cong, L., Zhou, R., Kuo, Y., Cunniff, M. and Zhang, F. (2012) Comprehensive Interrogation of Natural TALE DNA Binding Modules and Transcriptional Repressor Domains. *Nat. Commun.*, **3**, 968.

Deng, D., Yan, C., Pan, X., Mahfouz, M., Wang, J., Zhu, J.-K., Shi, Y. and Yan, N. (2012) Structural basis for sequence-specific recognition of DNA by TAL effectors. *Science*, **335**, 720–723.

Diallo, A., Wonni, I., Sicard, A., Blondin, L., Gagnevin, L., Vernière, C., Szurek, B. and Hutin, M. (2023) Genetic structure and TALome analysis highlight a high level of diversity in Burkinabe *Xanthomonas oryzae* pv. *oryzae* populations. *Rice N. Y. N*, **16**, 33.

Eom, J.-S., Luo, D., Atienza-Grande, G., et al. (2019) Diagnostic kit for rice blight resistance. *Nat. Biotechnol.*, **37**, 1372–1379.

Felix, G., Duran, J.D., Volko, S. and Boller, T. (1999) Plants have a sensitive perception system for the most conserved domain of bacterial flagellin. *Plant J.*, **18**, 265–276.

Ferreira, R.M., Oliveira, A.C.P. de, Moreira, L.M., et al. (2015) A TALE of transposition: Tn3-like transposons play a major role in the spread of pathogenicity determinants of *Xanthomonas citri* and other *Xanthomonads*. *mBio*, **6**, e02505-02514.

Grau, J., Reschke, M., Erkes, A., Streubel, J., Morgan, R.D., Wilson, G.G., Koebnik, R. and Boch, J. (2016) AnnoTALE: bioinformatics tools for identification, annotation and nomenclature of TALEs from Xanthomonas genomic sequences. *Sci. Rep.*, **6**, 21077.

Gupta, A., Liu, B., Raza, S., Chen, Q.-J. and Yang, B. (2024) Modularly assembled multiplex prime editors for simultaneous editing of agronomically important genes in rice. *Plant Commun.*, **5**, 100741.

Huai, B., Yang, Q., Wei, X., Pan, Q., Kang, Z. and Liu, J. (2020) TaSTP13 contributes to wheat susceptibility to stripe rust possibly by increasing cytoplasmic hexose concentration. *BMC Plant Biol.*, **20**, 49.

Ji, C., Ji, Z., Liu, B., Cheng, H., Liu, H., Liu, S., Yang, B. and Chen, G. (2020) *Xa1* allelic R genes activate rice blight resistance suppressed by interfering TAL effectors. *Plant Commun.*, **1**, 100087.

Jiang, N., Yan, J., Liang, Y., Shi, Y., He, Z., Wu, Y., Zeng, Q., Liu, X. and Peng, J. (2020) Resistance genes and their interactions with bacterial blight/leaf streak pathogens (*Xanthomonas oryzae*) in rice (*Oryza sativa L.*)—an updated review. *Rice*, **13**, 3.

Jiang, Y., Chai, Y., Qiao, D., et al. (2022) Optimized prime editing efficiently generates glyphosate-resistant rice plants carrying homozygous TAP-IVS mutation in EPSPS. *Mol. Plant*, **15**, 1646–1649.

Jones, J.D.G. and Dangl, J.L. (2006) The plant immune system. *Nature*, **444**, 323–329.

Lemonnier, P., Gaillard, C., Veillet, F., Verbeke, J., Lemoine, R., Coutos-Thévenot, P. and La Camera, S. (2014) Expression of *Arabidopsis* sugar transport protein STP13 differentially affects glucose transport activity and basal resistance to *Botrytis cinerea*. *Plant Mol. Biol.*, **85**, 473–484.

Loo, E.P.I., Szurek, B., Arra, Y., Stiebner, M., Buchholzer, M., Devanna, B.N., Vera Cruz, C.M. and Frommer, W.B. (2025) Closing the information gap between the field and scientific literature for improved disease management, with a focus on rice and bacterial blight. *MPMI*, **38**, 134–141.

Meyers, B.C., Kaushik, S. and Nandety, R.S. (2005) Evolving disease resistance genes. *Curr. Opin. Plant Biol.*, **8**, 129–134.

Moore, J.W., Herrera-Foessel, S., Lan, C., et al. (2015) A recently evolved hexose transporter variant confers resistance to multiple pathogens in wheat. *Nat. Genet.*, **47**, 1494–1498.

Nakagami, S., Wang, Z., Han, X. and Tsuda, K. (2024) Regulation of bacterial growth and behavior by host plant. *Annu. Rev. Phytopathol.*, **62**, 69–96.

Nelson, J.W., Randolph, P.B., Shen, S.P., et al. (2022) Engineered pegRNAs improve prime editing efficiency. *Nat. Biotechnol.*, **40**, 402–410.

Nowack, M.K., Holmes, D.R. and Lahaye, T. (2022) TALE-induced cell death executors: an origin outside immunity? *Trends Plant Sci.*, **27**, 536–548.

Oliva, R., Ji, C., Atienza-Grande, G., et al. (2019) Broad-spectrum resistance to bacterial blight in rice using genome editing. *Nat. Biotechnol.*, **37**, 1344–1350.

Pérez-Quintero, A.L., Lamy, L., Gordon, J., Escalon, A., Cunnac, S., Szurek, B. and Gagnevin, L. (2015) QueTAL: a suite of tools to classify and compare TAL effectors functionally and phylogenetically. *Front. Plant Sci.*, **6**, 545.

Richter, A., Streubel, J., Blücher, C., Szurek, B., Reschke, M., Grau, J. and Boch, J. (2014) A TAL effector repeat architecture for frameshift binding. *Nat. Commun.*, **5**, 3447.

Römer, P., Recht, S., Strauß, T., Elsaesser, J., Schornack, S., Boch, J., Wang, S. and Lahaye, T. (2010) Promoter elements of rice susceptibility genes are bound and activated by specific TAL effectors from the bacterial blight pathogen, *Xanthomonas oryzae* pv. *oryzae*. *New Phytol.*, **187**, 1048–1057.

Sakaguchi, S. (1967) Linkage studies on the resistance to bacterial leaf blight, *Xanthomonas oryzae* (Uzeda et Ishiyama) Dowson, in rice. *Bull. Natn. Inst. Agric. Sci. Ser*, **16**.

Sanjana, N.E., Cong, L., Zhou, Y., Cunniff, M.M., Feng, G. and Zhang, F. (2012) A transcription activator-like effector toolbox for genome engineering. *Nat. Protoc.*, **7**, 171–192.

Schene, I.F., Joore, I.P., Baijens, J.H.L., et al. (2022) Mutation-specific reporter for optimization and enrichment of prime editing. *Nat. Commun.*, **13**, 1028.

Schepler-Luu, V., Sciallano, C., Stiebner, M., et al. (2023) Genome editing of an African elite rice variety confers resistance against endemic and emerging *Xanthomonas oryzae* pv. *oryzae* strains. *eLife*, **12**, e84864.

Stella, S., Molina, R., Yefimenko, I., Prieto, J., Silva, G., Bertonati, C., Juillerat, A., Duchateau, P. and Montoya, G. (2013) Structure of the AvrBs3–DNA complex provides new insights into the initial thymine-recognition mechanism. *Acta Crystallogr. D Biol. Crystallogr.*, **69**, 1707–1716.

Streubel, J., Blücher, C., Landgraf, A. and Boch, J. (2012) TAL effector RVD specificities and efficiencies. *Nat. Biotechnol.*, **30**, 593–595.

Sugio, A., Yang, B., Zhu, T. and White, F.F. (2007) Two type III effector genes of *Xanthomonas oryzae* pv. *oryzae* control the induction of the host genes *OsTFIIAγ1* and *OsTFX1* during bacterial blight of rice. *Proc. Natl. Acad. Sci.*, **104**, 10720–10725.

Tian, D., Wang, J., Zeng, X., et al. (2014) The rice TAL Effector–dependent resistance protein XA10 triggers cell death and calcium depletion in the endoplasmic reticulum. *Plant Cell*, **26**, 497–515.

Tran, T.T., Pérez-Quintero, A.L., Wonni, I., et al. (2018) Functional analysis of African *Xanthomonas oryzae* pv. *oryzae* TALomes reveals a new susceptibility gene in bacterial leaf blight of rice. *PLOS Pathog.*, **14**, e1007092.

Wang, C., Zhang, X., Fan, Y., et al. (2015) XA23 Is an executor R protein and confers broad-spectrum disease resistance in rice. *Mol. Plant*, **8**, 290–302.

Wilkins, K.E., Booher, N.J., Wang, L. and Bogdanove, A.J. (2015) TAL effectors and activation of predicted host targets distinguish Asian from African strains of the rice pathogen *Xanthomonas oryzae* pv. *oryzicola* while strict conservation suggests universal importance of five TAL effectors. *Front. Plant Sci.*, **6**, 536.

Wu, L., Goh, M.L., Sreekala, C. and Yin, Z. (2008) XA27 depends on an amino-terminal signal-anchor-like sequence to localize to the apoplast for resistance to *Xanthomonas oryzae* pv. *oryzae*. *Plant Physiol.*, **148**, 1497–1509.

Xu, W., Zhang, S., Qin, H. and Yao, K. (2024) From bench to bedside: cutting-edge applications of base editing and prime editing in precision medicine. *J. Transl. Med.*, **22**, 1133.

Xu, Z., Xu, X., Li, Y., et al. (2023) Tal6b/AvrXa27A, a hidden TALE targeting the susceptibility gene *OsSWEET11a* and the resistance gene *Xa27* in rice. *Plant Commun.*, **5**, 100721.

Yamada, K. and Mine, A. (2024) Sugar coordinates plant defense signaling. *Sci. Adv.*, **10**, eadk4131.

Yamada, K., Saijo, Y., Nakagami, H. and Takano, Y. (2016) Regulation of sugar transporter activity for antibacterial defense in *Arabidopsis*. *Science*, **354**, 1427–1430.

Yang, J., Zhang, Y., Yuan, P., et al. (2014) Complete decoding of TAL effectors for DNA recognition. *Cell Res.*, **24**, 628–631.

Yoshimura, S., Yamanouchi, U., Katayose, Y., et al. (1998) Expression of *Xa1*, a bacterial blight-resistance gene in rice, is induced by bacterial inoculation. *Proc. Natl. Acad. Sci. U. S. A.*, **95**, 1663–1668.

Zárate-Chaves, C.A., Audran, C., Medina Culma, C.A., et al. (2023) CRISPRi in *Xanthomonas* demonstrates functional convergence of transcription activator-like effectors in two divergent pathogens. *New Phytol.*, **238**, 1593–1604.

Zhang, J., Yin, Z. and White, F. (2015) TAL effectors and the executor R genes. *Front. Plant Sci.*, **6**, 641.

Supplementary Material

Table S4.1. Differences of RVDs within PXO99APthXo1 and PthXo1 assembled from cloning kit. Deviations are indicated in bold and italic.

RVDs PXO99$^{A}_{PthXo1}$	**RVDs PthXo1 cloning kit (Cermak *et al.*, 2011)**
NN	NN
HD	HD
NI	NI
HG	NG
HD	HD
NG	NG
N*	HD
HD	HD
NI	NI
NG	NG
NG	NG
NI	NI
HD	HD
NG	NG
NI	NI
NI	NI
NI	NI
NI	NI
N*	HD
NS	NI
N*	HD

Table S4.2. RVD specificities based on position weight matrix for deviating RVDs between PXO99$^{A}_{PthXo1}$ and PthXo1 assembled from cloning kit. Weight matrix values extracted from AnnoTale (Grau *et al.*, 2016).

RVD position weights

RVD	A	C	G	T
HG	5	10	1	50
NG	5	10	5	50

N*	1	4	1	4
HD	15	50	5	5
NI	50	10	5	5
NS	50	20	50	20

Table S4.3. Oligo sequences for assembly of prime editing constructs.

Oligos	**Sequence (5' – 3')**
Nick forward	gataCCGGGAAAGCCGTCGCTGAC
Nick reverse	aaacGTCAGCGACGGCTTTCCCGG
Spacer forward	tgcaTGGGTCCCACCTATGCCACGTGG
Spacer reverse	aaacCCACGTGGCATAGGTGGGACCCA
Prime editing guide forward	gtgcAGGATGCGGCCACGTTTAGCACCTGGTTGGAGGGGGTTTATATAGGCATAGGTG
Prime editing guide reverse	cgcgCACCTATGCCTATATAAACCCCCTCCAACCAGGTGCTAAACGTGGCCGCATCCT

Figure S4.1. Script with code for R executed on "HILBERT" high performance computing platform at Heinrich-Heine University, Düsseldorf.

```
library(dplyr)
library(tidyr)
library(stringr)
DATA <- read.csv("RVDSeq.csv", sep = ";",
                 header = TRUE,
                 dec = ",", na.strings = "NA")

RVDspecs <- read.csv("RVD Specificity weight matrix.csv", sep = ",",
                     header = TRUE,
                     dec = ",", na.strings = "NA")

v<- c(letters[1:26], "A")
DATA_sep = DATA %>% separate (RVDseq, v, sep='-')
Data_frac <- DATA_sep %>%
  filter(Specie=='Xoo')
chunk <- 50
n <- nrow(Data_frac)
r <- rep(1:ceiling(n/chunk), each=chunk)[1:n]
DATA_split <- split(Data_frac,r)
file_names <- paste0("Total_seq_DF_", 1:ceiling(nrow(DATA[DATA_sep$Specie == "Xoo",]) / 50), ".csv")
for(z in 18:18){
DATA_subset = as.data.frame(DATA_split[z])
subClass = DATA_subset[1:nrow(DATA_subset),1:28]
RVD_combo_DF = subClass
isLowerCase = 0
#XooTalA <- subClass[which(subClass$Specie == "Xoo")]
#Part 1 - transferring RVDs to nulceotide bases based on Position-Weight-Matrix
for(i in 2:27) {
```

```
for (j in 1:nrow(subClass)) {
  baseVector = c()
  currentBase = ""
  isACGT=0
  for(k in 2:5){ # 5: A, C, T, G, empty ( )
    testRVD <- which(RVDspecs$X == subClass[j,i])
    currentBaseValue = RVDspecs[testRVD,k]
    totalBaseValues = sum(unlist(RVDspecs[testRVD,2:5]))
    if(totalBaseValues!=0){ #Normal case: RVD is listed in Position-Weight Matrix
      if(currentBaseValue/totalBaseValues>0.19){ #Threshold, only when relative weight in Position-Weight-Matrix is larger than 19%, the base is considered to be bound by the respective RVD
        currentBase = colnames(RVDspecs)[k]
        baseVector = append(baseVector,currentBase)
      }
    } else if(is.na(subClass[j,i])){#Case: RVD is NA (short TALE)
      currentBaseValue=0
      currentBase = ""
    } else if(grepl("\\*", subClass[j,i]) || subClass[j,i]=="NA"){#Case: RVD contains * but is not part if the Position-Weight-Matrix
      baseVectorcombined="ACGT"
      baseVector=""
      isACGT=1
    } else{
      testRVD <- which(RVDspecs$X == toupper(subClass[j,i]))#convert the lower case RVDs into upper case RVDs in order to match Position-Weight-Matrix PLUS add space as lower case RVDs can
      isLowerCase=1#also loop-out and "skip" a base
      currentBaseValue = RVDspecs[testRVD,k]
      totalBaseValues = sum(unlist(RVDspecs[testRVD,2:5]))
      if(length(currentBaseValue/totalBaseValues)==0){
        stop(paste("Error in line ",j," and column ",i))
      }
      if(currentBaseValue/totalBaseValues>0.19){ #Threshold, only when relative weight in Position-Weight-Matrix is larger than 19%, the base is considered to be bound by the respective RVD
        currentBase = colnames(RVDspecs)[k]
        baseVector = append(baseVector,currentBase)
      }
    }
  }
  if(isLowerCase==1){
    baseVector = append(baseVector," ")
    isLowerCase=0
  }
  if(isACGT==0){
    baseVectorcombined = paste(baseVector, collapse='')
    RVD_combo_DF[j,i] = baseVectorcombined
  } else{
    RVD_combo_DF[j,i] = baseVectorcombined
    isACGT=0
  }
 }
}

#Part 2 - Generate all combinations of the Base sequences and put them in final data frame
RVD_base_list = list()
Total_seq_DF = data.frame()

#RVD_combo_DF2 <- RVD_combo_DF %>% drop_na() # RVDs without any NA values; 27 RVDs

RVD_combo_DF<- RVD_combo_DF %>% replace(is.na(.), "")

for (i in 1:nrow(subClass)){
 if(i==1){
  start_time <- Sys.time()
 }
 RVD_base_list = list()
 for (j in 2:28){
  if(RVD_combo_DF[i,j]!=""){ #
    RVD_base_list = append(RVD_base_list,strsplit(RVD_combo_DF[i,j],""))
  }
```

```
  }
  in_between_list = expand.grid(RVD_base_list)
  while(ncol(in_between_list)<28){
    in_between_list = cbind(in_between_list, empty_column=NA)
  }
  for(k in 1:27){
    cName <- paste0("Base_",k)
    names(in_between_list)[k] <- cName
  }
  names(in_between_list)[28] <- "Strain_Info"
  in_between_list$Strain_Info <- subClass[i,29]
  if(i == 17+1 || i == 32+1){
    Total_seq_DF = in_between_list
  } else{
    Total_seq_DF = rbind(Total_seq_DF, in_between_list)
  }

  #Progress message
  percProgress <- signif(100*i/nrow(RVD_combo_DF), digits=5)
  end_time <- Sys.time()
  timePassed <- end_time - start_time
  futureTime <- ceiling(((timePassed/i)*(nrow(subClass)-i))*(2^nrow(subClass)))
  messProgress <- paste0("Progress: ",percProgress,"%. Step ", i, " of", nrow(subClass), ". Estimated remaining time: "
                         ,futureTime," ",units(futureTime),". Total number of rows in Total_seq_DF: ",
                         format(nrow(Total_seq_DF), nsmall=1, big.mark=","))
  print(messProgress)
  if((i %% 10) == 0){
    sizeMessage <- paste0("Data size of final data frame:", format(as.numeric(object.size(Total_seq_DF)/1000000),
                                                                   nsmall=0, big.mark=","), " MB.")
    print(sizeMessage)
  }
  if(i == 17 || i == 32 || i == nrow(subClass)){
    file_name_18 <- paste0("Total_seq_DF_18_", i, ".csv")
    write.csv(Total_seq_DF, file_name_18)
    Total_seq_DF <- data.frame("")
    print("File printed.")
  }
}
#Write csv file
#write.csv(Total_seq_DF, file_names[z])
}
```

9 Ratiometric Matryoshka MSucMeter sensors for sucrose

Contributions

MSucMeter cassettes were designed by Mayuri Sadoine. Cloning of MSucMeter components into pRSETb was performed by Susanne Paradies. Yuuma Ishikawa provided valuable insights in experimental design and sensor purification.

Introduction

Genetically encoded biosensors are powerful tools for visualizing and quantifying dynamic biological processes in living cells with high spatial and temporal resolution. A common approach for ratiometric measurement of analytes is based on sensors that are capable of Förster-Resonance-Energy-Transfer (FRET). FRET sensors are based on two fluorescent proteins (FPs), one acting as donor and other as acceptor. When the donor and acceptor approach each other closely, the donor transfers energy from an excitation photon to the acceptor, which then emits fluorescence at a longer (red-shifted) wavelength. A typical FRET sensor design links both FPs covalently to a cassette. Upon analyte binding, the cassette undergoes a conformational change that moves the donor and acceptor into close proximity and enables FRET. Ratiometric data can be obtained by normalization the bound fraction of FRET sensors to the unbound and total fraction (Table S5.1):

$$R = \frac{I_{\text{Ex: Donor; Em: Acc}}}{\sqrt{I_{\text{Donor; Em: Donor}} \; x \; I_{\text{Ex: Acc; Em: Acc}}}}$$

FRET-based sensors require a dual excitation wavelength for ratiometric read-outs. Development of FRET-based sensors requires the cassette FPs to meet certain criteria. For example, the dipoles of donor and acceptor FP need to be oriented to each other and brought to 10 nm vicinity upon analyte binding. Therefore, the recognition elements must undergo an extensive Venus-trap like conformational change upon binding (Okumoto *et al.*, 2012).

Matryoshka technology provides a sophisticated platform for the development of new biosensors and overcomes the limitations of FRET-based sensors (Ast *et al.*, 2017). Dependent on the studied analyte, a suitable recognition element is bisected and its fragments are arranged at the N- and C-terminus of the Matryoshka cassette, respectively. The Matryoshka cassette features a reporter and a reference fluorescent protein (FP). Due to the circular permutation of the reporter FP, local conformational changes lead to the reconstitution of the FP and reporter emission changes depended on analyte binding (Ast *et al.*, 2017). Absorption and emission maxima of the reference FP exhibit a large Stokes shift (LSS). As a result of the LSS, the reporter and reference FP of Matryoshka sensors are excitable by a single excitation wavelength. Thus, Matryoshka allows to extract information about the analyte concentration normalized

to the internal reference FP control (Ast *et al.*, 2017; Ejike *et al.*, 2024) according to the equation:

$$R_{Matryoshka} = \frac{I_{Matryoshka\ Reporter}}{I_{Matryoshka\ Reference}}$$

Biosensors are minimal invasive tools to study temporal and spatial distribution of analytes. The *in vivo* application of genetically encoded biosensors renders difficult because the experiment itself poses disturbances to the studied process. The ability to monochromatically excite Matryoshka sensors minimizes the interference with the biological system. In contrast to sugar monomers like glucose and fructose, the glycosidic bond of sucrose prevents the anomeric carbons of the fructosyl and glucosyl groups to participate in a reducing reaction. Because of its non-reducing properties, sucrose is the primary carbon compound for long-distance transport in plants. In bacteria, sugar transporters of the SWEET family were identified to facilitate the transport of sucrose (Lee *et al.*, 2015; Xuan *et al.*, 2013).

The *thu* operon of *Enisfer melioti* (formerly *Sinorhizobium meliolti)* encodes for transport and utilization of α-glucosides (Ampomah *et al.*, 2013). Homology analysis revealed 81 % similarity of *Agrobacterium tumefaciens* binding protein ThuE (AtThuE) to *E. melioti* ThuE (EmThuE). Lager *et al.* (2006) developed a FRET-based sucrose sensor using *AtThuE* as recognition element. Tryptophan 283 of *AtThuE* was predicted to sterically hinder the fructosyl moiety of sucrose. Mutations of W283 successfully altered the affinity to sucrose and yielded FRET sucrose sensors with a wide detection range (Lager *et al.*, 2006; Sadoine *et al.*, 2021).

In this study, the affinities and signal-to-noise ratio of unpublished Matryoshka-based sucrose sensors, MSucMeters, were analyzed *in vitro*. Proof-of-concept validation was performed by *in vivo* experiments in *Escherichia coli* (*E. coli*).

Material and Methods

Design of MSucMeter

The Matryoshka cassette encompasses an eight mutation deviant of superfolder GFP, spGFP1-10 and *Av*GFP11 (hereafter spGFP; Ast et al., 2017; Cabantous et al., 2005). The circular permutation breakpoint was determined based on experiences from the

single FP calcium sensor GCAMP1 and maltose sensor MBP-cpGFP (Baird *et al.*, 1999; Marvin *et al.*, 2011; Nakai *et al.*, 2001; Tallini *et al.*, 2006). Number 1-146 and 147-237 of amino acids from spGFP N- and C-terminus were cloned with a GGT and GSS linker flanked to the *LSSmOrange*. *LSSmOrange* was replaced with *LSSmApple* as a consequence of the improved spectral separation and shorter maturation time of LSSmApple (Ejike *et al.*, 2024). Linker encoding for amino acids proline, alanine (PA) and asparagine, proline (NP) were introduced to link *cpspGFP* to the fragmented recognition element *AtThuE* (Keller *et al.*, 2021). The 1-335 and 336-403 amino acid fragments of *AtThuE* were cloned to the N and C terminus of the Matryoshka cassette, respectively: $ThuE_{1\text{-}335}$-PA-$cpspGFP_{147\text{-}237}$-GGT-LSSmApple-GSS-$cpspGFP_{1\text{-}146}$ -NP-$ThuE_{336\text{-}403}$. Affinity variants were generated by amino acid substitution of W283. Tryptophan was replaced with Alanine, Isoleucine or Cysteine. Additionally, for each W283 polymorphism, one cassette with an additional mutation of D192N was generated (Sadoine *et al.*, 2021). The D192N mutation was initially found in the *AtThuE* clone used for FLIPsuc generation; whether this substitution was due to natural variation or occurred during the initial cloning remains untested (Lager *et al.*, 2006; Sadoine *et al.*, 2021).

Expression of MSucMeter in E. coli and fluorometric analysis

Affinity variants of MSucMeter were expressed under the pRSETb protein expression vector system in *E. coli* strain BL21 (NEB: C2527I). For *in vitro* assays, biosensor protein was purified exploiting the interaction of the MSucMeter N-terminal polyhistidine tag (6x His) with nickel-nitrilotriacetic (Ni-NTA) columns (Sadoine *et al.*, 2020). For *in vivo* measurements, *E. coli* cells from main cultures at OD_{600} 0.5 were transferred to minimal media (Table S5.1) at OD_{600} 0.2 for 16 hours at 37°C. Quantitative measurements of emission intensity were performed with the fluorometric microplate reader SparkControl™ (Tecan AG). Excitation wavelength was set at 453-488 nm, absorption spectra were recorded with 30 flashes, 2 nm wavelength step size and 20 nm bandwidth from 510 nm to 700 nm. Absorption point measurements were taken using the same settings at 515 nm for cpsfGFP and 605 nm for LSSmApple. Analysis was performed in Excel (Microsoft Office) and RStudio (version R-4.3.3).

Results

MSucMeter variants report sucrose concentration *in vitro*

Two biological replicates of each purified MSucMeter affinity variant (W283A, W283A D192N and W182C) were tested for *in vitro* response to sucrose in a fluorometric titration assay (**Figure 5.1**). Across fluorescence emission scans, the level of fluorescence for the reference FP LSSmApple was comparably stable spanning approximately a range of 1,000 AU (corresponding to 10 % variation) for W283A and 5,000 AU (42 % variation) for W283A D192N and W283C.

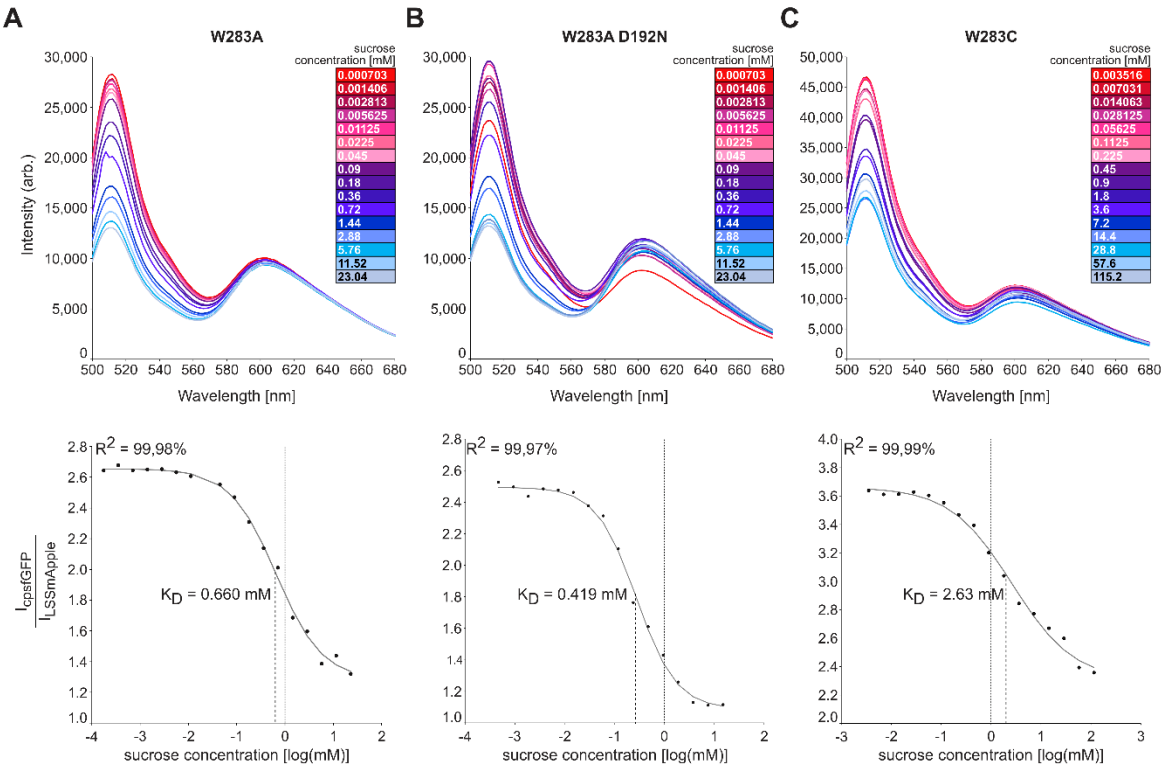

Figure 5.1 *In vitro* characterization of MSucMeter variants. MSucMeter constructs with LSSmApple reference and cpsfGFP reporter protein. Steady-state emission spectra (λ_{exc} 453 nm) of sensors titrated with sucrose and K_D values determined by ligand-dependent ratio change are shown for (A) W283A, (B) W283A D192N and (C) W283C.

The analyte concentration-dependent emission change of cpsfGFP at 515 nm indicated a dynamic response which covered approximately 20,000 AU (corresponding to 1.5x of baseline level) for the three tested variants. Sigmoidal curves ($f(x) = a + \frac{b-a}{1+10^{n*(\lg(x)-\lg(c))}}$) were fitted to $\frac{I_{cpsfGFP}}{I_{LSSmApple}}$ on a logarithmic scale to evaluate the K_D value. Calculated K_D were 0.66 mM for MSucMeter$_{W283A}$ (Figure **5.1**A), 0.419 mM for MSucMeter$_{W283A\ D192N}$ (Figure 5.1B) and 2.63 mM for MSucMeter$_{W283C}$ (**Figure 5.1C**).

MSucMeter$_{W283A}$ displayed limited response *in vivo* in starved E. coli cells

Genetically encoded biosensors harbor an immense potential to quantify levels of sugar pools and unravel oscillations *in vivo*. As proof-of-concept, *E. coli* with cytoplasmically expressed MSucMeter$_{W283A}$ were starved in minimal media and then exposed to extracellular sucrose. While the fluorescence scan revealed the presence and also response of MSucMeter$_{W283A}$ in *E. coli*, the dynamic range was smaller (5,000 AU; 0.5x of baseline) compared to the dynamic range of MSucMeter$_{W283A}$ *in vitro* (20,000 AU, 1.5x of baseline) (Figure 5.2). The sigmoidal fit for the logarithmically displayed ratio change indicated that MSucMeter$_{W283A}$ is not saturated *in vivo* at a maximal sucrose concentration of 23 mM in M9 media. Irrespective of the elapsed time between addition of sucrose and fluorescence measurement, MSucMeter$_{W283A}$ was not noted to be saturated (data of time-lapse experiments up to 16 hours not shown). Moreover, an increase of the extracellularly added sucrose to 115 mM did not result in MSucMeter$_{W283A}$ saturation (Figure 5.2). As a consequence, the criteria to determine the affinity of MSucMeter$_{W283A}$ *in vivo* were not met.

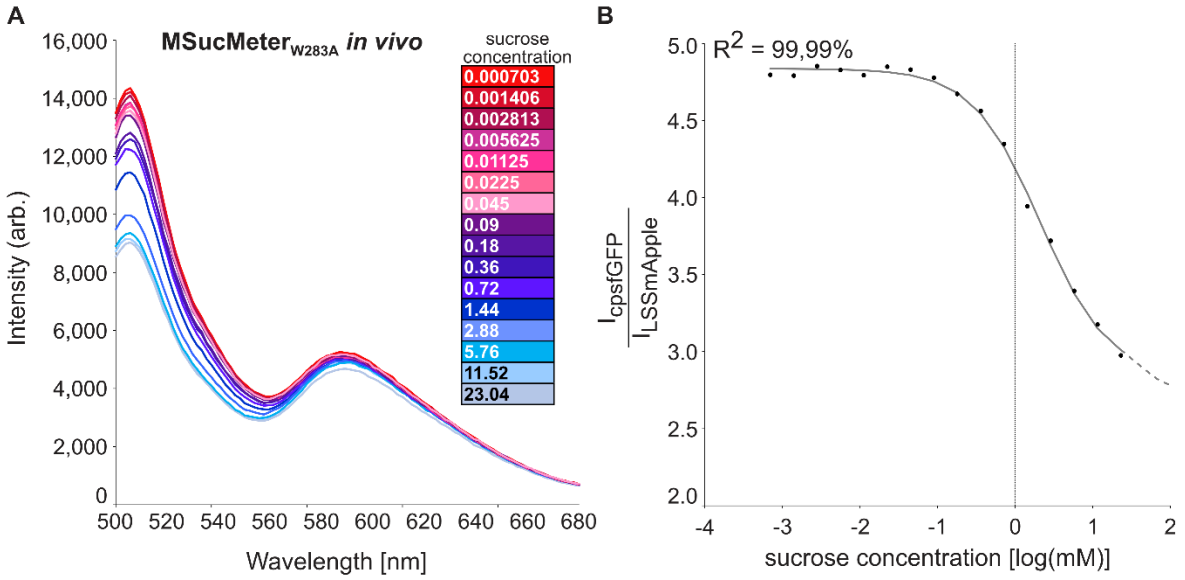

Figure 5.2 *In vivo* characterization of MSucMeter$_{W283A}$ in starved *E. coli* BL21 (C2527I). (A) Steady-state emission spectra (λ_{exc} 453 nm) of BL21 cells with MSucMeter$_{W283A}$. (B) Ligand-dependent ratio change indicates that MSucMeter$_{W283A}$ is not saturated by 23.04 mM externally added sucrose.

Discussion

MSucMeter affinity variants enable sucrose quantification with single excitation wavelength

Matryoshka based biosensors for sucrose were successfully developed. Mutations of W283 and D192 resulted in affinity variants with K_D values of 0.419 mM (W283A D192N), 0.66 mM (W283A) and 2.63 mM (W283C) (Figure 5.1). Additional variants of W283 coupled with D192N mutation (W283C D192N, W283I, W283I D192N, W283T, W283T D192N) were developed but not tested in this study. Compared to the FRET based sensors FLIPSuc$_{W283A}$ (K_D = 0.088 mM) and FLIPSuc$_{W283A\ D192N}$ (K_D = 0.065 mM), MSucMeter$_{W283A}$ and MSucMeter$_{W283A\ D192N}$ showed a higher K_D and thus a lower affinity to sucrose (Lager et al., 2006; Sadoine et al., 2021). The relative affinity shift ($\frac{K_{\mathrm{D\ FLIPSuc}}}{K_{\mathrm{D\ MSucMeter}}}$) between FLIPSuc$_{W283A}$ and MSucMeter$_{W283A}$ is 0.13 and 0.15 between FLIPSuc$_{W283A\ D192N}$ and MSucMeter$_{W283A\ D192N}$. Due to the comparable relative affinities across FLIPSuc and MSucMeter with identical mutations in the recognition element, it is likely that the overall design of MSucMeter contributes to a lower affinity for sucrose rather than the recognition element itself.

For the experimental application, a wide detection range across MSucMeter variants is crucial to match physiological concentrations, e.g. approximately 5 – 100 µM for *Xanthomonas campestris* pv. *campestris* (Blanvillain *et al.*, 2007). If the K_D can be matched to the actual sucrose levels within the studied organisms, sucrose level oscillation could be investigated. A repertoire of sensor variants with detection ranges spanning from the nanomolar to millimolar scale would be advantageous to match MSucMeter to physiological conditions *in vivo*. In comparison with FLIPSucs, MSucMeter exhibits a lower affinity to sucrose and the establishment of high affinity variants to complement a wide range of detection could be challenging. Nevertheless, the overall design of Matryoshka-based sensors is simpler than that of FRET-based sensors, which require precise dipole–dipole alignment and substantial Venus trap-like conformational changes. For *in vivo* experiments, the monochromatic excitation of MSucMeter imposes less stress on the biological system compared to the dual excitation wavelengths required for ratiometric measurements by FRET-based sensors.

Collectively, MSucMeter affinity variants assemble an excellent tool to discover sucrose pool levels *in vivo.*

Limitations of MSucMeter *in vivo* might be linked to sucrose uptake in *E. coli*

The inability of MSucMeter$_{W283A}$ to reach saturation *in vivo* may be attributed to limited sucrose uptake in *E. coli*. To reach the cytoplasmically localized MSucMeter, extracellular sucrose must traverse the outer and inner bacterial membranes. The outer membrane contains general porins such as OmpF and OmpC, which facilitate the passive diffusion of small hydrophilic molecules up to approximately 600 Da (Nikaido & Vaara, 1985). Given its molecular weight of approximately 342 Da, sucrose is expected to passively diffuse into the periplasm through OmpF and OmpC. However, the subsequent transport into the cytoplasm requires a specific permease, such as CscB or ScrA, to mediate inner membrane translocation. The absence of such transporters could limit intracellular accumulation.

The *E. coli* strain BL21 (DE3) originates from the phylogenetic group B. Group B is categorized into B1 and B2 (Daegelen *et al.*, 2009). B2 phylogroup members are associated with pathogenicity and distinct adaptions to host environments. BL21 (DE3) belongs to group B1 whose members are described as commensals lacking virulence genes (Lagerstrom et al., 2023). Nevertheless, partial genes of phylogroup B2 have been identified in the BL21 (DE3) chromosome (Andreishcheva et al., 2006). Two sucrose utilization pathways have been described in *E. coli.* The *csc* operon, that enables sucrose uptake and metabolism, is primarily found in phylogroup A and associates with slow growth on sucrose (Jahreis *et al.*, 2002). The *csc* operon lacks a porin for the outer membrane but encodes a sucrose permease (cscB) that facilitates transport from the periplasm to cytoplasm (Sahin-Tóth *et al.*, 2000). *E. coli* of phylogroup B1 and B2 have not been described to carry the *csc* operon.

In contrast, the *scr* operon facilitates more efficient sucrose utilization. The Scr pathway was originally described in *Enterobacteriaceae* and found to be present in some *E. coli* belonging to phylogroup B2 (Stephens *et al.*, 2024). A nucleotide blast of the *scr* operon (scrKYABR) to the BL21 (DE3) genome revealed 93 % identity and an E-value of 0 but a low query cover of 14 %. Although the low E-value highlights a low probability of a randomized hit, the low query cover indicates that only partial

sequences aligned. A nucleotide and protein blast of the inner membrane sucrose transporter *scrA* to BL21 (DE3) has not found any similarities.

The fluorescence scan of *E. coli* revealed the functional expression of MSucMeter$_{W283A}$ *in vivo* (Figure 5.2). However, MSucMeter$_{W283A}$ failed to saturate under increasing extracellular sucrose concentrations. Neither higher sucrose levels nor extended incubation times prior to measurement enhanced the cpsfGFP response.

If the sucrose transport into the cytoplasm would be solely passive, a delayed decrease of cpsfGFP upon sucrose binding would be expected as intracellular sucrose concentrations gradually rise, provided that rapid sucrose consumption does not mask the response and is undetected due to an insufficient acquisition frequency.

However, no such delayed response was observed, suggesting that either sucrose import occurs immediately upon addition or that other factors limit cytoplasmic accumulation.

Furthermore, no continued increase in cpsfGFP fluorescence (i.g. decrease of sucrose concentration) was detected following prolonged incubation, implying that the rate of sucrose consumption may match the import rate. It is important to note that the reversibility of MSucMeter has not been tested. Without this validation, interpretations regarding sucrose level dynamics remain limited.

An alternative explanation for the observed rapid response could be potential unspecific binding by the recognition element *ThuE*. FLIPsuc sensors have been reported to exhibit low-affinity binding to structurally similar sugars, including glucose, maltose and trehalose (Sadoine *et al.*, 2021). If MSucMeter shares this limitation, it may respond to other sugars present in the cytoplasm, confounding the sucrose-specific signal but would not explain the inability of MSucMeter saturation.

Conclusions and future considerations

In summary, MSucMeter provides a versatile, genetically encoded tool for ratiometric sucrose detection. While the *in vitro* performance of MSucMeter variants supports their utility for sucrose quantification across a broad detection range, *in vivo* application in *E. coli* did not result in sensor saturation. To resolve the uncertainty surrounding the limitation of saturation, *in vivo* validation should use an organism with the capacity for

sucrose import and metabolism, such as *Xanthomonas oryzae* pv. *oryzae*. In parallel, tests should assess MSucMeter specificity toward structurally related sugars *in vitro* to test selectivity for sucrose. It is also essential to test the reversibility of MSucMeter to determine its suitability for real-time monitoring of sucrose level changes within living systems. The suggested follow-up experiments would help to verify MSucMeter's functionality and inform its application in more complex biological systems, such as plant–microbe interactions

References

Ampomah, O.Y., Avetisyan, A., Hansen, E., Svenson, J., Huser, T., Jensen, J.B. and Bhuvaneswari, T.V. (2013) The thuEFGKAB operon of *Rhizobia* and *Agrobacterium tumefaciens* codes for transport of trehalose, maltitol, and isomers of sucrose and their assimilation through the formation of their 3-keto derivatives. *J. Bacteriol.*, **195**, 3797–3807.

Andreishcheva, E.N. and Vann, W.F. (2006) *Escherichia coli* BL21(DE3) chromosome contains a group II capsular gene cluster. *Gene*, **384**, 113–119.

Ast, C., Foret, J., Oltrogge, L.M., De Michele, R., Kleist, T.J., Ho, C.-H. and Frommer, W.B. (2017) Ratiometric Matryoshka biosensors from a nested cassette of green- and orange-emitting fluorescent proteins. *Nat. Commun.*, **8**, 431.

Baird, G.S., Zacharias, D.A. and Tsien, R.Y. (1999) Circular permutation and receptor insertion within green fluorescent proteins. *Proc. Natl. Acad. Sci. U. S. A.*, **96**, 11241–11246.

Blanvillain, S., Meyer, D., Boulanger, A., Lautier, M., Guynet, C., Denancé, N., Vasse, J., Lauber, E. and Arlat, M. (2007) Plant carbohydrate scavenging through TonB-dependent receptors: A feature shared by phytopathogenic and aquatic bacteria. *PLOS ONE*, **2**, e224.

Cabantous, S., Terwilliger, T.C. and Waldo, G.S. (2005) Protein tagging and detection with engineered self-assembling fragments of green fluorescent protein. *Nat. Biotechnol.*, **23**, 102–107.

Daegelen, P., Studier, F.W., Lenski, R.E., Cure, S. and Kim, J.F. (2009) Tracing ancestors and relatives of *Escherichia coli* B, and the derivation of B strains REL606 and BL21(DE3). *J. Mol. Biol.*, **394**, 634–643.

Ejike, J.O., Sadoine, M., Shen, Y., et al. (2024) A monochromatically excitable green–red dual-fluorophore fusion incorporating a new large Stokes shift fluorescent protein. *Biochemistry*, **63**, 171–180.

Jahreis, K., Bentler, L., Bockmann, J., Hans, S., Meyer, A., Siepelmeyer, J. and Lengeler, J.W. (2002) Adaptation of sucrose metabolism in the *Escherichia coli* wild-type strain EC3132†. *J. Bacteriol.*, **184**, 5307–5316.

Keller, J.P., Marvin, J.S., Lacin, H., et al. (2021) *In vivo* glucose imaging in multiple model organisms with an engineered single-wavelength sensor. *Cell Rep.*, **35**, 109284.

Lager, I., Looger, L.L., Hilpert, M., Lalonde, S. and Frommer, W.B. (2006) Conversion of a putative *Agrobacterium* sugar-binding protein into a FRET sensor with high selectivity for sucrose. *J. Biol. Chem.*, **281**, 30875–30883.

Lagerstrom, K.M. and Hadly, E.A. Under-appreciated phylogroup diversity of *Escherichia coli* within and between animals at the urban-wildland interface. *Appl. Environ. Microbiol.*, **89**, e00142-23.

Lee, Y., Nishizawa, T., Yamashita, K., Ishitani, R. and Nureki, O. (2015) Structural basis for the facilitative diffusion mechanism by SemiSWEET transporter. *Nat. Commun.*, **6**, 6112.

Marvin, J.S., Schreiter, E.R., Echevarría, I.M. and Looger, L.L. (2011) A genetically encoded, high-signal-to-noise maltose sensor. *Proteins Struct. Funct. Bioinforma.*, **79**, 3025–3036.

Nakai, J., Ohkura, M. and Imoto, K. (2001) A high signal-to-noise Ca2+ probe composed of a single green fluorescent protein. *Nat. Biotechnol.*, **19**, 137–141.

Okumoto, S., Jones, A. and Frommer, W.B. (2012) Quantitative imaging with fluorescent biosensors. *Annu. Rev. Plant Biol.*, **63**, 663–706.

Sadoine, M., Castro-Rodríguez, V., Poloczek, T., Javot, H., Sunal, E., Wudick, M. and Frommer, W. (2020) Affinity purification of GO-Matryoshka biosensors from *E. coli* for quantitative ratiometric fluorescence analyses. *BIO-Protoc.*, **10**.

Sadoine, M., Reger, M., Wong, K.M. and Frommer, W.B. (2021) Affinity Series of Genetically Encoded Förster Resonance Energy-Transfer Sensors for Sucrose. *ACS Sens.*, **6**, 1779–1784.

Sahin-Tóth, M., Frillingos, S., Lawrence, M.C. and Kaback, H.R. (2000) The sucrose permease of *Escherichia coli*: functional significance of cysteine residues and properties of a cysteine-less transporter. *Biochemistry*, **39**, 6164–6169.

Stephens, C., Martinez, M., Leonardi, V., Jaing, J. and Miller, A. (2024) The Scr and Csc pathways for sucrose utilization co-exist in *E. coli*, but only the Scr pathway is widespread in other *Enterobacteriaceae*. *Front. Microbiol.*, **15**, 1409295.

Tallini, Y.N., Ohkura, M., Choi, B.-R., et al. (2006) Imaging cellular signals in the heart *in vivo*: Cardiac expression of the high-signal Ca2+ indicator GCaMP2. *Proc. Natl. Acad. Sci.*, **103**, 4753–4758.

Xuan, Y.H., Hu, Y.B., Chen, L.-Q., Sosso, D., Ducat, D.C., Hou, B.-H. and Frommer, W.B. (2013) Functional role of oligomerization for bacterial and plant SWEET sugar transporter family. *Proc. Natl. Acad. Sci.*, **110**.

Supplermentary Material

Table S5.1. Recipe for minimal media used for *in vivo* measurement of MSucMeter

Minimal media	Final concentration	For 1 L
MOPS	100 mM	20.93 g
$MgSO_4$	1 mM	120.37 mg
$CaCl_2$	1 mM	110.98 mg
NH_4Cl	18.70 mM	1 g
NaCl	8.56 mM	0.5 g
KH_2PO_4	22.04 mM	3 g
Na_2HPO_4	42.27 mM	6 g
Distilled H_2O		To 1 L

Adjust the pH to 7.0 with KOH

Table S5.2. Parameters for ratiometric FRET-based sensor measurements

Symbol	**Meaning**	**Representation of molecule population**
R	Ratio that represents normalized FRET signal	Fraction of FRET molecules bound to analyte in relation to unbound FRET molecules and overall FRET molecule population
$I_{Ex: Donor; Em: Acc}$	Intensity of the signal emitted by the acceptor upon excitation of donor (= FRET)	Fraction of FRET molecules bound to analyte
$I_{Ex: Donor; Em: Donor}$	Intensity of the signal emitted by the donor upon excitation of donor	Fraction of unbound FRET molecules
$I_{Ex: Acc; Em: Acc}$	Intensity of the signal emitted by the donor upon excitation of donor	Total population of FRET molecules

10 Visualization of the injectisome to understand spatial dynamics of TALe delivery during *in planta* colonization

Introduction

Xanthomonas oryzae pv. *oryzae* (Xoo) injects transcription activator like effectors (TALes) via its innate Type-III-Secretion system (T3SS, “injectisome”) into host cells. Xylem vessels are primarily composed of rigid lignin. During initial stages of infection, Xoo was observed to colonize xylem pit membranes (Chapter 1). Hypothetically, Xoo specifically targets pliant hemicellulose pit areas to inject TAL effectors into xylem parenchyma cells. Additionally, a majority of Xoo bacteria were observed to orientate perpendicular to the xylem pit areas during the initial stage of infection. Because the fluid within the apoplasmic space of xylem vessel exhibits laminar flow, I hypothesized that the T3SS may serve as anchor and protect single Xoo bacteria that are not embedded in a protective biofilm matrix from the flowing xylem stream.

The T3SS system is composed of the basal body, anchored in the inner and outer membrane, acting as the secretion machinery. The needle filament extends up to 80 nm from the bacterial membrane and carries a contact-dependent needle tip at the needle filament top (Kubori *et al.*, 1998; Nans *et al.*, 2015; Radics *et al.*, 2014). The possibility of T3SS visualization by confocal microscopy is challenging due to the resolution limit of light microscopy and the constraint of photon density required by the detectors.

The diffraction limit of light (~200 nm) described by Abbe (5-13 nm range for the inner apparatus; 45-80 nm for the needle filament composed of several proteins) is not to overcome. However, the second limitation of confocal microscopy, photon density, remains addressable. Most biological applications of confocal microscopy are based on multiple copies of FPs, which increase signal intensity. In contrast, this experimental set-up focuses on visualizing individual bacteria that express copies of the T3SS. Tagging T3SS proteins with conventional fluorescent proteins (~27 kDa) was assumed to most likely interfere with proper folding and function. Hence, an imaging system was chosen, that only required attachment of scaffolds to proteins of interest and reduced the probability of interference with T3SS function.

SunTag is an imaging system that relies on epitope scaffolds tagged to the protein of interest. A single SunTag epitope consists of one GCNv4 peptide encoded by a 19 amino acid sequence (~2.1 kDa). A scaffold of multiple epitopes, usually 10 or 24, is designed to recruit multiple copies of antibody-fusion protein, such as a single-chain

variable fragment (scFv) fused to GFP (Tanenbaum *et al.*, 2014). The multimerization strategy significantly amplifies the signal and enables long-term imaging of single protein molecules in living cells under presence of scFv-FP (Dufourt *et al.*, 2021).

In this project, T3SS candidate proteins for visualization were identified and sequences for SunTag epitopes were integrated in frame with TAL effectors and candidate proteins by homologous recombination into the genome of Xoo.

Material and Methods

Identification of candidate T3SS protein

T3SS of plant pathogens diverge into Hrp-Hrc type I and type II (Wagner and Galan, 2020). Protein blast of T3SS components across species was used to identify *Xoo* T3SS homologues. After identification of HrpE as candidate for visualization, protein alignments were used to identify conserved structures and speculate which terminus may be suitable for tagging.

Homologous recombination and mutant selection

The SunTag scaffold was integrated in-frame with *HrpE* via homologous recombination. Genomic DNA of PXO99^{A} was extracted with DNeasy Blood & Tissue kit (QIAGEN). The *HrpE* sequence, along with additional 1.5 kb flanking sequences both the 3' and 5' end of *HrpE*, was amplified using PrimeSTAR Max DNA Polymerase (Takara) and ligated into pEN SacB (AddGene #196249, Table S5.2). After amplification of a single GCNv4 scaffold from LLP250 pEF1a-TALE-SunTag (Addgene: #100939), the amplicon was integrated via In-Fusion Assembly (Takara) in frame with *HrpE* in pEN SacB. After successful assembly of the pENSacB_HrpE-SunTag, electrocompetent PXO99^{A} were transformed with 500 ng of plasmid DNA electroporation for 5 seconds at 2.5 kV and 200 Ω in a 0.1 cm cuvette. Cells were recovered in Recovery Medium for Expression (Sigma, CMR001-8X12ML) and plated on NBA (1 g/L yest extract, 3 g/L beef extract, 5 g/L peptone, pH 7, 1.5% w/v agar, 100 µg/mL Ampicillin in distilled H_2O) and stored at 28 °C in dark conditions for four days. Transformants with Ampicillin tolerance were streaked onto NB media (NBA media lacking Ampicillin) and NBS (supplemented with 10 g/L sucrose) without antibiotics. Due to the SacB suicide cassette, transformants with tolerance to sucrose were expected to carry the homologous recombination cassette in the genome but have lost

the plasmid successfully. Colony PCR and Sanger sequencing were used to validate amplicon length and sequence of *HrpE-SunTag*. PXO99^{A} mutants carrying *HrpE-SunTag* were tested on virulence using the leaf clip infection protocol after Kauffman (1973) and the root clipping protocol (Chapter 2).

Results

The needle filament protein HrpE is a prime candidate for T3SS visualization

SunTags on extracellular proteins were predicted to pose a lower risk of interference with the overall T3SS structure compared to basal body components. Among the T3SS proteins, the needle filament and needle length regulator are exposed to the extracellular space. The needle filament, present in hundreds of copies, was chosen as the candidate protein for multiple considerations: Due to the presence of needle filament proteins in multiple copies, the detection of fluorescence might be facilitated. Moreover, the functionality of the needle filament has been shown to be essential for virulence. Thus, the risk of visualizing an artefact is lowered.

The Xoo protein HrpE was identified as a homolog of YscF, the well-studied T3SS needle filament protein of *Yersinia*, by protein blast. Across *Xanthomonas* species, needle filament proteins were observed to be highly conserved at the C terminus and carry variable residues at the N terminus (Figure 5.3A, Figure S5.1). *HrpE* was identified at position 66,754 to 66,473 within the PXO99^{A} genome and encodes 282 bp in antisense direction. HrpE is a beta-shapped protein of 8.9 kDa and constitutes a needle channel of ~15 Angstrom in diameter. Eleven subunits of HrpE build two turns of the needle helix (Jenkins *et al.*, 2022). Due to the conservancy of the HrpE C-terminus and exterior position of the N-terminus, the SunTag scaffold was integrated at the N-terminus. Conceptually, single copies of HrpE would be secreted via the sorting platform and basal body of the T3SS and extend the needle filament from the tip (Figure 5.3B). At the time of TALe secretion, Xoo would exert its needle filament within the xylem vessel. The needle filament would compose an epitope scaffold for antibody binding. After fixation and sectioning, the scaffold would allow to tag each epitope with single chain variable fragment antibodies fused to fluorescent proteins and allow an amplified signal for visualization. In addition, rice plants could be transformed with the SunTag plasmid carrying the scFV-GFP antibody sequence.

Hence, an *in vivo* observation of the spatial dynamics of the T3SS during infection would be possible.

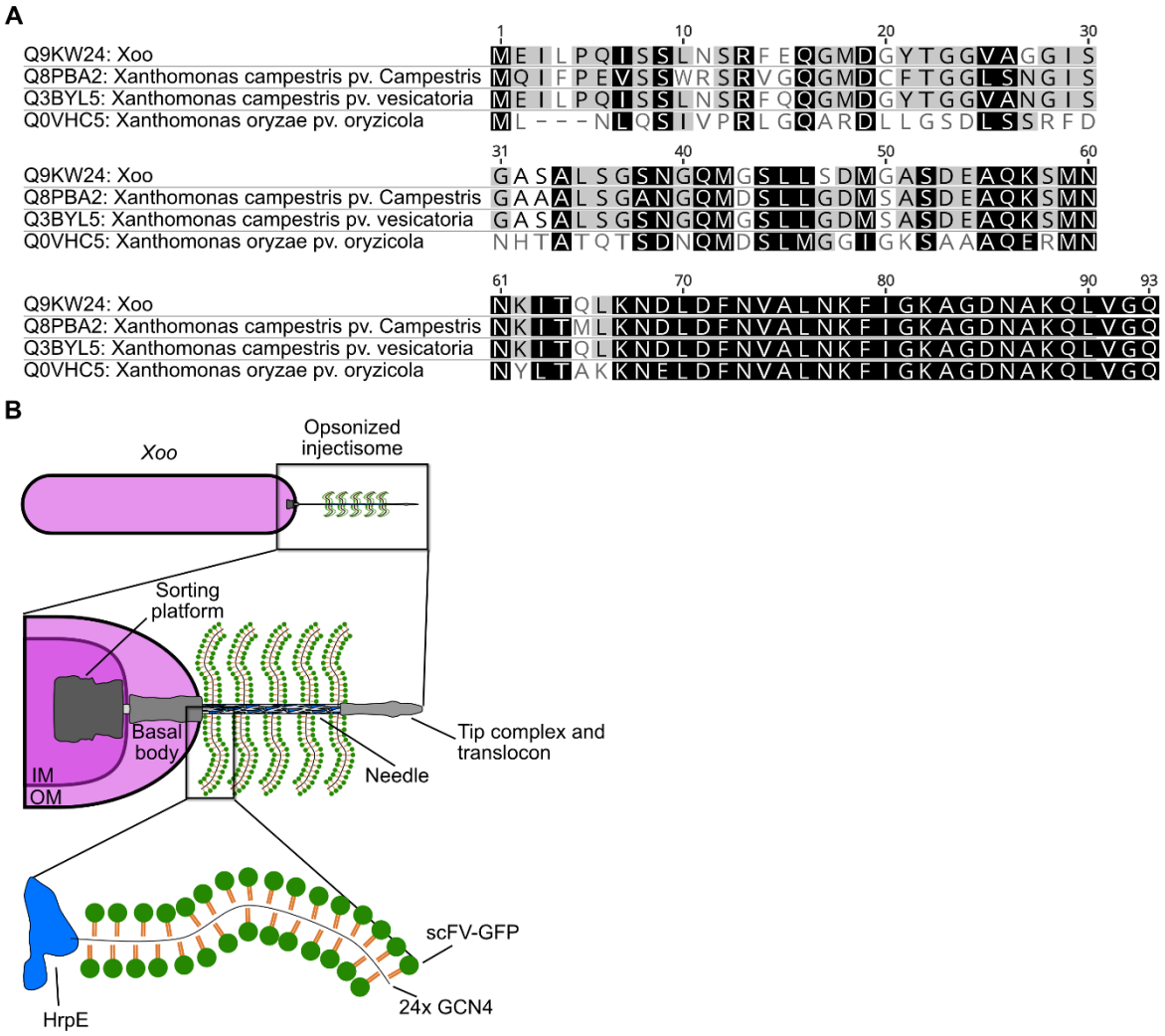

Figure 5.3 HrpE is a candidate for T3SS visualization. (A) Homology analysis of T3SS needle proteins reveals HrpE as *Xoo* needle protein and indicates variation at N-terminus among plant-pathogenic *Xanthomonas* spp. (B) Schematic visualization of SunTag at needle subunits and localization of scFV-GFP antibodies.

PXO99^{A} HrpE-SunTag render avirulent

Ten independent colonies of PXO99^{A} *HrpE-SunTag* were tested for virulence using the leaf clip assay. Additionally, the ability of PXO99^{A} *HrpE-SunTag* to induce *OsSWEET11a* was tested with the root infection protocol (Chapter 2) and translational SWEET reporter lines (Eom *et al.*, 2019). Despite efforts, none of the PXO99^{A} *HrpE-SunTag* colonies displayed lesions on rice leaves nor induction of *OsSWEET11a*. Therefore, although the SunTag strategy was employed to induce minimal disturbances to the T3SS, it appears that the ejection of TALes was hindered.

Discussion

HrpE seemed to be a promising candidate to observe the distribution of T3SS during infection of rice by Xoo with SunTag. In the pathosystem of citrus and *Xanthomonas campestris* pv. *campestris* (Xcc), the C- and N-terminus of the HrpE homolog were tested separately for the induction of plant defense (Gottig *et al.*, 2018). Interestingly, the treatment with the C-terminus displayed an increased plant defense response compared to treatment with the N-terminus. Across different *Xanthomonas* species, the C-terminus was observed to be highly conserved (Figure 5.3A). Potentially, the N-termini as outer barrel structure of the needle filament are subjected to a higher probability of recognition by the plant immune system. The selective pressure could be a factor that increases the odds for the observed N-terminal variation. The C-terminus is compacted into the needle filament. Thus, it is unlikely that plant immune receptors could detect the C-terminus from the needle filament surface. More likely, the C-terminus of HrpE acts as trigger for the plant immune system upon disintegration of the T3SS and bacterial membranes.

Xoo *hrpE* mutants were tested before for virulence activity and bacterial mobility but HrpE was solely suspected as protein within the T3SS but not specifically as needle filament protein (Sheikh *et al.*, 2019). Xoo *hrpE* mutants exhibited a slower growth curve, colony forming ability and signficiantly decreased twitching ability compared to wild-type Xoo. Interestingly, a pre-treatment with purified HrpE was discovered to increase stomatal conduction, photosynthetic activity and transpiration rate. While Xoo is a vascular pathogen during early infection stages, *Xanthomonas oryzae* pv. *oryzicola* (Xoc) invades rice mesophyll through stomata. Since Xoo and Xoc share HrpE proteins with one amino acid divergence, an opening of stomata upon HrpE recognition would be disadvantageous for rice leaf streak infection.

Although the SunTag approach failed to visualize the needle filament of Xoo during infection, the SunTag approach may still be useful to visualize molecular interactions between plant pathogens. If the SunTag cassette for the expression of scFv-FPs can be integrated into the plant genome, *in vivo* observation of spatial and temporal dynamics may be approachable. In 2024, the successful development of anti-HrpE scFv antibodies for Xcc was published with the intention to minimize infection (Raeisi *et al.*, 2024). Nanobodies have been used to visualize very small compartments, such

as components of the nuclear core complex (Pleiner *et al.*, 2015). An advancement of anti-HrpE scFv antbodies fused to fluorescent proteins or the use of nanobodies are a route to overcome the limitation of T3SS visualization due to interference effects

References

Dufourt, J., Bellec, M., Trullo, A., Dejean, M., Rossi, S.D., Favard, C. and Lagha, M. (2021) Imaging translation dynamics in live embryos reveals spatial heterogeneities. *Science*, **372**, 840–844.

Eom, J.-S., Luo, D., Atienza-Grande, G., et al. (2019) Diagnostic kit for rice blight resistance. *Nat. Biotechnol.*, **37**, 1372–1379.

Gottig, N., Vranych, C.V., Sgro, G.G., Piazza, A. and Ottado, J. (2018) HrpE, the major component of the *Xanthomonas* type three protein secretion pilus, elicits plant immunity responses. *Sci. Rep.*, **8**, 9842.

Jenkins, J., Worrall, L.J. and Strynadka, N.C.J. (2022) Recent structural advances towards understanding of the bacterial type III secretion injectisome. *Trends Biochem. Sci.*, **47**, 795–809.

Kauffman, H. (1973) An improved technique for evaluating resistance of varieties to *Xanthomonas oryzae* pv. *oryzae*. *Plant Dis. Rep*, **57**, 537–541.

Kubori, T., Matsushima, Y., Nakamura, D., Uralil, J., Lara-Tejero, M., Sukhan, A., Galán, J.E. and Aizawa, S.-I. (1998) Supramolecular structure of the *Salmonella typhimurium* Type III protein secretion system. *Science*, **280**, 602–605.

Nans, A., Kudryashev, M., Saibil, H.R. and Hayward, R.D. (2015) Structure of a bacterial type III secretion system in contact with a host membrane *in situ*. *Nat. Commun.*, **6**, 10114.

Pleiner, T., Bates, M., Trakhanov, S., et al. (2015) Nanobodies: site-specific labeling for super-resolution imaging, rapid epitope-mapping and native protein complex isolation. *eLife*, **4**, e11349.

Radics, J., Königsmaier, L. and Marlovits, T.C. (2014) Structure of a pathogenic type 3 secretion system in action. *Nat. Struct. Mol. Biol.*, **21**, 82–87.

Raeisi, H., Safarnejad, M.R., Alavi, S.M., De Oliveira Andrade, M., Farrokhi, N. and Elahinia, S.A. (2024) Transient expression of anti-HrpE scFv antibody reduces the hypersensitive response in non-host plant against bacterial phytopathogen *Xanthomonas citri* subsp. *citri*. *Sci. Rep.*, **14**, 7121.

Sheikh, T.M.M., Zhang, L., Zubair, M., et al. (2019) The Type III Accessory protein HrpE of *Xanthomonas oryzae* pv. *oryzae* surpasses the secretion role, and enhances plant resistance and photosynthesis. *Microorganisms*, **7**, 572.

Tanenbaum, M.E., Gilbert, L.A., Qi, L.S., Weissman, J.S. and Vale, R.D. (2014) A protein-tagging system for signal amplification in gene expression and fluorescence imaging. *Cell*, **159**, 635–646.

Wagner, S. and Galan, J.E. eds. (2020) *Bacterial Type III Protein Secretion Systems*, Cham, Switzerland: Springer International Publishing.

Supplementary Material

>tr|Q8PBA2|Q8PBA2_XANCP HrpE protein OS=Xanthomonas campestris pv. campestris (strain ATCC 33913 / DSM 3586 / NCPPB 528 / LMG 568 / P 25) OX=190485 GN=hrpE PE=4 SV=1

MLNLQSIVPRLGQARDLLGSDLSSRFDNHTATQTSDNQMDSLMGGIGKSAAAQERMNNYLTAKKNEL DFNVALNKFIGKAGDNAKQ LVGQ

>tr|Q9KW24|Q9KW24_XANOO HrpE OS=Xanthomonas oryzae pv. oryzae OX=64187 GN=hrpE PE=4 SV=1

MEILPQISSLNSRFQQGMDGYTGGVANGISGASALSGSNGQMGSLLGDMSASDEAQKSMNNKITQLKN
DLDFNVALNKFIGKAGDNA KQLVGQ

>tr|Q0VHC5|Q0VHC5_9XANT HrpE1 OS=Xanthomonas oryzae pv. oryzicola OX=129394 GN=hrpE1 PE=4 SV=1

MEILPQISSLNSRFEQGMDGYTGGVAGGISGASALSGSNGQMGSLLSDMGASDEAQKSMNNKITQLKN
DLDFNVALNKFIGKAGDNA KQLVGQ

>tr|Q3BYL5|Q3BYL5_XANC5 HrpE OS=Xanthomonas campestris pv. vesicatoria (strain 85-10) OX=316273 GN=hrpE PE=4 SV=1

MQIFPEVSSWRSRVGQGMDCFTGGLSNGISGAAALSGANGQMDSLLGDMSASDEAQKSMNNKITMLK
NDLDFNVALNKFIGKAGDNAK QLVGQ

>tr|Q3BYK4|Q3BYK4_XANC5 HrpB2 protein OS=Xanthomonas campestris pv. vesicatoria (strain 85-10) OX=316273 GN=hrpB2 PE=4 SV=1

MTLIPPVQAIAGTSAAATQALSPVATPNQALVNRFQALMQSSSPLPPAMQRVGNPSMMSRVVDVQNDG
VRTIAEHIDAFSMQAPT

MGLQEMAAQQIKLMHELTMVGFNLNVSVGVAQSGKNAVQTLVKNQ

>tr|Q8GQX7|Q8GQX7_RALSL Hrp pilus subunit HrpY protein OS=Ralstonia solanacearum OX=305 GN=hrpY PE=4 SV=1

MAGVPKPTTTNTTSTTSTFQSFANGVDDAASRTGFQAQYQAITAQGQQDMLDAAKMQNALNRTQML
AKLMEAGPKAAKDLIS

>sp|Q52473|HRPA_PSESM Hrp pili protein HrpA OS=Pseudomonas syringae pv. tomato (strain ATCC BAA-871 / DC3000) OX=223283 GN=hrpA PE=1 SV=3

MVAFAGLTSKLTNLGNSAVGGVGGALQGVNTVASNATLQKNILLGTGDSLSVDAQAKASKESDANGA
KLIAMQAQETMKKQTMDVLN

AIQAGKEDSTNKKISATATNAKGISY

>tr|Q3BYL7|Q3BYL7_XANC5 HpaE protein OS=Xanthomonas campestris pv. vesicatoria (strain 85-10) OX=316273 GN=hpaE PE=4 SV=1

MPKSQSRPQRRPSAMAQQLGLPANSAGLALLCPMAPVALSETHLAMSKPDTRASALACSPIQVWREIA
GLSCRLTAMADTAQNKGR

RRLMVYTVHTRDGS

Figure S5.1 1Protein sequences of T3SS proteins within *Xanthomonas* spp. and gram-negative plant pathogens

Table S5.3. Oligo sequences for homologous recombination of SunTag into in-frame with *HrpE*

Description	Primer Sequence (5'-3')	Template
5' flank forward	TATGGAAAAACGCCAGCAACTCATCACAGCGCCGTTGC	gDNA PXO99^{A}
5' flank reverse	GAGTCTTGTTTGGGCTTAGACATGCGCAG	gDNA PXO99^{A}
3' flank forward	TCTAAGCCCAAACAAGACTCCTACGTAGTGAACG	gDNA PXO99^{A}
3' flank reverse	CAACATATGCAGTCACTATGACAAGGCCACCGCGGCGG	gDNA PXO99^{A}
HrpE forward	AAACAAATAGGGGTTCCGCGTCACTGGCC	gDNA PXO99^{A}
HrpE reverse	TGGCAGTGGAATGGAAATACTTCCGC	gDNA PXO99^{A}
backbone linearization forward	CATAGTGACTGCATATGTTGTGT	pEN SacB (AddGene #196249)
backbone linearization reverse	GTTGCTGGCGTTTTTCCA	pEN SacB (AddGene #196249)
backbone linearization forward	CAACAAGACTCCTACGAACAAGACT	pEN SacB_flanks
backbone linearization reverse	CGCGGAACCCCTATTTGT	pEN SacB_flanks
1x GCNv4 forward	ATGGAAGAACTTTTGAGCAAGAATTATC	LLP250 pEF1a-TALE-SunTag (Addgene: #100939)
1x GCNv4 reverse	CTTCTCCACTGCCAGAACCTTTC	LLP250 pEF1a-TALE-SunTag (Addgene: #100939),
Colony PCR forward	CGCCAGCAACTCATCACAGC	gDNA PXO99^{A} sucrose tolerant transformant
Colony PCR reverse	GCAGTCACTATGACAAGGCC	gDNA PXO99^{A} sucrose tolerant transformant

11 Identification of *OsSWEET* promoter proxisome

Contributions

Chen Deng and Melissa Stiebner supported with experimental design, cloning and rice transformation.

Bacterial blight in rice occurs when Transcription Activator-Like effectors (TALes) from *Xanthomonas oryzae pv. oryzae* (Xoo) bind to Effector Binding Elements (EBEs) within *OsSWEET* gene promoters. TALes mimic eukaryotic transcription factors and induce *OsSWEET* expression. However, sequence polymorphisms in the EBE region can prevent TALe binding, which confers resistance to Xoo (Schepler-Luu *et al.*, 2023; Oliva *et al.*, 2019). The potential to create novel resistance traits through promoter edits highlights the importance of characterizing the proteomic landscapes at *OsSWEET* promoters to preserve native regulatory elements in editing strategies.

The ability of TALes to induce transcription regardless of the chromatin state promotes the hypothesis that TALes are capable to recruit histone modifying enzymes as well as parts of the pre-initiation complex of RNA Polymerase II. Although TALe technology is utilised in a wide range of biological fields, the recruitment mechanism as well as potential interactors are unknown. Here, the reorientation to the infection process of rice by Xoo utilising TALes might facilitate the exploration of open research questions. One route may be depicted by the recessive resistance gene *xa5* encoding a subunit of the general transcription factor TFIIA. A point mutation that converts a valine to a glutamine in the $TFIIA_{\gamma}$ subunit confers resistance to some Xoo strains (Carpenter *et al.*, 2020; Han *et al.*, 2020). For that reason, it is speculated whether the native subunit of TFIIA may build a contact site between TALes and the pre-initiation complex of RNA Polymerase II.

Minor changes in the repeat variable di-residue (RVD) region of TAL effectors allow them to adapt to DNA sequence variations, which laid the foundation for TALe-based technology. For instance, the design of two TALes fused to FokI endonucleases binding opposite but adjacent to each other on the same DNA strand, enabled TALEN-based genome editing. TALe-based technology has been successfully employed in a wide range of eukaryotic model organisms e.g. mammalian cells, drosophila and mice (Miyanari, 2014; Yang *et al.*, 2013; Zhang *et al.*, 2017) . The fusion of TALes to repressor or activator modules enabled adaptable gene regulation of cis elements, enhancers and epigenetic modellers (Bobola and Sagerström, 2024; Crocker and Stern, 2013; Gao *et al.*, 2014). Interestingly, TALes were able to interfere with EBEs despite the endogenous state of the chromatin region (Perez-Pinera *et al.*, 2013). In

comparison to deactivated Cas9 (dCas9), TALEN bind more robustly in heterochromatin regions with less off-target effects (Jain et al., 2021).

A deeper understanding of the proteomic environment at *OsSWEET* promoters tackles fundamental biological questions. Genome editing approaches that disrupt EBE sequences must account for potential effects on cis-regulatory elements essential for transcription factor binding. Alterations in these regions may interfere with native gene regulation and emphasize the importance of a detailed promoter-level analysis.

A proteomic survey of proteins associated with *SWEET* promoters may enable the prediction of transcription factor motifs that should remain intact to preserve gene function following editing approaches.

Proximity labeling techniques offer a precise approach to identify protein-protein interactions and subcellular proteomes with high spatial and temporal resolution. Proximity labeling methods use enzymes such as biotin ligases (e.g., BioID, TurboID) or peroxidases (e.g., APEX2) to catalyze the covalent attachment of biotin or other reactive tags to proteins within a defined radius. Labeled proteins undergo affinity purification and mass spectrometry analysis to reveal the proxisomal proteome. Typically, labeling enzymes are attached to candidate proteins of interest.

In this study, dCas9 (Cas9 without nuclease activity) was tagged to TurboID (biotin ligase). The application of a clustered interspaced short palindromic repeats (CRISPR)/dCas9-TurboID-mediated proximity labeling approach at *OsSWEET* promoters was developed to identify the transcriptional network of *OsSWEET* expression. The dCas9-TurboID complex was targeted by guide RNAs to 100 bp upstream of EBEs. Moreover, an analysis of plants exposed to TALe-injecting *Xoo* strains was performed to uncover proteins that associate with TALes at the *OsSWEET* promoter. RNA levels of *dCas9-TurboID* were evaluated to validate correct expression of the cassette. Functionality of dCas9-TurboID was tested by protein blots of biotinylated samples.

Material and Methods

pZmUbi:dCas9-TurboID plasmid construction and plant generation

The **TurboID** and dCas9 coding sequences were amplified by **polymerase chain reaction (PCR)** with **CloneAmp (Takara) polymerase** from two template vectors, respectively (Addgene: #127354 and #99907, Mair et al., 2019). Amplified products were equipped with complementary 15 bp overhangs via PCR and ligated with In-Fusion HD (Takara) into the binary expression vector pZmUbi1 (Frommer stock collection). Depending on the targeted promoter, protospacer sequences for the guide RNA were adapted (*OsSWEET11a*: "GTCATATGAATGCATAACTG", *OsSWEET13*: "ATGCGTACGTGAATGGCCAT", *OsSWEET14*: "TGGCACTTTCTGTCATGCAT"). *A. tumefaciens* strain AGL1 was transformed with the pZmUbi1:dCas9-TurboID construct by electroporation (2.5 kV, 200 Ω, 5 s). Rice calli were co-cultivated with AGL1 pZmUbi1:dCas9-TurboID and selected on hygromycin (Chapter 3; Luu et al., 2020). T_1 transformants were screened on hygromycin and genotyped for the presence of dCas9-TurboID.

RNA extraction and quantitative PCR

Total RNA from T_2 rice leaves was extracted with the RNeasy Kit (QIAGEN). Removal of genomic DNA and cDNA synthesis was performed with Maxima™ H Minus cDNA Synthesis Master Mix (Thermo Fisher Scientific). qPCR was executed on Stratagene Mx3000P (Agilent Technologies) using the Lightcycler 480 SYBR Green I Master Mix (Roche). Transcript levels were quantified with ΔΔCt to water and *OsEF-1*α controls. Analysis was performed in R. Oligo sequences are shown in Table 5.1.

Table 5.1. Oligo sequences used to perform quantitative PCR.

Amplified cDNA	**Sequence 5' -> 3'**	**Amplicon Length (bp)**
*OsEF-1*α forward	GAAGTCTCATCCTACCTGAAGAAG	147
*OsEF-1*α reverse	GTCAAGAGCCTCAAGCAAGG	147
dCas9 exon 1, forward	GAAGCACGAGAGACACCCAA	149
dCas9 exon 1, reverse	TGTGAGCAAGAGCAAGGTAGA	149

Biotinylation and protein blots

Leaf disks of T_2 hygromycin tolerant pZmUbi:dCas9-TurboID rice lines were harvested with a 10 mm diameter leaf plunger. Five leaves per replicate were exposed in a biotin solution (200 µM biotin, 0.1 % Triton-X 100 in phosphate buffer saline) for four hours at 37°C. Subsequently, leaves were washed three times in ice cold distilled H_20 and homogenized in liquid nitrogen with a mortar and pestle. The resulting homogenate was combined with 1 mL of RIPA buffer (150 mM NaCl, 0.5% sodium deoxycholate, 1 mM EDTA pH 8, 0.1% sodium dodecyl sulfate, 1% Triton-X 100, 1 mM phenylmethanesulfonylfluoride, 1 tablet of Roche cOmplete™ Protease Inhibitor Cocktail, 50 mM trisaminomethane, pH 7.4 in distilled H_20). After an incubation of 30 minutes on ice, samples were centrifuged at 10,000 rpm for 30 minutes at 4 °C. For the equilibration of desalting columns and Streptavidin agarose beads, a wash buffer composed of 20 mM Tris-HCl (pH 7.5), 1 mM EDTA, and 200 mM NaCl in distilled H_2O was used. The supernatant was transferred to equilibrated desalting Pierce Zebra™ columns (Thermo Fisher Scientific). To eliminate non-biotinylated proteins from the bulk-protein samples, the eluates were incubated with 20 µL of equilibrated Dynabeads MyOne Streptavidin C1 (Thermo Fisher Scientific) beads for 16 hours at 4°C. After three repetitions of rinsing with 500 µL wash buffer, the beads were reconstituted and boiled in 50 µL 4x Laemmli buffer supplemented with 20 mM DTT and 2 mM biotin for 5 min at 95°C.

Samples were transferred to a new 1.5 mL Eppendorf tube and stored at – 80 °C. For the assessment of biotinylated protein across samples, the protein concentrations were quantified with the Quick Start™ Bradford Protein Assay Kit (Bio-Rad) using the fluorometric plate reader (SparkControl™, Tecan AG) and adjusted to 20 µg/mL for protein blot analysis. Samples were transferred to NuPage™ Mini Protein Gels (Thermo Fisher Scientific) and run at 200 mA for 60 minutes at room temperature in MES buffer (Thermo Fisher Scientific). Proteins were transferred from the gel to a polyvinylidene fluoride membrane by application of 60 mA for 60 minutes at 4°C with NuPage™ Transfer buffer (Thermo Fisher Scientific) supplemented with methanol according to manufacturer's protocol in a wet blot chamber (Thermo Fisher Scientific). The membrane was washed twice with TBST (20 mM Tris, 150 mM NaCl, 0.1% Tween 20 in distilled H_2O) while being shaken. Non-specific binding of the antibody was prevented by a blocking step in TBST-BSA (20 mM Tris, 150 mM NaCl, 0.1% Tween

20, 3 % bovine serum albumin in distilled H_2O) for 16 hours at 4°C, shaking at 40 rpm. The blocked membranes were then incubated with 1:5,000 Streptavidin-horseradish peroxidase antibody (Abcam, ab7403) for 24 hours at 4 °C. After three washes with TBST, 1 mL of SuperSignal™ West Femto Maximum Sensitivity (Thermo Fisher Scientific) was added to the membrane. The emitted chemiluminesence was captured after 30 sec in UVP ChemStudio PLUS Touch.

Results

Quantification of dCas9-TurboID transcript levels

For each construct targeting *OsSWEET11a*, *OsSWEET13*, *OsSWEET14*, as well as a "no guide RNA" control (in which the binary vector was not carrying a sequence for guide RNA), approximately 20 independent transformation events were screened for hygromycin resistance. Events that displayed a Mendelian segregation ratio of ~3:1 (±0.5) were selected and advanced to the T_2 generation. To validate the specificity of the designed primers, a PCR was performed on genomic DNA of transformants and wild-type. The amplicon of *dCas9* primers was specifically observed for transformed rice lines but not in wild type plants while the amplicon of *OsEF-1*α has been present in all tested samples. Quantitative PCR on cDNA was performed to estimate whether the construct is successfully transcribed *in planta*. The presence for dCas9 RNA was detected in all tested events compared to wild-type plants (Figure 5.4). Detected transcripts for dCas9 indicated successful transcription of the construct *in planta*.

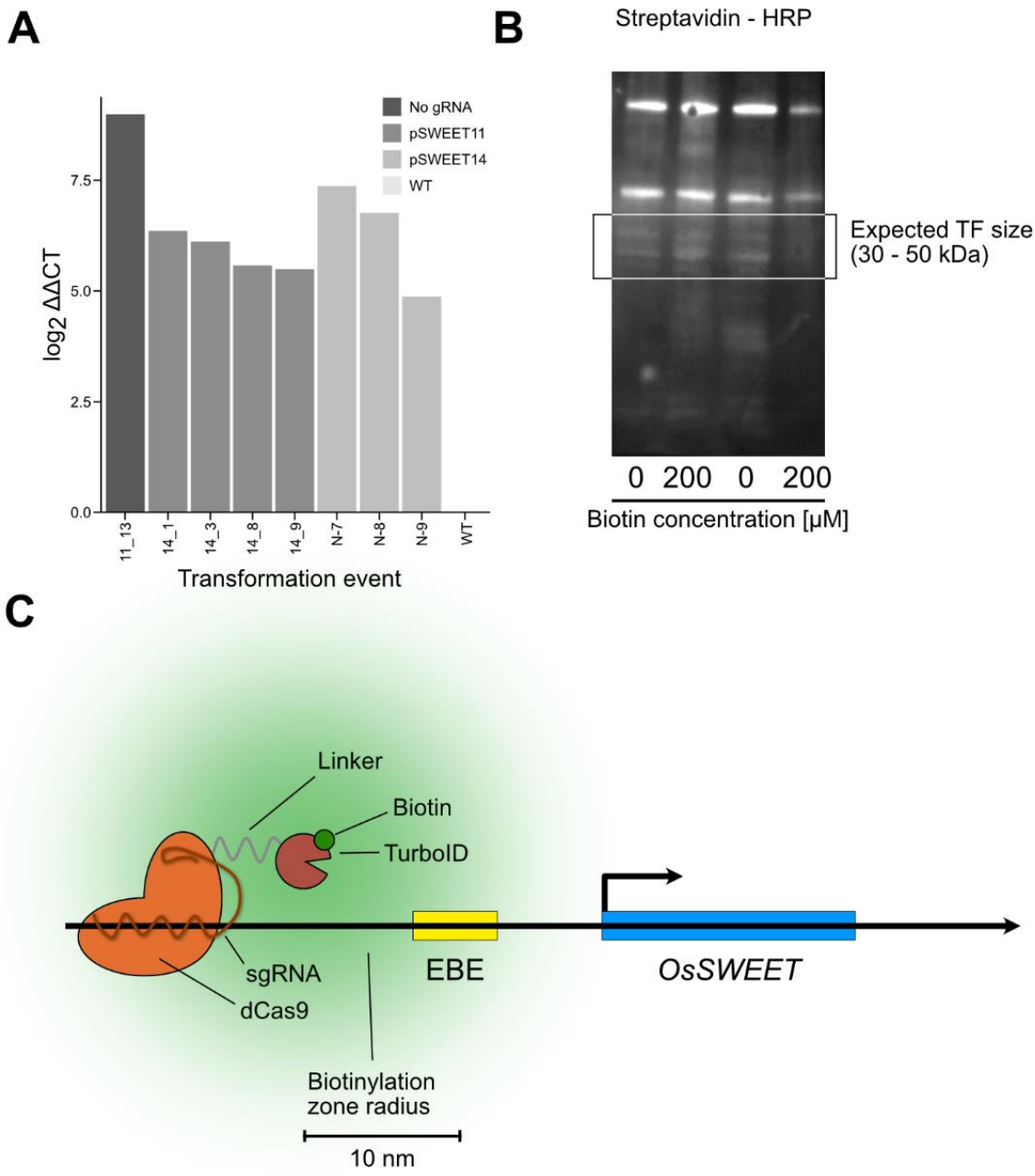

Figure 5.4 Assessment of dCas9-TurboID constructs *in planta*. (A) Transcript level of *dCas9-TurboID* in T_2 plants from transformation events of *dCas9-TurboID* constructs targeting the promoter of *OsSWEET11a* (pSWEET11), *OsSWEET14* (pSWEET14), no gRNA control constructs and wild-type plants. (B) Protein blot with biotinylated protein after TurboID assay. (C) Scheme of TurboID activity at *OsSWEET* promoters with 10 nm biotinylation radius covering EBE region in *dCas9-TurboID* set-up.

Assessment of dCas9-TurboID Biotin Ligase Activity

Transformants with dCas9-TurboID transcripts, were tested for biotin ligase functionality. Western blot analysis revealed no significant difference in overall biotinylated protein levels between transformed and wild-type plants (Figure 5.4B). The presence of *dCas9-TurboID* did not increase biotinylation, nor did it enrich proteins in

the 30–50 kDa range, where many transcription factors are expected. Interestingly, wild-type plants without externally supplied biotin showed higher biotinylation levels than those treated with 200 µM biotin, suggesting that endogenous biotinylated proteins contribute substantially to background signal. The presence of *dCas9-TurboID* did not result in higher abundance of biotinylated protein which points to a lack of functionality of the dCas9-TurboID construct.

Discussion

The absence of increased biotinylated protein in the transformed samples suggests that the dCas9-TurboID construct lacks functionality under tested conditions. One explanation involves unsuccessful localization or expression of the dCas9-TurboID fusion protein. To verify proper localization, a fluorescent protein tag could help confirm nuclear import of the dCas-TurboID construct by microscopy.

Another consideration involves the biotinylation activity of TurboID itself. The lack of enhanced biotinylation in biotin-treated plants suggests that TurboID may not fold or function properly in the plant cellular environment. Codon optimization for rice, re-evaluation of linker sequences between dCas9 and TurboID, or testing alternative ligase variants (e.g., miniTurbo) may improve enzymatic activity. As an initial step to investigate the functionality of dCas9-TurboID could be bacterial expression and purification of protein, followed by *in vitro* analysis. It may also be beneficial to confirm TurboID activity in a transient system (e.g. rice protoplasts) prior to stable transformation.

Additionally, using split-TurboID systems, where two inactive halves of the enzyme reconstitute only when brought into close proximity, may offer a strategy to facilitate functionality by size minimization. Combining dCas9 with epitope-tagged cofactors, followed by co-immunoprecipitation, could also serve as a complementary method to identify interacting proteins at *OsSWEET* promoters.

Moreover, the overall approach of using TurboID for proximity-labeling at promoters should be critically evaluated. TurboID generates the reactive intermediate biotin–5'-AMP from biotin and ATP. Yet, protein density in the nucleus might greatly differ from protein concentration in the cytoplasm, in which the majority of successful TurboID assay was performed in.

The observed high background signal in wild-type plants without biotin treatment underscores the fact that rice naturally harbors biotinylated proteins. This background complicates interpretation of proximity labeling results and highlights the need for stringent controls. In the current experimental set-up, the primary control for non-specific proteins is given by the “no guide RNA” control. Moreover, a TAL effector fused with an affinity tag (~135 kDa) could serve as a positive control; successful detection of the enriched TAL effector after streptavidin pull-down would confirm that the dCas9-TurboID system is operational and capable of labelling proteins present at the *OsSWEET* promoter. In general, additional steps to further differentiate between endogenously biotinylated proteins and TurboID-biotinylated proteins will be crucial, especially given further analysis using mass spectrometry as abundant “non TurboID-targets” could drastically decrease the chance of identifying traces of actual TurboID-biotinylated proteins. Adding a step on isolating nuclei to separate nucleic proteins from cytoplasmic proteins after the biotinylation assay could improve the overall outcome.

The system may benefit from further refinement through promoter walking: Delivering guide RNAs to a stable dCas9-TurboID line would enable investigation of multiple promoter regions, rather than limiting the analysis to a single site. Although the tobacco rattle virus system provides an effective guide RNA delivery method in dicots, no equivalent system has been established for monocots such as rice (Ellison *et al.*, 2020; Nagalakshmi *et al.*, 2022). However, monocot-specific viruses have demonstrated success in gene delivery and may serve as suitable alternatives (Mei *et al.*, 2019; Tamilselvan-Nattar-Amutha *et al.*, 2023; Zhu *et al.*, 2017). With adaptation, systems based on monocot viruses may support guide RNA delivery for CRISPR-based proximity labeling approaches in monocots.

Although the initial construct did not produce functional proximity labeling, several optimization strategies remain available. A clear evaluation of subcellular localization, demonstration of biotin ligase activity, reduction of background signal, and identification of alternative guide RNA delivery methods in monocots represent critical next steps. A functional dCas9-TurboID system for *in planta* promoter-level proteomics would offer strong potential to reveal transcriptional regulation in response to pathogen effectors and throughout developmental stages as well as into the mechanisms of TAL effector functionality.

References

Bobola, N. and Sagerström, C.G. (2024) TALE transcription factors: Cofactors no more. *Semin. Cell Dev. Biol.*, **152–153**, 76–84.

Carpenter, S.C.D., Mishra, P., Ghoshal, C., et al. (2020) An *xa5* resistance gene-breaking indian strain of the rice bacterial blight pathogen *Xanthomonas oryzae* pv. *oryzae* is nearly identical to a thai strain. *Front. Microbiol.*, **11**, 579504.

Crocker, J. and Stern, D.L. (2013) TALE-mediated modulation of transcriptional enhancers *in vivo*. *Nat. Methods*, **10**, 762–767.

Ellison, E.E., Nagalakshmi, U., Gamo, M.E., Huang, P., Dinesh-Kumar, S. and Voytas, D.F. (2020) Multiplexed heritable gene editing using RNA viruses and mobile single guide RNAs. *Nat. Plants*, **6**, 620–624.

Gao, X., Tsang, J.C.H., Gaba, F., Wu, D., Lu, L. and Liu, P. (2014) Comparison of TALE designer transcription factors and the CRISPR/dCas9 in regulation of gene expression by targeting enhancers. *Nucleic Acids Res.*, **42**, e155.

Han, J., Xia, Z., Liu, P., Li, C., Wang, Y., Guo, L., Jiang, G. and Zhai, W. (2020) TALEN-based editing of *TFIIAγ5* changes rice response to *Xanthomonas oryzae* pv. *oryzae*. *Sci. Rep.*, **10**, 2036.

Jain, S., Shukla, S., Yang, C., et al. (2021) TALEN outperforms Cas9 in editing heterochromatin target sites. *Nat. Commun.*, **12**, 606.

Luu, V., Stiebner, M., Maldonado, P., et al. (2020) Efficient *Agrobacterium*-mediated transformation of the elite–*indica* rice variety Komboka. *BIO-Protoc.*, **10**.

Mei, Y., Beernink, B.M., Ellison, E.E., Konečná, E., Neelakandan, A.K., Voytas, D.F. and Whitham, S.A. (2019) Protein expression and gene editing in monocots using foxtail mosaic virus vectors. *Plant Direct*, **3**, e00181.

Miyanari, Y. (2014) TAL effector-mediated genome visualization (TGV). *Methods*, **69**, 198–204.

Nagalakshmi, U., Meier, N., Liu, J.-Y., Voytas, D.F. and Dinesh-Kumar, S.P. (2022) High-efficiency multiplex biallelic heritable editing in *Arabidopsis* using an RNA virus. *Plant Physiol.*, **189**, 1241–1245.

Oliva, R., Ji, C., Atienza-Grande, G., et al. (2019) Broad-spectrum resistance to bacterial blight in rice using genome editing. *Nat. Biotechnol.*, **37**, 1344–1350.

Perez-Pinera, P., Ousterout, D.G., Brunger, J.M., Farin, A.M., Glass, K.A., Guilak, F., Crawford, G.E., Hartemink, A.J. and Gersbach, C.A. (2013) Synergistic and tunable human gene activation by combinations of synthetic transcription factors. *Nat. Methods*, **10**, 239–242.

Schepler-Luu, V., Sciallano, C., Stiebner, M., et al. (2023) Genome editing of an African elite rice variety confers resistance against endemic and emerging *Xanthomonas oryzae* pv. *oryzae* strains. *eLife*, **12**, e84864.

Tamilselvan-Nattar-Amutha, S., Hiekel, S., Hartmann, F., Lorenz, J., Dabhi, R.V., Dreissig, S., Hensel, G., Kumlehn, J. and Heckmann, S. (2023) Barley stripe mosaic virus-mediated somatic and heritable gene editing in barley (*Hordeum vulgare L.*). *Front. Plant Sci.*, **14**, 1201446.

Yang, J., Yuan, P., Wen, D., Sheng, Y., Zhu, S., Yu, Y., Gao, X. and Wei, W. (2013) ULtiMATE system for rapid assembly of customized TAL effectors. *PLOS ONE*, **8**, e75649.

Zhang, Y., Liu, L., Guo, S., Song, J., Zhu, C., Yue, Z., Wei, W. and Yi, C. (2017) Deciphering TAL effectors for 5-methylcytosine and 5-hydroxymethylcytosine recognition. *Nat. Commun.*, **8**, 901.

Zhu, L., Zhu, J., Liu, Z., Wang, Z., Zhou, C. and Wang, H. (2017) Host-induced gene silencing of rice blast fungus *Magnaporthe oryzae* pathogenicity genes mediated by the brome mosaic virus. *Genes*, **8**, 241.

12 Outlook

Overview of key findings

The collective findings of this thesis reveal a multifaceted strategy by which *Xanthomonas oryzae* pv. *oryzae* (Xoo) subverts rice carbon allocation networks to promote disease. Chapter 5 demonstrated that Xoo undergoes differentiation into filamentous cell forms during vascular bundle breach. I observed a transient filamentous phenotype emerging from the usual rod-shaped cells within rice xylem vessels. Rod-shaped bacteria predominated during early vascular colonization, at xylem pit membranes likely important during basipetal progression of infection. In contrast, filamentous Xoo cells appeared at later infection stages, breaching xylem vessels to invade surrounding xylem parenchyma, bundle sheath and even mesophyll tissue. This morphological switch was correlated with enhanced tissue colonization and leaf symptom development (chlorosis/necrosis), indicating that disease is not merely due to xylem blockage but also direct cellular damage in mesophyll caused by invasive filaments. Chapter 5 further confirmed that Xoo can be induced to form filaments *in vitro* under diverse abiotic growth conditions (e.g. high cell density and salinity), and that filamentation is reversible. This *in planta* differentiation suggests a developmental program in Xoo that likely aids virulence.

Chapter 6 focused on the infection route and systemic movement of Xoo, uncovering a strong root-to-shoot transmission barrier. Using a novel root inoculation assay, I found that Xoo can infect rice roots locally but is limited at the nodal translocation zone. Even when high inoculum loads were applied to roots, systemic colonization of aboveground tissues was not observed, in contrast to the efficient spread observed in leaf-initiated infections. The data indicate that rice's root anatomy and/or defenses impose a major bottleneck to Xoo movement, preventing efficient xylem ascent from roots to shoots. This result highlights the importance of natural entry routes (e.g. leaf hydathodes or wounds) for disease in the field, and suggests that soil-borne spread of bacterial blight is unlikely under normal conditions.

Chapters 7 and 8 addressed genetic interventions in the host to counteract the pathogen's strategies. Chapter 3 evaluated editing of TAL effector binding elements (EBEs) in promoters of rice *SWEET* sugar transporter genes as a means to block pathogen-induced susceptibility. Xoo relies on specific transcription-activator like effectors (TALes) to bind EBEs in *OsSWEET11a*, *OsSWEET13*, and *OsSWEET14*

promoters, activating these sugar efflux transporters and releasing sucrose that fuels infection. In this study, I found that the target EBEs are highly conserved in rice germplasm and overlap native regulatory motifs, suggesting they have important endogenous roles. Importantly, the extensive phenotypic assays under diverse abiotic conditions of *sweet* knockout mutants exhibited some alterations in development (e.g. flag leaf angle and root architecture), affirming that SWEETs contribute to carbon partitioning. However, no broad fitness penalty was observed. The data support that EBEs have a dual role: they are exploited by pathogen TAL effectors as susceptibility switches, but likely also serve as bona fide cis-regulatory elements for endogenous gene expression. This underscores the need to balance pathogen resistance and plant performance when deploying promoter edits.

Chapter 8 explores TAL effector traps: using prime editing to insert shared or strain-specific EBEs upstream of candidate executor genes to convert TALe attack into defense. A combinatorial screen highlighted numerous putative cross-lineage EBEs, and AvrXa7 designs were attempted as proof-of-concept with candidate R gene *OsMST4.* Although the specific prime-edited allele was not recovered, the work delineates concrete bottlenecks e.g. component expression and nuclear localization, pegRNA stability/structure, PBS/RT template design, chromatin access and provides a roadmap for improving edit efficiency and prioritizing EBEs with broad coverage across African and Asian Xoo TALe repertoires.

Chapter 9 described the development of a biosensor-based tool to monitor sucrose dynamics during infection. Given the centrality of sugar allocation to Xoo virulence, Matryoshka-based sucrose sensors for live imaging were established. by engineering Matryoshka-based, single-excitation sucrose biosensors (MSucMeters) that couple a cpsfGFP reporter to an LSSmApple reference within an AtThuE-split recognition scaffold. Affinity tuning via W283 substitutions (±D192N) yields KD values spanning ~0.42–2.63 mM, offering a practical dynamic range for diverse sucrose pools. In *E. coli*, sensors report uptake but do not saturate even at 23–115 mM external sucrose, implying transporter limitations in this chassis and motivating deployment in organisms/tissues with physiological sucrose transport.

Together with findings of Chapters 10–11, the toolkit to study rice-Xoo interaction expands further: attempts to visualize the T3SS injectisome via HrpE tagging

underscore the structural sensitivity of secretion machinery and point to alternative non-disruptive strategies; and a promoter-proximal dCas9–TurboID “proxisome” approach charts a path toward capturing the protein environment at *SWEET* promoters during TALe-driven transcriptional reprogramming. These chapters collectively advance methods for (i) quantifying sucrose dynamics, (ii) locating effector delivery, and (iii) defining proteomic landscapes at susceptibility loci, each informing mechanism-guided editing strategies for durable resistance

In summary, across five chapters we uncovered new insights into Xoo’s infection biology from cellular differentiation and movement in the host, to molecular host manipulation via TAL effectors and implementation of innovative genetic and imaging approaches to counteract and study the rice-Xoo pathosystem.

Implications

Collectively, these findings carry several biological and practical implications for plant pathology and crop protection. First, the discovery that Xoo can switch to a filamentous growth form *in planta* suggests a revision of the classic model of bacterial blight. Previously, Xoo was thought to cause disease primarily by multiplying inside xylem vessels and blocking water transport. The results indicate that tissue damage in blight is also due to invasive growth: filamentous Xoo physically breaching out of vessels into mesophyll likely exacerbates chlorosis and allows bacteria to access new cell types. This has practical implications, for instance, targeting the filamentation process itself could be a new anti-virulence strategy. If ways can be found that force Xoo to remain rod-shaped, they might contain the pathogen to xylem vessels where it causes less damage. In human medicine, inhibitors of filamentation have been explored to attenuate UPEC virulence (e.g. anti-UDPase compounds to prevent cell division arrest). One might screen for molecules that prevent Xoo filamentation (perhaps quorum-sensing disruptors or cell division triggers). However, caution is warranted because filamentation appears to be an adaptive response; completely blocking it might not kill the bacteria but could lead to other survival strategies. Nonetheless, recognition that Xoo differentiation is part of its pathogenic arsenal broadens our perspective on bacterial lifestyle *in planta* and could inform breeding.

The root infection barrier identified in Chapter 6 has implications for disease epidemiology and resistance breeding. It suggests that typical agricultural practices that limit leaf infection remain paramount, as root transmission is inefficient. Farmers do not be overly concerned about soilborne spread of Xoo under normal conditions, meaning resources can focus on foliar disease management. However, it also implies that if we could create rice varieties where even leaf infection mimics the root scenario (i.e. the bacteria are unable to go systemic from the entry point), we could effectively contain the disease. This might be achieved by strengthening xylem-based defenses, for example, inducing stronger pit membrane blocking or quicker occlusion of vessels upon infection (perhaps via bioengineering increased tylose formation or reactive oxygen bursts localized in xylem).

The findings in this thesis reinforce that editing *OsSWEET* promoters is a viable approach for durable blight resistance. A key implication is that regulatory approval and adoption of such edited crops could be more straightforward than undirected mutagenesis approaches, since the edits are small, precise, and can be designed to not interfere with native cis elements. This could accelerate the release of blight-resistant rice varieties carrying promoter edits. However, our findings also stress the importance of preserving the physiological roles of the targeted genes. For example, completely knocking out *OsSWEET14* might render roots stunted or less tolerant, whereas a subtle promoter edit can block pathogen induction but still allow adequate expression under native cues. Therefore, breeders and biotechnologists should aim for allele tweaks rather than null mutations in susceptibility genes to avoid negative pleiotropy. The dual role of EBEs we demonstrated means that each candidate edit should be evaluated in multiple environments (drought, high salt, etc.) to ensure no unintended sensitivities.

The concept of TAL effector traps/executor genes (Chapter 8) has far-reaching implications beyond just bacterial blight. If we can generalize this approach, we could engineer plants to turn the tables on pathogens that use transcriptional hijacking. For example, other *Xanthomonas* species that infect citrus or cassava also use TAL effectors to induce host genes (like *CsLOB1* in citrus canker). A similar trap strategy could be devised in those crops e.g. insert a TAL-binding sequence into a defense gene promoter. This expands the suite of resistance genes in breeding programs, essentially allowing endless customization of recognition specificities by editing

promoter sequences. One practical consideration is that pathogens could evolve away from the trap by simply not deploying that effector. However, because Xoo needs to induce at least one *SWEET* to cause disease, it cannot easily dispense with all effectors. Thus, any trap targeting a required effector should maintain selective pressure. It will be important though to stack multiple strategies: for instance, combine a promoter edit with an executor R gene so that even if one is bypassed, the other stops the pathogen. Such stacking could be done in a single variety thanks to multiplex genome editing. In a broader sense, this work exemplifies how precise genome editing enables creative resistance mechanisms that were not accessible via classical breeding.

Future research directions

This work opens several avenues for future investigation. One direction is to unravel the molecular mechanism and regulation of Xoo filamentation. Key questions include: *What triggers Xoo to filament inside the plant? Is filamentation cause or consequence of virulence?* The correlative data show filaments at late infection and associated tissue spread, but it remains possible that filamentation is simply an adaptive response with no direct role in virulence (e.g. cells filament as they exhaust nutrients, once the infection is already severe). I attempted to address this by monitoring timing: filaments appeared before extensive tissue collapse, hinting that they actively facilitate the spread. Genetic approaches would be needed to causally link filamentation to virulence. Future research could use transcriptomics or proteomics to compare rod-shaped vs. filamentous Xoo cells isolated from plants. This may reveal upregulated genes (for example cell division inhibitors, or cytoskeleton modifiers) during filamentation. Candidate regulators such as SOS response genes or the second messenger c-di-GMP pathway (which in many bacteria controls transitions between motile and biofilm lifestyles) merit exploration. Given that Xoo filaments were often observed near xylem pit membranes and entering new cells, it would be interesting to test if chemotaxis or nutrient sensing pathways are linked to filamentous growth. Perhaps filaments are guided by sucrose gradients. Live imaging with the MSucMeter sensor in Xoo-infected tissues could test if filaments are associated with regions of high sugar availability. From a broader perspective, comparing Xoo with *Xylella fastidiosa* or *Dickeya* (which also shows filamentation in some conditions) in terms of gene content might reveal common factors required for this phenotype.

Future research should also delve deeper into the Xoo–rice interaction in roots. The results raised the intriguing possibility that certain barriers prevent systemic movement. It would be valuable to identify what those barriers are. Does the nodal barrier simply never allow Xoo to pass (physical exclusion), or do rice roots mount a strong immune response? Using the root infection system, one could perform comparative transcriptomics of rice roots vs. leaves upon Xoo exposure. If roots massively upregulate defense genes relative to leaves, that might explain containment. A limitation is that the rapid inoculation system while novel, is an artificial scenario. In natural settings, Xoo would rarely encounter such immediate access to inner root tissues. Thus, the progression of infection front we measured using SWEET-GUS as proxy, may overestimate natural transmission. I also primarily monitored systemic movement over a relatively short time (days to weeks). It remains possible that given longer times or certain stress conditions (e.g. waterlogging), some cells could eventually reach the shoot. Ecologically, understanding if rice roots can harbor Xoo asymptomatically is also important. Even if disease doesn't show, roots could be a reservoir. Sensitive detection methods (qPCR, immunolocalization) after long-term co-culture of rice roots and Xoo could address this.

Conclusion

This thesis reframes bacterial blight as a disease of dynamic cellular differentiation, constrained movement, and exploitable transcriptional hijacking. I show that Xoo's switch to a filamentous state coincides with vascular bundle breach and mesophyll invasion, expanding pathology beyond simple xylem occlusion. I identified a stringent root-to-shoot transmission barrier that elevates the epidemiological importance of foliar entry routes. I demonstrate that precise editing of *OsSWEET* promoters can block TALe-driven susceptibility while preserving endogenous carbon partitioning, and I outline an extensible TAL effector trap framework to convert effector attack into defense. Complementing these insights, I introduce methodological concepts such as sucrose biosensors to quantify nutrient fluxes, visualize type III effector secretion, and biotinylation assays to identify proteomic landscape at susceptibility loci. Together, these advances argue for resistance strategies that aim for precise, fine-tuned editing sites that stack promoter edits with engineered executor R genes for durability. Future work dissecting the regulation and necessity of filamentation, defining the mechanistic

bases of root containment will further translate these findings into well informed breeding strategies and transferable concepts for other plant-pathogen systems.